THE MINISTRY OF SCIENCE AND HIGHER EDUCATION OF THE RUSSIAN FEDERATION

ST. PETERSBURG STATE POLYTECHNICAL UNIVERSITY

JOURNAL

Physics and Mathematics

VOLUME 16, No.1.3, 2023

Peter the Great St. Petersburg
Polytechnic University
2023

ST. PETERSBURG STATE POLYTECHNICAL UNIVERSITY JOURNAL. PHYSICS AND MATHEMATICS

The journal is included in the List of leading peer-reviewed scientific journals and other editions to publish major findings of theses for the research degrees of Doctor of Sciences and Candidate of Sciences.

The publications are presented in the VINITI RAS Abstract Journal and Ulrich's Periodical Directory International Database.

The journal is published since 2008 as part of the periodical edition 'Nauchno-tekhnicheskie vedomosti SPb-GPU'.

The journal is registered with the Federal Service for Supervision in the Sphere of Telecom, Information Technologies and Mass Communications (ROSKOMNADZOR). Certificate ПИ № ФС77-52144 issued December 11, 2012.

The journal is distributed through the CIS countries catalogue, the «Press of Russia» joint catalogue and the «Press by subscription» Internet catalogue. The subscription index is 71823.

The journal is in the **Web of Science** (Emerging Sources Citation Index), **Scopus,** the **Russian Science Citation Index** (RSCI) and the **Directory of Open Access Journals** (DOAJ) databases.

Address: 195251 Politekhnicheskaya St. 29, St. Petersburg, Russia.

Phone: (812) 294-22-85.

http://ntv.spbstu.ru/physics

PREFACE

24th Russian Youth Conference on Physics of Semiconductors and Nanostructures, Opto- and Nanoelectronics (RYCPS-2022)/ 24 Всероссийская молодежная конференция по физике полупроводников и наноструктур, полупроводниковой опто- и наноэлектронике

The 24th Russian Youth Conference on Physics of Semiconductors and Nanostructures, Opto- and Nanoelectronics (RYCPS-2022) was held in Saint Petersburg at Alferov University on November 28 – December 2, 2022. It was organized by Peter the Great St. Petersburg Polytechnic University, Alferov University, St. Petersburg State University, Ioffe Institute and Russian-Armenian University.

The program of the Conference included semiconductor technology, heterostructures with quantum wells and quantum dots, bulk properties of semiconductors, opto- and nanoelectronic devices and new materials. After two years of holding the Conference in a remote format, in 2022 it again was held as an in-person meeting. The Conference provided an opportunity for valuable discussions between the conference participants and experienced scientists.

The Conference included two invited talks given by leading scientists from Ioffe Institute, devoted to actual problems and major advances in physics and technology. The keynote speakers were *Andrey Bykov* (presentation "Antimatter in the Universe") and *Nikita Pikhtin* (presentation "The latest achievements and problems in the field of high-power injection lasers"). Students, graduate and postgraduate students presented their results on plenary and poster sessions. The total number of accepted abstracts published in Russian (the official conference language) was 109. Here we publish 32 selected papers in English.

Like previous years, the participants were involved in the competition for the best reports. Certificates and cash prizes were awarded to a number of participants for the presentations selected by the Program Committee. *Alexander Bazhenov* (Novosibirsk State University) was awarded for the best conference presentation among students with a report "Magneto-transport properties of thin films of topological insulator Bi_2Se_3". Alexey Romshin (Prokhorov General Physics Institute of the Russian Academy of Sciences, Moscow) was awarded for the best conference presentation among postgraduate students with a report "Enhancement of single-photon emission of "silicon-vacancy" centers in nanodiamonds on a gold film". *Sergey Melyakov*, a student at Moscow Institute of Physics and Technology, received the Evgeni Gross Prize for the best presentation on semiconductor optics with a report "Electronic spin dynamics in colloidal CdSe nanoplates". Works with potential applications were recommended for participation in the following competition for support from the Russian Foundation for Assistance to Small Innovative Enterprises in Science and Technology.

The conference was supported by the Ministry of Science and Higher Education of the Russian Federation (state assignment 075-03-2022-010/9), St. Petersburg Electrotechnical University and Tydex LLC, St. Petersburg.

The official conference website is http://www.semicond.ru/conf2022

Editors
R.A. Suris
D.A. Firsov
V.A. Shalygin
H.A. Sarkisyan

Contents

Bulk properties of semiconductors

Structure growth, surface, and interfaces

Heterostructures, superlattices, quantum wells

Quantum wires, quantum dots, and other low-dimensional systems

Optoelectronic and nanoelectronic devices

Novel materials

Bulk properties of semiconductors

Conference materials
UDC 537.6
DOI: https://doi.org/10.18721/JPM.161.301

Analytical and numerical calculations of the magnetic properties of a system of disordered spins in the Ising model

N.A. Bogoslovskiy ✉, P.V. Petrov, N.S. Averkiev

Ioffe Institute, St. Petersburg, Russia

✉ nikitabogoslovskiy@gmail.com

Abstract. We consider a system of randomly distributed magnetic atoms and describe the exchange interaction in the Ising model with a hydrogen-like dependence of the exchange energy on distance. The density of states for such system was calculated using an advanced numerical algorithm. Furthermore, the density of states was calculated analytically. We established that finding the density of states allows calculating the dependence of magnetic susceptibility of the system on temperature and magnetic field.

Keywords: Ising model, Wang–Landau algorithm, magnetic susceptibility

Citation: Bogoslovskiy N.A., Petrov P.V., Averkiev N.S., Analytical and numerical calculations of the magnetic properties of a system of disordered spins in the Ising model, St. Petersburg State Polytechnical University Journal. Physics and Mathematics. 16 (1.3) (2023) 7–13. DOI: https://doi.org/10.18721/JPM.161.301

Материалы конференции
УДК 537.6
DOI: https://doi.org/10.18721/JPM.161.301

Аналитический и численный расчеты магнитных свойств системы неупорядоченных спинов в модели Изинга

Н.А. Богословский✉, П.В. Петров, Н.С. Аверкиев

Физико-технический институт им. А.Ф. Иоффе, Санкт-Петербург, Россия

✉ nikitabogoslovskiy@gmail.com

Аннотация. Мы рассматриваем систему случайно распределенных магнитных атомов в модели Изинга с водородоподобной зависимостью обменной энергии от расстояния. Плотность состояний для такой системы посчитана численно и аналитически. Показано, что, зная плотность состояний, несложно рассчитать зависимость магнитной восприимчивости системы от температуры и магнитного поля.

Ключевые слова: модель Изинга, алгоритм Ванга-Ландау, магнитная восприимчивость

Ссылка при цитировании: Богословский Н.А., Петров П.В., Аверкиев Н.С. Аналитический и численный расчеты магнитных свойств системы неупорядоченных спинов в модели Изинга // Научно-технические ведомости СПбГПУ. Физико-математические науки. 2023. Т. 16. № 1.3. С. 7–13. DOI: https://doi.org/10.18721/JPM.161.301

Introduction

The exchange interaction of impurity atoms in semiconductors is actively studied. Interest in this topic grew significantly after the discovery of ferromagnetism in GaAs uniformly doped with a Mn magnetic impurity [1] (not due to Mn or MnAs clusters). At the moment, active experimental studies of the magnetic properties of semiconductors doped with non-magnetic impurities are being carried out [2-4]. The distribution of impurity atoms in semiconductors is random. However, the magnetic properties of materials are primarily theoretically studied in lattices that are either regular or close to regular. The magnetic properties of systems with a completely random distribution of magnetic atoms have not been thoroughly studied. This may be due both to the complexity of the considered model and to different approaches to describing regular and irregular systems. One of the main theoretical results in this field is the work [5], which predicts the absence of long-range magnetic order in a system of randomly distributed impurities with antiferromagnetic interaction. In our previous works [6, 7], we used a more correct expression for the dependence of the exchange energy on the distance. In the hydrogen-like model, the exchange energy of two spins at a distance r can be expressed as [8, 9]:

$$J = J_0 \left(\frac{r}{a} \right)^{2.5} \exp\left(-\frac{2r}{a} \right). \quad (1)$$

It was found in [6] that magnetic ordering is possible in a system of randomly distributed magnetic impurities. As the impurity concentration increases, the so-called spin-fluctuation phase transition occurs. In this case the amplitude of fluctuation of the magnetic moment increase, while the average magnetic moment of the system is equal to zero on both sides of the phase transition.

The magnetic properties of a system of randomly distributed impurities are often calculated using numerical methods, in particular, the Metropolis-Hastings algorithm [7, 10]. This algorithm starts with a random state of the spin system which is then thermalized to the required temperature. At low temperatures, the number of steps required for thermalization increases exponentially. In addition, the system may get in a pseudoground state, separated from lower energy states by a high energy barrier. In other words, at low temperatures the system is in the spin glass phase. Therefore, the Metropolis-Hastings algorithm is not efficient at low temperatures. In the present work, we used the Wang-Landau algorithm for accurate numerical calculation of the density of states and proposed an analytical expression for the density of states for a system of randomly distributed spins.

Numerical calculation

In this paper, we consider a system of randomly distributed spins and numerically and analytically calculate the dependence of the density of states on the total exchange energy E and the magnetic moment of the system M. For convenience, we denote the average magnetic moment of one spin, normalized to unity, by m. Then the total magnetic moment of the system $M = \mu mN$. Here μ is the magnetic moment modulus of one spin, N is the total number of spins in the system. Knowing the density of states $g(E, m)$, it is easy to calculate the average magnetic moment and magnetic susceptibility of the system as a function of temperature and magnetic field.

In the Ising model each spin can be directed up or down. That is, each spin has only two possible states. However, the number of possible states for a system of N spins is 2^N. For example, the number of different states for a system of only 100 spins is more than 10^{30}, and it is impossible to enumerate all the states even with the help of the fastest computers. The density of states can be found by the random walk method [10]. However, this method is only effective near the maximum of the density of states, producing large noise at the tails. A variation of the random walk method known as the Wang–Landau algorithm [11, 12] was used in this study.

Below we briefly consider the main idea of the Wang–Landau algorithm. Energy and magnetic moment are divided into small intervals. Initially, it is considered that the density of states for all values of energy and magnetic moment is equal to 1. Then random walks start, at each step

the density of states in the corresponding interval is increased by f times, where f is the so-called modification factor. Initially, modification factor is taken equal to e, this value is chosen for convenience. Then the modification factor is gradually reduced to increase the accuracy of the calculations. In addition to the density of states, we will count how many times the system appears in each interval during a random walk and save the corresponding value in the histogram $h(E, m)$.

At each step, we randomly select one spin and try to flip it. We calculate the energy E_1 and the magnetic moment m_1 before the spin flip, and the energy E_2 and the magnetic moment m_2 after the spin flip. The flip is accepted with probability $p(1 \to 2) = \min\left(\frac{g(E_1, m_1)}{g(E_2, m_2)}, 1\right)$. That is, we always accept transitions to less probable states, and the probability of transition to a more probable state depends on the ratio of densities of state in the initial and final states. Thus, the Wang–Landau algorithm is non-Markovian chain, the probability of transition to the next state depends on the history of previous transitions.

At the moment when the histogram $h(E, m)$ is flat enough, that is, the maximum and minimum values differ by no more than some specified amount (usually 80–90%), we decrease the modification factor and reset the histogram to zero. The algorithm terminates when the modification factor becomes small enough, so the density of states is known quite accurately.

Fig. 1 shows the calculated density of states for a system of $N = 512$ spins. The size of the system was chosen based on a reasonable calculation time. For example, it took about a week to calculate the density of states shown in the figure. The color in the figure shows the decimal logarithm of the density of states, that is, the maximum and minimum value of the density of states differ in this figure by 130 orders of magnitude. Notice that the noise on the tails of the density of states is minimal.

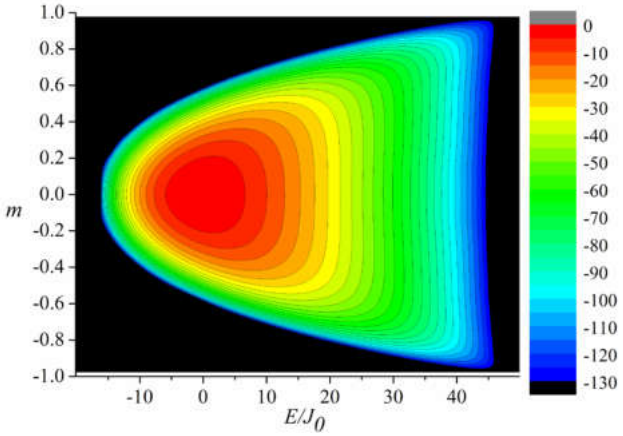

Fig. 1. Decimal logarithm of the density of states $g(E, m)$, normalized to the maximum value. Calculation for a system of $N = 512$ spins and concentration $na^3 = 0.03$

The complexity of the problem can be reduced and the size of the system can be increased if the density of states is calculated for a fixed value of the magnetic moment. The algorithm differs only in that at each step we try to simultaneously flip two randomly selected, oppositely directed spins in order to preserve the total magnetic moment of the system. Performing the numerical calculation, we generated a configuration of $N = 8192$ spins and then calculated the density of states for various values of the magnetic moment of the system for the same configuration of spins in space. The calculations were performed on the supercomputer at Peter the Great St. Petersburg Polytechnic University, allowing to calculate the density of states in parallel for 25 different values of the magnetic moment. The size of the system was determined based on a reasonable computation time, provided that the required computational accuracy is achieved.

It should be noted that the value of the energy of the system at the maximum of the density of states depends on the spatial distribution of the spins. This dependence is purely statistical in nature, the relative dispersion of the average energy decreases as $1/\sqrt{N}$ with an increase in the total number of particles in the system. However, the spread was still significant with the available size of the system. For this reason, we did not average over different spatial configurations.

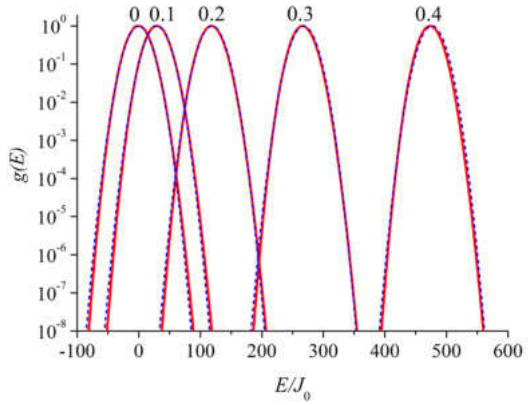

Fig. 2. Densities of states depending on the energy for different values of the magnetic moment m, the values are signed near the corresponding curves. Red lines correspond to numerical calculations using the Wang–Landau algorithm, blue dashed line to theoretical calculation by Eq. (5)
Calculations were performed for a system of $N = 8192$ spins and concentration $na^3 = 0.05$

The results of numerical calculations show that, at a fixed value of the magnetic moment, the density of states has a form close to a normal distribution (Fig. 2). Fig. 3 shows the position of the maximum and the dispersion of the distribution depending on the magnetic moment of the system m. It can be concluded that, in the considered range, the dispersion remains practically constant, and the position of the maximum has a quadratic dependence on m.

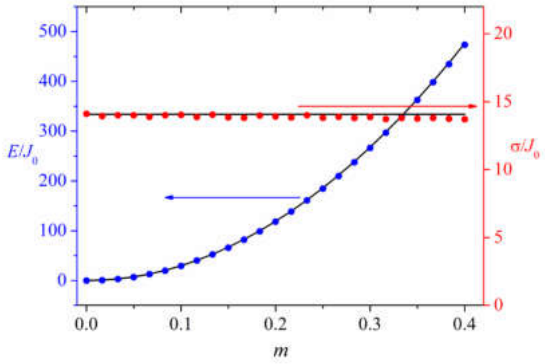

Fig. 3. Comparison of the average energy and dispersion of the distribution versus magnetic moment of the system, obtained by numerical simulation (dots) and by analytical equations (lines). The calculations were carried out for a system of $N = 8192$ spins and a concentration $na^3 = 0.05$

Analytical model

The density of states $g(E, m)$ can also be calculated analytically. The total exchange energy of the system of N interacting spins is the sum of $N(N-1)/2$ pair energies, each of which is a random variable. In accordance with the central limit theorem, the distribution of such a sum should be close to normal. This explains the form of the density of states obtained by numerical calculation. In order to write an analytical expression for the density of states, it is necessary to calculate the mean value and dispersion of the total exchange energy E. To calculate the average exchange energy, we first consider the system of spins with one orientation. We denote the average energy of the exchange interaction of one spin with all others as $\overline{J_1}$. The following expression [6] can be obtained for the exchange energy (1):

$$\overline{J_1} = \sqrt{\frac{\pi}{2}}\frac{945\pi}{2^8} na^3 J_0. \qquad (2)$$

Then, in a system of p "up" spins and q "down" spins, the average exchange energy is

$$\overline{E} = \frac{1}{2}\left(p\left(\frac{p-q}{p+q}\right) + q\left(\frac{q-p}{p+q}\right)\right)\overline{J_1} = \frac{1}{2}Nm^2\overline{J_1}. \quad (3)$$

For a system of randomly oriented spins, the average exchange energy of one spin is zero and the dispersion of the exchange energy of one spin will be equal to J_1^2. Then the dispersion of the total exchange energy will be equal to $\sigma^2 = \frac{1}{2}N\overline{J_1^2}$. For the exchange energy (1), one can obtain

$$\sigma^2 = \frac{7!\pi}{2^{15}}na^3NJ_0^2 = \frac{315\pi}{2^{11}}na^3NJ_0^2. \quad (4)$$

According to the results of numerical simulation, the dispersion of the exchange energy of the system is practically independent of m for $|m| < 0.4$. For large m, this is not the case; in particular, a fully magnetized system ($m = \pm 1$) has only one state, which means that the dispersion is zero. Therefore, the theoretical formulas written below are not applicable in the ferromagnetic phase at low temperatures.

Finally, in the Ising model, the total number of states in a system of N spins is 2^N, and the number of states with exactly p "up" spins is $C_N^p = C_N^{\frac{N(m+1)}{2}}$. Thus the density of states can be expressed as

$$g(E,m) = C_N^{\frac{N(m+1)}{2}}\frac{1}{\sqrt{2\pi\sigma}}\exp\left(-\frac{\left(E-\overline{E}\right)^2}{2\sigma^2}\right) = C_N^{\frac{N(m+1)}{2}}\frac{1}{\sqrt{2\pi\sigma}}\exp\left(-\frac{\left(E-\frac{1}{2}Nm^2\overline{J_1}\right)^2}{2\sigma^2}\right). \quad (5)$$

Let us assume that the density of states $g(E, m)$ is known from numerical or analytical calculations. In a magnetic field, the energy of the system will be the sum of the exchange energy E and the energy of interaction with the magnetic field $MB = \mu NmB$. Then the probability density versus energy E and magnetic moment m will be described by the Gibbs distribution and will be proportional to $g(E,m)\cdot\exp\left(-\frac{E+\mu NmB}{kT}\right)$. Using this expression, we can calculate all the parameters of the system of spins, such as the average magnetic moment or magnetic susceptibility:

$$\overline{M} = \frac{\mu N}{Z}\int dE\sum_m mg(E,m)\exp\left(-\frac{E+\mu NmB}{kT}\right), \quad (6)$$

where Z is statistical weight.

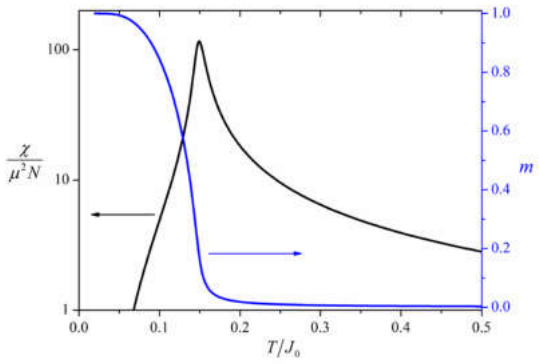

Fig. 4. Dependence of magnetic susceptibility and average magnetic moment per one spin on temperature

The main difficulty of analytical calculations in such a model is the calculation of binomial coefficients for large numbers. For example, for the studied system of 8192 spins, their value reaches 10^{2463}. However, the modern programming language julia supports both work with numbers of arbitrary length and parallel calculations, makes it possible to perform calculations in a reasonable time. As an example, Fig. 4 shows the calculated temperature dependence of magnetic susceptibility and average magnetic moment in a weak magnetic field.

Conclusion

To summarize, in this paper, we describe an efficient algorithm for numerical calculation of the density of states in a system of randomly distributed spins. Furthermore, we propose an analytical method for calculating the density of states in such a system. It is shown that knowing the density of states of the system allows to easily find the thermodynamic parameters of the system, in particular, the dependence of magnetic susceptibility and magnetic moment on temperature.

Acknowledgments

The results of the work were obtained using computational resources of the supercomputer center in Peter the Great Saint-Petersburg Polytechnic University Supercomputing Center.

REFERENCES

1. **Ohno H., Shen A., Matsukura F., Oiwa A., Endo A., Katsumoto S., Iye Y.** (Ga, Mn)As: A new diluted magnetic semiconductor based on GaAs, Applied Physics Letters 69 (1996) 363–365.

2. **Veinger A. I., Zabrodskii A. G., Lahderanta E., Semenikhin P. V.** Detection of the Ferromagnetic Properties of Si:P in the Region of an Insulator–Metal Phase Transition. Jetp Letters 115 (2022) 685–690.

3. **Zabrodskii A. G., Veinger A. I., Semenikhin P. V.** Effect of Compensation on Low-Temperature Spin Ordering in Ge:As Semiconductor Near the Insulator–Metal Phase Transition. Appl. Magn. Reson. 51 (2020) 327–347.

4. **Zabrodskii A. G., Veinger A. I., Semenikhin P. V.** Anomalous Manifestation of Pauli Paramagnetism and Coulomb Blockade of Spin Exchange upon the Compensation of Doped Semiconductors, Phys. Status Solidi B, 257(1) (2020) 1900249.

5. **Bhatt R. N., Lee P. A.** Scaling Studies of Highly Disordered Spin-S Antiferromagnetic Systems, Phys. Rev. Lett., 48 (1982) 344–347.

6. **Bogoslovskiy N. A., Petrov P. V., Averkiev N. S.** Spin-Fluctuation Transition in the Disordered Ising Model. Jetp Lett. 114, (2021) 347–353.

7. **Bogoslovskiy N. A., Petrov P. V., Averkiev N. S.** The Impurity Magnetic Susceptibility of Semiconductors in the Case of Direct Exchange Interaction in the Ising Model, Phys. Solid State 61 (2019) 2005–2009.

8. **Gor'kov L. P., Pitaevskii L. P.** Term Splitting Energy of the Hydrogen Molecule Soviet Physics Doklady, 8 (1964) 788.

9. **Herring C., Flicker M.** Asymptotic Exchange Coupling of Two Hydrogen Atoms, Phys. Rev., 134(2A) (1964) A362.

10. **Landau D. Binder K.** A guide to Monte Carlo simulations in statistical physics. Cambridge university press, 2021.

11. **Wang F., Landau D. P.** Efficient, multiple-range random walk algorithm to calculate the density of states, Physical Review Letters, 86(10) (2001) 2050.

12. **Landau D. P., Tsai, S. H., Exler, M.** A new approach to Monte Carlo simulations in statistical physics: Wang-Landau sampling, American Journal of Physics, 72(10) (2004) 1294–1302.

THE AUTHORS

BOGOSLOVSKIY Nikita A.
nikitabogoslovskiy@gmail.com
ORCID: 0000-0002-2265-0245

PETROV Pavel V.
pavel.petrov@gmail.com
ORCID: 0000-0001-7791-567X

AVERKIEV Nikita S.
averkiev@les.ioffe.ru
ORCID: 0000-0002-0772-7072

Received 29.11.2022. Approved after reviewing 23.01.2023. Accepted 25.01.2023.

Conference materials
UDC 535.3
DOI: https://doi.org/10.18721/JPM.161.302

Terahertz and stimulated near-infrared photoluminescence in bulk *n*-GaAs layers

A.D. Petruk [1] ✉, N.Yu. Kharin [1], M.Ya. Vinnichenko [1],
I.A. Norvatov [1], V.V. Fedorov [2], D.A. Firsov [1]

[1] Peter the Great St. Petersburg Polytechnic University, St. Petersburg, Russia;
[2] Alferov University, St. Petersburg, Russia
✉ ianton583@gmail.com

Abstract. The work considers the methods for increasing the intensity of low temperature terahertz luminescence in semiconductor structures with bulk epitaxial *n*-GaAs layers doped with silicon donors under interband optical pumping. Such an increase can be realized due to the accelerated depopulation of the ground impurity level by stimulated near-infrared radiation, which is created in the same structure. Stimulated interband emission was induced by a total internal reflection optical resonator. Samples were investigated by measuring the near-infrared photoluminescence and terahertz photoluminescence at liquid helium temperature. Impurity-assisted near-infrared spontaneous and stimulated photoluminescence and their dependences on optical pumping power was demonstrated. Impurity-assisted generation of terahertz radiation was observed in further intention to investigate the influence of near-infrared stimulated emission on it. Obtained results can be used in the development of new semiconductor terahertz emitters.

Keywords: photoluminescence, terahertz emission, gallium arsenide, impurities, stimulated radiation

Funding: This work was supported by the Russian Science Foundation (grant № 22 22 00105).

Citation: Petruk A.D., Kharin N.Yu., Vinnichenko M.Ya., Norvatov I.A., Fedorov V.V., Firsov D.A., Terahertz and stimulated near-infrared photoluminescence in bulk *n*-GaAs layers, St. Petersburg State Polytechnical University Journal. Physics and Mathematics. 16 (1.3) (2023) 14–19. DOI: https://doi.org/10.18721/JPM.161.302

Материалы конференции
УДК 535.3
DOI: https://doi.org/10.18721/JPM.161.302

Терагерцовая и стимулированная ближняя инфракрасная фотолюминесценция в объёмных слоях *n*-GaAs

А.Д. Петрук [1] ✉, Н.Ю. Х рин [1], М.Я. Винниченко [1],
И.А. Норв тов [1], В.В. Фёдоров [2], Д.А. Фирсов [1]

[1] Санкт-Петербургский политехнический университет Петра Великого, Санкт-Петербург, Россия;
[2] Академический университет им. Ж.И. Алфёрова РАН, Санкт-Петербург, Россия
✉ ianton583@gmail.com

Аннотация. Работа посвящена исследованию возможности увеличения интенсивности низкотемпературной терагерцовой люминесценции в полупроводниковых структурах с объёмными эпитаксиальными слоями *n*-GaAs, легированными донорной примесью кремния, при межзонной оптической накачке. Такое увеличение может быть реализовано за счет ускоренного опустошения основного примесного уровня стимулированным излучением ближнего инфракрасного диапазона, которое создается в той же самой структуре. Для организации вынужденного межзонного излучения были изготовлены образцы в геометрии оптического резонатора полного внутреннего отражения. Исследовалась

фотолюминесценция в ближнем инфракрасном и терагерцовом диапазонах при температуре жидкого гелия. Продемонстрирована спонтанная и стимулированная фотолюминесценция с участием примесных состояний в ближнем инфракрасном диапазоне, измерена эволюция спектров от мощности оптической накачки. Наличие в структуре излучения терагерцового диапазона с участием донорных состояний позволит в дальнейшем исследовать влияние на него стимулированного излучения ближнего инфракрасного диапазона. Полученные результаты могут быть использованы при разработке новых полупроводниковых источников терагерцового излучения.

Ключевые слова: фотолюминесценция, терагерцовая эмиссия, арсенид галлия, примеси, стимулированное излучение

Финансирование: Исследование влияния стимулированного излучения ближнего инфракрасного диапазона на терагерцовую люминесценцию в полупроводниковых микро- и наноструктурах, грант Российского научного фонда № 22-22-00105.

Ссылка при цитировании: Петрук А.Д., Харин Н.Ю., Винниченко М.Я., Норватов И.А., Фёдоров В.В., Фирсов Д.А. Терагерцовая и стимулированная ближняя инфракрасная фотолюминесценция в объёмных слоях *n*-GaAs // Научно-технические ведомости СПбГПУ. Физико-математические науки. 2023. Т. 16. № 1.3. С. 14–19. DOI: https://doi.org/10.18721/JPM.161.302

Introduction

Creating compact and efficient sources of radiation in the terahertz (THz) range is one of the urgent tasks of modern optoelectronics. Terahertz radiation finds application in systems of chemical, medical diagnostics, and security systems [1–2]. Now, the only high-power semiconductor sources of THz radiation are quantum-cascade lasers [3]. However, the complexity of the production technology greatly limits the usage of such lasers and creates the necessity to search for alternative semiconductor sources of THz radiation. One of the approaches to the development of such sources is the use of optical transitions of nonequilibrium charge carriers with the participation of shallow impurity states in semiconductors.

For the first time, impurity-assisted THz radiation upon optical pumping was observed in bulk silicon layers doped with phosphorus [4]. Intraband pumping was performed using CO_2 laser, whose radiation excites charge carriers from the ground and lower impurity states to the higher excited or band states. Terahertz photoluminescence was also observed in bulk semiconductors doped with donors (*n*-GaAs) upon interband optical pumping [5].

The intensity of impurity-assisted THz emission depends on the population of the ground state. For the first time, depopulation of the ground state with stimulated near-infrared (NIR) radiation was used in diode structures with quantum dots to obtain mid-IR radiation [6]. Further studies of the effect of stimulated depopulation of the ground donor state on the intensity of terahertz radiation were carried out in structures with quantum wells (QWs) based on GaAs/AlGaAs under optical interband excitation [7–8].

The current work is devoted to further investigation of possibilities to increase the intensity of THz photoluminescence in doped semiconductor structures. The use of bulk *n*-GaAs epitaxial layers will make it possible to increase the radiation intensity due to the larger volume of the active region compared to QW structures.

Materials and Methods

The structure was grown by molecular beam epitaxy on a semi-insulating GaAs substrate. The active region contained a 0.52 μm thick GaAs layer doped with silicon to a concentration of 10^{16} cm^{-3} and embedded into the waveguide. Symmetric waveguide for the NIR radiation was formed by $Al_xGa_{1-x}As$ graded layers. Terahertz radiation was observed on samples 5×5 mm^2 in size. To obtain the stimulated NIR radiation, total internal reflection optical resonator was formed with dimensions of 0.6×0.6 mm^2. To study photoluminescence in the substrate, the epitaxial layers were removed from one of the samples.

For measurements, samples were mounted in a Janis PTCM-4-7 closed-cycle optical cryostat and cooled down to about 4.2 K. The optical pumping was performed by Nd:YAG pulsed laser ($\lambda = 532$ nm, pulse duration 250 ns, repetition rate 8 kHz). The pumping power was varied using an attenuator consisted of a half wave plate and a Glan-Taylor prism and measured by Thorlabs PM100D optical power and energy meter. The pumping laser radiation was directed and focused on the sample surface using a series of mirrors and converging lens. The diameter of the laser spot on the surface of the structure was about 0.9 mm, covering the whole area of a sample with a resonator.

The NIR interband photoluminescence spectra were measured by Horiba Jobin Yvon FHR 640 monochromator with 1200 groves/mm holographic grating and CCD detector. The THz photoluminescence spectra were measured by Bruker Vertex 80v vacuum Fourier transform spectrometer with Mylar beamsplitter operated in step-scan mode. The pumping laser radiation was modulated with optical chopper at 87 Hz. The luminescence collected from the sample passed through TPX windows and black polyethylene filter. The intensity of THz radiation was detected by liquid helium-cooled silicon bolometer. The detector photoresponse signal was measured by the SR830 lock-in amplifier synchronized in phase and frequency with the chopper.

Results and Discussion

Near-infrared photoluminescence spectra of structure and substrate at 4.2 K are presented in Fig. 1. At a low pumping power, the spectra of a sample without a resonator and a sample with a resonator are similar and are presented by black curve in Fig. 1. The energy of GaAs band gap is marked by E_g arrow at 1.519 eV. The binding energy of shallow donors in GaAs is 5.9 ± 0.1 meV [9], which corresponds to the distance between the *D-h* arrow (optical transition from the ground donor state to the valence band), and E_g value. The X arrow marks donor-bound exciton recombination energy. Residual acceptors may be contained in the substrate or introduced during epitaxial growth. Typical GaAs residual impurity is carbon (the binding energy is about 26 meV [10]). Acceptor assisted transition is marked by *e-A* arrow at 1.492 eV. The photoluminescence spectra of sample with a resonator at high pumping power demonstrated the same features, but also shown up the peak of stimulated emission (see red curve in Fig. 1). The blue curve in Fig. 1 shows the spectrum of the substrate. Impurity-assisted *e-A* peak and low-intensity exciton recombination peak are observed in the substrate spectrum.

The evolution of the NIR photoluminescence spectra of the sample with a resonator upon increasing pumping power is presented in Fig.2. Relatively narrow and intense emission line on the longwave side of the *D-h* donor peak marked by an arrow *Stimulated* in Fig. 1 and 2 is the line of stimulated emission. This stimulated luminescence line is presented in the spectrum at a pumping intensity above 320 W/cm^2, which is the near-infrared lasing *Threshold* (marked with an arrow in the inset to Fig.2). The inset in Fig. 2 shows the dependences of the integrated THz luminescence intensity on the pumping power. The intensity of the stimulated peak makes a

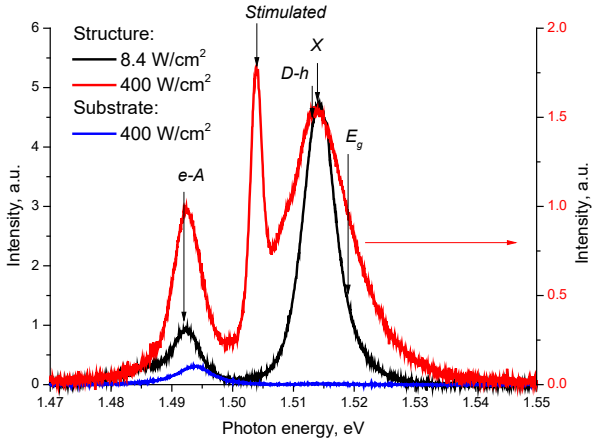

Fig. 1. Near-infrared photoluminescence spectra of the structure and substrate measured at the $T = 4.2$ K for different pumping levels. The spectral resolution is about 0.12 meV for structure spectra and 0.8 meV for substrate spectrum

significant contribution to the total intensity of the interband radiation of the sample (marked as *Sum*) at high pump power. At the level of threshold total intensity has an inflection point. The intensity of the spontaneous luminescence peak (marked as *D-h spontaneous*) saturates that is typical for semiconductor lasers.

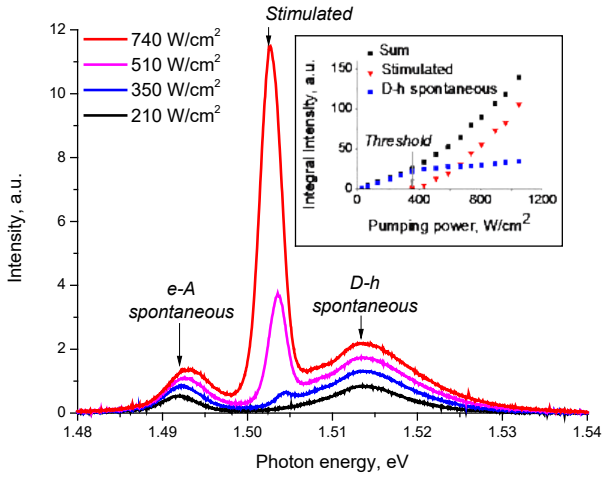

Fig. 2. Near-infrared photoluminescence spectra of the structure with a resonator measured at T = 4.2 K for different pumping levels. Spectral resolution is about 0.12 meV. The inset shows dependence of integrated near-infrared photoluminescence intensity on the optical pumping power

Fig. 3 shows the THz photoluminescence spectra at 4.2 K. The red curve shows the THz photoluminescence spectrum of sample without resonator. Binding energy of shallow silicon donors in GaAs is marked by *e-D* arrow at 5.9 meV [9]. The spectrum has a peak at a slightly higher photon energy (about 7.75 meV). This corresponds to the fact that the transition at exactly the photon energy equal to the binding energy is forbidden and to electron heating effects. The emission peak at 11 meV cannot correspond to electron transitions involving a silicon impurity. The same peak was observed in the measurements of THz photoluminescence in Ref. [5] where it was associated with residual extrinsic defects in GaAs. The emission band at energies of 15–28 meV replicates the photoluminescence spectrum of the substrate (see black curve in Fig. 3). Thus, residual acceptor-assisted radiative transitions both from the substrate and from the epitaxial layers may contribute to the THz luminescence. The THz emission band marked as *Substrate* is typical for such experiments and can either be observed [11] or not be observed [8] in similar samples, depending on the quality of the substrate and the grown structures. Based on this, we can conclude that the THz emission band in the range of 5–12 meV is associated precisely with the epitaxial layers, and not with the substrate.

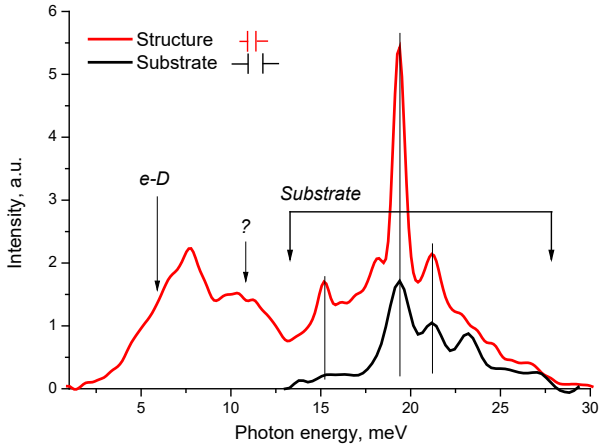

Fig. 3. Terahertz photoluminescence spectra of a structure without a resonator and of a substrate measured at T = 4.2 K

Conclusion

Impurity-assisted photoluminescence in the near-infrared and terahertz spectral ranges was demonstrated for the structure with bulk semiconductor *n*-GaAs epitaxial layers embedded in a waveguide. A narrow and intensive line of stimulated emission in the near-infrared range was observed for the samples with four cleaved facets resonator. The appearance of stimulated near-infrared radiation and spontaneous terahertz radiation makes it possible to study the effect of depopulation of the donor ground state on the characteristics of terahertz radiation in bulk *n*-GaAs layers.

Acknowledgments

This work was supported by the Russian Science Foundation (grant № 22-22-00105, https://rscf.ru/project/22-22-00105/).

REFERENCES

1. **Gong, A., Qiu, Y., Chen, X., Zhao, Z., Xia, L., Shao, Y.,** Biomedical applications of terahertz technology. Applied Spectroscopy Reviews. 55(5) (2020) 418–438.

2. **Bogue R.,** Sensing with terahertz radiation: a review of recent progress. Sensor. 38 (2) (2018) 216.

3. **Belkin M.A., Capasso F.,** New frontiers in quantum cascade lasers: high performance room temperature terahertz sources. Physica Scripta. 90 (11) (2015) 118002.

4. **Pavlov S.G., Zhukavin R.Kh., Orlova E.E., Shastin V.N., Kirsanov A.V., Hübers H.W., Auen K., Riemann H.,** Stimulated Emission from Donor Transitions in Silicon. Physical Review Letters. 84 (2000) 5220.

5. **Zakhar'in A.O., Andrianov A.V., Egorov A.Yu., Zinov'ev N.N.,** Terahertz photoluminescence from GaAs doped with shallow donors at interband excitation. Applied physics letters. 96 (21) (2010) 211118.

6. **Vorob'ev L.E., Firsov D.A., Shalygin V.A., Tulupenko V.N., Shernyakov Yu.M., Ledentsov N.N., Ustinov V.M., Alferov Zh.I.,** Spontaneous far-IR emission accompanying transitions of charge carriers between levels of quantum dots. JETP Letters. 67(4) (1998) 275.

7. **Makhov I.S., Panevin V.Yu., Sofronov A.N., Firsov D.A., Vorobjev L.E., Vinnichenko M.Ya., Vasil'ev A.P., Maleev N.A.,** The effect of stimulated interband emission on the impurity-assisted far-infrared photoluminescence in GaAs/AlGaAs quantum wells. Superlattices and Microstructures. 112 (2017) 79–85.

8. **Makhov I.S., Panevin V.Yu., Firsov D.A., Vorobjev L.E., Vasil'ev A.P., Maleev N.A.,** Terahertz photoluminescence of the donor doped GaAs/AlGaAs quantum wells controlled by the near-infrared stimulated emission. Journal of Luminescence. 210 (2019) 352–357.

9. **Almassy R.J., Reynolds D.C., Litton C.W., Bajaj K.K., McCoy G.L.,** Observation of shallow residual donors in high purity epitaxial GaAs by means of photoluminescence spectroscopy. Solid State Communications. 38 (1981) 1053.

10. **Kisker D.W., Tews H., Rehm W.,** Luminescence study of C, Zn, Si, and Ge acceptors in GaAs. Journal of Applied Physics. 54 (1983) 1332.

11. **Vorobjev L.E., Firsov D.A., Panevin V.Yu., Sofronov A.N., Balagula R.M., Makhov I.S.,** Near- and far-infrared emission from GaAs/AlGaAs quantum wells under interband optical excitation. St. Petersburg State Polytechnical University Journal. Physics and Mathematics. 4(182-2) (2013) 109–114.

THE AUTHORS

PETRUK Anton D.
ianton583@gmail.com
ORCID: 0000-0003-1824-9173

KHARIN Nikita Yu.
kharin.nikita66@gmail.com
ORCID: 0000-0002-2220-881X

VINNICHENKO Maksim Ya.
mvin@spbstu.ru
ORCID: 0000-0002-6118-0098

NORVATOV Ilya A.
norv2@mail.ru
ORCID: 0000-0002-0048-7512

FIRSOV Dmitry A.
dmfir@rphf.spbstu.ru
ORCID: 0000-0003-3947-4994

FEDOROV Vladimir V.
burunduk.uk@gmail.com
ORCID: 0000-0001-5547-9387

Received 06.12.2022. Approved after reviewing 08.12.2022. Accepted 14.12.2022.

Conference materials
UDC 535
DOI: https://doi.org/10.18721/JPM.161.303

Study of properties of the nuclear spin system in bulk *n*-GaAs by warm-up spectroscopy

V.M. Litvyak [1] ✉, R.V. Cherbunin [1], F.Yu. Soldatenkov [2], V.K. Kalevich [1,2], K.V. Kavokin [1]

[1] Spin Optics Laboratory, St. Petersburg State University, St. Petersburg, Russia;
[2] Ioffe Institute, St. Petersburg, Russia
✉ valiok.ok@gmail.com

Abstract. In this paper, we present an overview of the possibilities of nuclear spin warm-up spectroscopy method. Nuclear spin warm-up spectroscopy method is based on optical cooling and subsequent warming up of nuclear spins by oscillating magnetic field. Changes of nuclear spin temperature before and after applying of oscillating magnetic field are determined from the degree of photoluminescence polarization. This method is applied to studying the properties of the cooled nuclear spin system in bulk *n*-GaAs crystals. Using warm-up spectroscopy, we can investigate such thermodynamical characteristics of cooled nuclear spins as local fields, absorption coefficients and fluctuations spectral density (correlator spectrum). In particular, such experimental opportunities accompanied by theoretical interpretations allows us to investigate and control the presence of quadrupole interactions in structures. Furthermore, the nuclear spin fluctuations are reflected in the correlator spectrum, which can be recalculated from absorption coefficients. Measurements of the nuclear spin correlator are important experimental opportunity because fluctuations of nuclear spins are one of the main sources of electron spin decoherence in *n*-GaAs.

Keywords: nuclear spin system, optical cooling, absorption spectrum, nuclear spin correlator, local field

Funding: The study was carried out as part of State Assignment “SPbGU” (Topic ID [94030557]), whose funding was used to grow the structures considered. The authors express their gratitude to grant 22-42-09020 from the Russian Science Foundation for funding the experiments.

Citation: Litvyak V.M., Cherbunin R.V., Soldatenkov F.Yu., Kalevich V.K., Kavokin K.V., Study of properties of the nuclear spin system in bulk *n*-GaAs by warm-up spectroscopy, St. Petersburg State Polytechnical University Journal. Physics and Mathematics. 16 (1.3) (2023) 20–25. DOI: https://doi.org/10.18721/JPM.161.303

Материалы конференции
УДК 535
DOI: https://doi.org/10.18721/JPM.161.303

Изучение свойств ядерной спиновой системы объемных слоев n-GaAs методом спектроскопии отогрева

В.М. Литвяк [1] ✉, Р.В. Чербунин [1], Ф.Ю. Солдатенков [2], В.К. Калевич [1,2], К.В. Кавокин [1]

[1] Лаборатория Оптики Спина им. И. Н. Уральцева, СПбГУ, Санкт-Петербург, Россия;
[2] Физико-технический институт им. А.Ф. Иоффе РАН, Санкт-Петербург, Россия
✉ valiok.ok@gmail.com

Аннотация. В данной работе представлены возможности экспериментальной методики спектроскопии отогрева ядерных спинов. Данная методика основана на отогреве переменным магнитным полем оптически охлажденных ядерных спинов. Она позволяет изучать термодинамические характеристики охлажденной спиновой системы ядер объемных слоев *n*-GaAs. К таким характеристикам можно отнести спектры отогрева

и ядерного спинового коррелятора, а также ядерные локальные поля. Создание данной методики направлено на изучение и анализ ядерных спиновых флуктуаций с целью их дальнейшего контроля и подавления.

Ключевые слова: ядерная спиновая система, оптическое охлаждение, спектр поглощения, ядерный спиновый коррелятор, локальное поле

Финансирование: Работа выполнена в рамках Государственного задания «СПбГУ» (код темы [94030557]), с поддержкой которого были выращены изучаемые структуры. Авторы также выражают благодарность гранту РНФ No 22-42-09020 за финансовую поддержку в проведении экспериментальных исследований.

Ссылка при цитировании: Литвяк В.М., Чербунин Р.В., Солдатенков Ф.Ю., Калевич В.К., Кавокин К.В. Изучение свойств ядерной спиновой системы объемных слоев *n*-GaAs методом спектроскопии отогрева // Научно-технические ведомости СПбГПУ. Физико-математические науки. 2023. Т. 16. № 1.3. С. 20–25. DOI: https://doi.org/10.18721/ JPM.161.303

Introduction

One of the main tasks of modern spintronics is the realization of the possibility of using the electron spin as an information carrier. However, the main obstacle to this is the electron spin relaxation. We need to look for ways to increase the electron spin lifetime. In bulk *n*-GaAs structures, the maximum of an electron lifetime localized on a donor center is observed at a donor impurity concentration near the metal-insulator transition [1]. Therefore, it is promising to use *n*-GaAs samples with a donor concentration of the order of $n_D = 10^{15}$–10^{16} cm^{-3}. Wherein in such structures, one of the main mechanisms of electron spin relaxation is the interaction with nuclear spin fluctuations [1, 2]. To increase the electron spin lifetime, one must be able to control and, ideally, suppress the nuclear spin fluctuations.

Suppression of nuclear spin fluctuations is possible at ultralow nuclear spin temperatures, on the order of fractions of a microkelvin. At such temperatures, a transition of nuclear spins to a magnetic order is expected. In 1997, Merkulov proposed the theoretical concept of a nuclear spin polaron in bulk *n*-GaAs [3]. According to Merkulov, when the nuclear spin system (NSS) is cooled to temperatures of the order of fractions of a microkelvin, nuclear spins are expected to pass into an ordered state in the vicinity of the donor center, due to hyperfine interaction with the electron. To date, there have been published several theoretical works about on the nuclear spin ordering due to hyperfine interaction in semiconductors [4–6]. But none of these ordered states has yet been observed experimentally. However, this is one of the main possibilities for suppressing nuclear spin fluctuations. The detection of the pre-polaron state is supposed to be based on the change in the low-frequency part of the nuclear spin fluctuations spectrum (correlator spectrum) [3, 6]. It is expected that as the nuclear spin system (NSS) approaches to the ordered state, the low-frequency part of the correlator spectrum should increase its magnitude. To observe this effect, it is necessary to implement two conditions of the experiment. It is necessary to be able to cool the NSS to microkelvin spin temperatures and to reliably measure the nuclear spin correlator. The nuclear spin warm-up spectroscopy method, proposed in this paper, allows one to carry out experiments on deep cooling of the NSS in *n*-GaAs. Also, using this method, we can obtain the correlator spectrum of optically cooled nuclear spins by measuring the absorption coefficients at different frequencies of an oscillating magnetic field (OMF).

In this paper, we present the results obtained with nuclear spin warm-up spectroscopy method for bulk *n*-GaAs samples. The basics of this method were laid in early works of 1980s [7, 8], where first absorption spectra of the NSS in a bulk *n*-GaAs sample were measured, but the physical mechanisms of formation of the obtained spectra were not elucidated. To date, we have come closer to understanding the physical foundations of absorption spectra. In particular, it turned out that even otherwise insignificant quadrupole effects have a strong influence on their shape

[9, 10]. We have not yet fully explored the mechanisms which determine the nuclear spin correlator spectra. However, the correlators measured by our method are qualitatively consistent with the shapes of spin correlation functions, obtained earlier by numerical modeling [11, 12]. This gives us confirmation that our nuclear spin warm-up spectroscopy method really makes it possible to detect nuclear spin fluctuations. It means that the development of this method together with a theoretical analysis will eventually allow us to learn how to detect an approach of the NSS to the polaron state.

Materials and Methods

With the help of nuclear spin warm-up spectroscopy method, the NSS of bulk *n*-GaAs layers with donor impurity concentrations in the range of 10^{15}–10^{16} cm^{-3} was studied. The samples under studies were grown by liquid-phase epitaxy. The scheme of the experimental setup is given in [9]. The sample under study was placed in a closed cycle cryostat and cooled down to 6 K. Radiation from a laser diode at a wavelength of 780 nm passed through a quarter-wave plate, creating a circularly polarized optical pump, and was focused on the sample surface. The polarized photoluminescence (PL) signal passed through a photoelastic modulator (PEM) and a linear polarizer and was focused on the slit of the spectrometer. The spectrometer passed the PL line at a wavelength of 817–819 nm (depending on the sample under study), which then was focused on the photodiode chip. The PL intensity was determined using a two-channel photon counter connected to a photodiode and synchronized with the PEM. All measurements were carried out by detecting the change in the degree of PL polarization with time.

As some examples of experimental results, the measured absorption spectra in a zero magnetic field, the correlator spectrum, and the magnitude of the local field will be given in this work. To obtain these characteristics, we used a multi-stage experimental protocol proposed in [7, 8] and developed in [9, 10].

The experimental protocol used to obtain the absorption spectrum in zero magnetic field consisted of four stages. The first stage is called preparatory. The NSS was in the dark during the minute. By the end of this stage, the NSS came to thermodynamically equilibrium state. The next stage was optical cooling of the NSS. For a minute, the sample was pumped with circularly polarized light in a longitudinal magnetic field B_Z = 150 G. Spin-polarized electrons polarized nuclear spins due to hyperfine interaction. By the end of the second stage, a nuclear field and the corresponding spin temperature, different from the lattice temperature, were created. This was followed by adiabatic demagnetization to zero external field. The longitudinal field B_Z was switched off to zero during a time is equal to 20 ms. After demagnetization, the spin temperature decreased by several orders of magnitude. For structures under study at the described experimental conditions the nuclear spin temperature was about 100 μK. The third stage was the application of an OMF in the dark for 3 s at a fixed frequency. To obtain the absorption spectrum in a zero static magnetic field, the frequencies were chosen from the range from 100 Hz to 20 kHz at a fixed amplitude of OMF. After the applying of OMF, the nuclear spin temperature was increased. The heating process took place at the rate of $(1/T_\omega + 1/T_1)^{-1}$, where $1/T_\omega$ is the heating rate due to the impact of OMF on the NSS at a frequency ω, $1/T_1$ is the relaxation rate of the NSS due to spin-lattice relaxation. The last step was measuring the nuclear field B_N, which remain after OMF application. To do this, the pump and the transverse magnetic field B_X (measurement field) were switched on. Electron spins depolarized in the total field $B_X + B_N$, and then during the whole measuring stage (about 200 s) the nuclear field B_N decreased due to spin-lattice relaxation, and the electron polarization was restored. An example of the protocol described above is given in [9] in Fig. 3.

The rate of the NSS heating is related to the magnitude of the nuclear field B_N remaining after the application of OMF at frequency ω by the following formula: $1/T_\omega = (1/t_{OMF})\cdot\ln[B_N(\omega)/B_{N0}]$, where B_{N0} is the value of the nuclear field in the case, when in the third stage the OMF was not applied. Ref. [9] describes in detail how to extract the absorption coefficient $1/T_\omega$ from the fitting of a multi-stage curve.

Spectral fluctuation density G_ω (nuclear spin correlator) is related to the heating rate by the following formula: $G_\omega = (1/T_\omega)\cdot(4B_L^2/\omega^2 B_1^2)$ [7], where B_L is the local field, B_1 is the amplitude of OMF, ω is the frequency of OMF. Therefore, the experimental protocol for obtaining the correlator spectrum remains the same. The only difference is that the measurement takes place in a narrower and lower frequency range of OMF frequencies: from 10 Hz to 15 kHz.

To measure the magnitude of the local field B_L, the stage of an OMF application is not needed. Therefore, only three stages remain from the protocol described above: thermalization, optical cooling with adiabatic demagnetization and measurement. In order to determine the value of the local field, we proceeded to the last stage, carrying out measurements with the magnitude of B_X varied from 0.2 G to 7 G at a step from 0.1 to 1 G, depending on steepness of the dependence $B_N(B_X)$. Further, from each measurement the nuclear field B_N was extracted, and compared with the theoretical dependence:

$$B_N = b_N \hbar \langle \gamma_N \rangle \frac{I(I+1)}{3k_B} B_X \beta \sqrt{\frac{B_L^2}{B_L^2 + B_X^2}}, \quad (1)$$

where b_N is the Overhauser field at full nuclear polarization, k_B is the Boltzmann constant, $\hbar$ is the Planck constant, $\langle \gamma_N \rangle$ is the average gyromagnetic ratio of the NSS of GaAs, $I = 3/2$ is the nuclear spin, β is the inverse nuclear spin temperature. The obtained dependence $B_N(B_X)$ was fitted by Eq. (1) with the value of B_L as a free parameter. In this way, the value of the local field was determined.

Results and Discussion

In this section, examples of absorption spectra at zero external magnetic field, correlator spectrum and experiment for determination of the local field are presented. These results demonstrate the experimental possibilities of the nuclear spin warm-up spectroscopy method. Also, it should be noted, that for results, presented below, the value of the nuclear spin temperature that was reached by the end of the second stage of multistage measurements (after adiabatic demagnetization) was several orders of magnitude higher than the temperature required to achieve the polaron state. Obtaining ultralow nuclear spin temperatures is a separate experimental direction, not included in this paper.

Absorption spectra for the sample with the donor concentration $n_D = 5 \cdot 10^{15}$ cm^{-3} are shown in Fig. 1. These spectra were measured in three different points on the sample surface (Point *1*, Point *2*, Point *3*). The main difference between spectra is the frequency positions of the absorption peaks - they depend on the magnitude of the quadrupole interaction of nuclear spins. So, at the Point *1* (dots in Fig. 1) the magnitude of the quadrupole interaction is considered to be minimal, and at the Point *2* (triangles in Fig. 1) the magnitude of the quadrupole interaction is the largest. In this case, two absorption peaks at frequencies of the order of 4 kHz and 9 kHz (Point *2*, Point *3*) correspond to the precession of isotopes ^{75}As and ^{69}Ga together with ^{71}Ga in the local fields, determined by dipole-dipole and quadrupole interactions. These frequencies can vary depending on the magnitude of the quadrupole splitting [9, 10]. The experimental fact that in different points on the sample surface the different absorption spectra are obtained indicates the spatial inhomogeneity of the quadrupole interaction of nucleus in the sample, which can be revealed by our nuclear spin warm-up spectroscopy method.

The example of nuclear spin correlator spectrum, which was obtained for the sample with donor concentration $n_D = 1.2 \cdot 10^{16}$ cm^{-3}, is shown in Figure 2 by dots. This spectrum corresponds to the nuclear spin temperature of about 50 μK (optical cooling stage time was equal to 60). The low-frequency part of the correlator spectrum is described by a Lorentzian (dashed line), and high-frequency part is described by a Gaussian (dash-dotted line). Such a decomposition of the spectrum into contours is in agreement with the temporal spin correlation functions calculated within different models [11, 12], which are related to the frequency dependence through the Fourier transform. It should be noted that the shape of the nuclear spin correlator spectra is the same for all studied bulk *n*-GaAs crystals with donor concentrations in the range of 10^{15}–10^{16} cm^{-3}. This indicates, in particular, that the donor

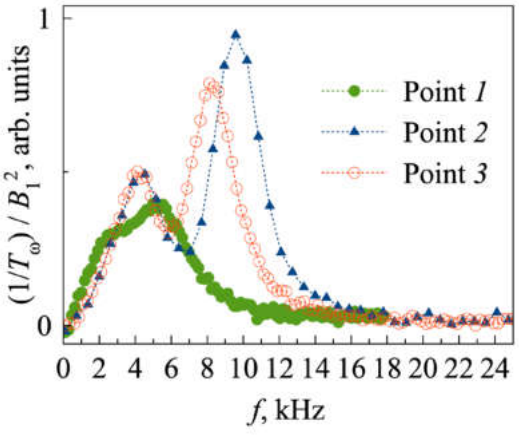

Fig. 1. Absorption spectra in three different points on the sample surface (Point *1*, Point *2*, Point *3*) at zero external magnetic field

concentration does not affect the formation of the spectra of nuclear spin fluctuations. In Fig. 3, the black dots show the dependence of the value of nuclear field B_N on the amplitude of the measuring field B_X, constructed according to the method described in the previous section. The obtained experimental dependence was described by Eq. (1) with the value of the local field B_L as a fitting parameter. For the sample under study, the value of local field is equal to $B_L = (1\pm0.1)$ G, which is close to the known literature data for bulk GaAs [13].

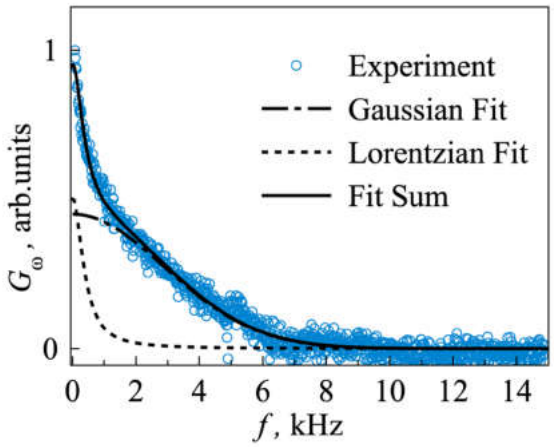

Fig. 2. Nuclear spin correlator spectrum for bulk *n*-GaAs (dots).
The spectrum was obtained by the warm-up spectroscopy method. The parts with low and high frequencies are described by Lorentzian and Gaussian functions, respectively

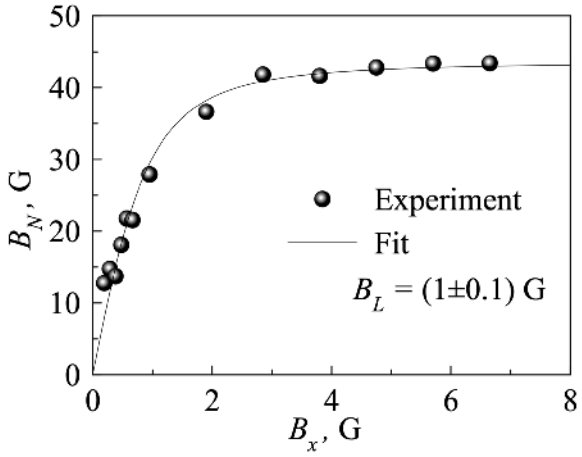

Fig. 3. Experimental dependence of nuclear field on the measurement transverse magnetic field for determination of the local field (black dots). Fitting experimental results by Eq. (1) with B_L as fitting parameter (black curve)

Conclusion

In this work, the experimental possibilities of nuclear spin warm-up spectroscopy method were presented for bulk *n*-GaAs samples with donor concentrations in the range of 10^{15}–10^{16} cm^{-3}. The proposed method makes it possible to obtain such characteristics of a cooled NSS as absorption and correlator spectra, and also makes it possible to measure nuclear local fields. In particular, we found that the absorption spectrum in a zero magnetic field reflects the spatial inhomogeneity of the quadrupole interaction, the correlator spectra consist of two contours, and their frequency shape does not depend on the donor concentration.

REFERENCES

1. **Dzhioev R. I., Kavokin K. V., Korenev V. L., Lazarev M. V., Meltser B. Ya., Stepanova M. N., Zakharchenya B. P., Gammon D., Katzer D. S.** Low-temperature spin relaxation in *n*-type GaAs, Physical Review B. 66 (2002) 245204.

2. **Merkulov I. A., Efros Al. L., Rosen M.** Electron spin relaxation by nuclei in semiconductor quantum dots, Physical Review B. 65 (2002) 205309.

3. **Merkulov I. A.** Formation of a nuclear spin polaron under optical orientation in GaAs-type semiconductors, Physics of the Solid State. 40 (1998) 930–933.

4. **Scalbert D.** Nuclear polaron beyond the mean-field approximation, Physical Review B. 95 (2017) 245209.

5. **Fischer A., Kleinjohann I., Anders F, Glazov M. M.** Kinetic approach to nuclear-spin polaron formation, Physical Review B. 102 (2020) 165309.

6. **Vladimirova M., Scalbert D., Kuznetsova M. S., Kavokin K. V.** Electron-induced nuclear magnetic odering in n-type semiconductors, Physical Review B. 103 (2021) 205207.

7. **Kalevich V. K., Fleisher V. G.** Optical detection of NMR with dynamic cooling of the nuclear spin system of a semiconductor by polarized light, Bull. Acad. Sci. USSR, Phys. Ser. 47 (1983) 5–9.

8. **Kalevich V. K., Kulkov V. D., Fleisher V. G.** Onset of a nuclear polarization front due to optical spin orientation in a semiconductor, JETP Lett. 35 (1982) 17–20.

9. **Litvyak V. M., Cherbunin R. V., Kalevich V. K., Lihachev A. I., Nashchekin A. V., Vladimirova M. and Kavokin, K.V.** Warm-up spectroscopy of quadrupole-split nuclear spins in n-GaAs epitaxial layers, Physical Review B. 104 (2021) 235201.

10. **Litvyak V. M., Cherbunin R. V., Kavokin K. V. and Kalevich V. K.** Determination of the Quadrupole Splitting in Bulk n - GaAs by Warm - Up Spectroscopy, Semiconductors. 54 (2020) 1728–1729.

11. **Knak Jensen S. J., Kjaersgaard Hansen E.** Dynamics of classical spins with dipolar coupling in a rigid lattice at high temperatures, Physical Review B. 13 (1976) 1903–1918.

12. **Florencio J., O. F. de Alcantara Bonfim.** Recent Advances in the Calculation of Dynamical Correlation Functions, Frontiers in Physic. 8 (2020) 1–13.

13. **Paget D., Lampel G., Sapoval B., Safarov V. I.** Low field electron-nuclear spin coupling in gallium arsenide under optical pumping conditions, Physical Review B. 15 (1977) 5780.

THE AUTHORS

LITVYAK Valentina M.
valiok.ok@gmail.com
ORCID: 0000-0001-9142-6821

CHERBUNIN Roman V.
r.cherbunin@gmail.com
ORCID: 0000-0002-8791-6227

SOLDATENKOV Fedor Yu.
f.soldatenkov@mail.ioffe.ru
ORCID: 0000-0002-6154-7208

KALEVICH Vladimir K.
kalevich@solid.ioffe.ru
ORCID: 0000-0002-8010-2714

KAVOKIN Kirill V.
kkavokin@gmail.com
ORCID: 0000-0002-0047-5706

Received 29.11.2022. Approved after reviewing 23.01.2023. Accepted 25.01.2023.

Conference materials
UDC 537.9
DOI: https://doi.org/10.18721/JPM.161.304

Magnetoresistivity and Hall effect in Weyl semimetal WTe_2

A.N. Perevalova [1], B.M. Fominykh [1, 2] ✉, V.V. Chistyakov [1], S.V. Naumov [1]
V.N. Neverov [1], V.V. Marchenkov [1, 2]

[1] M.N. Mikheev Institute of Metal Physics, UB RAS, Ekaterinburg, Russia;
[2] Ural Federal University, Ekaterinburg, Russia
✉ fominykh@imp.uran.ru

Abstract. A WTe_2 single crystal was grown by the chemical vapor transport method, and its electrical resistivity and galvanomagnetic properties were investigated. Single-band and two-band models were used to estimate the concentration and mobility of charge carriers in WTe_2 at temperatures from 4.2 to 150 K.

Keywords: WTe_2, Weyl semimetal, resistivity, magnetoresistivity, Hall effect

Funding: Magnetoresistivity studies were carried out within State Assignment of the Ministry of Science and Higher Education of the Russian Federation (theme "Spin", No. 122021000036-3), partially supported by Scholarship of the President of the Russian Federation for Young Scientists and Postgraduate Students (A.N.P., SP-2705.2022.1). Studies of the Hall effect were supported by a project of the Russian Science Foundation (Grant 22-42-02021). One of the authors (V.V.M.) thanks the Ural Federal University for support (Federal Academic Leadership Program Priority 2030).

Citation: Perevalova A.N., Fominykh B.M., Chistyakov V.V., Naumov S.V., Neverov V.N., Marchenkov V.V., Magnetoresistivity and hall effect in weyl semimetal WTe_2, St. Petersburg State Polytechnical University Journal. Physics and Mathematics. 16 (1.3) (2023) 26–32. DOI: https://doi.org/10.18721/JPM.161.304

Материалы конференции
УДК 537.9
DOI: https://doi.org/10.18721/JPM.161.304

Магнитосопротивление и эффект Холла в полуметалле Вейля WTe_2

А.Н. Перев лов [1], Б.М. Фоминых [1, 2] ✉, В.В. Чистяков [1]
С.В. Н умов [1], В.Н. Неверов [1], В.В. М рченков [1, 2]

[1] Институт физики металлов имени М.Н. Михеева УрО РАН, Екатеринбург, Россия;
[2] Уральский федеральный университет имени Б.Н. Ельцина, Екатеринбург, Россия
✉ fominykh@imp.uran.ru

Аннотация. Монокристалл WTe_2 был выращен методом химического газового транспорта, и исследованы его электросопротивление и гальваномагнитные свойства. Применены однозонная и двухзонная модели для оценки концентрации и подвижности носителей заряда при температурах от 4,2 до 150 K.

Ключевые слова: WTe_2, полуметалл Вейля, магнитосопротивление, эффект Холла

Финансирование: Результаты исследований магнитосопротивления получены в рамках государственного задания МИНОБРНАУКИ России (тема «Спин», № 122021000036-3) при частичной поддержке стипендии Президента Российской Федерации молодым ученым и аспирантам (А.Н.П., СП-2705.2022.1). Исследования эффекта Холла выполнены при поддержке проекта РНФ (грант № 22-42-02021). Один из авторов (В.В.М.) благодарит Уральский федеральный университет за поддержку (программа «Приоритет-2030»).

Ссылка при цитировании: Перевалова А.Н., Фоминых Б.М., Чистяков В.В., Наумов С.В., Неверов В.Н., Марченков В.В. Магнитосопротивление и эффект Холла в полуметалле Вейля WTe_2 // Научно-технические ведомости СПбГПУ. Физико-математические науки. 2023. Т. 16. № 1.3. С. 26–32. DOI: https://doi.org/10.18721/ JPM.161.304

Introduction

In recent years, WTe_2 has attracted great interest due to its extremely large magnetoresistance, which varies with the field according to a law close to quadratic without saturation up to 60 T [1]. It was assumed that the mechanism leading to the extremely large magnetoresistance in WTe_2 is electron-hole compensation [1]. Theoretical calculations of the electronic structure of WTe_2, as well as experimental studies using the angle-resolved photoemission spectroscopy (ARPES) and Shubnikov-de Haas oscillation measurements, revealed that the Fermi surface of this compound has a complex structure and consists of several pairs of electron-like and hole-like pockets, while the total volume of electron pockets is equal to that of hole pockets [1–4].

Another interesting feature of WTe_2 is that it was predicted as a candidate type-II Weyl semimetal [4], which was confirmed experimentally using ARPES and scanning tunneling microscopy [5, 6]. In such materials, the valence and conduction bands with a linear dispersion touch at points near the Fermi level, forming the so-called Weyl nodes. Instead of a point-like Fermi surface characteristic of a type-I Weyl cone, the type-II Weyl node is a touching point of the electron and hole pockets. Quasiparticles near such nodes behave similarly to massless Weyl fermions in high-energy physics. Weyl points always occur in pairs of opposite chirality and are topologically protected, resulting in unique surface states called Fermi arcs and unusual transport properties [7, 8]. The low effective mass of current carriers in Weyl semimetals leads to their high mobility ~10^3–10^6 $cm^2/(V{\cdot}s)$, which opens up prospects for the use of such materials for the development of ultrafast electronic devices.

The concentration and mobility of current carriers can be estimated based on data on the Hall effect and magnetoresistivity. On the one hand, such estimates are carried out within the framework of a single-band model, in particular, in [9, 10], where the transport properties of Weyl and Dirac semimetals were studied. On the other hand, to analyze the galvanomagnetic properties of such materials, the two-band model is often used, which takes into account the contributions of both electron and hole carriers [11, 12]. In [13], we compared the results of using these models to estimate the concentration and mobility of current carriers in WTe_2 at $T = 12$ K and obtained good agreement. However, it is of interest to carry out such an analysis over a wider temperature range. The aim of this work is to compare the results of using the single-band and two-band models for the analysis of the galvanomagnetic properties of WTe_2 in the temperature range from 4.2 K to 150 K.

Materials and Methods

WTe_2 single crystals were grown by the chemical vapor transport method, which was described in detail in [13]. The crystal structure of the synthesized crystals was studied by X-ray diffraction using CrKα radiation. It was found that the single crystals under study have an orthorhombic structure (space group $Pmn2_1$) with lattice parameters $a = 3.435(8)$ Å, $b = 6.312(7)$ Å, $c = 14.070(4)$ Å. Using X-ray energy-dispersive microanalysis on a Quanta 200 Pegasus scanning electron microscope with an EDAX attachment, it was established that the chemical composition of the grown crystals corresponds to stoichiometric WTe_2.

To measure the transport characteristics, a sample with dimensions of ~$4 \times 1 \times 0.4$ mm^3 was chosen. The resistivity and Hall resistivity were measured by the four-contact method in the temperature range from 4.2 K to 290 K and in magnetic fields up to 9 T on an Oxford Instruments setup for studying galvanomagnetic phenomena in strong magnetic fields and under low temperatures. During measurements, the electric current flowed in the *ab* plane, and the magnetic field was directed along *c* axis. To estimate the quality of the sample, the residual resistivity ratio (RRR) was determined, which is the ratio of resistivities at room temperature and

at liquid helium temperature and depends on the number of defects and impurities. In this work, the RRR value for the single crystal under study is $\rho_{300\,K}/\rho_{4.2\,K} \approx 50$, which is comparable with the RRR in [14], but at the same time, it is less than in [1, 11].

Results and Discussion

Fig. 1, *a* shows the temperature dependence of the electrical resistivity $\rho(T)$ of the WTe_2 single crystal in a zero magnetic field and in a field of 9 T. It can be seen that in the absence of a magnetic field, the sample exhibits a metallic behavior with an increase in the electrical resistivity from $0.13 \cdot 10^{-4}$ Ohm·cm to $5.7 \cdot 10^{-4}$ Ohm·cm with increasing temperature from 4.2 K to 290 K. While the magnetic field $B = 9$ T leads to the appearance of a minimum in the dependence $\rho(T)$ at $T \approx 60$ K. It is assumed that this minimum can be caused by the transition from effectively high ($\omega_c\tau >> 1$, where ω_c is the cyclotron frequency, τ is the relaxation time) to weak ($\omega_c\tau << 1$) magnetic fields [15, 16], which is observed for compensated conductors with a closed Fermi surface [17]. The term 'compensated' implies that the concentrations of electrons and holes are equal in such materials. To estimate the concentration n as well as mobility μ of charge carriers, a single-band model is often used for the analysis of data on the Hall effect, where $n = 1/R_H \cdot e$, $\mu = R_H/\rho$ (here R_H is the Hall coefficient; e is the electron charge; ρ is the electrical resistivity in a zero magnetic field). Fig. 1, *b* shows the temperature dependence of the Hall coefficient R_H of WTe_2 in a field $B = 9$ T. It can be seen that R_H has a negative sign, that is, electrons are the main charge carriers in the single crystal under study. The insets in Fig. 1, *b* show the temperature dependences of the concentration n and the mobility μ of current carriers in WTe_2, obtained using the single-band model. At $T = 4.2$ K, n and μ are $5 \cdot 10^{19}$ cm^{-3} and $7 \cdot 10^3$ cm^2/(V·s), respectively, where n increases and μ decreases with increasing temperature.

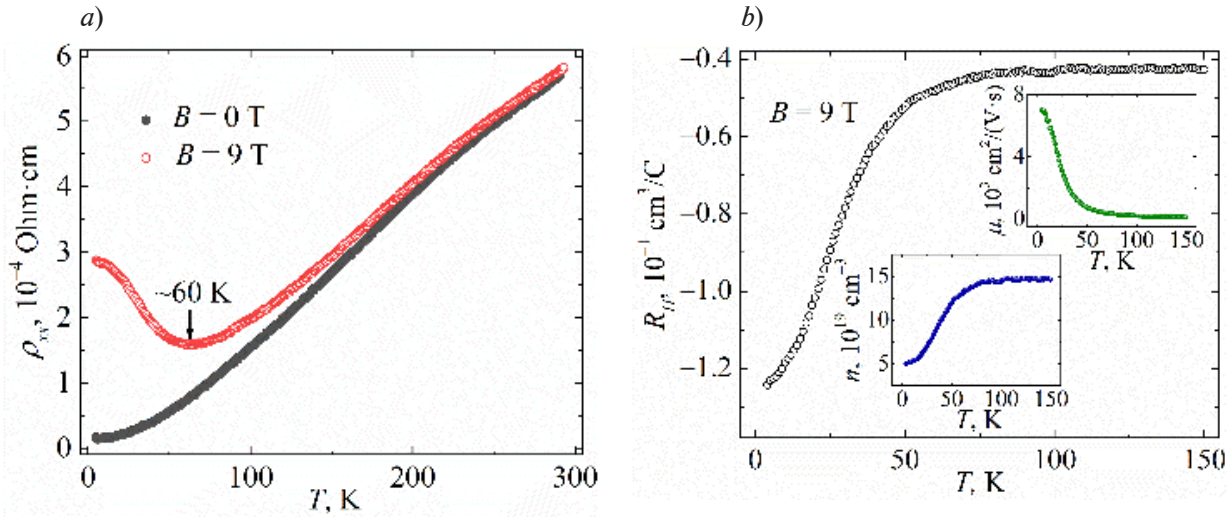

Fig. 1. Temperature dependence of electrical resistivity in a zero magnetic field and in a field of 9 T (*a*); Temperature dependence of the Hall coefficient R_H of WTe_2 in a field $B = 9$ T (*b*)
The insets show the concentration n and mobility μ of current carriers versus temperature, obtained using a single-band model

At the same time, since it is known [1–4] that WTe_2 is a compensated semimetal, it is of interest to estimate the concentrations and mobilities of separately electron and hole current carriers. In this case, a two-band model is used, where the resistivity ρ_{xx} and the Hall resistivity ρ_{xy} can be represented as [11]:

$$\rho_{xx} = \frac{1(n_h\mu_h + n_e\mu_e) + (n_h\mu_e + n_e\mu_h)\mu_h\mu_e B^2}{e(n_h\mu_h + n_e\mu_e)^2 + (n_h - n_e)^2\mu_h^2\mu_e^2 B^2}, \quad (1)$$

$$\rho_{xy} = \frac{B}{e}\frac{\left(n_h\mu_h^2 + n_e\mu_e^2\right) - \left(n_h - n_e\right)\mu_h^2\mu_e^2B^2}{\left(n_h\mu_h + n_e\mu_e\right)^2 + \left(n_h - n_e\right)^2\mu_h^2\mu_e^2B^2}. \quad (2)$$

Here n_e (n_h) and μ_e (μ_h) are the concentration and mobility of electrons (holes), respectively. From the simultaneous fitting of the experimental curves $\rho_{xx}(B)$ and $\rho_{xy}(B)$ in the framework of the two-band model, one can obtain the mobilities and concentrations of electron and hole current carriers. Fig. 2, *a* shows the $\rho_{xx}(B)$ and $\rho_{xy}(B)$ dependences for WTe_2. Open symbols correspond to experimental data, and solid lines correspond to curves obtained within the framework of the two-band model using a computer program [18]. It can be seen that the fitting curves describe the experimental results well. The error in determining the fitting parameters does not exceed 3%. Fig. 2, *b* shows the temperature dependences of the concentrations and mobilities of electrons and holes obtained using the two-band model. At $T = 4.2$ K, concentrations of electrons and holes are $4\cdot10^{19}$ cm^{-3} and $3.4\cdot10^{19}$ cm^{-3}, respectively, which is close to the value of n, obtained using the single-band model. At temperatures above 50 K, the electron concentration increases, while the hole concentration decreases. Whereas within the framework of the single-band model, an increase in the concentration of the main carriers is observed. At $T = 4.2$ K, the mobilities of electrons and holes are $6.3\cdot10^3$ cm^2/(V·s) and $3.7\cdot10^3$ cm^2/(V·s), respectively, and decrease with increasing temperature, which agrees with the results obtained using the single-band model. Note that the concentration and mobility of electrons mainly exceed that of holes, which means that electrons are the majority carriers, which is also consistent with the results of the single-band model. The inset in Fig. 2, *b* shows that the ratio n_h/n_e is close to 1 at temperatures below 50 K, which indicates a state close to electron-hole compensation in WTe_2. It was also shown in [11] by analyzing data on the Hall effect and magnetoresistivity in WTe_2 that the concentrations of electrons and holes are comparable at $T < 50$ K, which may be due to a change of the electron structure of this compound at low temperatures.

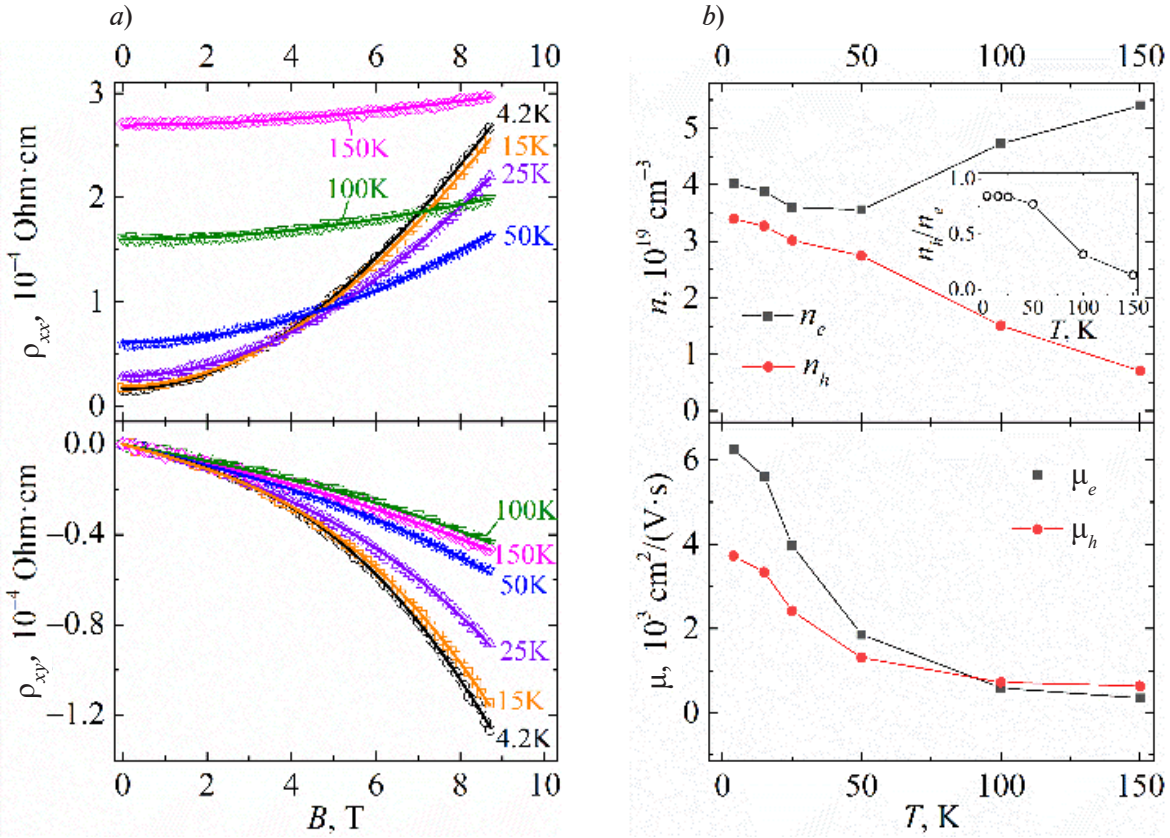

Fig. 2. Field dependences of the resistivity ρ_{xx} and Hall resistivity ρ_{xy} for WTe_2 at temperatures from 4.2 K to 150 K (*a*): open symbols are experimental data; solid lines are fitting curves obtained using Eq. (1) and (2); temperature dependences of the concentrations and mobilities of electrons and holes extracted using two-band model (*b*)
The inset shows the temperature dependence of the ratio n_h/n_e

According to Eq. (1), the magnetoresistivity (MR) $\Delta\rho/\rho$ can be expressed by the formula:

$$\frac{\Delta\rho}{\rho} = \frac{\rho_{xx} - \rho}{\rho} = \frac{\left(n_h\mu_h + n_e\mu_e\right)^2 + \left(n_h\mu_h + n_e\mu_e\right)\left(n_h\mu_e + n_e\mu_h\right)\mu_h\mu_e B^2}{\left(n_h\mu_h + n_e\mu_e\right)^2 + \left(n_h - n_e\right)^2 \mu_h^2\mu_e^2 B^2} - 1. \quad (3)$$

Thus, if the compensation condition is satisfied, $n_e = n_h$, the MR can be represented as $\Delta\rho/\rho = \mu_e\mu_h B^2$, that is, it changes with the field according to a quadratic law. Fig. 3 shows a plot of the MR versus magnetic field B for WTe_2 at $T = 4.2$ K. The MR reaches 1750% in a field of 9 T, which is less than the MR in [1, 11], which is apparently due to the lower value of the RRR for our crystal. Approximation of this dependence by a power function (red solid line in Fig. 3) revealed that $\Delta\rho/\rho \sim B^{1.87}$, i.e. at $T = 4.2$ K, the MR changes with the field according to a nearly quadratic law. The triangular symbols in Fig. 3 show the MR calculated by Eq. (3) for the case $n_e = n_h$, where the values of μ_e and μ_h were obtained using the two-band model. It can be seen that the MR calculated from the Eq. (3) exceed those obtained from the experimental data at $B \geq 5$ T. Apparently, this is due to non-ideal compensation in the WTe_2 single crystal under study.

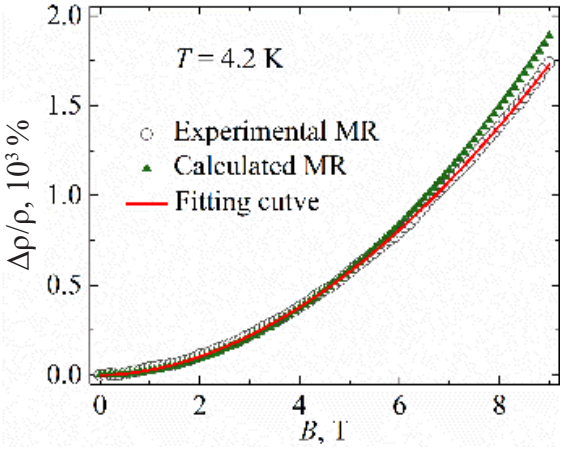

Fig. 3. Field dependence of the magnetoresistivity (MR) of WTe_2 at $T = 4.2$ K: open symbols represent the MR calculated from experimental data; the red solid line is the approximating function; triangles are the MR calculated from the compensation condition within the framework of the two-band model

Conclusion

The WTe_2 single crystal was grown and its galvanomagnetic properties were studied. Hall effect data as well as magnetoresistivity data were analyzed using both single-band and two-band models, followed by extracting the concentration and mobility of current carriers. It can be assumed that the results obtained within the framework of the two-band model are in good agreement with the results of applying the single-band model. Moreover, the two-band model, which provides information on the concentration and mobility of both electron and hole carriers, is preferable for systems containing different groups of carriers.

Acknowledgments

Structural and transport studies were carried out using equipment of the Collaborative Access Center “Testing Center of Nanotechnology and Advanced Materials” of the Ural Branch of the Russian Academy of Sciences.

REFERENCES

1. **Ali M. N., Xiong J., Flynn S., Tao J., Gibson Q. D., Schoop L. M., Liang T., Haldolaarachchige N., Hirschberger M., Ong N. P., Cava R. J.,** Large, non-saturating magnetoresistance in WTe_2, Nature. 514 (2014) 205–208.

2. **Wu Y., Jo N. H., Mou D., Huang L., Bud’ko S. L., Canfield P. C., Kaminski A.,** Three-dimensionality of the bulk electronic structure in WTe_2, Phys. Rev. B. 95 (2017) 195138.

3. **Zhu Z., Lin X., Liu J., Fauqué B., Tao Q., Yang C., Shi Y., Behnia K.,** Quantum oscillations, thermoelectric coefficients, and the Fermi surface of semimetallic WTe_2, Phys. Rev. Lett. 114 (2015) 176601.

4. **Soluyanov A. A., Gresch D., Wang Z., Wu Q., Troyer M., Dai X., Bernevig B. A.,** Type-II Weyl semimetals, Nature. 527 (2015), 495–498.

5. **Wang C., Zhang Y., Huang J., Nie S., Liu G., Liang A., Zhang Y., Shen B., Liu J., Hu C., Ding Y., Liu D., Hu Y., He S., Zhao L., Yu L., Hu J., Wei J., Mao Z., Shi Y., Jia X., Zhang F., Zhang S., Yang F., Wang Z., Peng Q., Weng H., Dai X., Fang Z., Xu Z., Chen C., Zhou X. J.,** Observation of Fermi arc and its connection with bulk states in the candidate type-II Weyl semimetal WTe_2, Phys. Rev. B. 94 (2016) 241119.

6. **Lin C.-L., Kawakami N., Arafune R., Minamitani E., Takagi N.,** Scanning tunneling spectroscopy studies of topological materials, J. Phys. Condens. Matter. 32 (2020) 243001.

7. **Lv B. Q., Qian T., Ding H.,** Experimental perspective on three-dimensional topological semimetals, Rev. Mod. Phys. 93(2) (2021) 025002.

8. **Hu J., Xu S.-Y., Ni N., Mao Z.,** Transport of topological semimetals, Annu. Rev. Mater. Res. 49 (2019) 207–252.

9. **Shekhar C., Nayak A. K., Sun Y., Schmidt M., Nicklas M., Leermakers I., Zeitler U., Skourski Y., Wosnitza J., Liu Z., Chen Y., Schnelle W., Borrmann H., Grin Y., Felser C., Yan B.,** Extremely large magnetoresistance and ultrahigh mobility in the topological Weyl semimetal candidate NbP, Nature Phys. 11 (2015) 645–649.

10. **Singh S., Süβ V., Schmidt M., Felser C., Shekhar C.,** Strong correlation between mobility and magnetoresistance in Weyl and Dirac semimetals, J. Phys. Mater. 3 (2020) 024003.

11. **Luo Y., Li H., Dai Y. M., Miao H., Shi Y. G., Ding H., Taylor A. J., Yarotski D. A., Prasankumar R. P., Thompson J. D.,** Hall effect in the extremely large magnetoresistance semimetal WTe_2, Appl. Phys. Lett. 107 (2015) 182411.

12. **Gong J.-X., Yang J., Ge M., Wang Y.-J., Liang D.-D., Luo L., Yan X., Zhen W.-L., Weng S.-R., Pi L., Zhang C.-J., Zhu W.-K.,** Non-Stoichiometry Effects on the Extreme Magnetoresistance in Weyl Semimetal WTe_2, Chin. Phys. Lett. 35 (2018) 097101.

13. **Perevalova A. N., Naumov S. V., Podgornykh S. M., Chistyakov V. V., Marchenkova E. B., Fominykh B. M., Marchenkov V. V.,** Kinetic properties of a topological semimetal WTe_2 single crystal, Phys. Met. Metallogr. 123 (2022) 1061–1067.

14. **Pan X. C., Pan Y., Jiang J., Zuo H., Liu H., Chen X., Wei Z., Zhang S., Wang Z., Wan X., Yang Z., Feng D., Xia Z., Li L., Song F., Wang B., Zhang Y., Wang G.,** Carrier balance and linear magnetoresistance in type-II Weyl semimetal WTe_2, Front. Phys. 12 (3) (2017), 127203.

15. **Marchenkov V. V.,** Quadratic temperature dependence of magnetoresistivity of pure tungsten single crystals under static skin effect, Low Temp. Phys. 37 (2011) 852–855.

16. **Marchenkov V. V., Perevalova (Domozhirova) A. N., Naumov S. V., Podgornykh S. M., Marchenkova E. B., Chistyakov V. V., Huang J. C. A.,** Peculiarities of electronic transport in WTe_2 single crystal, J. Magn. Magn. Mater. 549 (2022) 168985.

17. **Lifshitz I. M., Azbel M. Y., Kaganov M. I.,** Electronic Theory of Metals, Nauka, Moscow, 1971.

18. **Chistyakov V. V., Perevalova A. N., Marchenkov V. V.,** Certificate of State Registration of the Computer Program No. 2022660290 (2022).

THE AUTHORS

PEREVALOVA Aleksandra N.
domozhirova@imp.uran.ru
ORCID: 0000-0002-8540-8720

FOMINYKH Bogdan M.
fominykh@imp.uran.ru
ORCID: 0000-0002-4755-3839

CHISTYAKOV Vasiliy V.
wchist@imp.uran.ru
ORCID: 0000-0002-2684-256X

NAUMOV Sergey V.
naumov@imp.uran.ru
ORCID: 0000-0003-4527-6396

NEVEROV Vladimir N.
neverov@imp.uran.ru
ORCID: 0000-0002-3723-3321

MARCHENKOV Vyacheslav V.
march@imp.uran.ru
ORCID: 0000-0003-2044-1789

Received 13.12.2022. Approved after reviewing 26.01.2023. Accepted 27.01.2023.

Conference materials
UDC 535.37
DOI: https://doi.org/10.18721/JPM.161.305

Determination of donor and acceptor concentrations in GaN using yellow photoluminescence band

I.V. Osinnykh [1, 2] ✉, T.V. Malin [1], K.S. Zhuravlev [1]

[1] Rzhanov Institute of Semiconductor Physics Siberian Branch of RAS, Novosibirsk, Russia
[2] Novosibirsk State University, Novosibirsk, Russia
✉ igor-osinnykh@isp.nsc.ru

Abstract. In this paper, we present the results of the calculated and experimental dependence of photoluminescence on the excitation power density for GaN:Si layers grown by molecular beam epitaxy. A model was constructed for transitions in a compensated semiconductor upon interband generation of electron-hole pairs. It is shown that the dependence of the photoluminescence intensity on the excitation power density can be used to determine the recombination mechanism and concentrations of donors and acceptors in semiconductor.

Keywords: GaN, ammonia-MBE, photoluminescence, heterostructures, point defects

Funding: The study was funded by State Assignment "Ammonia molecular beam epitaxy of GaN heterostructures on silicon substrates for power and microwave transistors" (Topic ID FWGW-2022-0015).

Citation: Osinnykh I.V, Malin T.V., Zhuravlev K.S, Determination of donor and acceptor concentrations in GaN using yellow photoluminescence band, St. Petersburg State Polytechnical University Journal. Physics and Mathematics. 16 (1.3) (2023) 33–38. DOI: https://doi.org/10.18721/JPM.161.305

Материалы конференции
УДК 535.37
DOI: https://doi.org/10.18721/JPM.161.305

Определение концентраций доноров и акцепторов в GaN по желтой полосе фотолюминесценции

И.В. Осинных [1, 2] ✉, Т.В. М лин [1], К.С. Жур влев [1]

[1] Институт физики полупроводников им. А.В. Ржанова СО РАН, Новосибирск, Россия.
[2] Новосибирский государственный университет, Новосибирск, Россия
✉igor-osinnykh@isp.nsc.ru

Аннотация. В настоящей работе представлены результаты расчетной и экспериментальной зависимости интенсивности фотолюминесценции от плотности мощности возбуждения для легированных кремнием слоев GaN, выращенных методом молекулярно-лучевой эпитаксии. Показано, что анализ зависимости интенсивности фотолюминесценции от плотности мощности возбуждения с помощью модели электронных переходов в GaN при межзонной генерации электрон-дырочных пар позволяет определить механизм рекомбинации и концентрации доноров и акцепторов в полупроводнике.

Ключевые слова: GaN, аммиачная МЛЭ, фотолюминесценция, гетероструктуры, точечные дефекты

Финансирование: Государственное задание «Аммиачная молекулярно-лучевая эпитаксия GaN гетероструктур на подложках кремния для силовых и СВЧ транзисторов» (код темы FWGW-2022-0015).

Ссылка при цитировании: Осинных И.В., Малин Т.В., Журавлев К.С. Определение концентраций доноров и акцепторов в GaN по желтой полосе фотолюминесценции // Научно-технические ведомости СПбГПУ. Физико-математические науки. 2023. Т. 16. № 1.3. С. 33–38. DOI: https://doi.org/10.18721/ JPM.161.305

Introduction

III-nitrides and their alloys are direct-gap semiconductors, relevant for the manufacture of light-emitting devices for the visible and ultraviolet regions of the spectrum [1, 2]. Varying the Al content in AlGaN allows creating materials with band gap (E_g) from 3.43 to 6.2 eV, covering the spectral range from 200 to 365 nm. Formation of epitaxial GaN *n*-type conductivity layers using silicon (Si) as a donor is not difficult, the electron concentration can be increased to 10^{20} cm^{-3}. However, epitaxial growth of semiconductor structures is associated with formation of point defects, which can form acceptor-like states and compensate the doping impurity. Photoluminescence spectroscopy (PL) is a non-contact fast non-destructive method of characterizing such heterostructures, requiring a small amount of material to study. Several bands in the GaN luminescence spectra related to electronic transitions to the centers with energy levels in the band gap [3] are known, the most actively studied is the 'yellow band' of luminescence with the maximum of about 2.2 eV that is associated with the main GaN background impurities or their complexes with natural lattice defects: V_{Ga}-O_N complex [4–6] and C_N-O_N complex or isolated C_N impurity [7–9]. The yellow band provides information on the defects in the crystals and is actively used to improve their growth technology since the ratio of the intensities of the UV-edge band and the yellow band in the GaN luminescence spectrum can serve as a criterion of its crystalline perfection.

Usually the intensity of the yellow band linearly depends on the excitation power density (J) at low values of J and it saturates at high values of J. The approximation of this dependence by the function of the form $I(J) \sim \ln(1 + J/J_1)$ in [10] allows to determine the acceptor concentration from the magnitude J_1. This method requires the measurement of the external quantum efficiency of the yellow band, since within such a model this magnitude takes into account the influence of competing channels of the recombination. It is not possible to calculate the concentration of the donors by this model. A stricter account of other channels of the recombination consists in solving the system of the kinetic equations in the stationary case together with the electroneutrality equation. In the present work, we propose to use this approach to determine the mechanism of yellow band recombination in the Si-doped GaN layers and concentrations of donors and acceptors according to the dependence of yellow band intensity on the excitation power density. The proposed model is universal and can be used for any compensated semiconductors at high temperatures.

Materials and Methods

We investigated 1-μm-thick GaN layers grown by molecular beam epitaxy (MBE) from ammonia on Riber's CBE-32 machine. The substrates used were (0001) oriented polished 400 μm thick 2" sapphire wafers. The layers were doped with silicon (Si) from a monosilane gas source. The concentration of silicon atoms in the layers was determined by secondary ion mass spectrometry (SIMS) using the technique described in [11] and was approximately 8×10^{18} cm^{-3}. The electron concentration was determined by Hall effect measurements in Van der Pau geometry in a 0.5 Tesla magnetic field at room temperature and was about 3×10^{17} cm^{-3}. The PL spectra were measured at room temperature. The 4th harmonic of the stationary YAG laser (λ_{las} = 266 nm) with a maximum radiation power density of 12.6 W/cm^2 was used to measure the PL over a wide range of excitation power.

Results and Discussion

Fig. 1, *a* shows the experimentally measured PL spectra of a typical GaN sample, in which the near-band-edge PL band with a maximum at 3.45 eV and yellow PL band with a maximum at 2.18 eV dominate. Both bands are characterized by a monotonic growth of the integral intensity with the increase in the excitation power density (Fig. 1, *b*). The near-band-edge PL band intensity increases by the superlinear law throughout the range of excitation power density, approximation by the exponential function gives a power index $\gamma = 1.17$. The yellow band intensity increases linearly up to $J \sim 1$ W/cm^2, at higher values the dependence becomes sublinear, approximation by the exponential function gives a power index $\gamma = 0.66$, close to the value from work [12], which is typical for donor-acceptor recombination. The intensities of the edge and yellow bands are compared at $J_0 \sim 4.5$ W/cm^2. The approximation of the yellow band intensity by a function of the form $I(J) \sim \ln(1 + J/J_1)$ [10] gives the value $J_1 \sim 3.4$ W/cm^2, which depends on N_A as follows:

$$J_1 / E_{las} = N_A / \alpha\tau\eta, \qquad (1)$$

here $\tau = (n_0 W_{eA})^{-1}$ is the lifetime and η is the external quantum efficiency of the yellow band, respectively. Substituting the value $\eta = 0.06$, typical for the yellow band [10, 13], into relation (1) gives the estimation $N_A = 2\times10^{18}$ cm^{-3}.

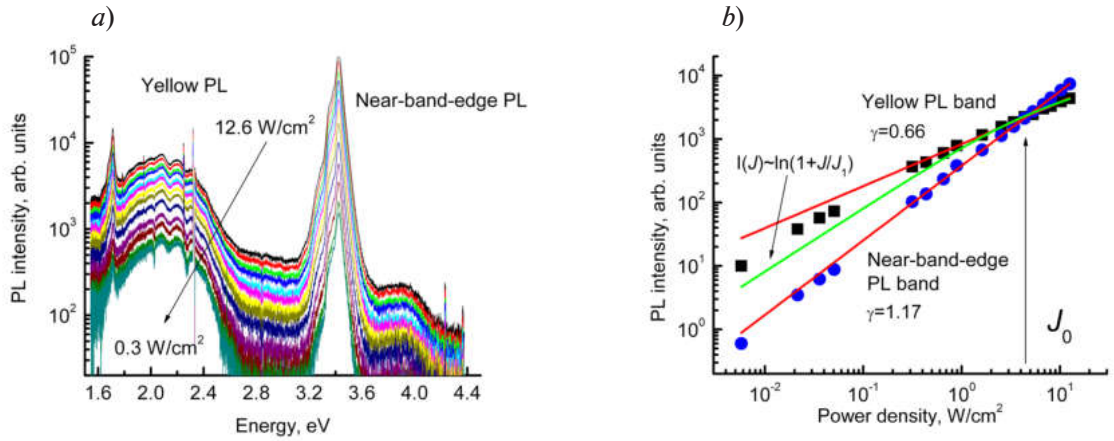

Fig. 1. Room-temperature PL spectra of GaN (*a*) and dependences of the intensity of the edge and yellow PL bands on the excitation power density (*b*). The solid lines depict the approximation curves (see the text for details)

Within the framework of the above model, the influence of competing recombination channels is taken into account by the value of η. This model does not allow us to calculate the concentration of donors. A more rigorous consideration of other recombination channels consists in solving a system of kinetic equations in the stationary case together with the electroneutrality equation. The dependence of intensity of various PL channels in a compensated semiconductor on the excitation power was calculated for the interband mechanism of electron-hole pair generation, Fig. 2 shows a scheme of electronic transitions. The semiconductor contains donors (D), acceptors (A), and non-radiative recombination (NR) centers. Within the model there are three channels of radiative recombination – band-band (BB), band-acceptor (eA) and donor-acceptor (DA) with participation of one type of acceptors and one channel of non-radiative recombination (NR).

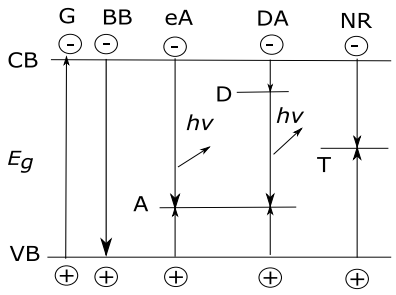

Fig. 2. Scheme of transitions in a compensated semiconductor at band-band generation of charge carriers

Following the transition scheme, we can write a system of continuity equations for free electrons n, free holes p,

neutral donors N_D^0, neutral acceptors N_A^0 and neutral non-radiative centers N_T^0 together with the electroneutrality equation.

$$\begin{gathered}
0 = \alpha J + W_t \cdot N_D^0 - W_f \cdot n \cdot p - W_{eD} \cdot n \cdot (N_D - N_D^0) - W_{eA} \cdot n \cdot N_A^0 - W_{eT} \cdot n \cdot N_T^0 \\
0 = W_{hT} \cdot p \cdot (N_T - N_T^0) - W_{eT} \cdot n \cdot N_T^0 \\
0 = W_{hA} \cdot p \cdot (N_A - N_A^0) - W_{eA} \cdot n \cdot N_A^0 - W_{DA} \cdot N_D^0 \cdot N_A^0 \\
0 = W_{eD} \cdot n \cdot (N_D - N_D^0) - W_{DA} \cdot N_D^0 \cdot N_A^0 - W_t \cdot N_D^0 \\
p + (N_D - N_D^0) = n + (N_T - N_T^0) + (N_A - N_A^0),
\end{gathered} \tag{2}$$

here N_D, N_A and N_T are total concentrations of donors, acceptors, and non-radiative centers, $\alpha = 1.8\times10^5$ cm^{-1} is absorption coefficient at the laser wavelength [14], $W_f = 1.1\times10^{-8}$ cm$^{-3}\times$c^{-1} is probability of radiative recombination of free charge carriers [14]. The probability of thermal ejection of an electron from the donor level into the conduction band was estimated as

$$W_t = W_{eD} \cdot N_{eff} \cdot e^{-\frac{E_d}{kT}}, \tag{3}$$

here N_{eff} is the effective density of states in the band, k is the Boltzmann constant, T is temperature, $E_d = 26$ meV is the ionization energy of the donor [15]. W_{eD}, W_{eA} and W_{eT} are probabilities of electron capture to the donor, to the acceptor and to the non-radiative center, W_{hA} and W_{hT} are probabilities of hole capture to the acceptor and to the non-radiative center [16]. Since the recombination probability in DA pairs depends on the distance between the donor and acceptor in the pair (r), it is impossible to describe the DA-channel by a simple expression for the transition rate with a fixed value of the transition probability W_{DA}. To avoid complicating the calculation scheme, we introduced an average value of the recombination probability showing the most possible value of this value:

$$\begin{gathered}
W_{DA} = \int_0^\infty W(r) f(r) dr, \\
W(r) = W_0 e^{-\frac{2r}{a}}, \\
f(r) = C_1 r^2 e^{-\frac{e^2}{\varepsilon r k T}} e^{-\frac{4\pi N r^3}{3}},
\end{gathered} \tag{4}$$

here $W(r)$ is the recombination probability in a donor-acceptor pair of radius r, $f(r)$ is the density distribution function of randomly located non-interacting donor-acceptor pairs along radius r. Here W_0 is a constant indicating recombination probability at $r = 0$, a is the Bohr radius of the electron on the donor, N is the concentration of the dominant impurity (donors in this case), ε is the dielectric permittivity, e is the elementary electric charge, C_1 is the normalization multiplier.

The solution of the system of equations (2) allows us to obtain the dependence of the concentrations of charge carriers and neutral centers on the excitation power density J. From these we can derive the dependences of recombination channel rates as a function of J.

$$\begin{gathered}
I_{BB}(J) = W_f \cdot n(J) \cdot p(J), \\
I_{eA}(J) = W_{eA} \cdot n(J) \cdot N_A^0(J), \\
I_{DA}(J) = W_{DA} \cdot N_D^0(J) \cdot N_A^0(J), \\
I_{NR}(J) = W_{eT} \cdot n(J) \cdot N_T^0(J).
\end{gathered} \tag{5}$$

Fig. 3 shows the calculated dependences of the rates of BB, NR, eA and DA recombination and G generation rate channels on the excitation power density J. The concentrations of donors, acceptors, non-radiative centers, and equilibrium electrons are taken to be $N_D = 8\times10^{18}$ cm^{-3}, $N_A = 2\times10^{18}$ cm^{-3}, $N_T = 3.5\times10^{18}$ cm^{-3} and $n_0 = 3\times10^{17}$ cm^{-3}. The calculated dependences of the rates of BB and DA channels coincide with the experimental dependences for the band-

band and yellow PL bands. In the experiment, it is most convenient to register the value of power density J_0, at which the intensities (or recombination rates) of BB and DA channels are equal, which depends on the selected concentrations. Donor concentration $N_D = 8\times10^{18}$ cm^{-3} which corresponds to $J_0 = 4.5$ W/cm^2 observed in the experiment coincides with the value of total silicon concentration obtained by SIMS method. This means that this technique provides reliable information on donor and acceptor concentrations. It should be noted that the kinetics of photoluminescence decay would allow to accurately determining the donor concentrations [17]. This is a point of further development of the proposed approach.

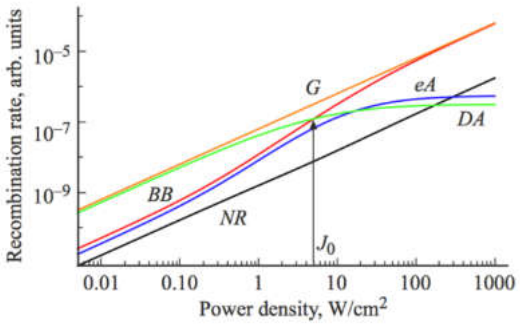

Fig. 3. Calculated dependences of the NR, BB, eA and DA recombination rate and the generation rate G on the excitation power density. The concentration of donors, equilibrium electrons, acceptors and non-radiative centers are $N_D = 8\times10^{18}$ cm^{-3}, $n_0 = 3\times10^{17}$ cm^{-3}, $N_A = 2\times10^{18}$ cm^{-3}, $N_T = 3.5\times10^{18}$ cm^{-3}

Conclusion

In this work, a model of electronic transitions in compensated GaN was established that takes into account radiative band-band, band-acceptor, donor-acceptor transitions and non-radiative transitions at band-band generation of electron-hole pairs. The dependences of the rates of these recombination channels on the excitation power density were calculated within this model. The dependences of the intensity of the near-band-edge and yellow photoluminescence bands on the excitation power density for n-doped GaN layers grown by molecular beam epitaxy were measured. It is shown that the yellow band in GaN is caused by donor-acceptor optical transitions. The analysis of band-band and donor-acceptor photoluminescence bands intensity dependences on the excitation power density allowed estimating the concentrations of donors and acceptors in GaN. The correctness of the concentration estimate demonstrates the coincidence of the donor concentration with the total silicon concentration.

REFERENCES

1. **Jones K., Chow T., Wraback M., Shatalov M., Sitar Z., Shahedipour F., Udwary K., and Tompa G.,** AlGaN devices and growth of device structures, J. Mater. Sci. 50 (2015) 3267–3307.

2. **Tsao J. Y., Chowdhury S., Hollis M. A., Jena D., Johnson N. M., Jones K. A., Kaplar R. J., Rajan S., Van De Walle C. G., Bellotti E., Chua C. L., Collazo R., Coltrin M. E., Cooper J. A., Evans K. R., Graham S., Grotjohn T. A., Heller E. R., Higashiwaki M., Islam M. S., and Simmons J. A.,** Ultrawide-Bandgap Semiconductors: Research Opportunities and Challenges, Adv. Electron. Mater. 4, (2018) 1600501.

3. **Reshchikov M. A. and Morkoc H.,** Luminescence properties of defects in GaN, J. Appl. Phys. 97 (2005) 061301.

4. **Sedhain A., Li J., Lin J. Y., and Jiang H. X.,** Nature of deep center emissions in GaN, Appl. Phys. Lett. 96 (2010) 151902.

5. **Ito S., Nakagita T., Sawaki N., Soo Ahn H., Irie M., Hikosaka T., Honda Y., Yamaguchi M., and Amano H.,** Nature of yellow luminescence band in GaN grown on Si substrate, Jpn. J. Appl. Phys. 53 (2014) 11RC02.

6. **Mattila T. and Nieminen R. M.,** Point-defect complexes and broadband luminescence in GaN and AlN, Phys. Rev. B 55 (1997) 9571.

7. **Lyons J. L., Janotti A., and Van de Walle C. G.,** Carbon impurities and the yellow luminescence in GaN, Appl. Phys. Lett 97 (2010) 152108.

8. **Reshchikov M. A., Demchenko D. O., Usikov A., Helava H., Makarov Yu.,** Carbon defects as sources of the green and yellow luminescence bands in undoped GaN, Phys. Rev. B 90 (2014) 235203.

9. **Jana D. and Sharma T. K.,** A correlation between the defect states and yellow luminescence in AlGaN/GaN heterostructures, J. Appl. Phys. 122 (2017) 035101.

10. **Reshchikov M. A.,** Determination of acceptor concentration in GaN from photoluminescence, Appl. Phys. Lett. 88 (2006) 202104.

11. **Osinnykh I.V., Malin T. V., Milakhin D. S., Plyusnin V. F., and Zhuravlev K. S.,** Donor-acceptor pair emission via defects with strong electron-phonon coupling in heavily doped $Al_xGa_{1-x}N$:Si layers with Al content $x > 0.5$, Jpn. J. Appl. Phys. 58 (2019) SCCB27.

12. **Tamulaitis G., Mickevičius J., Vitta P., Žukauskas A., Shur M.S., Liu K., Fareed Q., Zhang J.P., and Gaska R.,** Carrier lifetimes in GaN revealed by studying photoluminescence decay in time and frequency domains, ECS Transactions, 3 (2006) 307.

13. **Fujii K., Goto T., Nakamura S., and Yao T.,** Excitation light intensity dependence of 2.2 eV yellow photoluminescence of *n*-type GaN, Jpn. J. Appl. Phys. 60 (2021) 011002.

14. **Muth J.F., Lee J.H., Shmagin I.K., Kolbas R.M., Casey Jr H.C., Keller B.P., Mishra U.K., DenBaars S.P.,** Absorption coefficient, energy gap, exciton binding energy, and recombination lifetime of GaN obtained from transmission measurements, Appl. Phys. Lett. 71(18) (1997) 2572.

15. **Wickenden A.E., Rowland L.B., Doverspike K., Gaskill D.K., Freitas J.A., Simons D.S., Chi P.H.,** Doping of gallium nitride using disilane, J. Electron. Mater. 24 (1995) 1547.

16. **Reshchikov M. A., McNamara Toporkov J. D., M., Avrutin V., Morkoc H., Usikov A., Helava H., and Makarov Y.,** Determination of the electron-capture coefficients and the concentration of free electrons in GaN from time-resolved photoluminescence, Sci. Rep. 6 (2016) 37511.

17. **Goldys E. M., Godlewski M., Langer R., Barski A., Bergman P., Monemar B.,** Analysis of the red optical emission in cubic GaN grown by molecular-beam epitaxy. Phys. Rev. B 60 (1999) 5464.

THE AUTHORS

OSINNYKH Igor V.
igor-osinnykh@isp.nsc.ru
ORCID: 0000-0002-3165-7027

MALIN Timur V.
mal-tv@isp.nsc.ru

ZHURAVLEV Konstantin S.
zhur@isp.nsc.ru
ORCID: 0000-0002-3171-5098

Received 14.12.2022. Approved after reviewing 25.01.2023. Accepted 25.01.2023.

Structure growth, surface, and interfaces

Conference materials
UDC 538.911
DOI: https://doi.org/10.18721/JPM.161.306

Transfer of 3C-SiC heteroepitaxial layers grown on silicon to a 6H-SiC substrate by direct bonding technique

D.G. Amelchuk [1] ✉, M.G. Mynbaeva [1], A.N. Smirnov [1],
V.Yu. Davydov [1], S.P. Lebedev [1], A.A. Lebedev [1]
[1] Ioffe Institute, St. Petersburg, Russia
✉ mutranspet@gmail.com

Abstract. This paper reports on the development of direct bonding of 3C-SiC epitaxial layers grown by chemical vapor deposition on silicon substrates and 6H-SiC single crystal wafers. It has been found that the bonding temperature is a critical parameter to obtain mechanical contact between the transferred 3C-SiC layers and the 6H-SiC carrier plates. The results of structural characterization showed that the structure of epitaxial layers grown by sublimation on bonded substrates corresponds to a pure cubic phase of high quality.

Keywords: Silicon carbide, polytypes, direct splicing, templates, sublimation epitaxy

Citation: Amelchuk D.G., Mynbaeva M.G., Smirnov A.N., Davydov V.Yu., Lebedev S.P., Lebedev A.A., Transfer of 3C-SiC heteroepitaxial layers grown on silicon to a 6H-SiC substrate by direct bonding technique. St. Petersburg State Polytechnical University Journal. Physics and Mathematics. 16 (1.3) (2023) 39–43. DOI: https://doi.org/10.18721/JPM.161.306

Материалы конференции
УДК 538.911
DOI: https://doi.org/10.18721/JPM.161.306

Перенос гетероэпитаксиальных слоёв 3C-SiC, выращенных на кремнии, на подложку 6H-SiC методом прямого сращивания

Д.Г. Амельчук [1] ✉, М.Г. Мынб ев [1], А.Н. Смирнов [1],
В.Ю. Д выдов [1], С.П. Лебедев [1], А.А. Лебедев [1]
[1] Физико-технический институт им. А.Ф. Иоффе РАН, Санкт-Петербург, Россия
✉ mutranspet@gmail.com

Аннотация. В представленной работе сообщается о разработке метода прямого сращивания гетероэпитаксиальных слоев 3C-SiC, выращенных на Si подложках, и монокристаллических пластин 6H-SiC. Обнаружено, что температура сращивания является критическим параметром для получения механического контакта между переносимыми слоями и несущими пластинами. Результаты характеризации показали, что кристаллическая структура гомоэпитаксиальных слоёв 3C-SiC, выращенных на подложках, полученных методом сращивания, соответствует чистой кубической фазе высокого качества.

Ключевые слова: Карбид кремния, политипы, прямое сращивание, темплейты, сублимационная эпитаксия

Ссылка при цитировании: Амельчук Д.Г., Мынбаева М.Г., Смирнов А.Н., Давыдов В.Ю., Лебедев С.П., Лебедев А.А. Перенос гетероэпитаксиальных слоёв 3C-SiC, выращенных на кремнии, на подложку 6H-SiC методом прямого сращивания // Научно-технические ведомости СПбГПУ. Физико-математические науки. 2023. Т. 16. № 1.3. С. 39–43. DOI: https://doi.org/10.18721/ JPM.161.306

Introduction

Silicon carbide (SiC) is considered as a prime candidate to replace silicon in today's electronics due to inherent physical properties such as wide band gap, thermal and corrosion stability, as well as higher blocking voltage, lower losses, and faster switching speed [1]. Compared to the other two most known polytypes, hexagonal 4H- and 6H-SiC used in power microelectronics, the cubic 3C-SiC polytype is the promising material for high-frequency electronic devices [2]. A topic problem of 3C-SiC technology is the lack of methods for the 'bulk' growth of a single-crystal material necessary for the manufacture of substrates for 3C-SiC homoepitaxy. It could seem that in this case, a natural solution would be to use existing SiC wafers of hexagonal polytypes as substrates. However, achieving high-quality homoepitaxy of 3C-SiC on 4H- and 6H-SiC is problematic due to the difference in the types of crystal lattices. At the same time, cubic SiC can be grown on widely available silicon wafers with a similar syngony. At present, however, such heteroepitaxial technologies have not yet reached the crystalline quality acceptable for the production of electronic devices. There are two main problems to be resolved here. First, it is the level of internal stresses caused by the mismatch between the lattice parameters of 3C-SiC (4.36 Å) and Si (5.43 Å). The mismatch is the reason for the formation of a highly defective nucleation layer resulting in the formation of wide set of extended defects. The electrical activity of these defects is the dominant problem that adversely affects the efficiency of electronic devices based on 3C-SiC. The second problem is related to the presence of thermoelastic stresses arising from the difference in the thermal expansion coefficients of Si and 3C-SiC, which is 8%. As a result, cracking of epitaxial layers is often observed when they are cooled from the growth temperature to the room temperature. Cracking determines a significant deterioration in the quality of the epitaxial layers. A comprehensive solution of the problems mentioned above can be the development of an alternative substrate (template) using the approach of transferring the already grown 3C-SiC seeding layer onto a carrier wafer which would be close to the layer in terms of lattice parameters and thermal expansion coefficients. Notice that such transfer technologies (called *wafer bonding*) are widely used in epitaxial and device technologies of materials for which there is no matched substrate [3–6]. This paper reports on the development of a template by direct bonding of 3C-SiC epitaxial layers grown by chemical vapor deposition (CVD) on silicon substrates and single-crystal 6H-SiC wafers, for which the lattice mismatch with 3C-SiC does not exceed 0.3%; these two polytypes also have close thermal expansion coefficients. The effectiveness of the proposed transfer approach is confirmed by the results of sublimation homoepitaxy on the 3C-SiC/6H-SiC templates obtained.

Materials and Methods

CVD-grown (001)3C-SiC/Si structures with 40 μm-thick epitaxial layer and single-crystal (0001)6H-SiC wafers (manufactured by Nitride Crystals, LLC) were used for bonding experiments. The bonding was carried out at temperature T = 1300–1550 °C in vacuum without any adhesive layers and without applying external mechanical pressure. The next step after the bonding was the removal of silicon with a liquid etchant. Homoepitaxial 3C-SiC layers were grown on the resulting templates by the sublimation method at T = 1700–1800 °C in vacuum of (4–5) × 10^{-6} Torr. The layer thickness was 10–15 micrometers. Structural characterization was carried out with X-ray double-crystal diffractometry (XRD) and Raman spectroscopy. Room temperature Raman spectra were recorded in the backscattering geometry using a LabRAM HR Evo UV-VIS-NIR-Open spectrometer (Horiba, France). Nd:YAG laser with a wavelength of 532 nm was used as the excitation source. The laser beam was focused into a spot up to 1 μm in diameter using Olympus confocal microscope.

Results and Discussion

Fig. 1, *a*, *b* shows the technological scheme of the bonding process and photographs of the processed experimental samples.

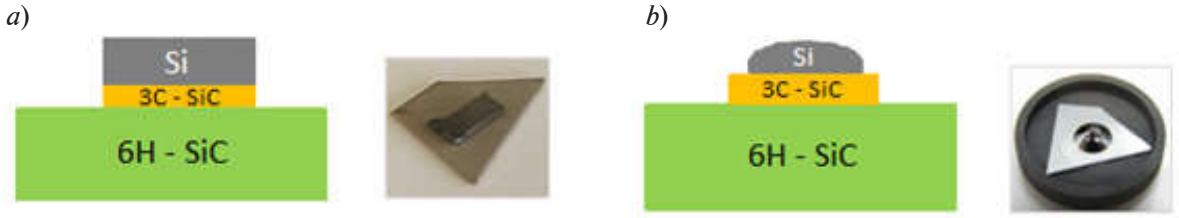

Fig. 1. Scheme of bonding process (left) and the corresponding photographs (right) of experimental samples: before annealing (*a*), after unloading from the annealing chamber (*b*)

It was found that the transferred CVD-layers had strong mechanical contact with SiC wafers when the annealing temperature exceeded the melting temperature of Si (1400 °C). Annealing under these conditions results in conversion of silicon substrate into a droplet of Si melt as shows the photograph in Fig. 1, *b*. Before using the bonded 3C-SiC/6H-SiC structures as a substrate for subsequent sublimation homoepitaxy, the solidified Si melt was removed by wet etching in a 1 : 3 mixture of hydrofluoric (HF) and nitric (HNO_3) acids, which has no etching effect on the underlying silicon carbide.

Structural characterization showed that the best quality was achieved for sublimation epitaxial layers grown on a bonded substrate fabricated at $T = 1500$ °C. XRD rocking curves (RC) obtained on homoepitaxial layers grown by sublimation on a substrate with a transferred CVD adlayer had a full width at half maximum (FWHM) in the range of 120–170 arc seconds whereas RC with FWHM of 300 arc seconds were recorded on starting heteroepitaxial 3C-SiC grown by CVD on a Si substrate. Based on the XRD data, two main conclusions can be drawn: (I) the quality of sublimation epitaxy of 3C-SiC on the combined substrates is at the level of epitaxy of cubic silicon carbide by chemical vapor deposition; (II) despite the fact that the transferred layer had the (001) orientation, its overgrowth proceeded in the [111] direction. To clarify the latter discrepancy, we can consider the data obtained by optical microscopy (Fig. 2, *a*, *b*). A micrograph of the back side of the 3C-SiC CVD layer transferred onto a SiC wafer is shown in Fig. 2, *a*.

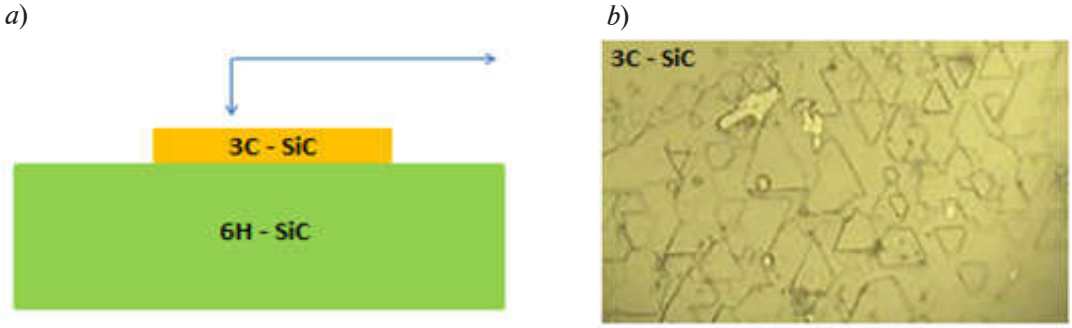

Fig. 2. Results obtained by optical microscopy: explanatory diagram of the studied sample (*a*); back side surface view of 3C-SiC layer transferred on 6H-SiC wafer (×500) (*b*)

An island-like character can be detected in the structure formed at the initial stage of 3C-SiC growth on the Si substrate. The structure is formed by small randomly distributed triangular islands, which are crystallographic twins lying in the (001) plane. Based on this observation and the results of XRD analysis, we can assume that the initial island-like microstructure develops into a microstructure with different island orientation in accordance with van der Drift model of self-regulation of crystal growth from the vapor phase on a substrate with randomly oriented nucleation islands. The evolutionary selection rules proposed in the model determine the termination of the growth in the direction of slowly growing orientations and the development of preferred orientations with a maximum growth rate. In case of cubic crystals, these regularities determine the growth transition from the [100] direction to the [111] direction [7].

Results obtained by XRD analysis were fully confirmed by the results of Raman spectroscopy studies of initial 3C-SiC CVD-grown layers and grown on combined substrates. Raman studies are used in SiC technologies as the main diagnostic method for determining the polytype of experimental samples, the presence of polytype inclusions in them, and evidence of polytype transformations. It is known that in the Raman spectra of 3C-SiC there are two characteristic lines corresponding to the transverse optical mode (TO) at a frequency of 796.2 cm^{-1} and the longitudinal optical mode (LO) at a frequency of 972.7 cm^{-1} [8, 9]. Fig. 3 shows the Raman spectra of CVD-grown 3C-SiC layer on Si and of the layer grown by sublimation layer on the bonded substrate.

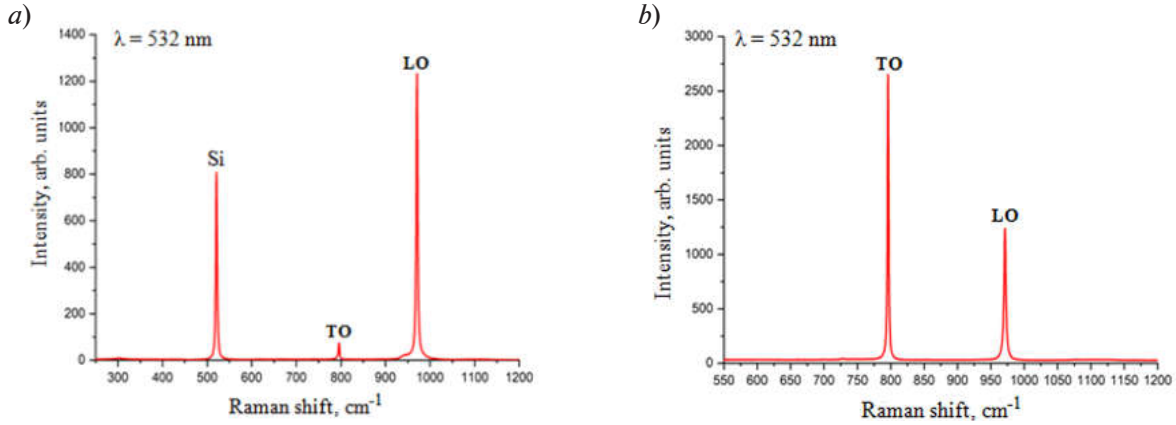

Fig. 3. Raman spectra measured in the starting 3C-SiC/Si sample (*a*) and in the layer grown by sublimation on the transferred 3C-SiC seed adlayer (*b*)

Both spectra contain narrow peaks of TO and LO phonon modes at frequencies ~794 cm^{-1} and ~968 cm^{-1}, respectively. This confirms that the layers correspond to the pure cubic phase of high quality. The spectrum of the CVD-grown layer additionally contains a peak at 520 cm^{-1} corresponding to the silicon substrate. Observed change in the ratio of intensity of the LO and TO phonon lines confirms the phenomenon of changing of orientation from [001] to [111] for the CVD layer and the layer grown by sublimation epitaxy, respectively.

Conclusion

We established that the transfer of 3C-SiC heteroepitaxial CVD-grown layers onto a 6H-SiC wafer makes it possible to develop combined 3C-SiC/6H-SiC structures suitable for use as substrates for high-quality homoepitaxy of cubic polytype silicon carbide. We found that a bonding temperature above the melting temperature of Si is a critical parameter for obtaining good mechanical contact between the transferred 3C-SiC layers and carrier 6H-SiC wafers. Interpretation of the observed phenomenon of the change in the crystallographic orientation of the grown layers relative to the transferred ones requires additional investigation.

REFERENCES

1. **Pensl G., Chobanu F., Frank T., Krieger M., Reshanov S., Schmid F., Weidner M.,** Material properties of SiC, International Journal of High Speed Electronics and Systems, 15 (2005) 705–7450.

2. **Kimoto T., Cooper J.,** Fundamentals of Silicon Carbide Technology: Growth, Characterization, Devices and Applications (John Wiley & Sons, Ltd. Singapore, 2014) 1–538.

3. **Christiansen S.H., Singh R., Gosele U.,** Wafer Direct Bonding: From Advanced Substrate Engineering to Future Applications in Micro/Nanoelectronics, in Proceedings of the IEEE, 94 (12) (2000) 2060–2106.

4. **Wang C., Xu J., Guo S., Kang Q., Wang Y., Wang Y., Tian Y.,** Method for Direct Bonding of Single-Crystalline SiC to Si, SiO_2 and Glass Using VUV Irradiation, Applied Surface Science, 471 (2019) 196–204.

5. **Kang Q., Wang C., Niu F., Zhou S., Xu J., Tian Y.,** Single-Crystalline SiC Integrated onto Si-Based Substrates via Plasma-Activated Direct Bonding, Ceramics International, 46 (2020) 22718–22726.

6. **Xu J., Wang. D., Li J., Cheng Y., Wang C., Hang, Tian Y.,** Fabrication of SiC/Si, SiC/SiO_2 and SiC/Glass Heterostructures via VUV/O_3 Activated Direct Bonding at Low Temperature Ceramics International, 45 (2019) 4094–4098.

7. **van der Drift A.,** Philips research reports, 22 (1967) 267–288.

8. **Okumura H., Sakuma E., Lee J.H., Mukaida H., Misawa S., Endo K., Yoshida S.,** Raman scattering of SiC: Application to the identification of heteroepitaxy of SiC polytypes, Journal of Applied Physics, 61(3) (1987) 1134–1136.

9. **Nakashima S., Harima H.,** Raman Investigation of SiC Polytypes Physics Status Solidi A, 16 (2) 39 (1997) 39–64.

THE AUTHORS

AMELCHUK Dmitriy G.
mutranspet@gmail.com

MYNBAEVA Marina G.
mgm@mail.ioffe.ru
ORCID: 0000-0002-6321-1724

SMIRNOV Alexander N.
Alex.Smirnov@mail.ioffe.ru
ORCID: 0000-0001-9709-5138

DAVYDOV Valery Yu.
Valery.Davydov@mail.ioffe.ru
ORCID: 0000-0002-5255-9530

LEBEDEV Sergey P.
lebedev.sergey@mail.ioffe.ru
ORCID: 0000-0002-5078-1322

LEBEDEV Alexander A.
Shura.lebe@mail.ioffe.ru
ORCID: 0000-0003-0829-5053

Received 12.12.2022. Approved after reviewing 20.02.2023. Accepted 28.02.2023.

Conference materials
UDC [66.061.16;544.163:621.793]:681.586.72
DOI: https://doi.org/10.18721/JPM.161.307

Improved polymer residuals removing after the graphene transfer to enhance sensors performance

L.A. Barsukov [1] ✉, N.P. Nekrasov [1], A.V. Romashkin [1],
I.I. Bobrinetskiy [1], D.D. Levin [1], V.K. Nevolin [1]

[1] National Research University of Electronic Technology, Moscow, Russia
✉ leonty.barsukov@gmail.com

Abstract. Graphene transfer using polymers as a supporting layer makes sensors with exceptional yield and few defects. It is still an issue to make scalable and versatile high-purity graphene transfer method. Current-voltage characteristic slope and hence the sensitivity of the graphene-based devices are limited by the residual polymer left after the transfer process that forms local defects and trapped states quenching charge transfer. Due to the strong interactions between polymer and graphene, residual removal remains an important problem to solve. In this work graphene on Cu foil was covered using spin-coating of poly(methyl methacrylate) (PMMA) with different molecular masses and the addition of a low volatile additive. The film obtained was transferred onto Si/SiO_2 substrates. In order to remove PMMA residues multiple cleaning techniques with different solvents were used and compared to each other; new methods were developed. The quality of the purified graphene was studied by analyzing AFM, Raman, fluorescence spectroscopy data. The structure was <1 nm thick with a 2D to G peak ratio, of ~ 5.

Keywords: graphene transfer, polymer removal, sensor, polymethylmethacrylate

Funding: This work was supported by grant of the Russian Science Foundation, agreement No. 19-19-00401 (https://www.rscf.ru/project/19-19-00401/, development of PMMA removing techniques); grant of the President of the Russian Federation MK-4010.2022.4 (AFM study).

Citation: Barsukov L.A., Nekrasov N.P., Romashkin A.V., Bobrinetskiy I.I., Levin D.D., Nevolin V.K., Improved polymer residuals removing after the graphene transfer to enhance sensors performance, St. Petersburg State Polytechnical University Journal. Physics and Mathematics. 16 (1.3) (2023) 44–49. DOI: https://doi.org/10.18721/JPM.161.307

Материалы конференции
УДК [66.061.16;544.163:621.793]:681.586.72
DOI: https://doi.org/10.18721/JPM.161.307

Повышение эффективности удаления остаточного полимера после переноса графена для повышения чувствительности сенсоров

Л.А. Б рсуков [1] ✉, Н.П. Некр сов [1], А.В. Ром шкин [1],
И.И. Бобринецкий [1], Д.Д. Левин [1], В.К. Неволин [1]

[1] Национальный исследовательский университет «МИЭТ», Москва, Россия
✉ leonty.barsukov@gmail.com

Аннотация. При переносе графена с использованием полиметилметакрилата удается формировать высокочувствительные сенсоры на основе графена с высокой воспроизводимостью геометрических параметров канала на микроуровне и малой дефектностью. Однако, удаление остаточного полимера остаётся актуальной проблемой. Было осуществлен перенос графена с использованием ПММА с различной молекулярной массой на Si/SiO_2 подложки. Для удаления слоя ПММА сравнивались различные методики с применением широко используемых растворителей. При использовании наиболее

эффективной методики очистки, толщина перенесённого графена с остаточным ПММА составила менее 1 нм, а соотношение 2D/G составило ~5. С помощью разработанных методик удаления остаточного ПММА может быть обеспечено увеличение чувствительности для недорогих многоразовых сенсоров на основе графена.

Ключевые слова: перенос графена, сенсор, удаление полимера, полиметилметакрилат

Финансирование: Работа выполнена при поддержке гранта Российского научного фонда, соглашение № 19-19-00401 (https://www.rscf.ru/project/19-19-00401/, разработка методики удаления ПММА); гранта Президента Российской Федерации № МК-4010.2022.4 (исследование АСМ).

Ссылка при цитировании: Барсуков Л.А., Некрасов Н.П., Ромашкин А.В., Бобринецкий И.И., Левин Д.Д., Неволин В.К. Повышение эффективности удаления остаточного полимера после переноса графена для повышения чувствительности сенсоров // Научно-технические ведомости СПбГПУ. Физико-математические науки. 2023. Т. 16. № 1.3. С. 44–49. DOI: https://doi.org/10.18721/ JPM.161.307

Introduction

Graphene transfer with the use of poly(methyl methacrylate) (PMMA) is the base method to manufacture devices based on graphene [1, 2], which is initially synthesized on Cu foil by chemical vapour deposition (CVD) and has an acceptable quality of the graphene. However, after graphene is transferred to a substrate, it usually contains PMMA residuals, which greatly decreases the effective sensibility of the work area. Therefore, the current-voltage slope and, hence, device performance depend on the quantity of residual PMMA left [3]. Apart from covering the surface and making it impossible to modify it, PMMA residuals also cause defects formation and trap-like behavior states on it. Despite the efficiency of the solvents, a thin layer of PMMA clusters stays coupled with the graphene as that is more energetically favorable than being removed by the solvent. Removing this residual layer is an important problem to solve, thus a special cleaning technique using two or more different solvents [3] and two-stage cleaning is to be developed [4] since the standard PMMA solvents (acetone, ethyl acetate, trichloroethylene etc. [5]) do not provide a sufficient degree of graphene purity. The quality of pristine graphene can be estimated by the 2D to G peaks ratio at Raman spectra, hence the effectiveness of the rinsing method applied evaluates this ratio and reaches ~2-5 at best [3, 4]. The high fluorescence of pristine and rinsed graphene is an effect of interactions between graphene, residuals and solvent molecules that can be used to evaluate the number of residuals on the surface [6-8]. However, its relation to the analysis of the graphene cleaning quality is not studied enough. Thus, it is required to develop efficient methods for the residual polymer removal after the main PMMA layer is removed with standard solvents, as well as study the performance of such methods using atomic force microscopy (AFM), fluorescence and Raman spectroscopy altogether.

Materials and Methods

In this work we used CVD-grown graphene (Graphenea, Spain) on Cu foil. PMMA with different molecular mass – 495 kDa (MicroChem, USA) with 2-phenyl ethanol (2PE) additive, as well as 350 kDa 2% solutions in anisole (Sigma-Aldrich, USA), was used to form the supporting layer required for transfer. PMMA was spin-coated onto graphene at 2.5 krpm and annealed at 80 °C after. In order to remove polymer residuals film was rinsed in different solvents: acetone, trichloroethylene (TCE), isopropanol (IPA), butyl acetate (BA), tetrahydrofuran (THF) (Komponent-Reaktiv, Russia), for about half an hour at ~50 °C to increase the dissolution rate. The quality of graphene was investigated using AFM (Solver-Pro, NT-MDT, Russia) for graphene transferred on Si/SiO_2 and Raman spectroscopy with background fluorescence intensity analysis (Centaur U HR, 532 nm laser, Nano Scan Technology, Russia) for graphene on Cu foil (without transfer, but with all processes of deposition and removing PMMA).

Results and Discussion

AFM images obtained (Fig. 1) show that the residual layer is whole, with small craters in different areas, that can also be identified as pores due to the probe's large curvature radius. Rinsing in acetone left a lot of PMMA residuals [1] with a total height of graphene with PMMA layer ~4 nm (Fig. 1, *c*). Sample re-rinsed with the mixture of commonly used solvents THF:BA, 6:4 decreased the size of individual PMMA clusters between clean areas of graphene, left after the first rinsing (Fig. 1, *d*). Since THF and BA are similar in properties to the solvents used in another work [4] this mixture can effectively remove polymer residual from graphene.

Rinsing with THF:BA mixture forms clean areas of graphene between residual PMMA clusters, while the best PMMA solvent – trichloroethylene [5] leaves the thin but continuous layer of PMMA residuals. Therefore, the near-surface layer removal has a weak dependence on polymer solubility and is determined by the interaction of polymer molecules with graphene. Solvents such as THF, especially in combination with the small non-solvent molecule, can provide a better polymer removal rate [9], which is why in our work we have switched from using THF:BA or IPA:H_2O [3], to the THF:H_2O.

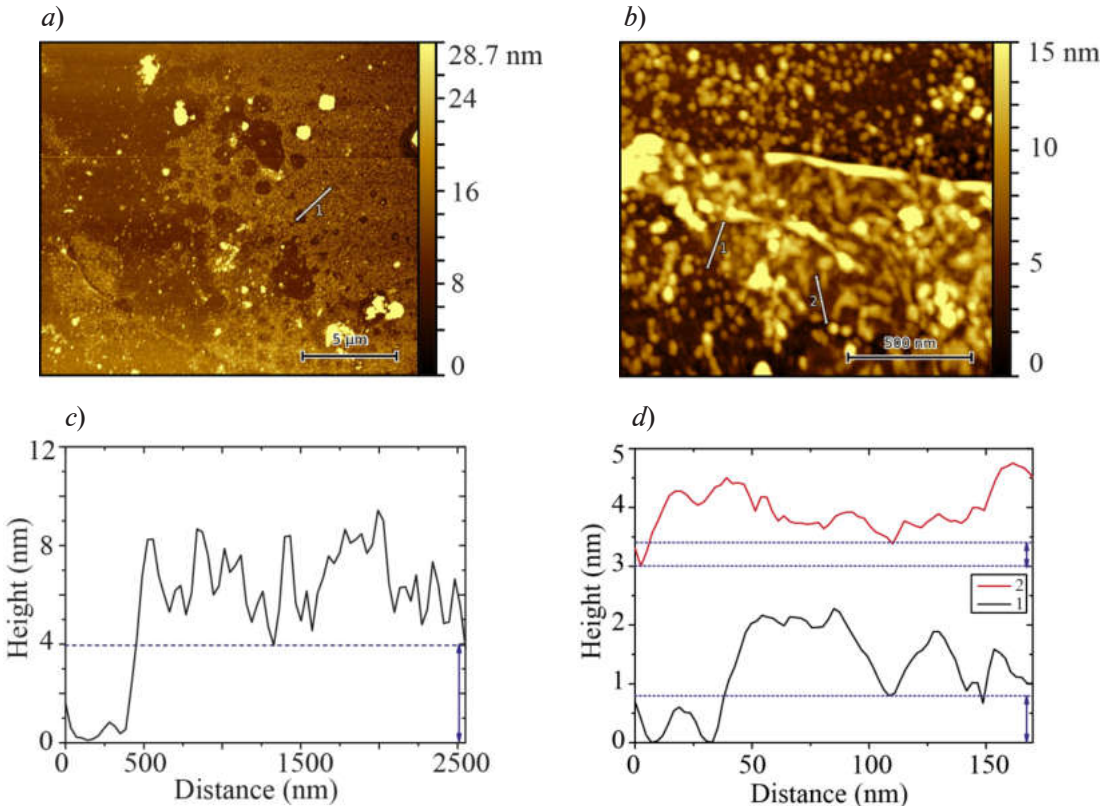

Fig. 1. AFM data of the 495 kDa PMMA on graphene rinsed with acetone (*a*, *c*), THF:BA (*b*, *d*)

AFM data does not provide sufficient information to estimate the number of defects in the crystal structure of graphene. However, Raman and fluorescence spectra show a strong correlation between residuals left and 2D peak width, position and 2D to G peak intensity ratio, which allows us to estimate the quality and purity of rinsed graphene. AFM data has shown that the 495 kDa PMMA sample cleaned with acetone average thickness of polymer residuals is larger than the 350 kDa one rinsed the same way, but Raman spectra 2D/G ratio is bigger for the 495 kDa one, proving that it is cleaner than for 350 kDa one. Hence, 350 kDa PMMA has formed the continuous layer with less clean graphene areas.

Intensive fluorescence was observed on the samples with graphene on the Cu foil (Fig. 2, *a*, *b*) [6], which can be an effect of interaction between graphene and residuals or impurities on its surface causing fluorescence similar to graphene quantum dots [7] with more than 20 nm sizes [8],

which can be formed between residual molecules at graphene. The spectra of the point with the least amount of graphene in the laser spot (looking the same as no graphene areas in the optics) show less fluorescence, proving that it is caused by interactions between graphene and other molecules. Moreover, fluorescence decreased for the samples with PMMA 350 kDa layer formed, and increased for the 495 kDa PMMA with 2PE ones, compared to the initial graphene. Using 495 kDa PMMA with 2PE additive forms non-homogeneous graphene regions with either more 2PE or PMMA. That is similar to the fluorescence signal from graphene regions with polymer molecules separated by the clean areas or vice versa. Trichloroethylene cleaned samples and the uncleaned ones full-covered with PMMA have almost the same fluorescence, especially for PMMA with smaller molecular weight, indicating that the residuals are not entirely removed, which can also be proved by the 2D to G ratio (Fig. 2, *c*, *d*). Both 495 kDa PMMA with 2PE additive and 350 kDa PMMA samples were rinsed with THF:water, which has led to fluorescence increase (Fig. 2, *a*, *b*), showing that this treatment still leaves residual molecules on the surface. Nonetheless, this particular re-rinsing procedure allows us to dramatically decrease the number of residuals left, resulting in larger 2D to G peaks ratios ~5 (Fig. 2, *c*, *d*), which is the high value [4]. Thus, most of the graphene is cleaned, but it still has nanoscale areas separated by residual molecules that are not entirely removed, hence the quality of the graphene obtained can be improved even further.

We found out that during re-rinsing with THF:water at 50 °C, the copper foil is a catalyst for the reaction between THF and water [10], resulting in Cu_2O formation [11]. Cu oxidation is characterized by Raman peaks in the spectra (from 534 to 540 nm, Fig 2, *a*, *b*). Oxidation has affected the reduction of the fluorescence suppression characteristic of the original metal surface.

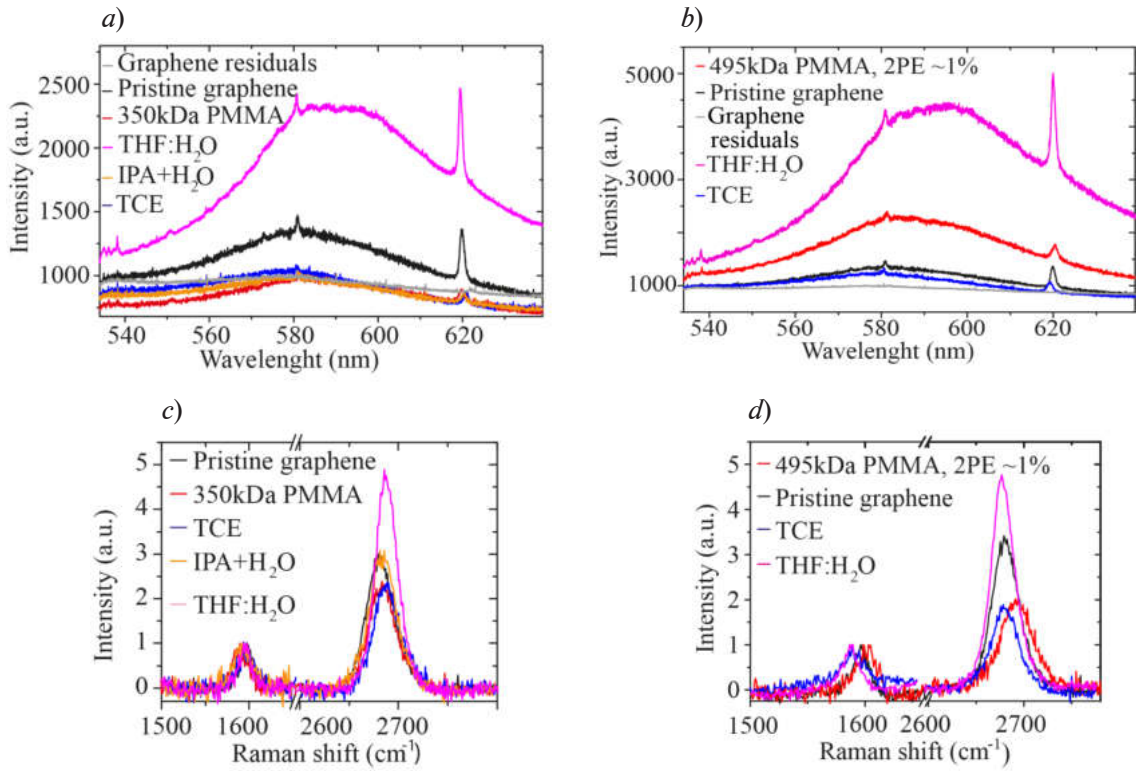

Fig. 2. Fluorescence (*a*, *b*) and Raman spectra (*c*, *d*) of the graphene with different treatment

Mechanical stress or changes in electronic structure in graphene with PMMA film deposited and removed are well characterized by 2D peak position (Fig. 3, *a*). Exfoliated graphene on a substrate, that has no residuals, has the 2D peak at ~2686 cm^{-1} [12]. The changes in the 2D peak position (Fig. 3, *a*) and in the 2D/G ratio (Fig. 3, *b*) compared to reference data for the deposited PMMA and rinsed one with TCE indicate different mechanisms of interaction with graphene for 495 kDa PMMA containing 2PE and 350 kDa PMMA.

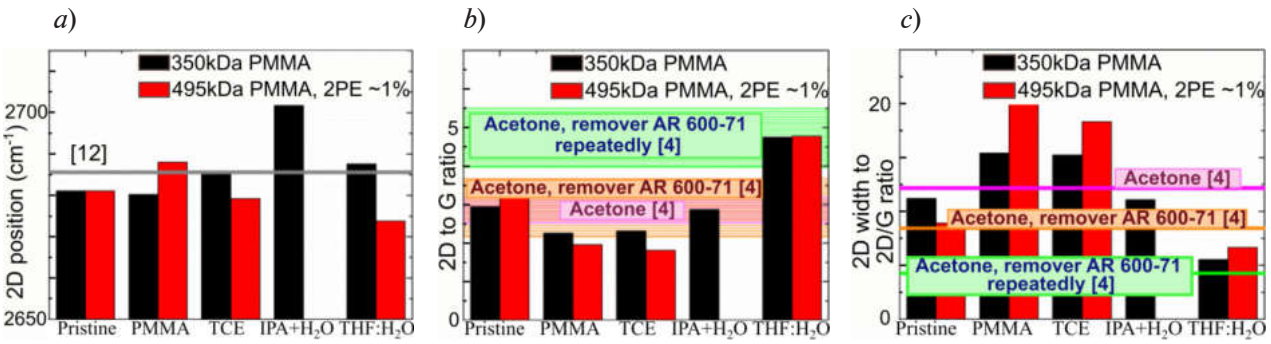

Fig. 3. Diagrams of the 2D peak position (*a*), 2D to G ratio (*b*), 2D width to intensity ratio (*c*)

This demonstrates the importance of the 2PE molecules remaining in the near-surface layer, which greatly affects the graphene properties. The significant improvement in the 2D/G ratio, as well as the narrowing of the 2D peak for samples rinsed with THF:water, in contrast to the behaviour of fluorescence, indicate the essential purity degree of the graphene. Due to the remaining shift of the 2D peak for the samples with the 2PE additive, it is evident that 2PE itself is still present after all purification procedures. The IPA:water treatment [3] provided an improvement over the TCE rinsing, but was less effective than THF:water.

Conclusion

New efficient method of PMMA residual removal from graphene was developed. This method includes post-processing in THF:water solution after traditional TCE washing. The main idea is to overcome the strong interaction between PMMA residuals and graphene by using specific solvent-non-solvent interactions with PMMA and removing all of them. Thus, high graphene purity was achieved, which is confirmed by the high-intensity ratio of the 2D/G peaks of about 5. However, these results can be further improved by removing the remaining molecules on the graphene, which is the goal of our further research. Clean graphene on the target substrate is a base for the further development of highly sensitive sensors of any sort able of detecting substances with extremely low molecule concentrations (~0.1 pM). This sensitivity can be improved by using the graphene channel purified with the proposed method. It allows us to make compact non-invasive reusable sensors able to detect diseases and viruses in outer body fluids like sweat and make gas sensors with improved sensitivity.

REFERENCES

1. **Nekrasov N., Jaric S., Kireev D., Emelianov A. V., Orlov A. V., Gadjanski I., Nikitin P.I., Akinwande D., Bobrinetskiy I.,** Real-time detection of ochratoxin A in wine through insight of aptamer conformation in conjunction with graphene field-effect transistor, Biosensors and Bioelectronics. 200 (2021) 113890.

2. **Romashkin A.V., Struchkov N.S., Lashkov A.V., Shpakov D.S., Nekrasov N.P., Emelianov A.V.,** Ammonia Recognition at Different Humidity with a Graphene Sensors Array Modified by a Focused Ion Beam. Proceedings of the 2022 International Conference on Actual Problems of Electron Devices Engineering, Saratov, IEEE, (2022) 186–190.

3. **Duan T., Li H., Papadakis R., Leifer K.,** Towards ballistic transport CVD graphene by controlled removal of polymer residues, Nanotechnology. 33 (49) (2022) 495704.

4. **Tyagi A., Mišeikis V., Martini L., Forti S., Mishra N., Gebeyehu Z. M., Giambra M.A., Zribi J., Fregnaux M., Aureau D., Romagnoli M., Betlam F., Coletti C.,** Ultra-clean high-mobility graphene on technologically relevant substrates, Nanoscale. 14 (6) (2022) 2167–2176.

5. **Evchuk I. Y., Musii R. I., Makitra R. G., Pristanskii R. E.,** Solubility of polymethyl methacrylate in organic solvents, Russian journal of applied chemistry. 78 (10) (2005) 1576-1580.

6. **Machac P., Cichon S., Lapcak L., Fekete L.,** Graphene prepared by chemical vapour deposition process, Graphene Technology. 5 (1) (2020) 9–17.

7. **Bradley, S.J., Kroon, R., Laufersky, G., Rųding, M., Goreham, R.V., Gschneidtner T., Schroeder K., Moth-Poulsen K., Andersson M., Nann T.,** Heterogeneity in the fluorescence of graphene and graphene oxide quantum dots, Microchimica Acta. 184 (3) (2017) 871–878.

8. **Kim S., Hwang S.W., Kim M.K., Shin D.Y., Shin D.H., Kim C.O., Yang S.B., Park J.H., Hwang E., Choi S. H., Ko G., Sim S., Sone C., Choi H.J., Bae S., Hong B.H.,** Anomalous behaviors of visible luminescence from graphene quantum dots: interplay between size and shape, ACS nano 6 (9) (2012) 8203–8208.

9. **Miller-Chou B.A., Koenig J.L.,** A review of polymer dissolution, Progress in Polymer Science 28(8) (2003) 1223–1270.

10. **Liu Y., Mellmer M.A., Alonso D.M., Dumesic J.A.,** Effects of Water on the Copper-Catalyzed Conversion of Hydroxymethylfurfural in Tetrahydrofuran, ChemSusChem. 8 (23) (2015) 3983–3986.

11. **Deng Y., Handoko A.D., Du Y., Xi S., Yeo B.S.,** In situ Raman spectroscopy of copper and copper oxide surfaces during electrochemical oxygen evolution reaction: identification of CuIII oxides as catalytically active species, Acs Catalysis. 6 (4) (2016). 2473–2481.

12. **Ferrari A.C., Basko D.M.,** Raman spectroscopy as a versatile tool for studying the properties of graphene, Nature nanotechnology. 8 (4) (2013) 235–246.

THE AUTHORS

BARSUKOV Leonty A.
leonty.barsukov@gmail.com
ORCID: 0000-0002-4802-0014

BOBRINETSKIY Ivan I.
bobrinet@mail.ru
ORCID: 0000-0003-2380-2594

NEKRASOV Nikita P.
8141147@gmail.com
ORCID: 0000-0003-1417-0177

LEVIN Denis D.
skaldd@yandex.ru
ORCID: 0000-0002-8414-6191

ROMASHKIN Alexey V.
romaleval@gmail.com
ORCID: 0000-0002-0101-6122

NEVOLIN Vladimir K.
vkn@miee.ru
ORCID: 0000-0003-4348-0377

Received 14.12.2022. Approved after reviewing 23.01.2023. Accepted 23.01.2023.

Conference materials
UDC 539.3
DOI: https://doi.org/10.18721/JPM.161.308

Curvature and bow of III-N HEMT structures during epitaxy on silicon substrates

O.A. Kelner [1,3] ✉, A.F. Tsatsulnikov [2], A.E. Nikolaev [2,3], E.E. Zavarin [2,3]

[1] Saint Petersburg Electrotechnical University "LETI", St. Petersburg, Russia;

[2] Submicron Heterostructures for Microelectronics, Research & Engineering Center, RAS, St. Petersburg, Russia;

[3] Ioffe Institute, St. Petersburg, Russia

✉ olegkelner08@gmail.com

Abstract. High Electron Mobility Transistor (HEMT) heterostructures based on III-N semiconductors (nitrides of Al and Ga) have become increasingly widespread in recent years. They are used in the manufacture of microwave transistors, high-power transistors for power electronics, etc. However, mass application of such transistors requires a reduction in the cost of heterostructures due to the use of cheap substrates and an increase in the area of one substrate. Thus, substrates of single-crystal Si(111) are of great interest. They are available in diameters up to 300 mm, and the possibility of growing III-N structures has already been demonstrated for them. Nevertheless, the epitaxy of III-N HEMT structures on Si substrates is complicated due to a number of technological difficulties in the epitaxy of such structures. In this paper, the dynamics of curvature and residual bow of III-N HEMT structures were experimentally studied during epitaxy and after cooling for Si(111) substrates with a diameter of 100 mm and various thicknesses of substrates and grown semiconductor films. It has been shown that the technology developing and optimization should be carried out on thin substrates, while device structures should be grown on thick substrates. Furthermore, the mechanical stresses can be controlled accurately enough so after epitaxy the bow of the structure is minimal.

Keywords: MOVPE, HEMT, elastic strain, silicon

Citation: Kelner O.A., Tsatsulnikov A.F., Nikolaev A.E., Zavarin E.E., Curvature and bow of III-N HEMT structures during epitaxy on silicon substrates, St. Petersburg State Polytechnical University Journal. Physics and Mathematics. 16 (1.3) (2023) 50–54. DOI: https://doi.org/10.18721/JPM.161.308

Материалы конференции
УДК 539.3
DOI: https://doi.org/10.18721/JPM.161.308

Кривизна и прогиб III-N HEMT структур при эпитаксии на кремниевых подложках

О. А. Кельнер [1,3] ✉, А. Ф. Цацульников [2], А. Е. Николаев [2,3], Е. Е. Заварин [2,3]

[1] Санкт-Петербургский государственный электротехнический университет «ЛЭТИ» им. В.И. Ульянова (Ленина), Санкт-Петербург, Россия;

[2] НТЦ микроэлектроники РАН, Санкт-Петербург, Россия;

[3] Физико-технический институт им. А.Ф. Иоффе РАН, Санкт-Петербург, Россия

✉ olegkelner08@gmail.com

Аннотация. В настоящей работе проведено экспериментальное исследование динамики кривизны и остаточного прогиба III-N HEMT структур во время и после эпитаксии для подложек Si(111) диаметром 100 мм различной толщины; была определена динамика кривизны от толщины структуры во время роста, что позволяет определить параметры эпитаксии для получения необходимого прогиба структур после остывания.

Ключевые слова: ГФЭ МОС, полевые транзисторы, упругие напряжения, кремний

Ссылка при цитировании: Кельнер О.А., Цацульников А.Ф., Николаев А.Е., Заварин Е.Е. Кривизна и прогиб III-N HEMT структур при эпитаксии на кремниевых подложках // Научно-технические ведомости СПбГПУ. Физико-математические науки. 2023. Т. 16. № 1.3. С. 50–54. DOI: https://doi.org/10.18721/ JPM.161.308

Introduction

High Electron Mobility Transistor (HEMT) heterostructures based on III-N semiconductors (nitrides of Al and Ga) have become increasingly widespread in recent years [1]. They are used for manufacturing microwave transistors, high-power transistors for power electronics, etc. However, the mass application of such transistors requires a reduction in the cost of heterostructures through the use of cheap substrates and an increase in the area of each of them. From this point of view, substrates of single-crystal Si(111) are of great interest. They are available in diameters up to 300 mm [2] and have already been shown to grow III-N structures. However, epitaxy of III-N HEMT structures on Si substrates is very difficult due to the significant difference in lattice parameters and in thermal expansion coefficients (TEC) of the substrate and III-N layers [3]. There are also a number of technological difficulties in the epitaxy of such structures associated with the solubility of Ga in Si, warping of large-diameter substrates due to temperature inhomogeneity, leading to their plastic deformation, etc.

Materials and Methods

Equipment. The experiments were carried out on a MOVPE Dragon D-125 growth system [4] with an inductively heated susceptor and custom-built gas injector allowing high growth rate and uniformity. The setup has a horizontal flow reactor and a laser reflectometry system with the ability to measure the structures curvature in-situ.

Structure growth method on silicon. One of the main epitaxy problems is the difference between the TEC of the substrate and III-N layers, which leads to a strong contortion of the structure after epitaxy and cooling. To eliminate this effect, the technique of creating mechanical stresses in the growing III-N layers during growth is used [5–9] to compensate for the stresses that arise during the cooling of the structure. Since the structures are highly stressed, after the epitaxy process, they can have a different bow, which affects the subsequent stages of transistor fabrication. The order of growing HEMT structures is shown in Fig. 1.

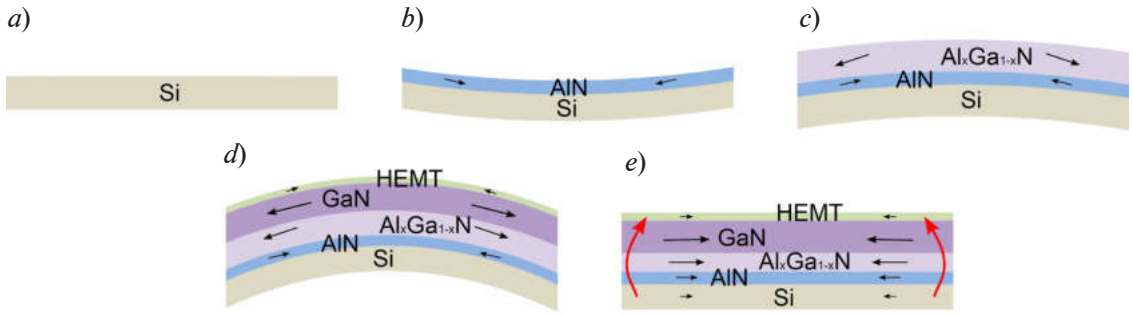

Fig. 1. Order of growing HEMT structures: flat silicon substrate (*a*); first AlN layer protecting Si from Ga and creating initial stresses (*b*); AlGaN buffer of several variable composition layers to maintain the coherence of GaN growth on AlN and stress accumulation (*c*); GaN layer for the accumulation of mechanical stresses, the creation of a non-conductive buffer layer and the active region of the HEMT (*d*); structure distortion during cooling after epitaxy (*e*).
The black arrows show the direction of layer contortion at each stage; the red ones show the distortion of the whole structure during cooling

Structure growth starts with substrate annealing (T = 1130 °C; p = 100 mbar) to get rid of silicon oxide covering the substrate (Fig. 1, *a*). After that an AlN layer is deposited (T = 1100 °C [10]; p = 110 mbar; growth rate ≈ 0.5 μm/h) to prevent etching of Si by Ga melt (Fig. 1,*b*). Then a set of AlGaN layers (T = 1050 °C; p = 100 mbar; 6 layers of different composition; composition being controlled by concentration of Al and Ga ratio; Al concentration in solid solution: 80%, 60%, 45%, 35%, 15%, 10%) for stress compensation are grown (Fig. 1,*c*). HEMT structure is finalized (T = 1050–1100 °C; p = 100–400 mbar) with doped with Fe and C and undoped GaN layers, AlN spacer (f = 1 nm), $Al_{0.23}Ga_{0.77}N$ barrier layer (f = 23 nm) and in-situ deposited SiN (f = 5 nm) (Fig. 1,*d*). At the end of epitaxy grown structure is cooled down ($t \approx 30$ min) to the room temperature (Fig. 1, *e*).

Geometry of the structures. The curvature coefficient, defined as the reciprocal of the curvature, at constant mechanical stresses in the structure layers according to the Stoney equation (1) is directly proportional to the thickness of the grown film and inversely proportional to the square of the substrate thickness:

$$k = \frac{1}{R} \sim \frac{f}{H^2}, \tag{1}$$

where k is the curvature coefficient, R is the curvature, f is the film thickness, H is the substrate thickness.

Based on geometric considerations (Fig. 2) and the smallness of bow h in relation to the curvature R and substrate diameter d, we can obtain expression (2) for calculating h.

$$h = \frac{d^2}{8R} = \frac{kd^2}{8}. \tag{2}$$

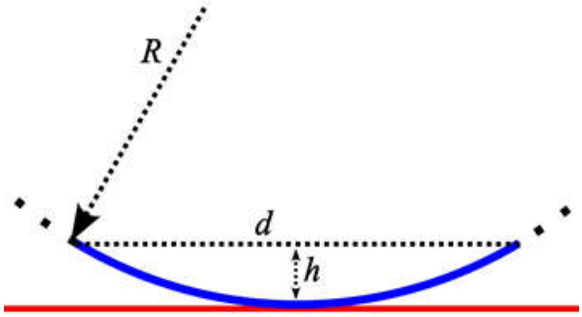

Fig. 2. Relation between curvature R and substrate diameter d and bow h

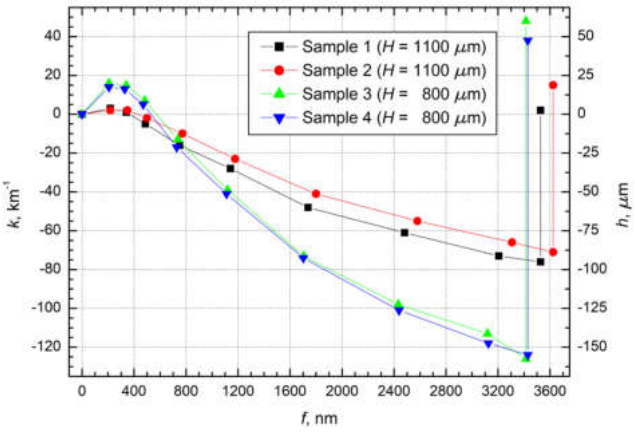

Fig. 3. Graph of the curvature k and bow h vs thickness of the growing structure f at different thicknesses of substrate H (given in brackets for each sample)

The structure bow is proportional to the square of the substrate diameter, so as substrates increase in size, it is necessary to significantly reduce the residual curvature. The condition for post-growth processing is a bow of no more than 50 μm, which corresponds to a curvature of 40 km^{-1} for a 100 mm substrate.

Results and Discussion

The curvature of the grown structure, as well as the growth rate of each layer, was determined from data in-situ measured during growth for each layer. The structure layers thicknesses were calculated based on the known growth times and corresponding for each layer rates, and the bow was calculated based on the curvatures and structure geometric dimensions.

Dependence on substrate thickness. Fig. 3 shows the curvature and bow dependence on thickness of the growing structure at different thicknesses of substrate. It is clearly seen that the thinner substrate is contorting more than thick one.

Dependence on structure thickness. Fig. 4 shows the curvature and bow dependence on thickness of the growing structure for different thicknesses of final films. Substrate thicknesses were equal. It is seen that controlling compositions and thicknesses of the buffer layers allow to control the

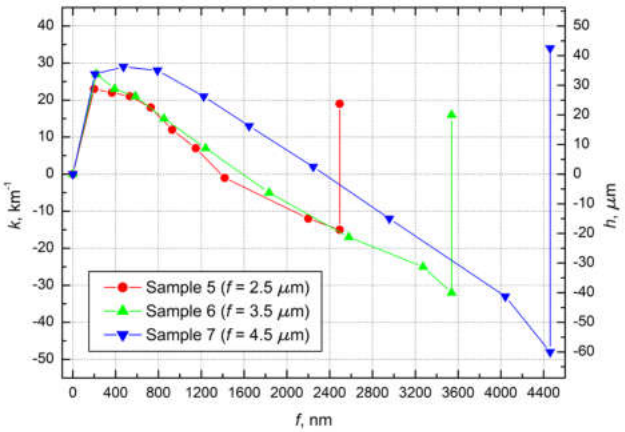

Fig. 4. Graph of the curvature k and bow h vs thickness of the growing structure f at different total thicknesses of structure (given in brackets for each sample)

mechanical stresses in the layers during the growth.

Table 1 shows the final bows of the heterostructures. The best result was demonstrated by sample 1, while sample 3 did not fit into the tolerance at all (II.C).

Table 1

Final bow of heterostructures after cooling

Sample	1	2	3	4	5	6	7
h, μm	2.5	18.8	60.0	47.5	23.8	20.0	42.5

Conclusion

To conclude, it has been shown that under certain mechanical stresses in the layers, the curvature and bow of the structure are inversely proportional to the square of the substrate thickness. Therefore, the technology developing and optimization should be carried out on thin substrates so that the sensitivity is higher and the response to stress changes is more noticeable, while device structures should be grown on thick substrates so that the final bow is minimal.

Furthermore, the mechanical stresses can be controlled accurately enough by compositions and thicknesses of the buffer layers so that after epitaxy the bow of the structure is minimal.

REFERENCES

1. **Kuliev M. V.,** Overview of today's GaN transistors and development trends, Electronic engineering Series 2 Semiconductor devices, 2 (245) (2017) 18–28.

2. Enkris Semiconductor Inc. URL: http://en.enkris.com/index.php?c=show&id=133. Accessed October 13, 2022.

3. **Liu H. F., Dolmanan S. B., Zhang L., Chua S. J., Chi D. Z., Heuken M., Tripathy S.,** Influence of stress on structural properties of AlGaN/GaN high electron mobility transistor layers grown on 150 mm diameter Si(111) substrate, Journal of Applied Physics. 113 (2) (2013) 023510-1–7.

4. **Fedotov S. D., Lundin W. V., Zavarin E. E., Tsatsulnikov A. F., Sokolov E. M., Statsenko V. N.,** Ga(Al)N HEMT Heteroepitaxy on Ultrahigh-Resistivity Silicon Epitaxial Wafers, Nanoindustry, 13 (5) (2020) 209–212.

5. **Cai Y., Zhu C., Jiu L., Gong Y., Yu X., Bai J., Esendag V., Wang T.,** Strain analysis of GaN HEMTs on (111) silicon with two transitional $Al_xGa_{1-x}N$ layers, Materials, 11 (10) (2018) 1968.

6. **Wosko M., Paszkiewicz B., Szymanski T., Paszkiewicz R.,** Optimization of AlGaN/GaN/Si(111) buffer growth conditions for nitride based HEMTs on silicon substrates, Journal of Crystal Growth, 414 (2015) 248–253.

7. **Lee J.-H., Im K.-S.,** Growth of High Quality GaN on Si (111) Substrate by Using Two-Step Growth Method for Vertical Power Devices Application, Crystals, 11 (3) (2021) 234.

8. **Rudinsky M., Yakovlev E., Talalaev R., Novak T., Kostelnik P., Sik J.,** Analysis of strain and dislocation evolution during MOCVD growth of an AlGaN/GaN power high-electron-mobility transistor structure, Japanese Journal of Applied Physics, 58 (SC) (2019) SCCD26.

9. **Cheng J., Yang X., Sang L. et al.,** Rowth of high quality and uniformity AlGaN/GaN heterostructures on Si substrates using a single AlGaN layer with low Al composition, Scientific Reports, 6 (23020) (2016) 1–7.

10. **Novak T., Kostelnik P., Konecny M., Cechal J., Kolibal M., Sikola T.,** Temperature effect on Al predose and AlN nucleation affecting the buffer layer performance for the GaN-on-Si based high-voltage devices, Japanese Journal of Applied Physics, 58 (SC) (2019) SC1018.

THE AUTHORS

KELNER Oleg A.
olegkelner08@gmail.com
ORCID: 0000-0002-4222-7145

NIKOLAEV Andrey E.
aen@mail.ioffe.ru
ORCID: 0000-0001-6522-4484

TSATSULNIKOV Andrey F.
andrew@beam.ioffe.ru
ORCID: 0000-0002-5078-8946

ZAVARIN Evgenii E.
zavarin@yandex.ru
ORCID: 0000-0001-8380-3172

Received 14.12.2022. Approved after reviewing 18.01.2023. Accepted 18.01.2023.

Conference materials
UDC 538.915
DOI: https://doi.org/10.18721/JPM.161.309

Formation and magnetic properties of ultrathin cobalt silicides films on Si surface

A.A. Monyak [1] ✉, G.S. Grebenyuk [2], E.Yu. Lobanova [3], M.V. Kuzmin [2]

[1] Saint Petersburg Electrotechnical University "LETI", St. Petersburg, Russia;
[2] Ioffe Institute, St. Petersburg, Russia;
[3] ITMO University, St. Petersburg, Russia
✉ andreimonyak@gmail.com

Abstract. High-resolution photoelectron spectroscopy with synchrotron radiation and magnetic linear dichroism in Co 3p core-level photoemission have been used to study the initial stages of formation and ferromagnetic ordering of Co/Si(100) and Co/Si(111) interfaces. The correlation between the phase composition, electronic structure and magnetic behavior of the interfaces has been established during Co deposition on Si surface and subsequent sample annealing. It is shown that ferromagnetic ordering has a threshold nature and arises after the deposition of 6 Å of Co in both systems. At higher Co coverages a continuous film of a Si solid solution in cobalt is found to develop. Further increase of ferromagnetic ordering of the interface is caused by the growth of pure metal film. Annealing of the samples covered with a Co film of few nm thickness leads to the gradual disappearance of the metal film and formation of four silicide phases: a metastable ferromagnetic Co_3Si silicide obtained at room temperature for the first time and three stable non-magnetic cobalt silicides: Co_2Si, CoSi and $CoSi_2$. It is shown that solid-phase reactions start at ~250 °C and ~320 °C in Co/Si(100) and Co/Si(111) systems respectively.

Keywords: cobalt, magnetic properties, silicides, photoelectron spectroscopy

Citation: Monyak A.A., Grebenyuk G.S., Lobanova E.Yu., Kuzmin M.V., Formation and magnetic properties of the ultrathin cobalt silicides films on Si surface, St. Petersburg State Polytechnical University Journal. Physics and Mathematics. 16 (1.3) (2023) 55–61. DOI: https://doi.org/10.18721/JPM.161.309

Материалы конференции
УДК 538.915
DOI: https://doi.org/10.18721/JPM.161.309

Формирование и магнитные свойства ультратонких пленок силицидов кобальта на поверхности кремния

А.А. Моняк [1] ✉, Г.С. Гребенюк [2], Е.Ю. Лоб нов [3], М.В. Кузьмин [2]

[1] Санкт-Петербургский государственный электротехнический университет «ЛЭТИ» им. В.И. Ульянова (Ленина), Санкт-Петербург, Россия;
[2] Физико-технический институт им. А.Ф. Иоффе РАН, Санкт-Петербург, Россия;
[3] Университет ИТМО, Санкт-Петербург, Россия
✉ andreimonyak@gmail.com

Аннотация. Начальные стадии формирования и ферромагнитное упорядочение интерфейсов Co/Si(100) и Co/Si(111) были исследованы с помощью фотоэлектронной спектроскопии высокого разрешения с использованием синхротронного излучения и магнитного линейного дихроизма в фотоэмиссии Co 3p остовных уровней. Показано, что ферромагнитное упорядочение носит пороговый характер и возникает после напыления 6 Å Co в обеих системах. Отжиг образцов приводит к образованию четырех

силицидных фаз: метастабильного ферромагнитного силицида Co_3Si, впервые полученного при комнатной температуре, и трех стабильных немагнитных силицидов кобальта: Co_2Si, CoSi и $CoSi_2$.

Ключевые слова: магнитные свойства, силициды, фотоэлектронная спектроскопия

Ссылка при цитировании: Моняк А.А., Гребенюк Г.С., Лобанова Е.Ю., Кузьмин М.В. Формирование и магнитные свойства ультратонких пленок силицидов кобальта на поверхности кремния // Научно-технические ведомости СПбГПУ. Физико-математические науки. 2023. Т. 16. № 1.3. С. 55–61. DOI: https://doi.org/10.18721/ JPM.161.309

Introduction

In the past decades, formation of thin cobalt silicide films on silicon has drawn much attention because it represents interesting science and promising applications [1–3]. The initial effort was focused on the fabrication of defect-free epitaxial $CoSi_2$ films. Low resistivity, high thermal stability and small lattice mismatch with silicon allow the films to be used as very attractive contact and interconnect materials in integrated circuit technology [1, 2]. A new impetus to this research came from the studies of magnetic Si-based heterostructures and the mechanism of interlayer exchange coupling through nonmetallic spacers in Co/Si multilayers [3]. These structures are of especially high technological interest due to the possibility of being used as low-resistivity contacts in electronic devices, which could save steps in the manufacturing process. However, in contrast to Fe/Si system, Co/Si heterostructures have been much less studied and available experimental results are contradictory [3]. The reason for the different magnetic behavior is a very high sensitivity of diffusion processes at the Co/Si interface to experimental conditions, such as the initial state of the substrate surface, the metal deposition rate, and others. For example, the authors of Ref. [2] have found that Co film grows on the Si(100) surface in the layer-by-layer mode at room temperature. As to magnetic properties of Co/Si interface there are only few reports related to the Si(111) surface [4]. These studies were performed in situ using surface magneto-optic Kerr effect and scanning tunneling microscopy. However, the influence of both the chemical composition of the interfacial layers and their electronic structure on the magnetic properties of a Co/Si interface is poorly understood. In this article, the initial stages of Co/Si(100)2×1 and Co/Si(111)7×7 interfaces formation have been studied for the first time by high resolution photoelectron spectroscopy as well as their ferromagnetic ordering have been investigated using magnetic linear dichroism method. The use of these surface sensitive techniques in the frame of a single experiment allowed to reveal certain correlations between the phase composition, electronic structure, and magnetic behavior of the interfaces.

Materials and Methods

The experiments were carried out using the Russian-German beamline at the Helmholtz-Zentrum Berlin (BESSY). Most of the spectra were measured at 135 eV, the energy at which the surface sensitivity of the Si 2p spectra has a maximum [5]. The magnetic properties of the interface were analyzed by a method based on magnetic linear dichroism (MLD) in Co 3p photoemission. The energy position and shape of the photoelectron peak measured within a narrow solid angle around the normal to the sample surface appears to vary with the sample magnetization [6]. The sample to be studied was magnetized with a pair of Helmholtz coils fixed inside the vacuum chamber. The measurements of the Co 3p spectra were performed in remanence.

The pure Si(100)2×1 and Si(111)7×7 surfaces were prepared in the conventional manner by annealing the samples to 1200 °C for several seconds and then slowly cooling them to room temperature. The procedure provided a well-defined low-energy electron diffraction pattern (LEED) and a surface uncontaminated with carbon and oxygen. The chemical composition of the surfaces was monitored using the photoelectron spectra. Cobalt was evaporated from a thoroughly degassed source, in which a wire of highly purified material (99.99 %) was heated by electron

bombardment. The Co flux was 0.3 Å/min in the standard operation mode. The film thickness was varied up to 20 Å. To study thermostimulated reactions at the interface, the samples were subjected to 5 min annealing at fixed temperatures which were varied from room temperature to 600 °C. All the photoelectron spectra were measured at room temperature in vacuum less than 1.5×10^{-10} mbar.

Results and Discussion

The typical Si 2p spectra taken during the deposition of Co on Si(100)2×1 and Si(111)7×7 at room temperature are shown in Fig. 1. It is seen that the line shape is quite sensitive to the Co coverage demonstrating change of chemical state of Si atoms during the deposition of Co. More detailed information can be obtained using decomposition of the spectra into surface and bulk components by using the least-square fitting procedure. This was done as described in [7]. Each spectral component was approximated by the spin-orbit doublet with the splitting into $2p_{3/2-}$ and $2p_{1/2-}$ sublevels equal to 0.61 eV. The line intensity ratio for these sublevels with the account of their populations was taken to be two. Fig. 1 also shows the results of spectra decomposition. According to the data reported in Ref. [8], the initial spectrum of a reconstructed Si(100)2×1 surface includes a bulk mode (*B*), two modes (S_u and S_d) for the top and bottom dimer atoms, and the modes for the first (S_1') and the second (S_1'') silicon monolayers. The initial spectrum of the Si(111)7×7 surface consists of bulk mode *B* and four surface modes of S_A, S_R, S_P, and SD that can be assigned to adatoms, rest atoms, pedestal atoms, and dimers, respectively.

In both cases, the next spectra, measured after Co deposition, show no surface modes of Si atoms, indicating the absence of Si surface reconstruction or exposed sites of the substrate. Instead of the surface components, we find new features in the Si 2p spectrum: *I*, *C* and *S* modes. The *I* mode can be attributed to an ultrathin CoSi interface film, on which the phase of the C mode is to be formed. Mode *C* can be assigned to silicon atoms dissolved in the cobalt matrix. A new component *S* exhibits a negative energy shift relative to mode *C*. Such a shift is typical of surface components accompanying volume modes in the spectra of solid solutions and silicides. Thus, the *S* component is to be identified to silicon atoms segregated on the surface. For both investigated systems we obtained the same modes, but their intensities are different.

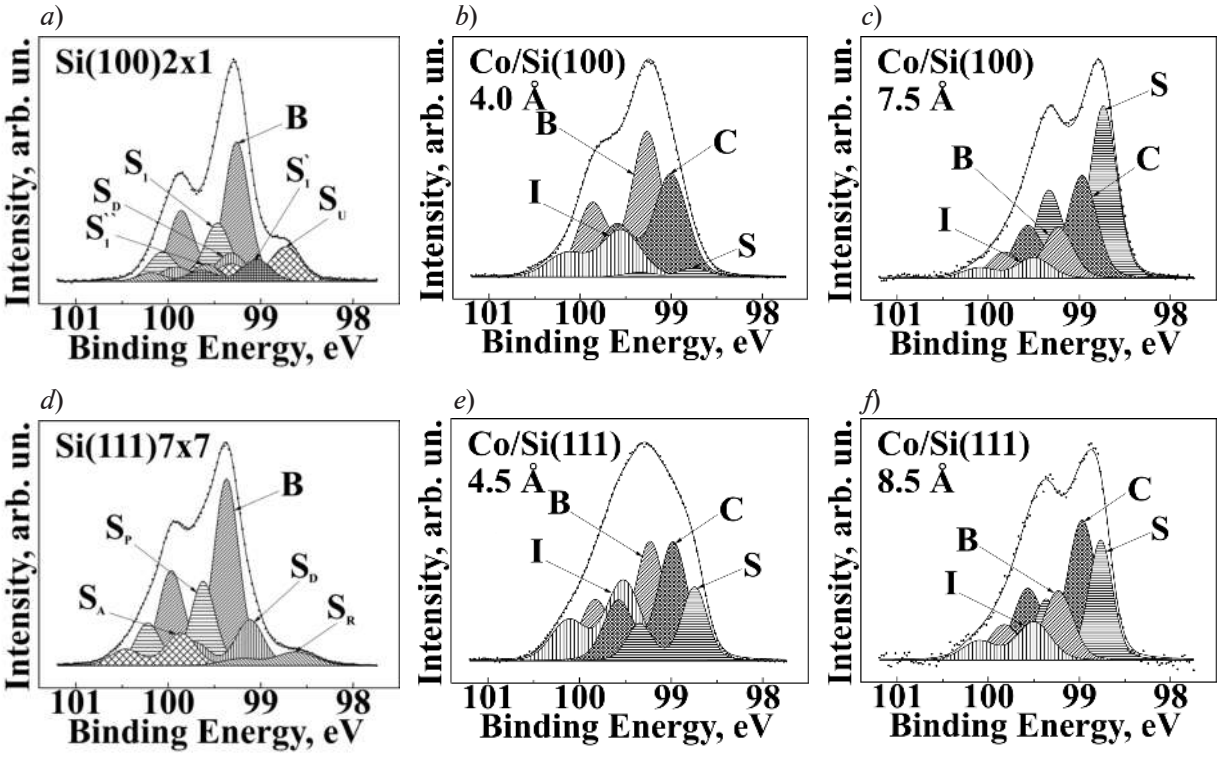

Fig. 1. Si 2p core-level spectra taken from Si(100)2×1 and Si(111)7×7 surfaces and after the deposition of Co films of different thickness at room temperature. Their decomposition is shown as well

Consider now the solid-phase reactions occurring at the interface during annealing of the samples covered with 16 Å of Co. The spectra of valence electrons obtained after the deposition of cobalt on Si(100) surface and taken after each annealing of the sample are illustrated in Fig. 2. One can see that there are the curves of three types corresponding to the different formed phases. The curves of the first type are observed at temperatures less than 340 °C. These spectra are similar to the first curve measured after Co deposition. The spectra of the second type can be seen at temperatures equal to 360 °C and 420 °C. According to Ref. [9], they correspond to the stable monosilicide ε-CoSi. Finally, the spectrum taken after the annealing at 600 °C demonstrates the characteristic features of $CoSi_2$ silicide [10].

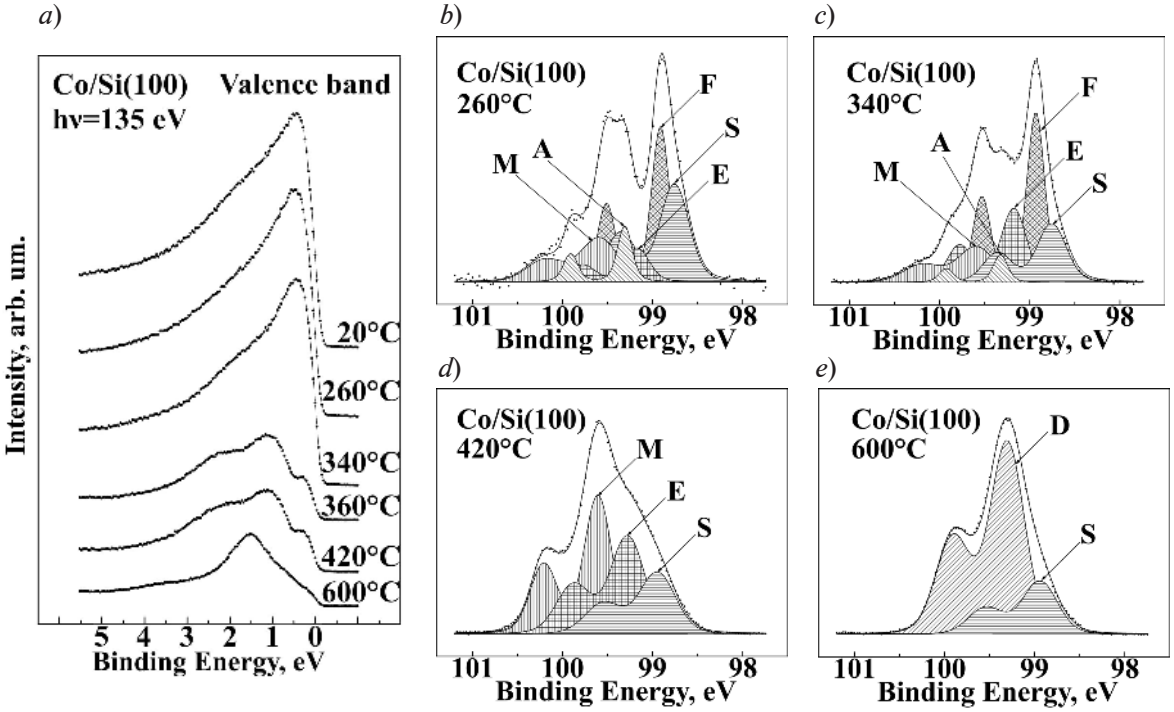

Fig. 2. Valence band and Si 2p spectra taken from the Si(100)2×1 surface with 16 Å of Co deposited at room temperature and after the sample annealing to different temperatures

The initial Si 2p spectrum measured after the deposition of 16 Å of Co shows only traces of the Si line due to its damping by the Co layer. Well defined Si 2p signal indicating a start of solid-phase reactions in the analyzed layer was found after annealing of Si(100) sample at ~ 260 °C (Fig. 2). The spectrum taken after annealing at 260 °C consists of several modes (*A*, *S*, *M*, *E*, *F*), two of them have already been obtained before the sample annealing. The first one is the anomalously narrow mode typical for silicon atoms adsorbed on the metal surface. We observed this mode after the deposition of 12 Å of Co. The second one is *S* mode of segregated Si. The new M mode corresponds to the cobalt monosilicide since this mode dominates in the Si 2p spectra after annealing at 420 °C and the corresponding valence band is typical of CoSi. The E mode corresponds to Co_2Si silicide (we obtained the value of binding energy for this mode after annealing of Si(110) sample at 360 °C in another experiment).

The interpretation of the F mode is of the greatest interest. This mode is the most pronounced in the temperature range from 260 to 340 °C. Its energy position is close to the binding energy of the silicon atoms in the solid solution Co-Si. However, the width of the line (250 meV) is significantly lower than the corresponding characteristic value of the solid solution mode (420 meV), indicating the formation of another phase. The only remaining known cobalt silicide is Co_3Si (our further calculation also showed that the concentration ratio of Co and Si is close to 3:1). However, this compound is stable only in a narrow temperature range in the area of 1200 °C. In our case, due to the non-equilibrium conditions this is a metastable phase. The further temperature rise to 340 °C slightly reduces the segregated Si and adatoms features and increases the Co_2Si mode intensity. The shape of the spectrum line completely changes after

annealing at 420 °C: Co_3Si silicide and adatoms modes disappear and the monosilicide feature greatly increases. The last solid-phase reaction in this system was observed at 600 °C. Instead of the *M* and *E* modes, we found a new *D* feature. Since the whole Si 2p spectrum consists only of this mode with a small mode of segregated Si and a valence band spectrum is typical of disilicide, we concluded that the *D* mode corresponds to $CoSi_2$ silicide. Since the process of silicide formation is due to the bonds breaking in the silicon substrate and diffusion of released silicon atoms through the interface, the temperature of silicide formation can depend on the orientation of the substrate.

Consider now the magnetic properties of Co/Si interface observed during the Co deposition. Representative Co 3p spectra taken after the deposition of increasing Co doses at room temperature for Co/Si(100) surface are present in the left side of Fig. 3. They were obtained for two oppositely directed sample magnetizations parallel to its surface and oriented, accordingly, up (M_{up}) and down (M_{down}). In order to show the possible spectral differences between the curves more clearly we plotted the appropriate difference curves. The effect was detected after the deposition of 6 Å of Co. Maxima and minima appear on the difference curves, corresponding, according to [11], to the sublevels $m_j = \pm 3/2$ of the Co 3p multiplet.

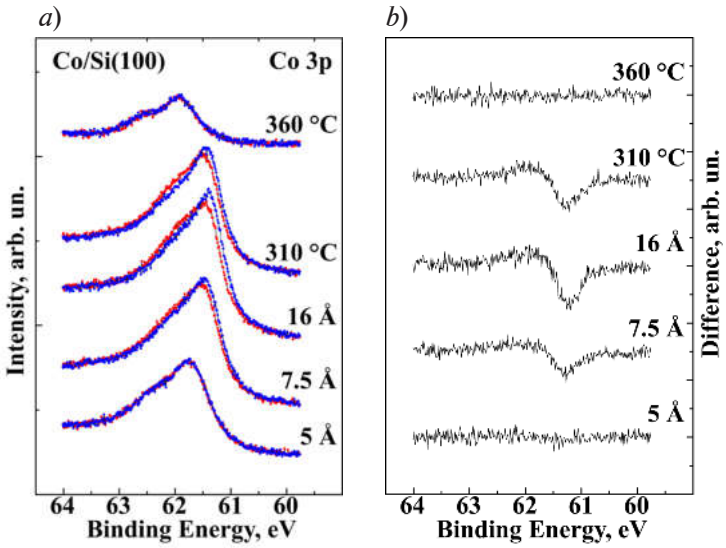

Fig. 3. Co 3p electron spectra taken after deposition of Co of different thickness at room temperature for two opposite directions of the magnetic field (*a*) and their difference curves (*b*)

The magnetic asymmetry of a difference spectrum is commonly estimated using the quantity *S* defined as follows:

$$S(E) = [I_{up}(E) - I_{down}(E)]/[I_{up}(E) + I_{down}(E)].$$

The normalization of the difference spectrum to the total intensity makes *S* dimensionless value independent of the Co content in the analyzing surface range of the sample. A quantitative parameter to describe the effect is the amplitude *A* of the magnetic asymmetry defined as:

$$A = \{\mathrm{MAX}[S(E)] - \mathrm{MIN}[S(E)]\} \times 100\%,$$

where the values of MAX[*S*(*E*)] and MIN[*S*(*E*)] correspond to the above sublevels $m_{\pm 3/2}$. The parameter A characterizes its remanent magnetization. The ferromagnetic ordering of the interface has a threshold nature and arises after the deposition of ~ 6 Å Co. This coverage corresponds to the formation of Co-Si solid solution. The absence of in-plane ferromagnetic ordering in the range of Co coverages less than 6 Å may be explained by abrupt change in the direction of magnetization of Co-Si ferromagnetic layer with an increase of its thickness or with the size dependence of the Curie temperature, which is typical for thin films [4]. The value of the amplitude A for Co/Si(100) system is significantly higher than that for Co/Si(111) one. We suppose that it may be explained by the difference in the morphology of the films.

Let us consider now the influence of the sample annealing on a surface ferromagnetic ordering. Co 3p spectra taken in these experiments were measured also for two oppositely directed magnetizations. The obtained dependencies of the A amplitude on the annealing temperature are presented in Fig. 4. As one can see in figure, the magnetic ordering of the surface remains constant up to 260 °C for Co/Si(100). Further, when the temperature rises to 310 °C, it is reduced from 17% to ~13 % and remains constant until annealing at 340 °C. Finally, it falls to zero at 360 °C. As for the Co/Si(111) system, the amplitude of magnetic asymmetry remains constant up to 320 °C, than it rapidly falls to zero as well.

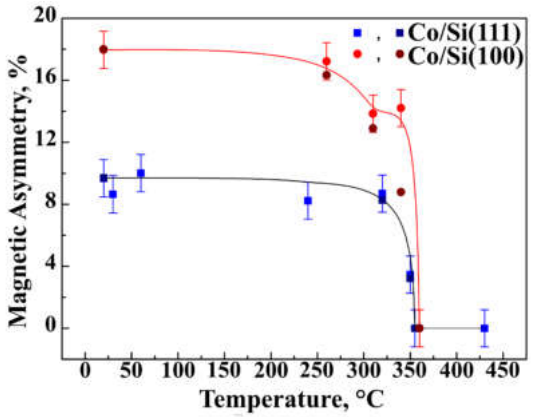

Fig. 4. Dependence of magnetic asymmetry amplitude A of the Co 3p spectra on the annealing temperature

The decline of the amplitude A with temperature raise correlates well with the decrease of metal Co film thickness on the sample surface and the formation of Co_3Si silicide in the analyzed surface layer. MLD effect remains after the disappearance of metal Co film but vanishes after the disappearance of Co_3Si silicide during the sample annealing at 360 °C.

Conclusion

In this paper, we established the correlations between the phase composition and magnetic properties of ultrathin films formed on the Si(100)2×1 and Si(111)7×7 surfaces upon Co deposition at room temperature and subsequent annealing of the samples to 600 °C. In particular, it was found that the interface silicide CoSi and Co-Si solid solution are formed at the initial stage of Co deposition on Si substrate. It was shown that in-plane ferromagnetic ordering has a threshold nature and was found to appear at Co coverage of 6 Å for both systems corresponding to solid-solution phase. After the samples annealing, the first synthesized phases are the metastable ferromagnetic Co_3Si and non-magnetic Co_2Si silicides. They transform to CoSi and $CoSi_2$ silicides at higher temperatures. The temperature ranges of stability and values of Si 2p binding energies were determined for all mentioned silicides formed on Si(100) and Si(111) surfaces.

REFERENCES

1. **Bulle-Lieuwma C.W.T.,** Epitaxial growth of $CoSi_2$/Si structures, Applied Surface Science. 1 (68) (1993) 1–18.

2. **Ilge B., Palasantzas G., De Nijs J., Geerlings L.G.,** The temperature evolution of ultra-thin films in solid-phase reaction of Co with Si (111) studied by scanning tunneling microscopy, Surface Science. 1–2 (414) (1998) 279–289.

3. **Yaacoub N., Meny Ch., Ulhaq-Bouillet C., Acosta M., Panissod P.,** Short period magnetic coupling oscillations in Co/Si multilayers: Role of crystallization and interface quality, Physical Review. 75 (2007).

4. **Chang H.W., Tsay J.S., Hung Y.C., Yuan F.T., Chan W.Y., Su W.B., Chang C.S., Yao Y.D.,** Magnetic properties and microstructure of ultrathin Co/Si (111) films, Applied Physics. 101 (2007).

5. **Hong S., Wetzel P., Gewinner G., Bolmont D., Pirri C.,** Formation of epitaxial $Fe_{3-x}Si_{1+x}$ $(0 \le x \le 1)$ silicides on Si (111), Applied Physics. 9 (78) (1995) 5404–5411.

6. **Roth Ch., Hillebrecht F.U., Rose H.B., Kisker E.,** Linear magnetic dichroism in angular resolved Fe 3p core level photoemission, Physics Review Letters. 70 (1993).

7. **Gomoyunova M.V., Pronin I.I., Malygin D.E., Gall N.R., Vyalikh D.V., Molodtsov S.L.,** Photoemission experiments and density functional calculations for the W(1 1 2) stepped surface with submonolayer Au coverages, Surface Science. 600 (2006) 2449

8. **Pi T.-W., Ouyang C.-P., Wen J.-F., Tien L.-S., Hwang J., Cheng Z.C.-P., Wertheim G.K.,** Early nucleation on the Si (100)-2×1 surface, Surface Science. 1–3 (514) (2002) 327–331.

9. **Pirri C., Hong S., Tuilier M. H., Wetzel P., Gewinner G., Cortés R.,** Epitaxy of $CoSi_x$ ($1 < x < 2$) silicides on Si (111) studied by photoemission and extended x-ray-absorption fine-structure techniques, Physical Review. 53 (1996).

10. **Gomoyunova M.V., Pronin I.I., Gall N.R., Vyalikh D.V., Molodtsov S.L.,** Interaction of cobalt with the Si (100)2×1 surface studied by photoelectron spectroscopy, Surface Science. 1–3 (578) (2005) 174–182.

11. **Sirotti F., Rossi G.,** Magnetic asymmetry in photoemission from Fe (100) with linearly polarized synchrotron radiation, Physical Review. 49 (1994).

THE AUTHORS

MONYAK Andrey A.
andreimonyak@gmail.com

GREBENYUK Georgy S.
georgijmail@gmail.com

LOBANOVA Evgeniya Yu.
elobanova@itmo.ru

KUZMIN Mikhail V.
m.kuzmin@mail.ioffe.ru

Received 13.12.2022. Approved after reviewing 30.01.2023. Accepted 30.01.2023.

Conference materials
UDC 539.23
DOI: https://doi.org/10.18721/JPM.161.310

Transformation kinetics of a two-dimensional GaN thin layer grown on AlN surface during ammonia flow cycling

Y.E. Maidebura [1]✉, T.V. Malin [1], K.S. Zhuravlev [1]

[1] Rzhanov Institute of Semiconductor Physics, SB RAS, Novosibirsk, Russia

✉ maid@isp.nsc.ru

Abstract. In this work the transformation kinetics of GaN pseudomorphic layer and the lattice constant evolution of 2D GaN “frozen” layer under sequential switching off/on of ammonia flow at a growth temperature of 740 °C were investigated by reflection high energy electron diffraction method (RHEED). It was shown by the Bragg spot kinetics intensity of GaN layer that when ammonia flow is turned off, the intensity of Bragg spot reaches saturation and does not change during the exposure time in vacuum, while the maximum achieved intensity decreases when ammonia flow is turned off/on sequentially. Hence there is practically no effect of thermal decomposition on the change in the morphology of the GaN layer. It was found experimentally that the GaN layer formed with each cycle of 2D "frozen" is partially relaxed, which is explained within the Mariette equilibrium model. Thus, relaxation of elastic energy of 2D "frozen" GaN layer is due to the fact that some amount of 3D islands remains on the surface and the decrease of elastic energy value is caused by losses for islands faceting maintenance.

Keywords: GaN quantum dots, surface morphology, 2D-3D transition, surface processes, ammonia MBE, RHEED

Funding: The study was carried out within the framework of the state task of the Rzhanov Institute of Semiconductor Physics, Siberian Branch, Russian Academy of Sciences.

Citation: Maidebura Y.E., Malin T.V., Zhuravlev K.S., Transformation kinetics of a two-dimensional GaN thin layer grown on AlN surface during ammonia flow cycling, St. Petersburg State Polytechnical University Journal. Physics and Mathematics. 16 (1.3) (2023) 62–66. DOI: https://doi.org/10.18721/JPM.161.310

Материалы конференции
УДК 539.23
DOI: https://doi.org/10.18721/JPM.161.310

Кинетика преобразования тонкого двумерного слоя GaN, выращенного на поверхности AlN, при циклировании потока аммиака

Я.Е. М йдэбур [1]✉, Т.В. М лин [1], К.С. Жур влев [1]

[1] Институт физики полупроводников им. А.В. Ржанова СО РАН, г. Новосибирск, Россия

✉ maid@isp.nsc.ru

Аннотация. В данной работе была исследована кинетика трансформации псевдоморфного слоя GaN и изучена эволюция постоянной решетки слоя GaN при периодическом выключении/включении потока аммиака при ростовой температуре 740 °C. По кинетике преобразования слоя GaN было показано, что термическое разложение практически отсутствует и не влияет на изменение морфологии слоя GaN. Экспериментально было обнаружено, что образующийся с каждым циклом 2D "замороженный" слой GaN является частично релаксированным. Частичная релаксация объясняется в рамках модели равновесия Mariette, и связана с незавершенностью обратного перехода 3D островков в 2D слой.

Ключевые слова: квантовые точки GaN, морфология поверхности, 2D-3D переход, поверхностные процессы, аммиачная МЛЭ, ДБЭО

Финансирование: Исследование выполнено в рамках государственного задания Института физики полупроводников им. А.В. Ржанова СО РАН.

Ссылка при цитировании: Майдэбура Я.Е., Малин Т.В., Журавлев К.С. Кинетика преобразования тонкого двумерного слоя GaN, выращенного на поверхности AlN, при циклировании потока аммиака // Научно-технические ведомости СПбГПУ. Физико-математические науки. 2023. Т. 16. № 1.3. С. 62–66. DOI: https://doi.org/10.18721/JPM.161.310

Introduction

Group III nitrides such as InN, GaN and AlN, combined with solid solutions, can extend the spectral range of optoelectronic devices from infrared to ultraviolet, thus attracting significant research interest. A problem in III-nitrides based optoelectronic devices is the high density of dislocations and structural defects in grown heterostructures, acting as centers of non-radiation recombination and reducing the efficiency of optoelectronic devices. A possible approach is to use three-dimensional nanostructures, known as quantum dots (QDs), which act as traps for charge carriers and prevent them from diffusing to the non-radiation recombination centers.

The typical method of QDs formation is the Stranski–Krastanov (S-K) growth mechanism, where the transformation of two-dimensional (2D) layer into three-dimensional (3D) islands, i.e. 2D-3D transition, occurs during growth when the critical thickness of the growing layer is reached. It has been demonstrated in [1] that GaN QDs on AlN surface are formed by S-K mechanism when they are grown by molecular beam epitaxy (MBE) with plasma nitrogen source. GaN QDs formation by S-K mechanism has also been demonstrated using metal-organic chemical vapor deposition technology [2]. However, when GaN QDs are grown by ammonia MBE method, a 2D-3D transition with increasing 2D layer thickness is not observed and relaxation of elastic strains accumulated in the GaN layer occurs through the formation of mismatch dislocations. GaN QDs formation requires surface modification and an increase in surface energy, which occurs when the ammonia flux is switched off [3, 4] and is referred to as growth by the modified S-K mechanism.

In the case of growth according to the modified S-K mechanism, the process of GaN QD formation is reversible, i.e., turning on the ammonia flow after turning it off leads to reverse transformation of 3D islands into 2D layer (reverse 3D-2D transition) [5]. As shown in [6], with each ammonia turn-off/on cycle a portion of the GaN layer is formed that has a 2D surface morphology and is no longer transformed when ammonia is turned off. The reversibility of the 2D-3D transition has the potential to produce GaN QDs with a certain set of parameters (QD density and size), which is a significant technological challenge at the moment.

In this work, the kinetics of forward and reverse 2D-3D transitions and the lattice constant evolution of the GaN layer under periodic on/off ammonia flow were experimentally investigated and the experimental results were explained within the framework of the previously developed kinetic model and the Mariette equilibrium model.

Materials and Methods

The 2D↔3D transition was investigated on a Riber CBE-32 MBE machine with ammonia as the nitrogen source and Knudsen effusion cells as the gallium and aluminum sources. In situ reflection high energy electron diffraction (RHEED) has been used to investigate the transformation of GaN layer morphology. The evolution of diffraction patterns was analyzed using the kSA 400 system by k-Space Associates. The substrate temperature was measured using an Ircon pyrometer, thermocouple and Ocean Optics USB4000 miniature spectrometer. The ammonia pressure in the growth chamber was set and controlled using a mass flow controller.

The growth experiments were as follows. An AlN buffer layer of ~365 nm thickness was grown on a sapphire substrate with orientation (0001), on top of which a GaN layer of 2 nm thickness was grown. The gallium flow was then switched off, GaN growth was stopped and the GaN layer was kept in a flow of ammonia for 5 minutes to prevent surface modification. The ammonia flow was then switched off for 300 seconds to eliminate the effect of thermal decomposition and turned on for 120 seconds followed by a total of 4 more ammonia switch-off/on cycles with typical times of 60 and 120 seconds respectively.

Results and Discussion

Figure 1 shows the kinetics of the Bragg spot (black line) and rod (red line) intensities from GaN when the GaN layer is exposed to vacuum and subsequent on/off cycles of ammonia flow at a growth temperature of 740 °C. The insets in the figure shows the diffraction patterns for the two selected reflexes indicated by the yellow rectangles. The area for the 2D reflex measurement was chosen so that the Bragg spot contribution is minimal. The initial position of the red curve is explained by the fact that the measured rod-shaped 2D reflex is only distinguishable after the 2nd cycle of ammonia switching off/on. Consequently, the black and red curves represent simultaneously coexisting reflexes corresponding to the 3D and 2D surface states, respectively. Figure 1 clearly shows that when the ammonia flow is switched off, the intensity of the 3D reflex increases, then reaches saturation and remains unchanged after 300 seconds of exposure in vacuum, indicating the formation and stabilization of 3D islands. When the ammonia flow is turned on, the intensity of the Bragg spot decreases and increases sharply when it is switched off afterwards. As can be seen from the figure, the maximum achievable intensity of the Bragg spot decreases from cycle to cycle. This behavior indicates the presence of a mechanism other than thermal decomposition, which leads to a decrease of the Bragg spot intensity, as has been reported in [4, 5]. Conversely, the intensity of the 2D reflex decreases when ammonia is switched off and increases when ammonia is switched on again. As can be seen from the figure, with each cycle the 2D reflex becomes brighter and the maximum achievable intensity increases. This means that with each cycle the 2D part of the GaN layer develops, and it is no longer transformed when the ammonia flow is switched off. This behaviour is due to the fact that part of the NH_2, NH and N fragments move to energetically favorable positions on the GaN layer surface, desorption from which is significantly inhibited when the ammonia flow is switched off. Consequently, the surface energy of such a 'frozen' surface does not change when the ammonia is turned off and, according to the Mariette model [7], the surface remains 2D.

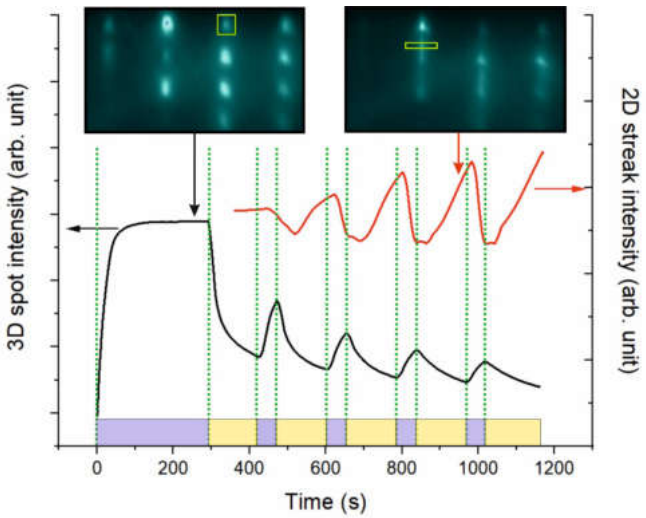

Fig. 1. Intensities of the 3D spot (black curve) and 2D streak (red curve) from the GaN surface with sequential switching off/on of the ammonia flow at T = 740 °C. The insets illustrate diffraction patterns for the two selected reflexes indicated by the yellow rectangles. The green dotted line indicates the ammonia flow off/on, and the purple/yellow areas indicate surface exposure in vacuum/ammonia, respectively

More surprisingly, the 2D layer, which no longer converts into islands, is partially relaxed. Assuming that the original GaN layer 2 nm thick is pseudomorphic and has a lattice constant of the buffer AlN layer (equal to about 3.12 Å at growth temperature), the in-plane lattice constant evolution of the 'frozen' GaN layer during the experiment was obtained from the relative spacing of the 2D reflex intensity peaks, shown in Fig. 2. The insets show GaN 2D reflex intensity profiles before and after 5 cycles of ammonia switching off/on. It should be noted that a reliable identification of the intensity peak position from a 2D partially relaxed GaN layer is only possible after two cycles of ammonia switching off/on. As can be seen from the figure, the lattice constant of the 2D 'frozen' GaN layer periodically increases and decreases. As the reflex from the 2D 'frozen' layer appears when the ammonia is turned on, its lattice constant decreases, i.e., the layer acquires elastic stress, and conversely, as the reflex intensity decreases, the lattice constant increases and relaxation of the elastic energy occurs. With each ammonia on/off cycle the stress in the layer increases and the lattice constant tends to that of the pseudomorphic GaN layer (3.12 Å). The partial relaxation of the 2D GaN layer can be explained in terms of the Mariette equilibrium model [7], according to which the 2D-3D transition occurs when the energy gain from the decrease of elastic energy stored in the pseudomorphic layer exceeds the energy loss in the creation of QD surfaces. Based on [6], after 5 cycles of ammonia switching off/on at 740 °C the fully original GaN layer is not recovered and the GaN layer morphology is a 2D layer on which lie 3D islands with characteristic lateral sizes of 100 nm. The total energy of such a surface, according to [7], consists of the elastic energy, the surface energies of the 2D layer and the facets of the 3D islands, which differs from a purely 2D layer by the presence of the surface energy of the facets. Then relaxation of elastic energy of 2D 'frozen' GaN layer is due to the fact that some number of 3D islands is kept on the surface and the decrease of elastic energy value is caused by the costs of maintaining faceting of islands.

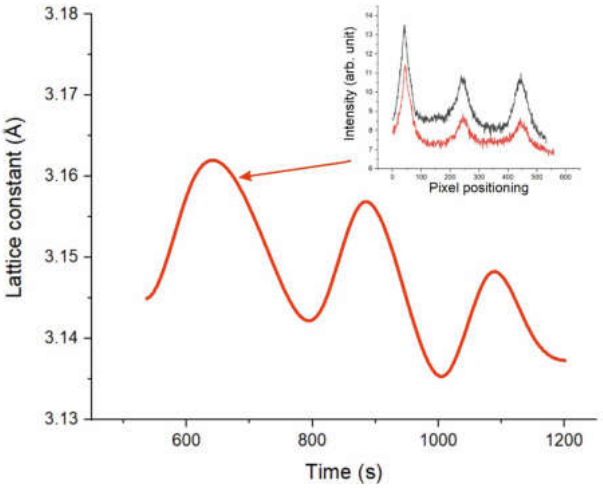

Fig. 2. Evolution of the lattice constant 2D 'frozen' GaN layer. The insets show GaN 2D reflection intensity profiles before and after 5 cycles of ammonia switching off/on

Conclusion

In this work, the transformation kinetics of GaN pseudomorphic layer and lattice constant evolution of GaN layer under periodic switching off/on of ammonia flux at a growth temperature of 740 °C have been experimentally investigated by RHEED method. It has been experimentally shown that when ammonia is turned off for the first time in vacuum (300 seconds), the Bragg spot intensity reaches saturation and does not change, whereas when ammonia is cycled, the maximum achievable intensity decreases with each cycle, indicating no thermal decomposition. It was also found that the 2D 'frozen' GaN layer, which does not transform into 3D islands and increases with each switch-off/ switch-on cycle, is partially relaxed. This behavior is related to the incomplete reverse transformation of 3D islands into a 2D layer and is explained within the Mariette equilibrium model, according to which part of the elastic energy is spent to maintain the faceting of the islands.

REFERENCES

1. **Daudin B., Widmann F., Feuillet G., Samson Y., Arlery M., Rouvi´ere J.L.,** Stranski-Krastanov growth mode during the molecular beam epitaxy of highly strained GaN. Phys. Rev. B, 56, R7069 (1997).

2. **Miyamura M., Tachibana K., Arakawa Y.,** High-density and size-controlled GaN self-assembled quantum dots grown by metalorganic chemical vapor deposition. Appl. Phys. Lett., 80, 3937 (2002).

3. **Damilano B., Brault J., Massies J.,** Formation of GaN quantum dots by molecular beam epitaxy using NH_3 as nitrogen source. J. Appl. Phys., 118, 024304 (2015).

4. **Maidebura Y.E., Mansurov V.G., Malin T.V., Zhuravlev K.S.,** Transformation of the elemental composition on the GaN surface during a 2D-3D transition. Appl. Surf. Sci., 577, 151802 (2022).

5. **Maidebura Y.E., Malin T.V., Zhuravlev K.S.,** Modification of the surface energy and morphology of GaN monolayers on the AlN surface in an ammonia flow. Appl. Phys. Lett., 120, 053101 (2022).

6. **Maidebura Y.E., Malin T.V., Milakhin D.S., Ponomarev S.A., Zhuravlev K.S.,** Morphology of GaN Monolayers Grown on AlN Surface During Ammonia Flow Cycling. In: IEEE 23nd Int. Conf. Young Professionals in Electron Devices and Materials, 29 (2022).

7. **Mariette H.,** Formation of self-assembled quantum dots induced by the Stranski–Krastanow transition: a comparison of various semiconductor systemsComptes Rendus Physique, 6, 23 (2005).

THE AUTHORS

MAIDEBURA Yan E.
maid@isp.nsc.ru
ORCID: 0000-0001-6380-950X

MALIN Timur V.
mal-tv@isp.nsc.ru
ORCID: 0000-0001-6015-0631

ZHURAVLEV Konstantin S.
zhur@isp.nsc.ru
ORCID: 0000-0002-3171-5098

Received 14.12.2022. Approved after reviewing 30.01.2023. Accepted 02.03.2023.

Heterostructures, superlattices, quantum wells

Conference materials
UDC 538.9
DOI: https://doi.org/10.18721/JPM.161.311

Magneto-intersuband resistance oscillations in a one-dimensional lateral superlattice

I.S. Strygin [1] ✉, A.A. Bykov [1]

[1] Rzhanov Institute of Semiconductor Physics, Siberian Branch, RAS, Novosibirsk, Russian
✉ vanya-91@yandex.ru

Abstract. This paper presents the results of a study of magneto-intersubband resistance oscillations in a one-dimensional lateral superlattice fabricated on the basis of a single GaAs quantum well with two filled energy subbands. A strong modification of magneto-intersubband oscillations both in amplitude and in phase has been observed. The obtained experimental data are explained by the role of Van Hove singularities in resonant intersubband transitions.

Keywords: magneto-intersubband oscillations, lateral superlattice

Funding: This study was funded by the Russian Science Foundation grant number RSF-22-22-00726, https://rscf.ru/en/project/22-22-00726/.

Citation: Strygin I.S., Bykov A.A., Magneto-intersuband resistance oscillations in a one-dimensional lateral superlattice, St. Petersburg State Polytechnical University Journal. Physics and Mathematics. 16 (1.3) (2023) 67–72. DOI: https://doi.org/10.18721/JPM.161.311

Материалы конференции
УДК 538.9
DOI: https://doi.org/10.18721/JPM.161.311

Магнето-межподзонные осцилляции сопротивления в одномерной латеральной сверхрешетке

И.С. Стрыгин [1] ✉, А.А. Быков [1]

[1] Институт физики полупроводников им. А. В. Ржанова Сибирского отделения РАН, г. Новосибирск, Россия
✉ vanya-91@yandex.ru

Аннотация. В работе приводятся результаты исследования магнето-межподзонных осцилляций сопротивления в одномерной латеральной сверхрешетке, изготовленной на основе одиночной GaAs квантовой ямы с двумя заполненными энергетическими подзонами. Обнаружена сильная модификация магнето-межподзонных осцилляций по амплитуде и фазе. Полученные экспериментальные данные объясняются ролью особенностей Ван Хова в резонансных межподзонных переходах.

Ключевые слова: магнето-межподзонные осцилляции, латеральная сверхрешетка

Финансирование: Исследование выполнено за счет гранта Российского научного фонда номер РНФ-22-22-00726, https://rscf.ru/project/22-22-00726/.

Ссылка при цитировании: Стрыгин И.С., Быков А.А. Магнето-межподзонные осцилляции сопротивления в одномерной латеральной сверхрешетке // Научно-технические ведомости СПбГПУ. Физико-математические науки. 2023. Т. 16. № 1.3. С. 67–72. DOI: https://doi.org/10.18721/ JPM.161.311

Introduction

Landau quantization in quasi-two-dimensional electronic systems in which several size-quantization subbands E_j are filled (j is the subband index) leads not only to several series of Shubnikov-de Haas (SdH) oscillations, but also to magneto-intersubband resistance oscillations (MISO) of ρ_{xx} versus magnetic field B [1]. The MISO are due to elastic intersubband scattering, which becomes resonant when the Landau levels of different subbands coincide. In a two-subband system with a large number of filled and strongly overlapping Landau levels, MISO are described by the following relation [2]:

$$\Delta\rho_{\mathrm{MISO}} / \rho_0 = A_{\mathrm{MISO}} \exp\left(-2\pi / \omega_c \tau_q^{\mathrm{MISO}}\right) \cos\left(2\pi\Delta_{12} / \hbar\omega_c\right), \quad (1)$$

where $\rho_0 = \rho_{xx}(\mathrm{B} = 0)$, $A_{\mathrm{MISO}} = 2\tau_{tr}/\tau_{12}$, τ_{tr} is the transport scattering time, τ_{12} is the intersubband scattering time, $\tau_q^{\mathrm{MISO}} = 2\tau_{q1}\tau_{q2}/(\tau_{q1} + \tau_{q2})$, τ_{qj} is the quantum lifetime, Δ_{12} is the intersubband splitting, $\omega_c = eB/m^*$ is the cyclotron frequency, and m^* is the electron effective mass. MISO are not suppressed by temperature broadening of the Fermi distribution function, which makes it possible to use them to study quantum transport under conditions when SdH oscillations are suppressed [3].

This work considers MISO in a two-subband unidirectional lateral superlattice (ULSL), a quasi-two-dimensional electron system with one-dimensional periodic potential modulation: $V(x) = V_0\cos(2\pi x/a)$, where V_0 is the potential amplitude and a is the modulation period. The most striking phenomenon found in the ULSL is the commensurate oscillations (CO) of the resistance [4]. The maxima and minima of CO occur when the following conditions are satisfied:

$$2R_{cj}/a = (i + 1/4), \quad (2)$$

$$2R_{cj}/a = (i - 1/4), \quad (3)$$

where R_{ci} is the cyclotron radius and i is a positive integer. Within the framework of the classical model, COs arise due to the commensurability between R_{cj} and a [5], and within the framework of the quantum mechanical model they result from a periodic change in the width of the Landau bands with $1/B$ [6].

The one-dimensional periodic potential removes the degeneracy of the Landau levels with respect to the coordinate of the center of the wave function x_0, which leads to the formation of Landau bands. Under the conditions $V_0 << E_F - E_j = \varepsilon_{Fj}$ (E_F is the position of the Fermi level), the dependence of the Landau level E_{Nj} with $N_j >> 1$ on x_0 is given by the expression [6]:

$$E_{Nj}\left(x_0\right) \approx E_j + \left(N_j + 1/2\right)\hbar\omega_c + V_{Bj}\cos\left(2\pi x_0 / a\right), \quad (4)$$

$$V_{Bj} = V_0 J_0\left(2\pi R_{cj} / a\right). \quad (5)$$

For $2\pi R_{cj}/a \geq 1$ the width of the Landau bands $\Gamma_{Bj} = 2|V_{Bj}|$ reaches maximum if Eq. (2) holds true and is equal to zero if Eq. (3) is satisfied.

The density of states D_j under the conditions $V_0 << \varepsilon_{Fj}$, $N_j >> 1$ and $1/\tau_{qj} \sim \omega_c$ is given by the following relationship [7]:

$$D_j / D_0 \approx 1 - 2J_0\left(2\pi V_{Bj} / \hbar\omega_c\right)\exp\left(-\pi / \omega_c\tau_{qj}\right)\cos\left(2\pi\varepsilon_{Fj} / \hbar\omega_c\right), \quad (6)$$

where $D_0 = m^*/\pi\hbar^2$. Using relations (1) and (6), the behavior of MISO in a two-subband ULSL can be described by formula [8]:

$$\Delta\rho_{\mathrm{MISO}} / \rho_0 = A_{\mathrm{MISO}} J_0\left(2\pi V_{B1} / \hbar\omega_c\right) J_0\left(2\pi V_{B2} / \hbar\omega_c\right)\exp\left(-2\pi / \omega_c\tau_q^{\mathrm{MISO}}\right)\cos\left(2\pi\Delta_{12} / \hbar\omega_c\right). \quad (7)$$

In this formula, the role of $V(x)$ is taken into account by the factors $J_0(2\pi V_{Bj}/\hbar\omega_c)$, which are absent in Eq. (1).

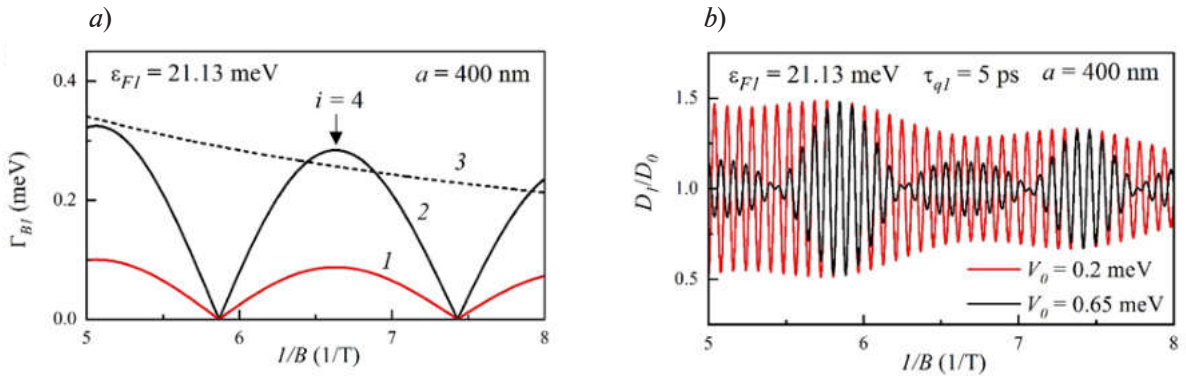

Fig. 1. Dependences $\Gamma_{B1}(1/B)$ calculated by Eq. (5) for two different values of V_0: 0.2 (*1*), 0.65 meV (*2*), dependence $\hbar\omega_c(1/B)$ (*3*), the arrow indicates the maximum position for $i = 4$ (*a*); dependences of D_1/D_0 on $1/B$, calculated by Eq. (6) (*b*)

Figure 1, *a* shows the dependences $\Gamma_{B1}(1/B)$ for weak (1) and strong (2) modulation of the potential $V(x)$ with respect to $\hbar\omega_c$. In the strong modulation regime, there are intervals of $1/B$ where $\Gamma_{B1}(1/B) \sim \hbar\omega_c$. Fig. 1, *b* shows the dependences of D_1/D_0 on $1/B$, calculated by Eq. (6) for a fixed ε_{F1} and for two different values of V_0. It can be seen that the dependences of D_1/D_0 on $1/B$ for weak and strong potential modulation are out of phase in the regions where $\Gamma_{B1}(1/B) \sim \hbar\omega_c$. This behavior is due to the role of Van Hove singularities in the spectrum of states at the edges of the Landau bands. Eqs. (6) and (7) predict a significant transformation of the MISO when $\Gamma_{B1}(1/B) \sim \hbar\omega_c$. The purpose of this work is to experimentally detect the MISO under such conditions.

Materials and Methods

The initial heterostructure was a single GaAs quantum well 26 nm wide with short-period AlAs/GaAs superlattice barriers [9, 10]. The charge carriers in the quantum well were provided by means of Si δ doping. Single Si δ-doped layers were located on both sides of a single GaAs quantum well at a distance of 29.4 nm from its boundaries. The heterostructure was grown by molecular beam epitaxy on a (100) GaAs substrate. The studies were carried out on double bridges 100 μm long and 50 μm wide. They were fabricated using optical photolithography and liquid etching. One bridge was the control one, and the ULSL was formed on the second one (see inset to Fig. 2, *a*).

The ULSL was a set of Ti/Au strips with a period $a = 400$ nm. The ULSL was fabricated using electron beam lithography. The experiments were carried out at $T = 4.2$ K in fields $B < 2$ T. The resistance of the samples ρ_{xx} and ρ_{xy} was measured at an alternating current not exceeding 1 μA with a frequency of ~ 1 kHz. In the control bridge, the electron concentration and mobility were: $n_H \approx 8.2\times10^{15}$ m^{-2}; $\mu \approx 115$ m^2/Vs. The presence of superlattice slightly reduces n_H and μ. In the ULSLs under study, the modulating potential arises without applying voltage V_g to the metal strips. One of the reasons for such modulation is the elastic mechanical stresses that arise between the metal strips and the heterostructure [11].

Results and Discussion

The results of ρ_{xx}/ρ_0 versus B measurements in the control bridge and in the ULSL are shown in Fig. 2, *a*. The MISO with frequency $f_{12} \approx 8.8$ T are detected in the control bridge. The intersubband splitting determined from the frequency f_{12} is $\Delta_{12} \approx 15$ meV. In the ULSL the more pronounced are the oscillations whose maxima and minima positions are given by Eqs. (2) and (3), which allows us to consider them commensurate. The Fourier analysis of CO shows two frequencies ($f_{CO1} = 0.64$ T and $f_{CO2} = 0.36$ T) in good agreement with their expected values. Figure 2, *b* shows the dependences of ρ_{xx}/ρ_0 versus $1/B$ in the region of magnetic fields, where the MISO in the control bridge and the ULSL are in antiphase.

The dependences of $\Delta\rho_{MISO}/\rho_0$ versus $1/B$ for the control bridge and the ULSL, obtained after subtracting from the experimental curves the CO and monotonic components, are shown in Fig. 3, *a*. The amplitude of MISO in the ULSL is strongly suppressed compared to the control

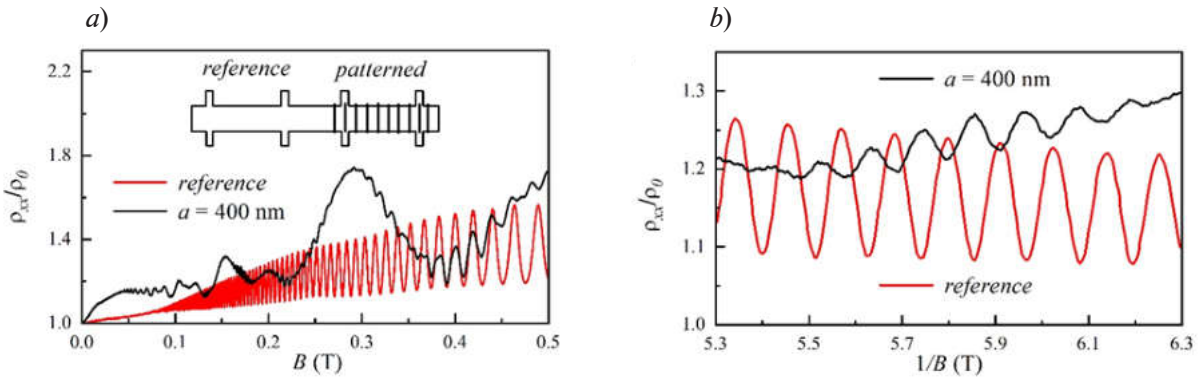

Fig. 2. Dependences of ρ_{xx}/ρ_0 versus B measured at T = 4.2 K in the control bridge and in the ULSL: the inset shows the schematics of the sample (*a*); dependences of ρ_{xx}/ρ_0 on $1/B$ in the region of the MISO phase flip (*b*)

bridge. The dependences of $\Delta\rho_{MISO}/\rho_0$ on $1/B$ for the control bridge and the ULSL calculated from Eq. (7) are shown in Fig. 3, b. Good agreement between the experimental dependences and those calculated is observed for $V_0 = 0$ and $\tau_q^{MISO} = 8$ ps for the control bridge, and for $V_0 = 0.65$ meV and $\tau_q^{MISO} = 6$ ps for the ULSL. A decrease in τ_q^{MISO} in the ULSL indicates that the deposition of a grating leads to an increase in the random scattering potential in the two-subband electron system under study.

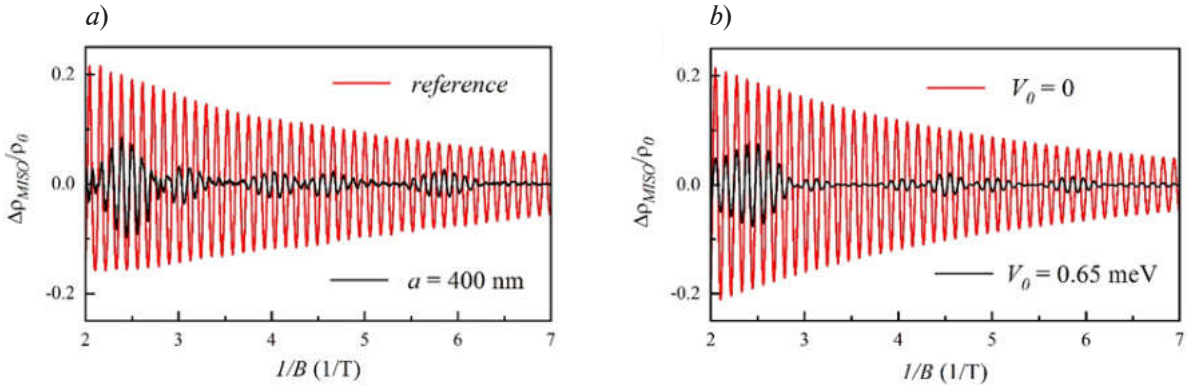

Fig. 3. Dependences of $\Delta\rho_{MISO}/\rho_0$ versus $1/B$ for the control bridge and the ULSL (*a*); dependences of $\Delta\rho_{MISO}/\rho_0$ versus $1/B$, calculated by Eq. (7): $n_1 = 6\times10^{15}$ m^{-2}, $n_2 = 1.9\times10^{15}$ m^{-2}, $A_{MISO} = 0.4$, for the control bridge $\tau_q^{MISO} = 8$ ps, for the ULSL $\tau_q^{MISO} = 6$ ps (*b*)

Fig. 4, *a* shows $\Delta\rho_{MISO}/\rho_0$ versus $1/B$ for the control bridge and the ULSL in two regions where they are in-phase and out-of-phase. The dependences of Γ_{Bj} on $1/B$ calculated for $V_0 = 0.65$ meV are shown in Figs. 4, *b*. Two regions are highlighted in gray in which MISO for the control bridge and the ULSL are in-phase and out-of-phase. In region 1: $\Gamma_{Bj} < \hbar\omega_c/2$. In region 2: $\Gamma_{B1} < \hbar\omega_c/2$, and $\Gamma_{B2} \sim \hbar\omega_c$. In region 1, the oscillations of D_1/D_0 and D_2/D_0 versus $1/B$ for the control bridge and for the ULSL are in phase under condition that $1/\tau_{qj} \sim \omega_c$. In this case, $V(x)$ leads only to a decrease in the amplitude of MISO, but does not change their phase. In region 2, the oscillations D_1/D_0 and D_2/D_0 are out of phase. In this situation, $V(x)$ leads not only to a suppression of the MISO amplitude, but also to a change in their phase. Thus, the "reversal" of MISO is due to the fact that in region 2: $\Gamma_{B1} < \hbar\omega_c/2$, and $\Gamma_{B2} \sim \hbar\omega_c$.

The observed flip of the MISO is fundamentally different from the flip of the SdH oscillations in the ULSL [12]. The SdH oscillations in quasi-two-dimensional systems are due to the Landau levels induced modulation of the density of states D_j. When $\hbar\omega_c$ changes, the regions with a higher D_j cross E_F periodically in $1/B$, which leads to SdH oscillations. The one-dimensional potential leads to Van Hove singularities in the dependence of D_j on energy ε. The density of states at the edges of the Landau bands has a maximum, while in the center it has a minimum.

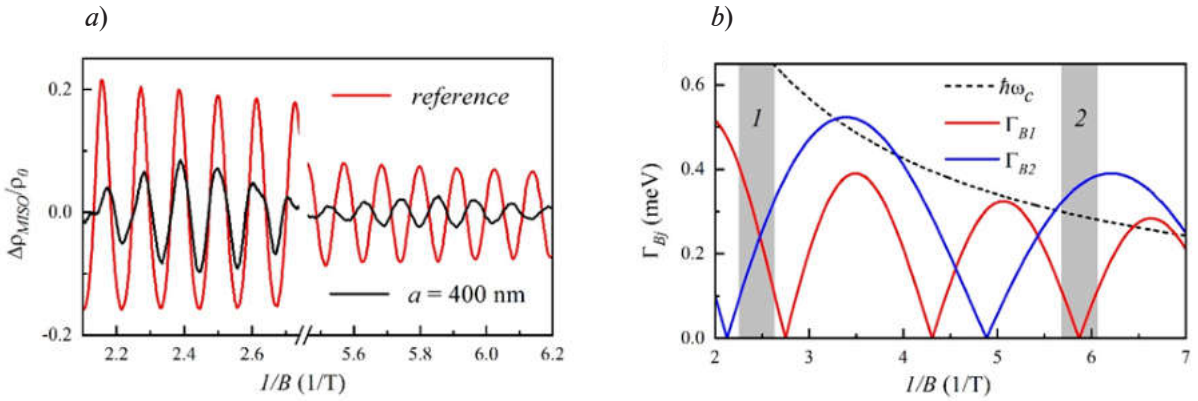

Fig. 4. Dependences of $\Delta\rho_{MISO}/\rho_0$ versus $1/B$ in two narrow intervals (*a*); dependences of Γ_{Bj} on $1/B$, calculated by Eq. (5): $n_1 = 6\times10^{15}$ m^{-2}, $n_2 = 1.9\times10^{15}$ m^{-2}, $a = 400$ nm, $V_0 = 0.65$ meV, shaded regions *1* and *2* denote intervals of $1/B$, in which the MISO for the control bridge and the ULSL are in-phase and out-of-phase (*b*)

Such a "splitting" in $D_j(\varepsilon)$ leads, under the conditions $\Gamma_{Bj} \sim \hbar\omega_c$ and $1/\tau_{qj} \sim \hbar\omega_c$, to a flip of the SdH oscillations [12].

In a two-subband system, as $1/B$ changes, resonant transitions of electrons between the Landau levels of different subbands occur periodically giving rise to the MISO. The resonant nature of such transitions is not related to the position of E_F, which makes the physics behind the MISO fundamentally different from that of the SdH oscillations. The MISO maxima arise when the Landau levels of different subbands coincide. The one-dimensional periodic potential by changing $D_j(\varepsilon)$ significantly transforms the conditions for resonant transitions. In this case, the conditions for resonant magneto-intersubband transitions arise only in certain intervals of B, which is observed experimentally.

Conclusion

To summarize, we fabricated an ULSL based on a highly mobile two-subband electron system; MISO were considered in this ULSL assuming overlapping Landau bands. We observed a "flip" of the MISO in some ranges of magnetic fields. We established that the "flip" of the MISO occurs when the width of the Landau bands in the first subband is significantly less than the cyclotron energy, while the width of the Landau bands in the second subband is comparable to the cyclotron energy.

REFERENCES

1. **Polyanovskii V.M.,** Anomalous temperature-dependence of the amplitude of quantum oscillations of the magnetoresistance in quasitwo-dimensional systems, Sov. Phys. Semicond. 22 (1988) 1408.

2. **Raichev O.E.,** Magnetic oscillations of resistivity and absorption of radiation in quantum wells with two populated subbands, Phys. Rev. B 78 (2008) 125304.

3. **Bykov A.A., Nomokonov D.V., Goran A.V., Strygin I.S., Bakarov A.K., Abedi S., Vitkalov S.A.,** Suppression of magneto-intersubband resistance oscillations by large-scale fluctuations of the intersubband energy splitting, JETP Lett. 114 (2021) 423.

4. **Weiss D., von Klitzing K., Ploog K., Weimann G.,** Magnetoresistance oscillations in a two-Dimensional electron gas induced by a submicrometer periodic potential, Europhys. Lett. 8 (1989) 179.

5. **Beenakker C.W.J.,** Guiding-center-drift resonance in a periodically modulated two-dimensional electron gas, Phys. Rev. Lett. 62 (1989) 2020.

6. **Winkler R.W., Kotthaus J.P., Ploog K.,** Landau band conductivity in a two-dimensional electron system modulated by an artificial one-dimensional superlattice potential, Phys. Rev. Lett. 62 (1989) 1177.

7. **Endo A., Iye Y.,** Modulation of the Shubnikov–de Haas oscillation in unidirectional lateral superlattices, J. Phys. Soc. Jpn. 77 (2008) 054709.

8. **Bykov A.A., Strygin I.S., Goran A.V., Nomokonov D.V., Marchishin I. V., Bakarov A.K., Rodyakina E.E., Latyshev A.V.,** Modulation of magneto-intersubband oscillations in a one-dimensional lateral superlattice, JETP Lett. 110 (2019) 354.

9. **Friedland K.-J., Hey R., Kostial H., Klann R., Ploog K.,** New concept for the reduction of impurity scattering in remotely doped GaAs quantum wells, Phys. Rev. Lett. 77 (1996) 4616.

10. **Bykov A.A., Strygin I.S., Goran A.V., Nomokonov D.V., Bakarov A.K.,** Dependences of the transport scattering time and quantum lifetime on the two-dimensional electron gas density in modulation-doped single GaAs quantum wells with AlAs/GaAs short-period superlattice barriers, JETP Lett. 112 (2020) 437.

11. **Larkin I.A., Davies J.H., Long A.R., Cuscy R.,** Theory of potential modulation in lateral surface superlattices. II. Piezoelectric effect, Phys. Rev. B 56 (1997) 15242.

12. **Edmonds K.W., Gallagher B.L., Main P.C., Overend N., Wirtz R., Nogaret A., Henini M., Marrows C.H., Hickey B.J., Thoms S.,** Magnetoresistance oscillations due to internal Landau band structure of a two-dimensional electron system in a periodic magnetic field, Phys. Rev. B 64 (2001) 041303(R).

THE AUTHORS

STRYGIN Ivan S.
vanya-91@yandex.ru
ORCID: 0000-0002-0254-2925

BYKOV Aleksei A.
bykov@isp.nsc.ru
ORCID: 0000-0002-2776-1657

Received 07.12.2022. Approved after reviewing 08.12.2022. Accepted 06.02.2023.

Conference materials
UDC 621.383.52
DOI: https://doi.org/10.18721/JPM.161.312

Investigation of infrared photoresponse from structure with GeSiSn/Si multiple quantum wells

V.A. Timofeev [1]✉, V.I. Mashanov [1], A.I. Nikiforo[v] [1], I.V. Skvortsov [1],
A.A. Bloshkin [1], I.D. Loshkarev [1], I.A. Azarov [1], V.V. Kirienko [1]

[1] A.V. Rzhanov Institute of Semiconductor Physics SB RAS, Novosibirsk, Russia
✉ Vyacheslav.t@isp.nsc.ru

Abstract. The current-voltage (I-V) characteristics and spectral dependences of the photocurrent of *p-i-n* structures, including GeSiSn/Si multiple quantum wells (MQWs) with the Sn content up to 15%, are studied. It is shown that the increase in the Sn content from 4.5 to 13% leads to a gradual increase in the dark current density from 6×10^{-6} A/cm^2 to 5×10^{-5} A/cm^2 at the reverse bias of 1 V. The further rise in the Sn content to 15% results in the increase of the dark current density to 5×10^{-4} A/cm^2, which is an order of magnitude lower than the known values for GeSn-based photodiodes. The shift of the cutoff wavelength of the photoresponse with the Sn content increase in heterostructures is demonstrated. The photoresponse spectrum of the detector extends up to wavelengths of larger than 2 μm at the Sn content of more than 10%.

Keywords: multiple quantum well, band diagram, dark current, photocurrent

Funding: This work was supported by the Russian Science Foundation (RSF), Grant No. 20-79-10092.

Citation: Timofeev V.A., Mashanov V.I., Nikiforov A.I., Skvortsov I.V., Bloshkin A.A., Loshkarev I.D., Azarov I.A., Kirienko V.V., Investigation of infrared photoresponse from structure with GeSiSn/Si multiple quantum wells St, Petersburg State Polytechnical University Journal. Physics and Mathematics. 16 (1.1) (2023) 73–78. DOI: https://doi.org/10.18721/JPM.161.312

Материалы конференции
УДК 621.383.52
DOI: https://doi.org/10.18721/JPM.161.312

Исследование инфракрасного фотоотклика от структуры с множественными квантовыми ямами GeSiSn/Si

В.А. Тимофеев [1]✉, В.И. М ш нов [1], А.И. Никифоров [1], И.В. Скворцов [1],
А.А. Блошкин [1], И.Д. Лошк рев [1], И.А. Аз ров [1], В.В. Кириенко [1]

[1] Институт физики полупроводников им. А. В. Ржанова СО РАН, Новосибирск, Россия
✉ Vyacheslav.t@isp.nsc.ru

Аннотация. Исследованы вольт-амперные характеристики и спектральные зависимости фототока *p-i-n* структур, включающих множественные квантовые ямы GeSiSn/Si с содержанием Sn вплоть до 15%. Показано, что увеличение содержания олова от 4.5 до 15% приводит к увеличению плотности темнового тока с 6×10^{-6} А/см^2 до 5×10^{-4} А/см^2 при обратном смещении 1 В. Продемонстрировано, что увеличение содержания олова в гетероструктурах приводит к увеличению длинноволновой границы фотоответа вплоть до 2.25 μm.

Ключевые слова: множественная квантовая яма, зонная диаграмма, темновой ток, фототок

Финансирование: Работа выполнена при поддержке Российского научного фонда (РНФ), грант № 20-79-10092.

Ссылка при цитировании: Тимофеев В.А., Машанов В.И., Никифоров А.И., Скворцов И.В., Блошкин А.А., Лошкарев И.Д., Азаров И.А., Кириенко В.В. Исследование инфракрасного фотоотклика от структуры с множественными квантовыми ямами GeSiSn/Si // Научно-технические ведомости СПбГПУ. Физико-математические науки. 2023. Т. 16. № 1.1. С. 73–78. DOI: https://doi.org/10.18721/ JPM.161.312

Introduction

The new class of Ge-Si-Sn materials demonstrates promise for creating infrared photodetectors with the operation wavelengths from 1.55 up to 8 μm [1–3]. This range represents the best option for remote reading and the visualization of information due to reduced Rayleigh scattering and due to the transparency windows of the Earth's atmosphere near 1.6 μm, 3–5 μm and 8–14 μm. Infrared photodetectors based on GeSiSn are of great importance in applications ranging from fiber-optic communications to thermal imaging. Since Sn is the isovalent element with respect to Ge and Si, and also has the diamond-like crystal structure, photodetectors based on new GeSiSn materials will be able to compete with the group II-VI (HgCdTe)-based photodetectors due to better compatibility of the material with the existing Si technology.

Nowadays, there are many publications related to the GeSiSn-based photodetectors with the indication of their electrophysical parameters, such as the dark current, responsivity and cutoff wavelength [4, 5]. These parameters were included in tables presented in contributions [6, 7]. The dark current magnitude determines the signal-to-noise-ratio of the photodetectors, therefore it should be minimized. The lowest reported value of the dark current around 6×10^{-3} A/cm^2 was achieved for $Ge_{0.964}Sn_{0.036}$-based photodiodes [8]. The dark current has two components, namely: bulk and surface leakage currents. The first part is directly associated with the number of dislocations [9], whereas the second contribution is related to the surface defects of the mesa sidewall region. The later may be suppressed by the sidewall surface passivation [10].

The most photodiode structures grown on the Si substrate contain relaxed GeSn layers on the Ge layer. The GeSn and Ge layer thickness can reach several hundred nanometers. Due to the large lattice parameter mismatch between GeSn, Ge and Si, the dislocations are introduced. These defects increase the dark current of the photodiode. The issue may be solved by the application of the elastic strained layers. In this article such elastic strained (pseudomorphic) layers were used in the GeSiSn/Si multiple quantum well structures (MQW), which were embedded in the active region of the *p-i-n* diode. The lowest dark current density value in the GeSiSn/Si MQW diodes was about 6×10^{-6} A/cm^2. This dark current density is three orders of magnitude smaller than one of literature.

Materials and Methods

To study the photoelectric properties of structures with GeSiSn/Si MQWs, a series of samples with different tin content was grown. All samples were obtained on p^+-Si substrates. The 200 nm thick buffer layer was formed on the Si surface. After the growth of the buffer layer an active region was grown. It consisted of ten $Ge_{0.3}Si_{0.7-y}Sn_y$ quantum wells of the 2 nm thickness, which were separated by 7 nm thick Si layers. The Sn content in the samples varied from 3.5 to 15%. Further, the 100 nm thick undoped Si layer and the 50 nm thick n+-Si layer were grown. The *p-i-n* diodes in the form of mesa-structures with the diameter of 1.7 mm were fabricated using standard technological processes such as optical lithography, plasma etching and metal deposition in vacuum. The etching was performed down to the Si substrate. Au/Ti layers deposited in a high-vacuum setup were used to create ring electrodes to the heavily doped n^+-Si layers. The schematic photodetector structure is shown in Fig.1, *a*. Before mounting detectors fabricated into a cryostat for photoelectric measurements, the current-voltage (I–V) characteristics of devices were

measured at room temperature. The compositions and quality of epitaxial structures were studied by X-ray diffractometry. The diffraction reflection curves were obtained using the symmetric two-crystal scheme with the DSO-1T diffractometer and the Ge(004) single-crystal monochromator. The photocurrent spectra were measured using a Bruker Vertex-70 infrared Fourier spectrometer. The samples were placed in the Janis cryostat and cooled to the temperature of 77 K with liquid nitrogen. The photocurrent was recorded using an SR570 low-noise preamplifier from Stanford Research System. A halogen lamp was used as a light source.

The calculation of the energy band diagrams of the Si/$Ge_{1-x-y}Si_xSn_y$/Si heterocomposition, including a pseudomorphic $Ge_{1-x-y}Si_xSn_y$ layer, was carried out using a model-solid theory, which makes it possible to take into account the effects of strain on the band structure [11]. The model parameters for the GeSiSn ternary compound were determined by a linear interpolation of data for Ge, Si, and Sn [12–14]. The band gaps of the solid solution were calculated by the quadratic interpolation:

$$E^{\xi}\left(Ge_{1-x-y}Si_xSn_y\right) = E^{\xi}(Ge)\cdot(1-x-y) + E^{\xi}(Si)\cdot(x) + E^{\xi}(Sn)\cdot(y) - \\ -b^{\xi}_{SiGe}\cdot(1-x-y)\cdot x - b^{\xi}_{GeSn}\cdot(1-x-y)\cdot y - b^{\xi}_{SiSn}\cdot x\cdot y, \quad (1)$$

where, E^{ξ}(Ge), E^{ξ}(Si) and E^{ξ}(Sn) are Ge, Si and Sn band gaps, respectively; b^{ξ}_{SiGe}, b^{ξ}_{GeSn} and b^{ξ}_{SiSn} correspond to the bowing parameters; index $\xi = \Gamma, L, X$ refers to the different conduction valleys [13]. The effects of confinement were taken into account using effective mass theory. The interpolation suggested in [15] was used to calculate the effective masses.

Results and Discussion

A series of *p-i-n* diodes including $Ge_{0.3}Si_{0.7-y}Sn_y$/Si MQWs was obtained. The pseudomorphic state of $Ge_{0.3}Si_{0.7-y}Sn_y$ layers was confirmed by the presence of diffraction peaks on the diffraction reflection curves (Fig. 1, *b*). Diffraction peaks are marked with integers from −3 to +1.

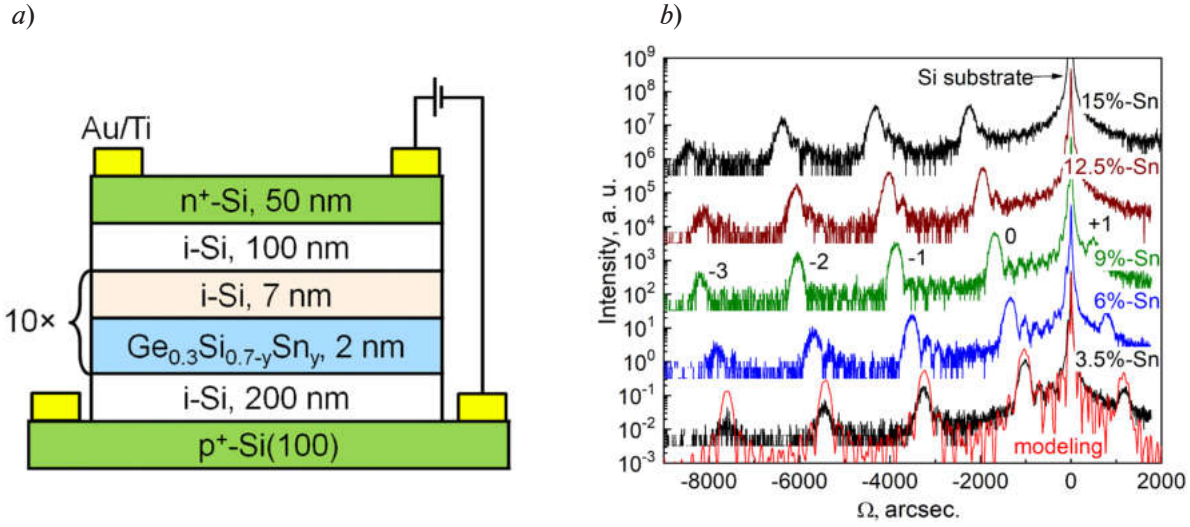

Fig. 1. Schematic cross section of a *p-i-n* diode with the $Ge_{0.3}Si_{0.7-y}Sn_y$/Si MQWs (*a*) and the (004) diffraction reflection curves from the MQWs containing 10 periods with the pseudomorphic $Ge_{0.3}Si_{0.7-y}Sn_y$ films for different Sn contents (*b*). The peak from the Si substrate is indicated by the arrow and the diffraction maxima are pointed out by the integers from −3 to +1

The distance between the satellites corresponds to the period in MQWs. The average composition was determined from the distance between the zero satellite and the peak from the Si substrate. The shift of the zero satellite is observed with the Sn content increase from 3.5 to 15%. The rocking curves were simulated taking into account the pseudomorphic state of the $Ge_{0.3}Si_{0.7-y}Sn_y$ layers. The modeling curve for the Sn content of 3.5% is shown as the example. It is in good agreement with the experimental dependence for the same composition.

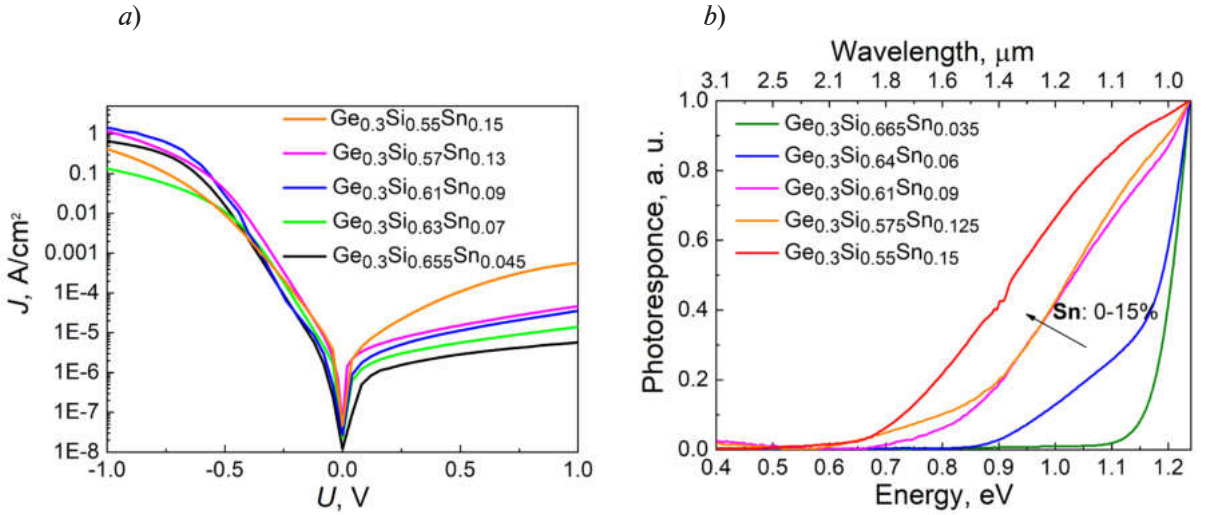

Fig. 2. Dark current-voltage (I–V) characteristics of p-i-n diodes for different Sn contents in GeSiSn quantum wells (*a*), photocurrent spectra of p-i-n diodes measured in short circuit regime at zero bias (*b*)

Based on the measurements of I–V characteristics and photocurrent spectra the photoelectric properties of p-i-n diodes obtained were studied. The I–V characteristics for samples containing up to 15% tin in quantum wells are shown in Fig. 2, *a*. All devices had diode I–V characteristics. It is shown that the increase in the Sn content from 4.5 to 13% leads to a gradual increase in the dark current density from 6×10^{-6} A/cm^2 to 5×10^{-5} A/cm^2 at a reverse bias of 1 V. The further rise in the Sn content to 15% results in the increase of the dark current density to 5×10^{-4} A/cm^2. The increase of the dark current density can be associated with the Sn segregation on the surface. It is confirmed by the appearance of the two-domain (4×1) superstructure during the growth on the reflection high energy electron diffraction pattern (RHEED). Such superstructure corresponds to the submonolayer Sn cover on the Si surface. The Sn segregation probably causes the surface leakage current increase on the sidewall surface of the mesa [10]. Despite the absence of the passivation and optimization of p-i-n diode dimensions, we achieved record values of the dark current density, which are a thousand times lower than the dark current densities of GeSn-based diodes presented in the literature for approximately the same Sn content [8]. The photocurrent spectra for the Sn content from 3.5 to 15% are shown in Fig. 2, *b*. The spectra were normalized

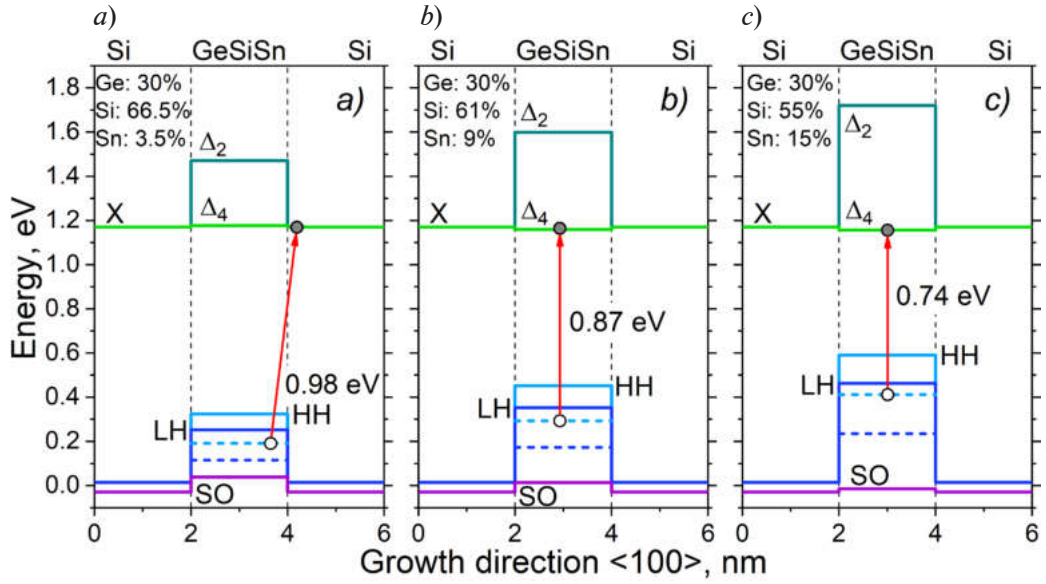

Fig. 3. Band diagrams for Si/$Ge_{0.3}Si_{0.7-y}Sn_y$/Si heterostructures with the Sn content of 3.5 (*a*), 9 (*b*) and 15% (*c*)

to the photocurrent maximum. For all samples, the large photoresponse signal with the energy near 1.2 eV is observed. This signal is associated with the interband optical transitions in silicon. The gradually decreasing photocurrent signal is observed with the photon energy decrease below the Si band gap. The cutoff wavelength of the photoresponse was determined by equating to zero of the first derivative of the photocurrent. The obtained values are presented in the inset in Fig. 2, *b*. The increase of the cutoff wavelength of the photoresponse from 1.18 to 2.25 μm is observed with the tin content increase from 3.5 to 15% in the $Ge_{0.3}Si_{0.7-y}Sn_y$ layers. According to band diagram calculations for $Si/Ge_{0.3}Si_{0.7-y}Sn_y/Si$ heterostructures (Fig. 3), the contribution to the photocurrent can occur from interband optical transitions between the valence band and X-valley in silicon, as well as transitions between subbands of heavy or light holes in the $Ge_{0.3}Si_{0.7-y}Sn_y$ solid solution layer and the X-valley in silicon or the Δ_4 subband in the $Ge_{0.3}Si_{0.7-y}Sn_y$ layer. The optical transitions with minimum energy are indicated by arrows in Fig. 3. However, the experimentally obtained values of the cutoff wavelength are lower than the calculated ones in terms of energy. This result can be explained by smearing of the GeSiSn/Si heterointerface. It is associated with the Sn segregation, which leads to a decrease in the optical transition energy.

Conclusion

A series of *p-i-n* diodes, including GeSiSn/Si MQWs with the Sn content up to 15%, was obtained. The gradual increase of the dark current density from 6×10^{-6} A/cm^2 to 5×10^{-5} A/cm^2 at the reverse bias of 1 V was observed with the Sn content increase from 4.5 to 13%. The further Sn content rise to 15% led to the dark current density increase up to 5×10^{-4} A/cm^2. However, these dark current densities are the smallest among those known from the literature for the GeSiSn/Si system. It was shown that the Sn content increase in heterostructures leads to the shift of the cutoff wavelength of the photoresponse up to 2.25 μm. Further investigation will be aimed at reducing the dark current by optimizing the size of the diode mesa and its sidewall passivation, as well as at increasing the cutoff wavelength of the spectral responsivity due to the higher Ge and Sn contents in the GeSiSn quantum wells.

Acknowledgments

This work was supported by the Russian Science Foundation (RSF), Grant No. 20-79-10092.

REFERENCES

1. **Chang C., Li H., Ku C.-T., Yang S.-G., Cheng H. H., Hendrickson J., Soref R. A., Sun G.,** $Ge_{0.975}Sn_{0.025}$ 320 × 256 imager chip for 1.6-1.9 μm infrared vision, Applied Optics. 55 (36) (2016) 10170–10173.

2. **Atalla M. R. M., Assali S., Attiaoui A., Lemieux-Leduc C., Kumar A., Abdi S., Moutanabbir O.,** All-Group IV Transferable Membrane Mid-Infrared Photodetectors, Advanced Functional Materials. 31 (3) (2020) 2006329.

3. **Xu C., Ringwala D., Wang D., Liu L., Poweleit C. D., Chang S. L. Y., Zhuang H. L., Menendez J., Kouvetakis J.,** Synthesis and Fundamental Studies of Si-Compatible (Si)GeSn and GeSn Mid-IR Systems with Ultrahigh Sn Contents, Chemistry of Materials. 31 (2019) 9831–9842.

4. **Su S., Cheng B., Xue C., Wang W., Cao Q., Xue H., Hu W., Zhang G., Zuo Y., Wang Q.,** GeSn *p-i-n* photodetector for all telecommunication bands detection, Optics Express. 19 (7) (2011) 6400.

5. **Xu S., Wang W., Huang Y.-C., Dong Y., Masudy-Panan S., Wang H., Gong X., Yeo Y.-C.,** High-speed photo detection at two-micron-wavelength: technology enablement by GeSn/Ge multiple-quantum-well photodiode on 300 mm Si substrate, Optics Express. 27 (4) (2019) 5798.

6. **Zheng J., Liu Z., Xue C., Li C., Zuo Y., Cheng B., Wang Q.,** Recent progress in GeSn growth and GeSn-based photonic devices, Journal of Semiconductors. 39 (6) (2018) 061006.

7. **Tran H., Pham T., Margetis J., Zhou Y., Dou W., Grant P. C., Grant J. M., Al-Kabi S., Sun G., Soref R. A., Tolle J., Zhang Y.-H., Du W., Li B., Mortazavi M., Yu S.-Q.,** Si-Based GeSn Photodetectors toward Mid-Infrared Imaging Applications, ACS Photonics. 6 (11) (2019) 2807–2815.

8. **Zhang D., Xue C., Cheng B., Su S., Liu Z., Zhang X., Zhang G., Li C., Wang Q.,** High-responsivity GeSn short-wave infrared *p-i-n* photodetectors, Applied Physics Letters. 102 (2013) 141111.

9. **Giovane L. M., Luan H.-C., Agarwal A. M., Kimerling L. C.,** Correlation between leakage current density and threading dislocation density in SiGe p-i-n diodes grown on relaxed graded buffer layers, Applied Physics Letters. 78 (4) (2001) 541–543.

10. **Dong Y., Wang W., Lei D., Gong X., Zhou Q., Lee S. Y., Loke W. K., Yoon S.-F., Tok E. S., Liang G., Yeo Y.-C.,** Suppression of dark current in germanium-tin on silicon *p-i-n* photodiode by a silicon surface passivation technique, Optics Express. 23 (14) (2015) 18611.

11. **Chris G. Van de Walle,** Band lineups and deformation potentials in the model-solid theory, Phys. Rev. B. 39 (1989) 1871–1883.

12. **El Kurdi M., Sauvage S., Fishman G., Boucaud P.,** Band-edge alignment of SiGe/Si quantum wells and SiGe/Si self-assembled island, Phys. Rev. B. 73 (2006) 195327.

13. **Moontragoon P., Soref R. A., Ikonic Z.,** The direct and indirect bandgaps of unstrained $Si_xGe_{1-x-y}Sn_y$ and their photonic device applications, J. Appl. Phys. 112 (2012) 073106.

14. **Attiaoui A., Moutanabbir O.,** Indirect-to-direct band gap transition in relaxed and strained $Ge_{1-x-y}Si_xSn_y$ ternary alloys, J. Appl. Phys. 116 (2014) 063712.

15. **Sant S., Schenk A.,** Pseudopotential calculations of strained-GeSn/SiGeSn hetero-structures, Appl. Phys. Lett. 105 (2014) 162101.

THE AUTHORS

TIMOFEEV Vyacheslav A.
Vyacheslav.t@isp.nsc.ru
ORCID: 0000-0003-4093-7802

BLOSHKIN Alexey A.
bloshkin@isp.nsc.ru
ORCID: 0000-0002-4128-6143

MASHANOV Vladimir I.
mash@isp.nsc.ru
ORCID: 0000-0003-4420-6695

LOSHKAREV Ivan D.
idl@isp.nsc.ru
ORCID: 0000-0003-4771-3705

NIKIFOROV Alexander I.
nikif@isp.nsc.ru
ORCID: 0000-0003-0583-0508

AZAROV Ivan A.
azarov_ivan@mail.ru
ORCID: 0000-0001-9571-2227

SKVORTSOV Ilya V.
i.skvortsov@isp.nsc.ru
ORCID: 0000-0002-2153-1615

KIRIENKO Viktor V.
victor@isp.nsc.ru
ORCID: 0000-0002-8842-5323

Received 29.11.2022. Approved after reviewing 23.01.2023. Accepted 25.01.2023.

Conference materials
UDC 535.3
DOI: https://doi.org/10.18721/JPM.161.313

Modeling of coherent dynamics of excitons in a GaAs quantum well in the pump-probe experiment

O.S. Sultanov [1]✉, I.A. Yugova [1,2], A.V. Mikhailov [2]

[1] Faculty of Physics, St. Petersburg State University, St. Petersburg, Russia;
[2] Spin Optics Laboratory, St. Petersburg State University, St. Petersburg, Russia
✉ st064743@student.spbu.ru

Abstract. We investigated polarization-dependent quantum beats of excitons with light and heavy holes observed in the pump-probe experiment. Oscillations in the energy of exciton resonances have been experimentally observed upon simultaneous excitation of exciton levels. To explain this effect, a theoretical model was formulated based on the consideration of a five-level scheme with the inclusion of nonlinearity in the form of an exchange exciton-exciton interaction. It has been found that the shift of energy resonances can be described only if the exciton-exciton exchange interaction is taken into account. The results of theoretical calculations of the coherent dynamics of excitons in this model are in agreement with the experimental data.

Keywords: quantum well, excitons, coherent dynamics, computer modeling

Funding: The authors would like to thank St. Petersburg State University, Grant 94030557, and the Russian Foundation for Basic Research, Grant 19-52-12059, for financial support of theoretical studies. Experimental studies were carried out as part of the Russian Science Foundation grant No. 19-72-20039.

Citation: Sultanov O.S., Yugova I.A., Mikhailov A.V., The modeling of coherent dynamics of excitons in a GaAs quantum well in the pump-probe experiment, St. Petersburg State Polytechnical University Journal. Physics and Mathematics. 16 (1.3) (2023) 79–84. DOI: https://doi.org/10.18721/JPM.161.313

Материалы конференции
УДК 535.3
DOI: https://doi.org/10.18721/JPM.161.313

Моделирование когерентной динамики экситонов в квантовой яме GaAs, наблюдаемой в эксперименте «накачка-зондирование»

О.Ш. Султ нов [1,2]✉, И.А. Югов [1,2], А.В. Мих йлов [2]

[1] Физический факультет Санкт-Петербургского Государственного Университета, Санкт-Петербург, Россия;
[2] Лаборатория Оптики Спина Санкт-Петербургского Государственного Университета, Санкт-Петербург, Россия
✉ st064743@student.spbu.ru

Аннотация. В данной работе рассмотрены поляризационно-зависимые квантовые биения экситонов с лёгкой и тяжёлой дыркой, наблюдаемые в эксперименте «накачка-зондирование». Экспериментально обнаружены осцилляции энергии экситонных резонансов при одновременном возбуждении экситонных уровней. Для объяснения этого эффекта сформулирована теоретическая модель, основанная на рассмотрении пятиуровневой схемы с введённой нелинейностью в виде обменного экситон-экситонного взаимодействия. Обнаружено, что сдвиг энергетических линий удается описать только при учете обменного экситон-экситонного взаимодействия. Результат теоретических расчетов когерентной динамики экситонов в данной модели находятся в согласии с экспериментальными данными.

Ключевые слова: квантовая яма, экситоны, когерентная динамика, компьютерное моделирование

Финансирование: Авторы благодарят Санкт-Петербургский Государственный Университет, грант № 94030557, и Российский Фонд Фундаментальных исследований, грант № 19-52-12059, за финансовую поддержку теоретических исследований. Экспериментальные исследования были выполнены в рамках гранта Российского Научного Фонда № 19-72-20039.

Ссылка при цитировании: Султанов О.Ш., Югова И.А., Михайлов А. Моделирование когерентной динамики экситонов в квантовой яме GaAs, наблюдаемой в эксперименте «накачка-зондирование» // Научно-технические ведомости СПбГПУ. Физико-математические науки. 2023. Т. 16. № 1.3. С. 79–84. DOI: https://doi.org/10.18721/JPM.161.313

Introduction

Studies of low-dimensional systems are promising areas of semiconductor physics. In particular, in GaAs/AlGaAs quantum wells, there are a number of effects that are not fully understood and are of considerable interest due to the possibility of using them for the purposes of optoelectronics. Investigation of exciton resonances in such systems can show such effects as polarization-sensitive dynamic shifts of the transition energy and quantum beats [1].

In this work we use an experimental pump-probe technique with spectral resolution and polarization selection to study coherent nonlinear dynamics of heavy and light hole excitons in GaAs/AlGaAs quantum well. This technique makes it possible to distinguish the observed effects by analyzing the shape of exciton resonances with high precision. We developed a theoretical model that allowed us to describe the observed coherent phenomena and obtained that the energy oscillations appear due to the exchange interaction of excitons in quantum well created in a superposition state.

Experimental Details

The experimental sample used in this work is a high-quality GaAs/AlGaAs 14-nm quantum well grown by molecular beam epitaxy. The sample was cooled in a closed-cycle helium cryostate to the temperature of 4 K. The kinetics of the secondary emission of this quantum well have been studied by the pump-probe method where the time-integrated reflectivity is studied as a function of the time delay between the pump and probe pulses [1]. In the experiment both heavy-hole and light-hole exciton resonances are excited with a spectrally wide pulses generated by a fs Ti:Sapphire laser. The pump beam has either linear or circular polarization. The probe beam has linear polarization which is split into either co- and cross-linear components or co- and cross-circular components with respect to the pump beam by a quarter-wave plate and a Wollaston prism. Both probe beam components are then detected at the same time by a spectrometer with a CCD camera. The probe beam spectra are detected at small time delays between pump and probe pulses with a sub-picosecond step.

Fig. 1, *a* shows the typical reflection spectrum of the sample in the absence of a pump pulse. Resonances of light and heavy hole excitons are seen in the form of reflection peaks and marked by Xhh and Xlh labels. Due to the small width and small depth of the well, it was possible to achieve a situation where the well contains only one exciton level, which is split into a levels with a heavy hole angular momentum 3/2 and with a light hole angular momentum 1/2. This splitting is clearly seen in the spectrum and is equal to 3.6 meV. The shape of the resonances is the result of a special design of the sample structure. The figure 1 also shows the spectrum fitting. All measured spectra were analyzed within the framework of the theory of non-local dielectric response. This allows to extract such characteristics of the states of heavy and light excitons as the resonance energy, radiative and non-radiative broadening [2–6]. The basic formulas used to fit the spectra are [7]:

$$r_{QW}(\omega) = \frac{i\Gamma_R}{\omega_x - \omega - i(\Gamma_R + \Gamma_{NR})}, \quad (1)$$

$$R(\omega) = \left| \frac{r_s + r_{QW}(\omega)e^{iz\phi}}{1 + r_s r_{QW}(\omega)e^{iz\phi}} \right|. \quad (2)$$

Here, rQW(ω) describes the amplitude reflection from the exciton resonance, Γ_R and Γ_{NR} are the rates of radiative and nonradiative decay of the exciton polarization, ω_x is the frequency of the exciton transition, ϕ is the phase shift of the light from the sample surface to the center of the quantum well, r_s is the amplitude reflection from the sample surface, R is the intensity of the reflection from the sample.

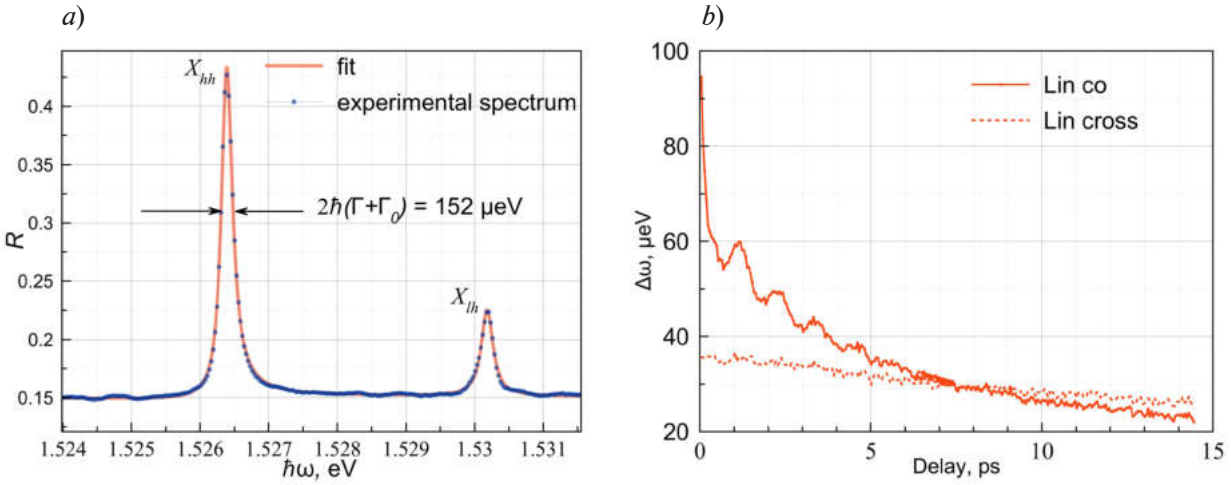

Fig. 1. Reflection spectrum of the GaAs/AlGaAs quantum well studied in the experiment (*a*). X_{hh} and X_{lh} correspond to optical transitions for heavy-hole and light-hole excitons respectively. Energy shift oscillations for the heavy-hole exciton in the linear co and cross configurations (*b*)

The dynamics of light-hole and heavy-hole exciton resonances have been studied in co- and cross- circular and linear polarizations of the pump pulse and the probe pulse. The results indicate the presence of an oscillating energy shift of the exciton lines in the reflection spectrum (see Fig. 1, *b*), as well as amplitude beats depending on the delay. Observation of these effects is associated with significant difficulties due to the need for a very high spectral resolution (of the order of 1 μeV). However, by using the high quality sample (ideal surface geometry, absence of defects) and modern technology such resolution can be achieved. The frequency of the energy shift oscillations is equal to the energy splitting of the exciton states with heavy and light holes. However, the observed beats are not present in all configurations, but only in those where the polarizations of the pump pulse and the probe pulse are coincided. As well, a very small energy shift has been observed in the cross-linear-polarizations configuration.

Theoretical model

For a theoretical description of the observed effect, a five-level exciton model is proposed, in which there are one ground state and four states of excitons with heavy and light holes, separated by spin. The action of light pulses on the system was described by the optical Bloch equations. It turned out that the detected oscillating component of the radiative broadening of exciton resonances in various polarization configurations can be interpreted as a manifestation of quantum beats of the states of excitons with light and heavy holes [8]. However, the energy shift can only be described if the exchange exciton-exciton interaction is taken into account, which has not been considered before. In our model the nonlinearity in the form of the exchange interaction between pump-produced excitons and probe beam excitons is considered in accordance with Ref. [1], and generalized to a five-level energy scheme. Such consideration required a transition to the second quantization formalism for excitons. During the simulation, the dynamics of excitons created by

light pulses was considered sequentially: 1) A pump pulse creates a coherent superposition of exciton states in dependence on the polarization of light. 2) The probe pulse also produces an exciton in the superposition state and its further dynamics is determined by the exciton-exciton interaction with excitons produced by pump. It should be emphasized that the effect of energy shift oscillations is due to the exciton-exciton exchange interaction and arises only if the excitons are in the superposition quantum state. 3) Next, the intensity of reflection of the probe beam from the sample is calculated taking into account the resonant exciton reflection. Such consideration leads to an oscillating shift of exciton resonances for the same linear or circular polarizations of light beams, and to a small non-oscillating shift in crossed polarizations.

Let us consider in more detail the theoretical description of exciton coherent nonlinear dynamics.

The Hamiltonian of the system (without the interaction with light) is

$$H_{tot} = \hbar \sum_i \omega_i c_i^\dagger c_i + H_{int}, \tag{3}$$

where H_{int} is the exciton-exciton interaction Hamiltonian.

The interaction with light is described in the dipole approximation. The wavefunction of the exciton created by the pump pulse is

$$|\psi_{pump}>=\sum_i a_i c_i^\dagger |0>, a_i = \alpha_i e^{-i\omega_{0i}t}, \alpha_i \sim \frac{id_i}{\hbar}\int_{-\infty}^{t} E_{pump}(t')e^{-i\omega_{0i}(t-t')}dt', \tag{4}$$

where E_{pump} is the strength of the electric field of the pump pulse, d_i and ω_{0i} are the dipole moments and frequencies of exciton optical transitions, c_i^+ are creation operators. Likewise, the probe exciton wavefunction is

$$|\psi_{pr}>=\left(1+\sum_i a_i' c_i'^\dagger\right)|0>. \tag{5}$$

Assuming that only identical excitons interact, the interaction Hamiltonian takes the form of the exchange interaction

$$H_{int} = \hbar\omega_{ex}\sum_i c_i^\dagger c_i c_i'^\dagger c_i'. \tag{6}$$

Here c_i and c_i' (c_i^+ and $c_i'^+$) are the annihilation (creation) operators for the pump and probe exciton, respectively. Since the pump and probe pulses are spectrally wide, superposition states of the heavy-hole and the light-hole state are excited. This corresponds to a linear transform of the complex amplitudes and the field operators

$$\gamma_j = \sum_k m_{jk}\alpha_k, c_j' = \sum_k m_{jk}c_k, \tag{7}$$

where m_{jk} is the transform matrix.

Applying the field operators to the pump and probe wavefunction, we can write down the Schrödinger equations for the complex amplitudes

$$\dot{\gamma}_j = -i\left(\left(\omega_0+\omega_{ex,j}\right)\gamma_j + \sum_{k\neq j}\gamma_k\sum_l \omega_l m_{lj}m_{jk}\right), \tag{8}$$

where

$$\begin{cases}
\omega_{ex,1} = \omega_{ex0}\left(\tilde{N}_0+\frac{1}{2}Re[\left(\alpha_1^*+\alpha_3^*\right)\left(\alpha_2+\alpha_4\right)e^{i(\omega_h-\omega_l)(t+\tau)}+\alpha_1^*\alpha_3+\alpha_2^*\alpha_4]e^{-\Gamma_c(t+\tau)}\right),\\
\omega_{ex,2} = \omega_{ex0}\left(\tilde{N}_0+\frac{1}{2}Re[-\left(\alpha_1^*+\alpha_3^*\right)\left(\alpha_2+\alpha_4\right)e^{i(\omega_h-\omega_l)(t+\tau)}+\alpha_1^*\alpha_3+\alpha_2^*\alpha_4]e^{-\Gamma_c(t+\tau)}\right),\\
\omega_{ex,3} = \omega_{ex0}\left(\tilde{N}_0+\frac{1}{2}Re[\left(\alpha_1^*+\alpha_3^*\right)\left(\alpha_2+\alpha_4\right)e^{i(\omega_h-\omega_l)(t+\tau)}-\alpha_1^*\alpha_3-\alpha_2^*\alpha_4]e^{-\Gamma_c(t+\tau)}\right),\\
\omega_{ex,4} = \omega_{ex0}\left(\tilde{N}_0+\frac{1}{2}Re[-\left(\alpha_1^*+\alpha_3^*\right)\left(\alpha_2+\alpha_4\right)e^{i(\omega_h-\omega_l)(t+\tau)}-\alpha_1^*\alpha_3-\alpha_2^*\alpha_4]e^{-\Gamma_c(t+\tau)}\right),
\end{cases} \tag{9}$$

$\Gamma_0 = 2\Gamma_R$, $\Gamma_c = 2(\Gamma_R + \Gamma_{NR})$, τ is the delay time between pump and probe pulses,

$$\tilde{N}_0 = \frac{1}{4}\sum_i |\alpha_i|^2 e^{-\Gamma_0(t+\tau)}. \quad (10)$$

Integrating (8), we can obtain the reflectance of the quantum well

$$r_{QW}(\omega) = \int_0^\infty \sum_j d_j \gamma_j(t) e^{i\omega t} dt. \quad (11)$$

The exciton reflectance can then be obtained using (2).

Results and Discussion

Fig. 2 shows the results of theoretical calculation using the Runge-Kutta method for linearly polarized beams (similar results are also obtained for circular polarization). The reflection spectra of heavy hole exciton are shown in Fig. 2, *a* as the color map. These spectra calculated by using of the Eq. (2) with taking into account the obtained r_{QW} (Eq. (11)) in dependence on the delay between the pump and probe pulses. The reflection amplitude is shown in color. Zero energy shift corresponds to the position of the exciton line without pumping.

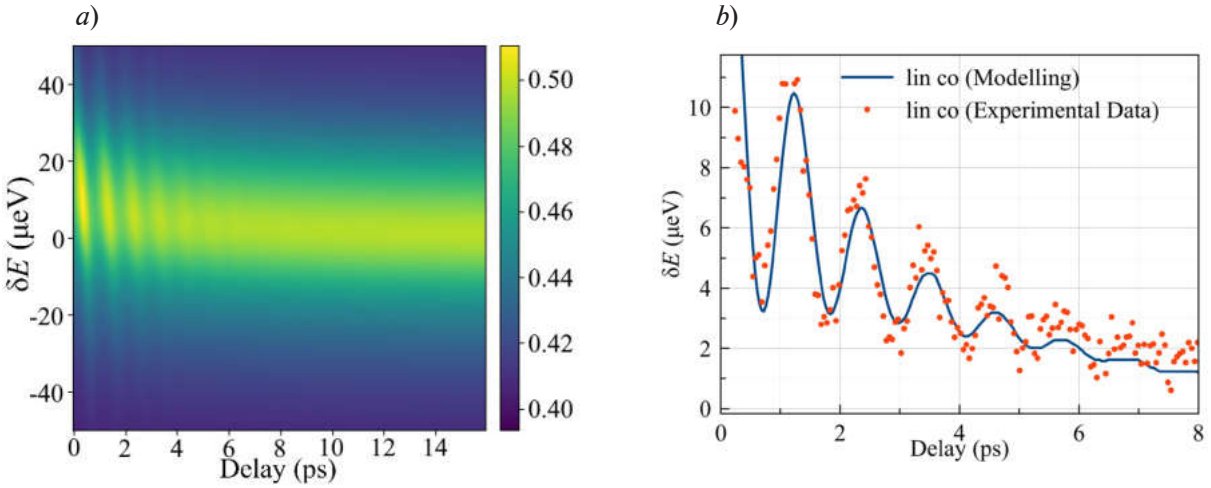

Fig. 2. Modelled reflectance spectrum of heavy hole exciton in dependence on delay between the pump and the probe pulses (*a*). Comparison of the energy shift in the experiment and the theoretical model (*b*)

The energy position of the exciton resonance as a function of the delay is shown in Fig. 2, *b*. The red dots show the experimental data, the blue curve is the simulation result. Calculation parameters such as the splitting between exciton states (it corresponds to $\Omega = 5.47$ ps^{-1}) and the values of radiative and nonradiative broadenings $\Gamma_R = 0.02\Omega$ and $\Gamma_{NR} = 0.04\Omega$ are obtained from the direct fitting of experimental spectra within the framework of the theory of nonlocal dielectric response as described above. The exchange interaction energy was an adjustable parameter and is equal to $\omega_{ex0} = 0.0175\Omega$. There is still a long-lived energy shift in the dynamics of the experimental spectra due to the incoherent interaction with the reservoir of non-radiating excitons. To compare with the experimental dependence, we added this long-lived bias to the calculated curve in Fig. 2, *b*. One can see that the results of theoretical calculations of the coherent exciton dynamics in the frame of our model are in agreement with the experimental data.

Conclusion

The coherent nonlinear dynamics of heavy and light hole excitons in GaAs/AlGaAs quantum well upon coherent excitation of exciton resonances by short laser pulses is investigated experimentally and theoretically. We found delay-dependent oscillations of the exciton resonance energies. Theoretical model for the interaction of excitons with light in a GaAs/AlGaAs quantum well in the pump-probe experiment has been proposed. It was found that the energy shift can only be

described if the nonlinearity in the form of the exchange exciton-exciton interaction is taken into account, which has not been considered before. The results of the modeling using the Runge–Kutta method agree with the experimental data. Further study may include the overview of negative delays, where four-wave mixing effects are prevalent, as well as taking "dark" exciton states into account, which are less likely to interact with the pulse and have much lower decay rates.

REFERENCES

1. **Trifonov A.V., Kurdyubov A.S., Gerlovin I.Ya., Smirnov D.S., Kavokin K.V., Yugova I.A., Assmann M., Kavokin A.V.,** Exciton energy oscillations induced by quantum beats, Physical Review B, 102, (2020) 205303.

2. **Trifonov A.V., Khramtsov E.S., Kavokin K.V., Ignatiev I.V., Kavokin A.V., Efimov Y.P., Eliseev S.A., Shapochkin P.Yu., Bayer M.,** Nanosecond Spin Coherence Time of Nonradiative Excitons in GaAs/AlGaAs Quantum Wells, Physical Review Letters, 122, (2019) 147401.

3. **Khramtsov E.S., Belov P.A., Grigoryev P.S., Ignatiev I.V., Verbin S.Yu., Efimov Yu.P., Eliseev S.A., Lovtcius V.A., Petrov V.V., Yakovlev S.L.,** Radiative decay rate of excitons in square quantum wells: Microscopic modeling and experiment, Journal of Applied Physics, 119, (2016) 184301.

4. **Grigoryev P.S., Kurdyubov A.S., Kuznetsova M.S., Ignatiev I.V., Efimov Yu.P., Eliseev S.A., Petrov V.V., Lovtcius V.A., Shapochkin P.Yu.,** Excitons in asymmetric quantum wells, Superlattices and Microstructures, 97, (2016) 452–462.

5. **Shapochkin P.Yu., Eliseev S.A., Lovtcius V.A., Efimov Yu.P., Grigoryev P.S., Khramtsov E.S., Ignatiev I.V.,** Excitonic Probe for Characterization of High-Quality Quantum-Well Heterostructures, Physical Review Applied, 12, (2019) 034034.

6. **Kurdyubov A.S., Trifonov A.V., Gerlovin I.Ya., Gribakin B.F., Grigoryev P.S., Mikhailov A.V., Ignatiev I.V., Efimov Yu.P., Eliseev S.A., Lovtcius V.A., Assmann M., Bayer M., Kavokin A.V.,** Optical control of a dark exciton reservoir, Physical Review B, 104, (2021) 035414.

7. **Ivchenko E.L.,** Optical Spectroscopy of Semiconductor Nanostructures (Springer, Berlin 2004).

8. **Mikhailov A.V., Trifonov A.V., Sultanov O.S., Yugova I.A., Ignatiev I.V.,** Quantum beats of light and heavy-hole excitons in reflection spectra of GaAs/AlGaAs quantum well, Fizika I Technika Poluprovodnikov, vol. 56, issue 7, (2022) 672–677.

THE AUTHORS

SULTANOV Oleg S.
st064743@student.spbu.ru

YUGOVA Irina A.
i.yugova@spbu.ru
ORCID: 0000-0003-0020-3679

MIKHAILOV Andrey V.
mikhailovav@yandex.ru
ORCID: 0000-0001-7580-4992

Received 14.12.2022. Approved after reviewing 31.01.2023. Accepted 08.02.2023.

Conference materials
UDC 621.382.2
DOI: https://doi.org/10.18721/JPM.161.314

Peculiarities of low frequency noise and non-radiative recombination in AlGaN QWs emitting at 280 nm

N.A. Talnishnikh [1]✉, A.E. Ivanov [1], E.I. Shabunina [2], N.M. Shmidt [2]

[1] SHM R&E Center, RAS, St. Petersburg, Russia;
[2] Ioffe Institute, RAS, St. Petersburg, Russia
✉ nadya.fel@mail.ru

Abstract. A prominent source of charge carrier losses due to non-radiative recombination in AlGaN QWs, caused by the presence of charged centers localized at disordered hetero interfaces, has been experimentally revealed. It was found out that the spectral density of current low-frequency noise, which carries integral information about single defects and a defect system, is an order of magnitude higher in AlGaN QWs than in effective blue InGaN/GaN QWs. Thus, non-radiative recombination losses are still the source responsible for the low quantum efficiency of ultraviolet LEDs.

Keywords: AlGaN/GaN, LEDs, UV LEDs, EQE, low-frequency noise, non-radiative recombination, QWs

Citation: Talnishnikh N.A., Ivanov A.E., Shabunina E.I., Shmidt N.M., Peculiarities of low frequency noise and non-radiative recombination in AlGaN QWs emitting at 280 nm, St. Petersburg State Polytechnical University Journal. Physics and Mathematics. 16 (1.3) (2023) 85–89. DOI: https://doi.org/10.18721/JPM.161.314

Материалы конференции
УДК 621.382.2
DOI: https://doi.org/10.18721/JPM.161.314

Особенности низкочастотного шума и безызлучательной рекомбинации в MQW AlGaN/GaN, излучающих на длине волны 280 нм

Н.А. Тальнишних [1]✉, А.И. Иванов [1], Е.И. Шабунин [2], Н.М. Шмидт [2]

[1] НТЦ микроэлектроники РАН, Санкт-Петербург, Россия;
[2] Физико-технический институт им. А.Ф. Иоффе РАН, Санкт-Петербург, Россия
✉ nadya.fel@mail.ru

Аннотация. Экспериментально выявлен значительный источник потерь носителей заряда на безызлучательную рекомбинацию в AlGaN QWs, вызванный присутствием заряженных центров, локализованных на разупорядоченных гетеро границах. Выяснено, что спектральная плотность токового низкочастотного шума, несущая интегральную информацию о единичных дефектах и дефектной системе, на порядок выше в AlGaN QWs, чем в эффективных голубых InGaN/GaN QWs. Таким образом, потери на безызлучательную рекомбинацию по-прежнему являются источником, ответственным за низкую квантовую эффективность ультрафиолетовых светодиодов.

Ключевые слова: AlGaN/GaN, светодиоды, УФ светодиоды, внешняя квантовая эффективность, низкочастотный шум, безызлучательная рекомбинация, квантовые ямы

Ссылка при цитировании: Тальнишних Н.А., Иванов А.Е., Шабунина Е.И., Шмидт Н.М. Особенности низкочастотного шума и безызлучательной рекомбинации в MQW AlGaN/GaN, излучающих на длине волны 280 нм // Научно-технические ведомости

СПбГПУ. Физико-математические науки. 2023. Т. 16. № 1.3. С. 85–89. DOI: https://doi.org/10.18721/ JPM.161.314

Introduction

AlGaN QWs are the foundation for deep ultraviolet light-emitting diodes (DUV LEDs). DUV LEDs have been widely explored for their potential applications in a variety of areas including air/water purification, disinfection, bio-medical detection [1, 2]. However, as of today DUV LEDs still demonstrate low light output external quantum efficiency (*EQE*) < 10% and life time < 1500 hours [1–3]. The efficiency of AlGaN-based DUV LEDs is found to decrease drastically with decreasing emission wavelength. There are several factors that limit *EQE* values such as high dislocation density, insufficient carrier injection, and quantum confined Stark effect (QCSE) in MQWs. Some works also point out a number of contributions related to the epitaxial growth and chip fabrication technologies of DUV LEDs that have to be overcome [1]. The conductivity is limited not only by the increasing dopant ionization energy and formation of a stable DX center but also by the potential formation of cation vacancy defects VIII that are known to act as compensating acceptors in n-type AlN [3]. The latter issue derives mainly from the series of total internal reflections of photons at the interface between high-refraction epitaxial layers/substrate and the ambient medium [4]. It should be noted that the majority of works rarely consider the influence of the quality of hetero interfaces on the decrease in *EQE* at the maximum of DUV LEDs.

The studies carried out in this work were aimed at showing the contribution of non-radiative recombination of charge carriers in a system of defects and at the hetero interfaces to a decrease in *EQE* values at the maximum in DUV LEDs and assessing this contribution compared to more efficient blue InGaN/GaN LEDs. To achieve this, we employed the study of the low-frequency noise (LFN) alongside the conventional techniques. LFN is known to contain the integral information on the properties of extended defect system as well as single defects.

Materials and Methods

The study was carried out a comparative investigations on commercial DUV LEDs emitting at 278–280 nm whose *EQE* is about 4% and blue LEDs with 70% *EQE* emitting at 445 nm. Electroluminescence spectra and *EQE* dependences versus current density were examined at the direct current and in pulse mode (at pulse widths of 5 μs up to 2 A and 100 ns up to 20 A and repetition rates of 50 Hz) by OL 770-LED System (Optronic Laboratories Inc.) in integrated sphere. Optical power was determined by photodetector THORLABS DET02AFC/M. I-U characteristics were measured by the KEITHLEY 6487 power source. The noise spectra were measured within frequency range of 1 Hz to 50 kHz. The studied LEDs were connected in series with a low-noise load resistor R whose resistance varied from 100 Ω to 13.8 kΩ, depending on the current passing through the LEDs. The voltage fluctuations S_U at the resistors R were amplified by a low noise preamplifier SR 560 (Stanford Research Systems, Sunnyvale, CA, USA) and subsequently measured by an SR 770 FET NETWORK Analyzer (Stanford Research Systems, Sunnyvale, CA, USA). The background noise of the preamplifier did not exceed 4nV/√Hz at 1 kHz, which is approximately equivalent to the Johnson-Nyquist noise of a 1000-Ω resistance.

Results and Discussion

The maximum *IQE* in LEDs based on nitrides is determined by tunneling radiative recombination in MQW, located in the space charge region (SCR) around *p-n* junction [5, 6].

Thus, we considered the processes of non-radiative recombination (NR) at current values corresponding to the voltage range up to the *p-n* junction opening, i.e. up to threshold voltage (U_{th}). The U_{th} values were derived from forward *I-U* characteristics in DUV AlGaN and blue InGaN/GaN LEDs (Fig. 1).

Currents $I < 20$ mA correspond to this voltage range. Fig. 2, *a*, *b*) shows typical low-frequency noise spectra (i.e. dependences of power spectral density of current noise S_I versus frequency) in this current range for the same LEDs. The shape of the noise spectra is observed to be $S_I(f) \sim 1/f$ in the entire frequency range, which means the $1/f$ noise dominates at all currents (Fig. 2, *a*).

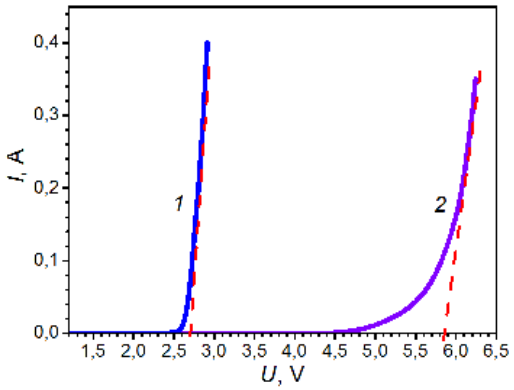

Fig. 1. Linear $I-U$ characteristics of InGaN/GaN (curve *1*) and AlGaN (curve *2*) LEDs

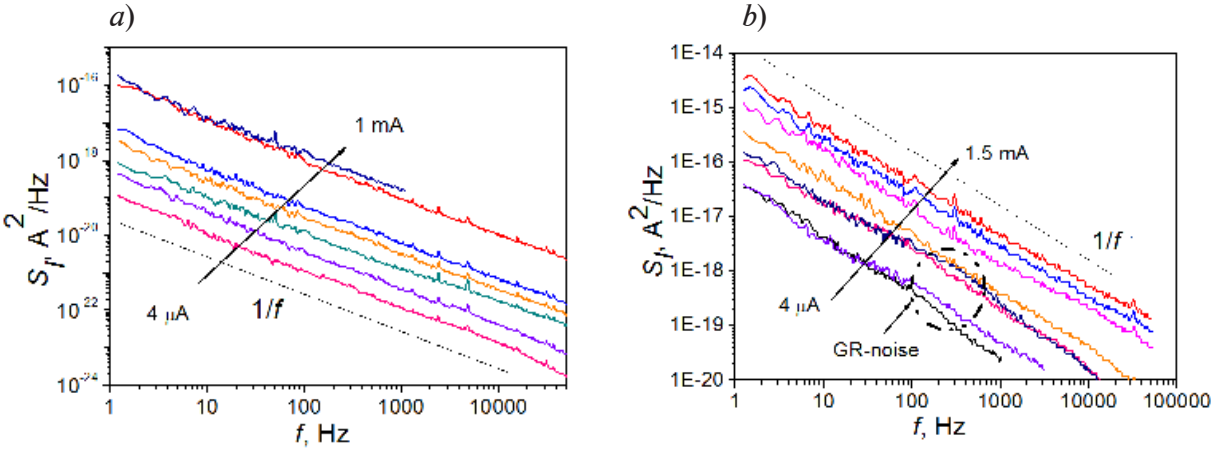

Fig. 2. Noise spectra in blue InGaN/GaN (*a*) and DUV AlGaN/GaN (*b*) LEDs

According to [7], this indicates the predominant contribution of the system of defects to NR in blue InGaN/GaN LEDs.

For the DUV LEDs, the values of spectral density of current fluctuations S_I is observed to be at least an order of magnitude higher than that in blue InGaN/GaN LEDs (Fig. 2, *b*). Moreover, the noise spectra of current fluctuations at high currents were close to the $1/f$ noise. However, the noise spectra at low currents were a superposition of the $1/f$ and generation-recombination (GR) noise caused by the presence of Shockley-Read-Hall (SRH) centers. The GR noise has a form of Lorentzian that typically doesn't depend on frequency at low frequencies and follows the law of $\sim 1/f^2$ at high frequencies. The contribution of GR noise to the spectra is shown in a deviation from the shape of $1/f$ noise at $f > 100$ Hz. In our case, however, the contribution of GR noise and, thus, SRH centers is insignificant because there is little change in the slope of the noise spectra (Fig. 2, *b*). Additionally, for both types of LEDs, the dependence of spectral density of voltage fluctuations (S_U) on the current deviates remarkably from the classic shape characterized by $S_U(j) \sim I^{-1}$ that, according to [8], is typical for semiconductor devices with uniform current distribution in SCR (Fig. 3). Thus, this deviation shows identifies the non-uniform current distribution in SCR for both types of LEDs. Moreover, the inhomogeneity of the current distribution is more prominent in DUV LEDs than that in blue LEDs (Fig. 3, curve *2*).

The obtained results correlate with peculiarities of I–U characteristics such as non-ideality factor n being significantly higher than 2 at $U < 5$ V, strong dependence of reverse current on U, and poor rectifying properties of p-n junction in DUV LEDs. (Fig. 4, curve *2*).

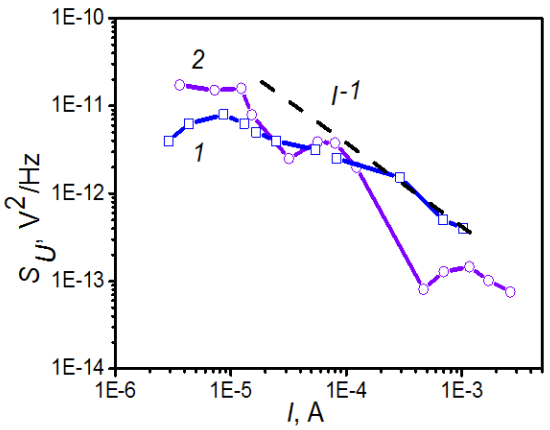

Fig. 3. Dependences of the spectral density of voltage fluctuations (S_U) on the current in InGaN/GaN (curve *1*) and AlGaN/GaN (curve *2*) LEDs

According to [9, 10], such peculiarities of I–U characteristics are related to the presence of charged centers in abrupt p-n junction. In our case, the presence of charged centers in SCR around p-n junction can be associated with imperfect hetero interfaces caused by random fluctuations in the AlGaN alloy composition, small thickness, less than 3 nm quantum wells, and Ga segregation.

The disordered hetero interface is indicated by the large difference (1.3 V) between U_{th} = 5.8 V (Fig. 1, curve *2*) and the voltage of 4.46 V corresponding to the emission wavelength of 280 nm. A similar difference in voltage values is observed in green InGaN/GaN LEDs with low EQE ~ 10%. Moreover, in these LEDs, the disordered of hetero interfaces caused by indium segregation was experimentally observed in [11].

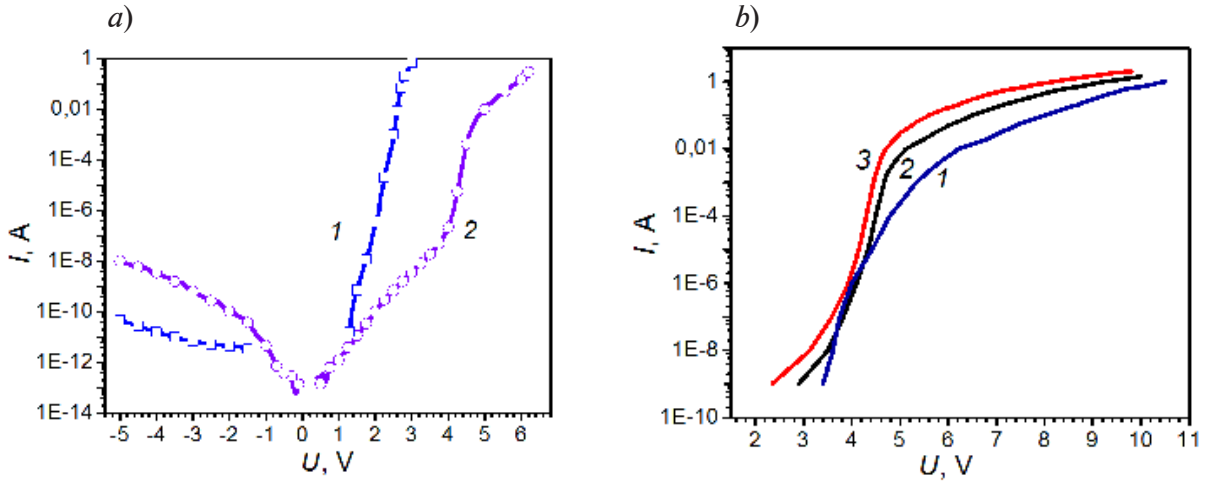

Fig. 4. I–U characteristics of blue (*1*) and DUV (*2*) LEDs (*a*); change in I–U characteristics of DUV LED over the temperature range (*b*): *1* – 200 K, *2* – 300 K, *3* – 350 K

At the same time, in effective blue LEDs, the difference in the values of these voltages is less than 0.1 V (Fig. 1, curve *1*). As a result, the charged centers localized at disordered hetero interfaces take part in NR and reduce EQE values at maximum in AlGaN QWs situated in SCR around p-n junction. To reduce these losses, it is necessary to avoid Ga segregation and to provide a step-flow growth mode during. The change in forward characteristics of DUV LEDs in the temperature range 200–350 K (Fig. 4, *b*) at $U < 5$ V differs significantly from that when single SRH centers determine NR mechanisms. It should be noted that the weak temperature dependence of forward I–U characteristics, tunneling transport of charge carriers and the a shape of the characteristics themselves at the temperature range 200 – 350 K are closest to the characteristics calculated for nitride-based LEDs by the multi-phonon-elastic trap assisted tunneling model. Thus, in addition to the loss of charge carriers on NR, the loss of charge carriers in multi-phonon emission is also possible.

Conclusion

A comparative investigation of low-frequency noise features and I–U characteristics in AlGaN and efficient blue InGaN QWs in commercially-available LEDs shows that the loss of charge

carriers in non-radiative recombination is much more prominent in AlGaN QWs. The sources of these losses are charged centers localized at disordered hetero-interfaces, a system of defects including donor-acceptor pairs, extended defects, local regions with a random fluctuations in AlGaN composition, and, to a lesser extent, single SRH centers. Thus, the losses due to non-radiative recombination are still responsible for the low quantum efficiency in ultraviolet LEDs. To increase the efficiency of DUV LEDs, it is necessary to improve the growth conditions of AlGaN alloy, to prevent the segregation of gallium at hetero-interfaces, and to ensure layer growth in the step-flow growth mode.

Acknowledgments

This work was carried out at the Center of Multi-User Facilities "Element Base of Microwave Photonics and Nanoelectronics: Technology, Diagnostics, and Metrology".

REFERENCES

1. **Lobo-Ploch N., Mehnke F., Sulmoni L., Cho H. K., Guttmann M., Glaab J., Hilbrich K., Einfeldt S., Kneissl M.,** Milliwatt power 233 nm AlGaN-based deep UV-LEDs on sapphire substrates, Applied Physics Letters. 117 (2020) 111102.

2. **Frankerl Ch., Hoffmann M. P., Nippert F., Wang H., Brandl Ch., Tillner N., Lugauer H.-J., Zeisel R., Hoffmann A., Davies M. J.,** Challenges for reliable internal quantum efficiency determination in AlGaN-based multi-quantum-well structures posed by carrier transport effects and morphology issues, Journal of Applied Physics. 126 (2019) 075703.

3. **Prozheev I., Mehnke F., Wernicke T., Kneissl M., Tuomisto F.,** Electrical compensation and cation vacancies in Alrich Si-doped AlGaN, Applied Physics Letters. 117 (2020) 142103.

4. **Liu X., Zhao S., Le B. H., Mi Z.,** Molecular beam epitaxial growth and characterization of AlN nanowall deep UV light emitting diodes, Applied Physics Letters. 111 (2017) 101103.

5. **Bochkareva N.I., Rebane Y.T., Shreter Y.G.,** Efficiency droop and incomplete carrier localization in InGaN/GaN quantum well light-emitting diodes, Applied Physics Letters. 103 (2013) 191101.

6. **Morgan T.N.,** Recombination by Tunneling in Electroluminescent Diodes, Physical Review. 148 (1966) 890–903.

7. **Zhigal'skii G.P.,** Non-equilibrium $1/f^{\gamma}$ noise in thin films and contacts (in Russian), Uspekhi Fizicheskikh Nauk 173 5 (2003) 465–490.

8. **Kleinpenning T.G.M.,** $1f$ Noise in p-n diodes, Physica B+C 98 4 (1980) 289–299.

9. **Steingrube S., Breitenstein O., Ramspeck K., Glunz S., Schenk A., Altermatt P.P.,** Explanation of commonly observed shunt currents in c-Si solar cells by means of recombination statistics beyond the Shockley-Read-Hall, Journal of Applied Physics. 110 (2011) 014515.

10. **Shmidt N.M., Chernyakov A.E., Tal`nishnih N.A., Nikolaev A.E., Sakharov A.V., Petrov V.N., Gushchina E.V., Shabunina E.I.,** The impact of the surface morphology on optical features of the green emitting InGaN/GaN multiple quantum wells, Journal of Crystal Growth. 520 (2019) 82–84.

11. **Mandurrino M., Goano M., Vallone M., Bertazzi F., Ghione G., Verzellesi G., Meneghini M., Meneghesso G., Zanoni E.,** Semiclassical simulation of trap-assisted tunneling in GaN-based light-emitting diodes, Journal of Computational Electronics. 14 (2015) 444–455.

THE AUTHORS

TALNISHNIKH Nadezhda A.
nadya.fel@mail.ru
ORCID: 0000-0003-1127-0973

SHABUNINA Evgeniia I.
jenni-85@mail.ru
ORCID: 0000-0003-4457-8149

IVANOV Anton E.
a-e-ivanov@yandex.ru
ORCID: 0000-0003-2819-1534

SHMIDT Natalia M.
natalia.shmidt@mail.ioffe.ru
ORCID: 0000-0003-3585-5116

Received 14.12.2022. Approved after reviewing 03.02.2023. Accepted 19.02.2023.

Conference materials
UDC 621.383
DOI: https://doi.org/10.18721/JPM.161.315

Study of photoconvertion heterojunction *n*-GaP/*p*-Si obtained by PE-ALD

S.Yu. Kiianitsyn [1,2], A.I. Baranov [2]✉, A.V. Uvarov [2],
A.A. Maksimova [2], E.A. Vyacheslavova [2], A.S. Gudovskikh [2]

[1] Saint Petersburg State Electrotechnical University "LETI", St Petersburg, Russia;
[2] Alferov University, St Petersburg, Russia
✉ baranov_art@spbau.ru

Abstract. Plasma-enhanced atomic layer deposition is an attractive method for producing *n*-GaP layers at low temperatures on *p*-Si wafers for further photovoltaic application of *n*-GaP/*p*-Si heterostructures. In this study, we explore the influence of growth conditions on the electrophysical quality of thin *n*-GaP layers. It was established from admittance spectroscopy and current-voltage characteristics that the activation energy of conductivity in GaP decreases from 0.08 eV to 0.04 eV, with an increase in phosphine flow during the phosphorous step, and a subsequent drop to an extremely low value (< 0.02 eV) when additional flow of silane was added. This leads to extreme improve photovoltaic performance of the ITO/*n*-GaP/*p*-Si sample due to suppression of inflection on the $I-V$ curve leading to an increase in the short-circuit current and the fill factor. Fruthermore, a deep level with the activation energies ranging from 0.50 to 0.55 eV and the capture cross-section $\sigma_T = (1–10)\cdot 10^{-16}$ cm^2 was detected in all layers.

Keywords: solar cell, GaP/Si heterojunction, admittance spectroscopy, atomic-layer deposition

Funding: The reported study was supported by the Russian Science Foundation under the grant number 21-79-10413, https://rscf.ru/project/21-79-10413/

Citation: Kiianitsyn K.S., Gudovskikh A.S., Uvarov A.V., Maksimova A.A., Vyacheslavova E.A., Baranov A.I., Study of photoconvertion heterojunction *n*-GaP/*p*-Si obtained by PE-ALD, St. Petersburg State Polytechnical University Journal. Physics and Mathematics. 16 (1.3) (2023) 90–95. DOI: https://doi.org/10.18721/JPM.161.315

Материалы конференции
УДК 621.383
DOI: https://doi.org/10.18721/JPM.161.315

Исследование фотопреобразовательных гетеропереходов *n*-GaP/*p*-Si, полученных методом PE-ALD

С.Ю. Кияницын [1,2], А.И. Б р нов [2]✉, А.В. Ув ров [2],
А.А. М ксимов [2], Е.А. Вячесл вов [2], А.С. Гудовских [2]

[1] Санкт-Петербургский электротехнический университет «ЛЭТИ", Санкт-Петербург, Россия;
[2] Академический университет им. Ж.И. Алфёрова, Санкт-Петербург, Россия
✉ baranov_art@spbau.ru

Аннотация. Атомно-слоевое плазменно-стимулированное осаждение является одним из перспективных методов для формирование *n*-GaP слоев при низких температурах на подложках *p*-Si для последующего использования в качестве фотопреобразовательных структур гетероперехода *n*-GaP/*p*-Si. В данной работе, было исследовано влияние остовых параметров на электрофизические свойства *n*-GaP. Согласно измерениям

спектроскопии полной проводимости и вольт-амперных характеристик показано, что энергия активации проводимости в GaP слое уменьшается с 0.08 эВ до 0.04 эВ с увеличением потока фосфина и времени его взаимодействия с подложкой во время шага осаждения фосфора, а при добавлении дополнительного потока силана на шаге осаждения фосфора она значительно уменьшается и становится меньше 0.02 эВ. Это приводит к значительному улучшению производительности солнечного элемента ITO/*n*-GaP/*p*-Si вследствие уменьшения перегиба на ВАХ, что приводит к увеличению тока короткого замыкания и фактора заполнения. Кроме того, во всех образцах был обнаружен глубокий дефектный уровень с энергией активации E_a = 0.50–0.55 eV и сечением захвата $\sigma_T = (1–10)\cdot10^{-16}$ cm^2.

Ключевые слова: солнечный элемент, GaP/Si гетеропереход, спектроскопия полной проводимости, атомно-слоевое осаждение

Финансирование: Представленные в работе исследования выполнены за счет гранта Российского научного фонда (проект № 21-79-10413, https://rscf.ru/project/21-79-10413/).

Ссылка при цитировании: Кияницын С.Ю., Гудовских А.С., Уваров А.В., Максимова А.А., Вячеславова Е.А., Баранов А.И. Исследование фотопреобразовательных гетеропереходов *n*-GaP/*p*-Si, полученных методом PE-ALD // Научно-технические ведомости СПбГПУ. Физико-математические науки. 2023. Т. 16. № 1.3. С. 90–95. DOI: https://doi.org/10.18721/ JPM.161.315

Introduction

GaP is one of the promising materials for double-junction solar cells on silicon wafers [1] since the lattice mismatch between Si and GaP is less than 0.4%, and adding nitrogen to GaP will make it possible to vary the band gap of GaP(N) in the wide range from 1.7 eV to 2.1 eV [2]. Recently, an interesting method of plasma-enhanced atomic-layer deposition (PE-ALD) at temperatures below 400 °C was demonstrated for obtaining thin layers of GaP on *p*-Si wafers [3]. This technology is based on alternative interaction of phosphorous and gallium precursors with silicon surface in PECVD chamber. The main advantage of this method is that the film growth is based on the self-limiting mechanism, i.e., it is impossible to deposit more than one monolayer in one cycle, which ensures high uniformity and conformity of the film thickness. Previously, the fundamental possibility of donor doping of a GaP film grown by the PE-ALD method with the additional silane flow was shown [4], but direct influence of silane flow on quality of doping have not been shown yet. However, this process includes argon treatment leading to the formation of defects with a high concentration in bulk silicon wafers [5]. In addition, high power of hydrogen plasma also leads to defect formation in near interface area in silicon [6]. Therefore, a more complicated growth process should be used to obtain silicon incorporation for *n*-type doping of GaP layers without deterioration of bulk properties of wafers, and direct influence of silane flow on doping will be studied here.

Materials and Methods

In this study, three different GaP layers with thickness of 10–20 nm were grown using an Oxford Instruments PlasmaLab System 100 PECVD (13.56 MHz) setup on boron-doped silicon (100) wafers ($p = 1\cdot10^{16}$ cm^{-3}) in PE-ALD mode. The main parameters were the same as in [7] except for the steps described in Table 1: lower PH_3 flux in OX856 than in OX860, and additional silane flow of 10 sccm in OX858. Indium tin oxide (ITO) layers were deposited by magnetron sputtering in first series of samples for photovoltaic measurements. Further, silver paste was applied to ITO for fabrication of metallic top contact, and bottom ohmic contact to *p*-Si was formed by indium. On the other hand, gold was evaporated in BOC Edwards Auto500 setup through a hard mask in the form of a circle with a diameter of 1 mm. Then, these samples were etched in wet solution H_2SO_4:H_2O_2 = 3:1 down to silicon wafer: in result, GaP/Si heterojunction

remained only under gold circle. Finally, ohmic contact by indium was formed to bottom side. This series were explored by capacitance methods to probe only heterojunction *n*-GaP/*p*-Si without contribution of additional barrier ITO/*n*-GaP.

Current–voltage characteristics were measured at 25 °C using a Keithley 2400 source-meter under AM1.5G illumination provided by a SunLiteTM Solar Simulator from ABET Technologies. Admittance spectroscopy (AS) [8] measurements were performed using a precision E4980A-001 Keysight (former Agilent) LCR-meter in frequency range with test voltage amplitude of 50 mV from 20 Hz to 2 MHz in helium cryostat Janis CCS-400H/204 from 12 to 800 K.

Table 1

Different parameters of PE-ALD processes of GaP layers

Sample	Pre-PH_3 step					PH_3 step		
	t, s	PH_3, sccm	Ar, sccm	H, sccm	SiH_4, sccm	*t*, s	PH_3, sccm	H, sccm
OX856	3	30	50	200	0	3	10	200
OX860	4	40			0		20	
OX858	4	40			10		20	

Results and Discussion

Current-voltage characteristics of ITO/*n*-GaP/*p*-Si samples under AM1.5G illumination are presented in Fig. 1.

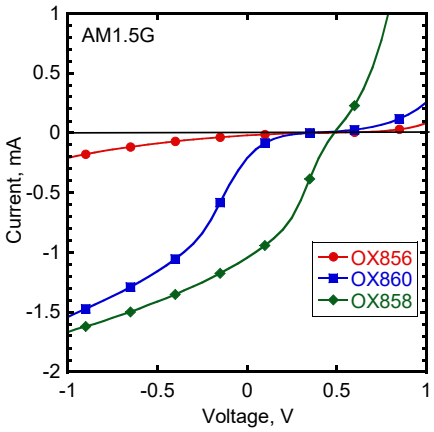

Fig. 1. Current-voltage characteristics of ITO/*n*-GaP/*p*-Si samples under AM1.5G illumination

All *I–V* curves exhibit a knee near the open circuit voltage, which leads to significant decrease of fill factor (*FF*) and even short circuit current (I_{sc}). The most pronounced drop of *FF* is observed for OX856, a medium one for OX860, and the weakest is for OX858. A possible reason explaining such behavior lies in the differences in conductivity of the GaP layer due to the growth parameters. A similar knee in the *I–V* curve could be observed for non-sufficient HIT solar cells based on a *p*-*a*-Si:H/*i*-*a*-Si:H/*n*-*c*-Si heterojunction when *p*-layer is not enough doped leading to parasitic barrier in structure and decrease of *FF*. Here, the shape of the *I–V* curve is dramatically improved when PH_3 flow increases for OX860 in both stages (Table 1), and silane flow also reduces the inflection of the *I-V* curve leading to a greatly increasing Isc. Therefore, the parameters of the PH_3 step in PE-ALD mode have a critical influence on the quality of conductivity in *n*-GaP.

Initially, gold was evaporated to these GaP layers grown on *n*-Si ($n = 1 \cdot 10^{16}$ cm^{-3}) wafers to form structure with Schottky diodes to explore their defect properties. However, classical rectifying behavior is not observed due to extremely high conductivity between contacts. In this case, structures Au/*n*-GaP/*p*-Si were explored by capacitance methods since gold does not form a potential barrier on Au/*n*-GaP and does not lead to contribution in total capacitance of samples. It is also confirmed by measurements of capacitance-voltage characteristics (not presented here) for all samples for 100 kHz, and estimated concentration from $1/C^2$ corresponds to the doping level in silicon wafers.

Admittance spectroscopy were performed in the temperature range from 60 to 400 K for different applied voltage bias. The *C–f* curves for different temperatures for $V_{DC} = 0$ V and +0.8 V are presented in Fig. 2. The admittance spectroscopy is based on the measurement of the capacitance and conductance of *p–n* junctions using a small signal alternating voltage at different

frequencies and at various temperatures. If the Fermi level (or quasi Fermi level) crosses the defect level in the space charge region, we may detect an additional contribution to the capacitance. This leads to a step-like behavior in the capacitance versus frequency as in *C–f* in Fig. 2.

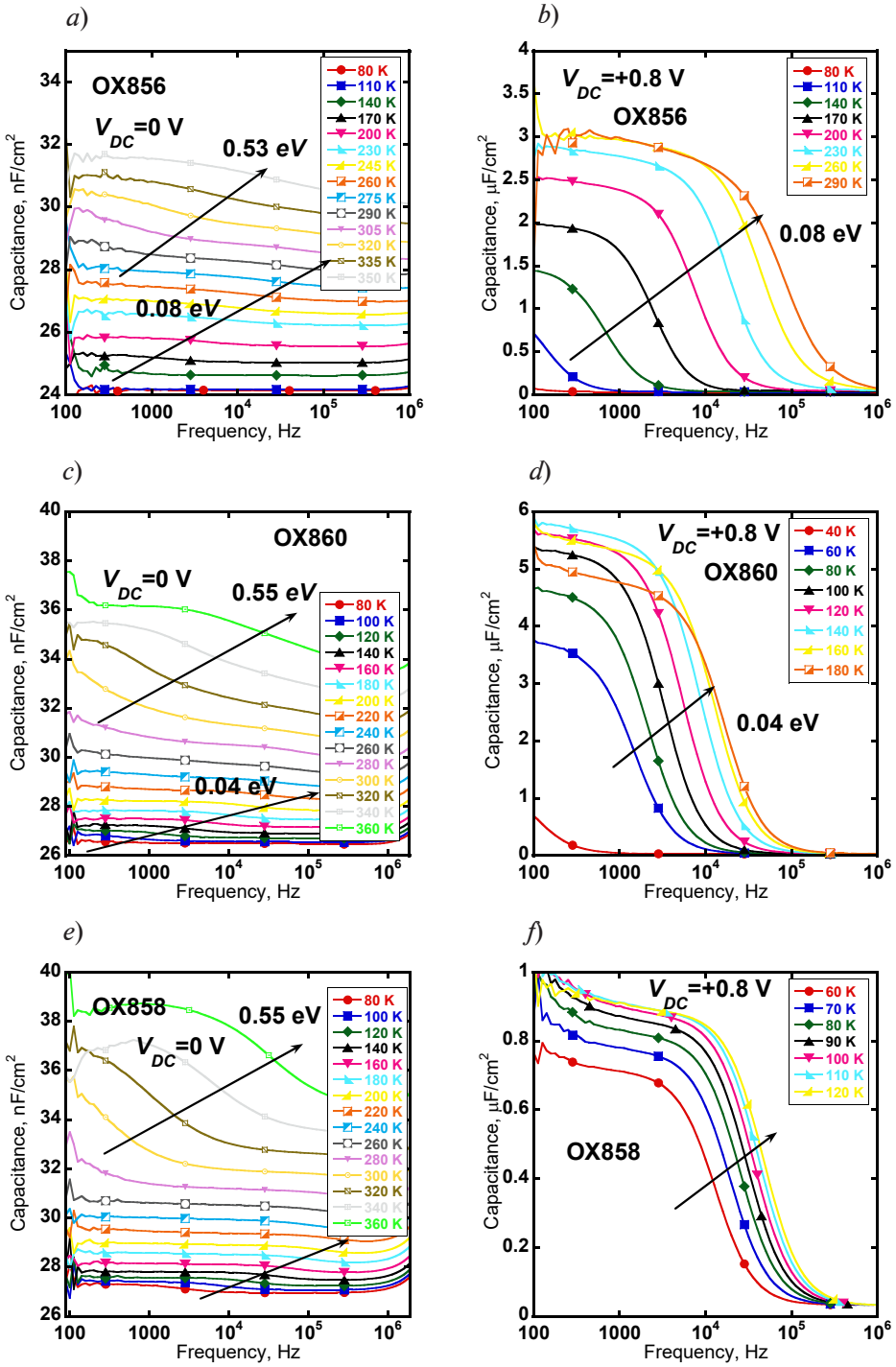

Fig. 2. *C–f* curves for different temperatures for V_{DC} = 0 V (*a*, *c*, e) and V_{DC} = +0.8 V (*b*, *d*, *f*)

A similar behavior of the curves is observed for all samples at $V_{DC} = 0$ V (left panels in Fig. 2). A first step on the $C–f$ curve can be seen at low temperatures of 80–240 K and a second one at higher temperatures, 300–360 K (the sequence of steps is indicated by arrows). As shown, the position of the turn-on frequency (f where $-f \cdot dC/df$ has maxima) shifts toward higher frequencies with a temperature increase, allowing to obtain the Arrhenius plot and estimate the parameters of the defect, activation energy E_a and the capture cross section σ_T.

Parameters of high-temperature responses (300–360 K) are almost the same for all samples since the position of the turn-on frequency is similar for the same temperature, amounting to $E_a = 0.50–0.55$ eV and $\sigma_T = (1–10) \cdot 10^{-16}$ cm^2. The parameters do not depend on the process conditions so the differences in the $I–V$ curves can hardly be explained by its influence. Furthermore, a similar defect was detected by DLTS in our previous work where it was associated with a deep defect level in GaP layer, but its nature is still unclear.

In contrary, the parameters of low temperature response depend on the deposition conditions. Low temperature feature is characterized by low values of σ_T ($1 \cdot 10^{-20}$ cm^2) and E_a being equal to 0.08 eV and 0.04 eV for OX856 and OX860, respectively. For OX858 E_a is too low to be estimated ($E_a < 0.02$ eV). Thus, the highest value of E_a is observed in OX856, then increasing of phosphine flow leading to decreasing of Ea in OX860, and the lowest one is in OX858 with additional flow of silane. The $C–f$ curves were also measured at $V_{DC} = +0.8$ V (Fig. 2, *b*, *d*, *f*) to prove the difference in E_a for the samples. In this case, in addition to the capacitance of space charge (which is closer to the GaP layers) a diffusion capacitance should dominate in the total capacitance. The absolute value of the capacitance at low frequency is much higher compared to that at 0 V being typical for diffusion capacitance. However, high amplitude steps are detected for all samples, and their responses correspond well to the low temperature response observed at 0 V with the same values of E_a. In fact, if we consider the equivalent circuit the space charge capacitance is connect in parallel to diffusion capacitance, i.e. contribution of each should be presented in the equivalent capacitance. Only the contribution of series capacitance could provide such high amplitude steps. When series capacitance is much lower compared to diffusion capacitance the total capacitance is determined by series capacitance. If the series capacitance is shunted by conductivity, for example due to temperature activation, the total capacitance is determined by diffusion capacitance. Similar behavior has already observed for *a*-Si:H/*c*-Si heterojunctions [9]. An activation of the conductivity of doped *a*-Si:H layer leads to appearance of low temperature response in the admittance spectra. An activation of GaP conductivity could explain the observed behavior of the admittance spectra at +0.8 V as well as dependence of the E_a on deposition conditions. Also it is in good correlation with our suggestion from $I–V$ curves: lower E_a leads to better conductivity in GaP with silane flow. Therefore, detected response is related to conductivity of GaP layers, and it can be controlled in future experiments.

Conclusion

Plasma-enhanced atomic layer deposition is attractive method for formation of *n*-GaP layers on *p*-Si wafer for further photovoltaic application. Here, we explore influence of growth conditions on electrophysical quality of thin *n*-GaP layers. Admittance spectroscopy and current-voltage characteristics were used to establish a decrease in the activation energy of conductivity in GaP with increasing phosphine flow during the phosphorous step from 0.08 eV to 0.04 eV, with a subsequent drop to extremely low values when additional flow of silane was added. This serves to greatly improve the photovoltaic performance of ITO/*n*-GaP/*p*-Si sample. Moreover, a deep level with $E_a = 0.50–0.55$ eV and $\sigma_T = (1–10) \cdot 10^{-16}$ cm^2 was detected in all layers.

Acknowledgments

The study was supported by the Russian Science Foundation grant 21-79-10413, https://rscf.ru/project/21-79-10413/

REFERENCES

1. **Meillaud F., Shah A., Droz C., Vallat E.,** Efficiency limits for single-junction and tandem solar cells, Sol. Energy Mater. Sol. Cells. 2006. 90 (18–19). P. 2952–2959.

2. **Geisz J.F., Friedman D.J.,** III-N-V semiconductors for solar photovoltaic applications, Semicond. Sci. Technol. 17 (8) (2002) 769–777.

3. **Gudovskikh A.S., Uvarov A. V., Morozov I., Baranov A.I.,** Si doped GaP layers grown on Si wafers by low temperature PE-ALD, J. Renew. Sustain. Energy. 10 (2) (2018) 021001.

4. **Baranov A.I., Morozov I., Uvarov A. V., Yakovlev G.,** Silicon doping of GaP layers grown by time-modulated PECVD, Journal of Physics: Conference Series. 1124 (2018) 041036.

5. **Baranov A.I., Morozov I., Uvarov A.V., Kudryashov D.,** Influence of plasma on electrophysical properties of the GaP/n-Si isotype heterojunction grown by PE-ALD, J. Phys. Conf. Ser. 1482 (2020) 012017.

6. **Gudovskikh A.S., Uvarov A. V., Morozov I., Baranov A.I.,** Interface Properties of GaP/Si Heterojunction Fabricated by PE-ALD, Phys. Status Solidi Appl. Mater. Sci. 216 (10) (2018) 1800617.

7. **Uvarov A.V., Gudovskikh A.S., Baranov A.I., Nevedomsky V.,** Low temperature epitaxial growth of GaP on Si by atomic-layer deposition with plasma activation, J. Phys. D. Appl. Phys. Vol. 53 (34) (2020) 345105.

8. **Losee D.L.,** Admittance spectroscopy of impurity levels in Schottky barriers, J. Appl. Phys. 46 (5) (1975) 2204–2214.

9. **Gudovskikh A.S., Kleider J.P., Terukov E.I.,** Characterization of an a-Si:H/c-Si interface by admittance spectroscopy, Semiconductors Vol. 39 (2005) 904–909.

THE AUTHORS

KIIANITSYN Sergey Yu.
serg-kianitsyn@mail.ru
ORCID: нет

MAKSIMOVA Alina A.
deer.blackgreen@yandex.ru
ORCID: 0000-0002-3503-7458

BARANOV Artem I.
itiomchik@yandex.ru
ORCID: 0000-0002-4894-6503

VYACHESLAVOVA Ekaterina A.
cate.viacheslavova@yandex.ru
ORCID: 0000-0001-6869-1213

UVAROV Alexander V.
lumenlight@mail.ru
ORCID: 0000-0002-0061-6687

GUDOVSKIKH Alexander S.
gudovskikh@spbau.ru
ORCID: 0000-0002-7632-3194

Received 14.12.2022. Approved after reviewing 01.02.2023. Accepted 09.02.2023.

Quantum wires, quantum dots, and other low-dimensional systems

Conference materials
UDC 538.975
DOI: https://doi.org/10.18721/JPM.161.316

Modeling of interfacial profile of axial GaAs/AlAs nanowire heterostructures

E. D. Leshchenko [1]✉, V. G. Dubrovskii [2]

[1] Submicron Heterostructures for Microelectronics, Research & Engineering Center, RAS, St. Petersburg, Russia;
[2] St. Petersburg State University, St. Petersburg, Russia
✉ leshchenko.spb@gmail.com

Abstract. We describe the formation of axial GaAs/AlAs heterostructured nanowires grown via the vapor-liquid-solid method. The calculations are based on the combination of mass balance of atoms in the droplet and the nucleation-limited composition of ternary $Al_xGa_{1-x}As$ nanowires. We examine the influence of growth temperature, atomic Al flux and the Au concentration in the liquid on the interfacial abruptness. In particular, we compare the compositional profiles of heterostructures in Au-catalyzed and self-catalyzed nanowires. The obtained results might be useful for growth of GaAs/AlAs heterostructured nanowires.

Keywords: interfacial profile, axial heterostructures, AlGaAs, nanowires, modeling

Funding: VGD gratefully acknowledges financial support of St. Petersburg State University under the research grant No. 93020138.

Citation: Leshchenko E.D., Dubrovskii V.G., Modeling of interfacial profile of axial GaAs/AlAs nanowire heterostructures, St. Petersburg State Polytechnical University Journal. Physics and Mathematics. 16 (1.3) (2023) 96–100. DOI: https://doi.org/10.18721/JPM.161.316

Материалы конференции
УДК 538.975
DOI: https://doi.org/10.18721/JPM.161.316

Моделирование профиля состава осевой гетероструктуры GaAs/AlAs в нитевидных нанокристаллах

Е.Д. Лещенко [1]✉, В.Г. Дубровский [2]

[1] НТЦ микроэлектроники РАН, Санкт-Петербург, Россия
[2] Санкт-Петербургский государственный университет, Санкт-Петербург, Россия
✉ leshchenko.spb@gmail.com

Аннотация. Проведено теоретическое исследование формирования осевой гетероструктуры GaAs/AlAs в нитевидных нанокристаллах, выращенных по механизму пар-жидкость-кристалл. В основе модели лежит материальный баланс в капле, где встраивание атомов в нитевидный нанокристалл лимитировано нуклеацией. Изучено влияние температуры роста, потока алюминия и концентрации золота в капле на резкость гетероперехода. В частности, мы сравниваем профили состава гетероструктурных авто-каталитических и Au-каталитических нитевидных нанокристаллов. Полученные результаты могут быть полезны при росте осевых гетеростуктур GaAs/AlAs в нитевидных нанокристаллах.

Ключевые слова: профиль состава, осевые гетероструктуры, AlGaAs, нитевидные нанокристаллы, моделирование

Финансирование: ВГД благодарит исследовательский грант СПбГУ (ID 93020138) за финансовую поддержку аналитических исследований.

Ссылка при цитировании: Лещенко Е.Д., Дубровский В.Г. Моделирование профиля состава осевой гетероструктуры GaAs/AlAs в нитевидных нанокристаллах // Научно-технические ведомости СПбГПУ. Физико-математические науки. 2023. Т. 16. № 1.3. С. 96–100. DOI: https://doi.org/10.18721/ JPM.161.316

Introduction

Semiconductor nanowire heterostructures are one of the most promising nanoscale objects whose properties have attracted much attention from researchers [1]. Axial nanowire heterostructures are usually produced by the so-called vapor-liquid-solid mechanism [2]. A combination of binary compounds provides advanced functionality. Consequently, a wide range of devices based on nanowire heterostructures have been developed, including electronic, photonic and thermoelectric applications [3]. One of the key features of heterostructured nanowires is the heterointerface which determines the quality of optoelectronic applications. Ideally, such nanostructures should be grown with atomic precision which is impossible without understanding the formation mechanism. A particular factor limiting interfacial abruptness is the reservoir effect [4]. Thus, modeling the growth of heterostructured nanowires is of paramount importance. Recent studies [5, 6] have reported on an analytical approach to describing the compositional profiles of axial heterostructures in Au-catalyzed and self-catalyzed nanowires. In this study, we apply our model to a GaAs/AlAs heterojunction and examine the influence of growth temperature, atomic flux of Al and concentration of Au on the interfacial abruptness of heterostructured nanowires grown via the vapor-liquid-solid (VLS) mechanism.

Materials and Methods

Within the model, we consider VLS growth of an axial nanowire heterostructure from a droplet which initially contains Ga, As, and Au elements (in the case of self-catalyzed growth the Au concentration equals zero). Then we vary the vapor phase composition introducing the flux of Al which makes the droplet quaternary. As a result, an $Al_xGa_{1-x}As$ ternary solid solution forms. It has been shown [6] that the compositional profile across an axial heterostructure can be found from

$$\frac{d\xi}{dx} = \frac{1}{g}\frac{1}{a-x}\frac{dy}{dx}c_{tot}. \quad (1)$$

Here ξ is the axial coordinate across the heterointerface, x is the content of AlAs pairs in the solid, g is the geometrical coefficient, $c_{tot} \approx 1 - c_{\mathrm{Au}}$ is the total concentration of group III elements, a is the dimensionless influx of Al, $y = c_{\mathrm{Al}} / (c_{\mathrm{Al}} + c_{\mathrm{Ga}})$ is the liquid composition, c_{Al}, c_{Ga}, c_{As} and c_{Au} are the concentrations of Al, Ga, As and Au in the droplet, respectively. Eq. (1) is solved by introducing an mechanism to incorporate atoms into the solid, which determines the liquid-solid composition dependence. In our case, we consider the nucleation-limited growth regime which can be applied if supersaturation is low. Then the liquid-solid composition dependence can be written as [7]

$$y = \frac{1}{1 + \frac{1-x}{x} e^{2\omega_{\mathrm{AlAs\text{-}GaAs}}(x-1/2)+b}}. \quad (2)$$

Here $\omega_{\mathrm{AlAs\text{-}GaAs}}$ is the pseudobinary interaction parameter in the solid and b is a coefficient depending on the As, Ga, Al and Au concentrations in the droplet, the chemical potential differences for the pure components and the interaction parameters in the liquid. All details can be found in [7].

Results and Discussion

We start to investigate the formation of GaAs/AlAs heterostructured nanowires with analysis of the interfacial profile $x(\xi)$ for different growth temperatures. The values of binary and ternary interaction parameters and Gibbs free energies can be found in [7]. Fig. 1 shows the compositional profile of a GaAs/AlAs nanowire heterostructure at a fixed $c_{Au} = 0$ (self-catalyzed growth), $a = 2$, $g = 0.001$ and $c_{As} = 0.01$. Within the nucleation-limited regime, the compositional control of $Al_xGa_{1-x}As$ nanowires over the entire range is possible at all presented growth temperatures which can be explained by the fact that the AlAs-GaAs pseudobinary interaction parameter has a low enough value. It is seen that the slope of the GaAs/AlAs heterojunction at small and high solid compositions is different (a steep slope at $x < 0.8$ which means that the solid composition changes rapidly with the axial coordinate across the heterointerface (less than 10 monolayers) and a long tail at $x > 0.8$ meaning that a large number of ternary monolayers (~70 monolayers) is needed to achieve the pure AlAs binary). The shape of the $x(\xi)$ curves can be explained by the shape of the liquid-solid composition dependence: a small addition of Al atoms to the droplet leads to a tremendous increase of the Al concentration in the ternary nanowire, except the range of high AlAs content in the solid. Increasing the temperature broadens the heterointerface.

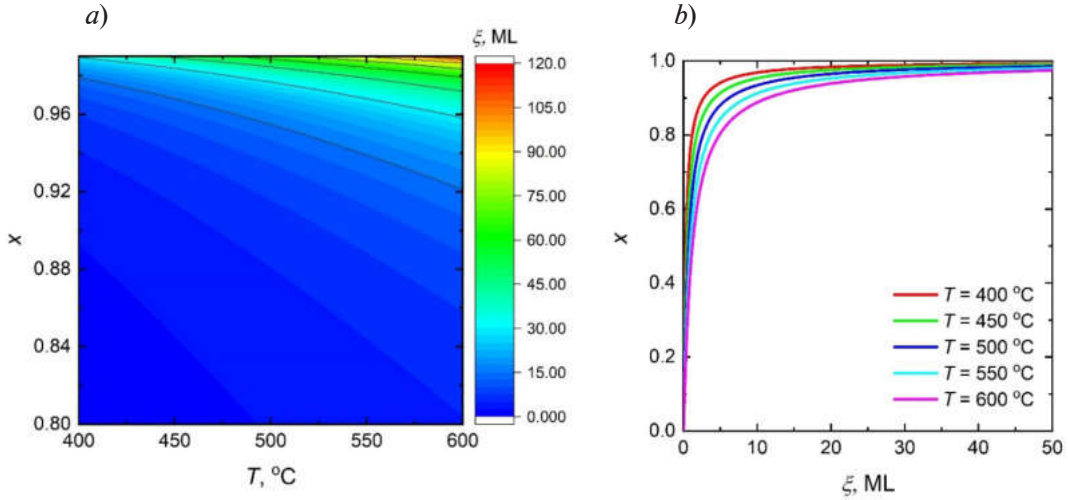

Fig. 1. Contour plot of the GaAs content x in the GaAs/AlAs NW heterostructure NW versus distance ξ and temperature T (*a*); composition profiles $x(\xi)$ across the GaAs/AlAs NW heterostructures at different temperatures T (*b*).

The temperatures T are given in the inset to Fig. 1, *b*. The distance along the nanowire is measured in monolayers (MLs)

Next, we analyze the influence of the concentrations of the foreign catalyst (for the particular case of Au) on the interfacial abruptness of GaAs/AlAs heterostructures. It should be noted that such analysis makes it possible to compare Au-catalyzed and self-catalyzed growth of heterostructured nanowires. The contour plot for variation of the distance ξ with AlAs content x and Au concentration c_{Au} in the GaAs/AlAs nanowire heterostructure and the $x(\xi)$ dependence calculated for different Au concentrations at a fixed $c_{As} = 0.01$, $T = 610$ °C, $a = 2$ and $g = 0.001$ are presented in Fig. 2. Such high temperature might be relevant for GaAs/AlAs heterostructured nanowires [8]. Within the considered range of Au concentrations ($0 < c_{Au} < 0.4$), increasing the Au concentration broadens the heterointerface. However, a heterointerface might be sharper in the case of Au-catalyzed growth as compared to the case of self-catalyzed growth if Au concentration is very high. This is due to the non-monotonic behavior of interfacial abruptness with varying Au concentration. Roughly the same number of monolayers is needed to obtain pure AlAs regardless of Au concentration.

Finally, let us consider the effect of the dimensionless atomic flux on the compositional profile of axial GaAs/AlAs nanowire heterostructures. Fig. 3 shows the contour plot for variation of the distance ξ with AlAs content x and dimensionless atomic flux a in the GaAs/AlAs nanowire heterostructure and the $x(\xi)$ dependence calculated for different dimensionless atomic fluxes at fixed $c_{As} = 0.01$, $T = 610$ °C, $c_{Au} = 0$ and $g = 0.001$. Lower atomic fluxes a result in broader GaAs/AlAs heterointerfaces. This effect is especially crucial when a tends to 1.

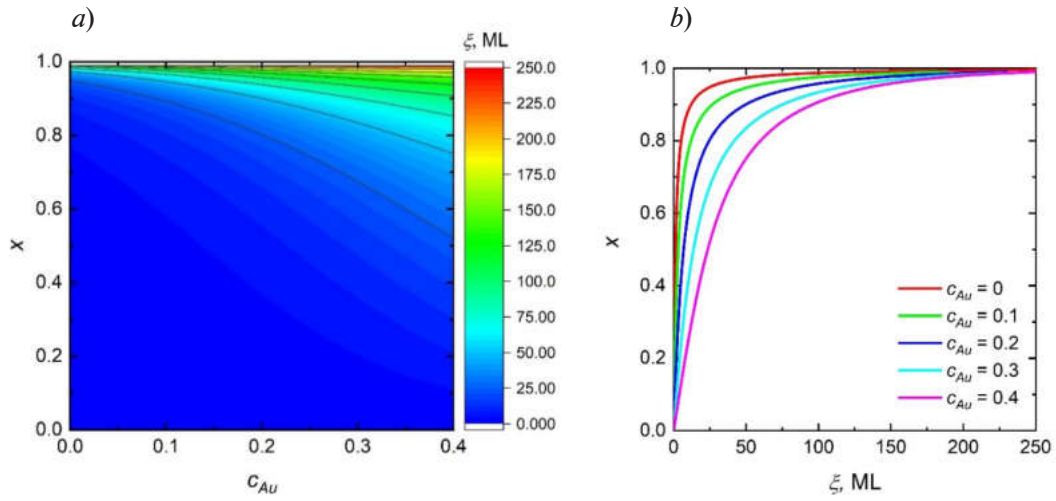

Fig. 2. Contour plot of the GaAs content x in the GaAs/AlAs NW heterostructure NW versus distance ξ and Au concentration c_{Au} (*a*);composition profiles $x(\xi)$ across the GaAs/AlAs NW heterostructures at different Au concentrations c_{Au} in the droplet (*b*).
The concentrations c_{Au} are given in the inset to Fig. 2, *b*

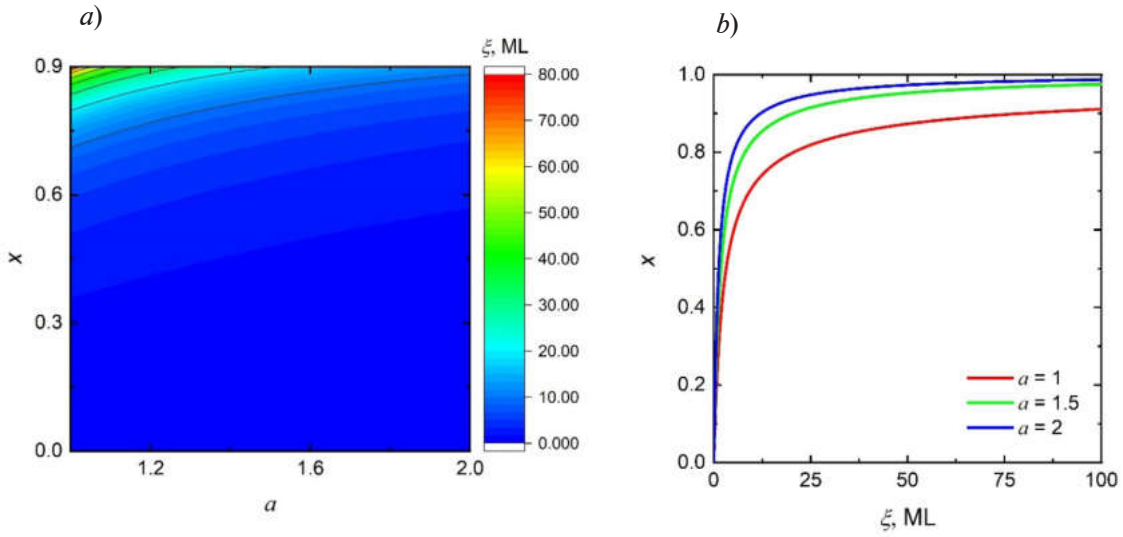

Fig. 3. Contour plot of the GaAs content *x* in the InAs/GaAs NW heterostructure NW versus distance ξ and dimensionless atomic flux *a* (*a*); composition profiles $x(\xi)$ across the GaAs/AlAs NW heterostructures at different dimensionless atomic fluxes *a* (*b*).
The dimensionless atomic fluxes a are given in the inset to Fig. 3, *b*

Conclusion

To summarize, we have calculated the interfacial profiles of axial GaAs/AlAs heterostructures in self-catalyzed and Au-catalyzed nanowires grown in the nucleation-limited regime. Special attention is paid to the influence of the concentrations of the foreign catalyst (on the example of gold), temperature and atomic flux on the interfacial abruptness of GaAs/AlAs heterostructures. Our findings confirm that decreasing the growth temperature and Au concentration and increasing the atomic flux can improve the interface abruptness of the GaAs/AlAs heterojunction. The obtained results may be useful for growth of GaAs/AlAs heterostructured nanowires.

Acknowledgments

VGD gratefully acknowledges financial support of St. Petersburg State University under the research grant No. 93020138.

REFERENCES

1. **Johansson J., Dick K.A.,** Recent advances in semiconductor nanowire heterostructures, CrystEngComm. 13(24) (2011) 7175.

2. **Wagner R.S., Ellis W.C.,** Vapor-Liquid-Solid Mechanism of Single Crystal Growth, Applied Physics Letters. 4(5) (1964) 89–90.

3. **Lauhon L.J., Gudiksen M.S., Lieber C.M.,** Semiconductor nanowire heterostructures, Philos Trans A Math Phys Eng Sci. 362(1819) (2004) 1247–60.

4. **Li N., Tan T.Y., Gösele U.,** Transition region width of nanowire hetero- and pn-junctions grown using vapor–liquid–solid processes, Applied Physics A. 90(4) (2008) 591–596.

5. **Dubrovskii V.G., Koryakin A.A., Sibirev N.V.,** Understanding the composition of ternary III-V nanowires and axial nanowire heterostructures in nucleation-limited regime, Materials & Design. 132 (2017) 400–408.

6. **Leshchenko E.D., Johansson J.,** Interfacial profile of axial nanowire heterostructures in the nucleation limited regime, CrystEngComm. (2022).

7. **Leshchenko E.D., Ghasemi M., Dubrovskii V.G., Johansson J.,** Nucleation-limited composition of ternary III–V nanowires forming from quaternary gold based liquid alloys, CrystEngComm. 20(12) (2018) 1649–1655.

8. **Priante G., Glas F., Patriarche G., Pantzas K., Oehler F., Harmand J.-C.,** Sharpening the Interfaces of Axial Heterostructures in Self-Catalyzed AlGaAs Nanowires: Experiment and Theory, Nano Letters. 16(3) (2016) 1917–1924.

THE AUTHORS

LESHCHENKO Egor D.
leshchenko.spb@gmail.com
ORCID: 0000-0002-2158-9489

DUBROVSKII Vladimir G.
dubrovskii.ioffe@mail.ru
ORCID: 0000-0003-2088-7158

Received 11.12.2022. Approved after reviewing 27.01.2023. Accepted 31.01.2023.

Conference materials
UDC 535.3
DOI: https://doi.org/10.18721/JPM/161.317

Interband photoluminescence of InAs(P)/Si nanowires

R.V. Ustimenko [1]✉, M.Ya. Vinnichenko [1], D.A. Karaulov [1], D.A. Firsov [1], V.V. Fedorov [1,2], A.M. Mozharov [2], D.A. Kirilenko [3,4], I.S. Mukhin [1,2]

[1] Peter the Great St. Petersburg Polytechnic University, St. Petersburg, Russia;
[2] Alferov University, St. Petersburg, Russia;
[3] ITMO University, St. Petersburg, Russia;
[4] Ioffe Institute, St. Petersburg, Russia;
✉ ratmirustimenko@yandex.ru

Abstract: Semiconductor nanowires have a number of advantages over thin films and bulk analogues, which allow them to be used to develop efficient detectors and light sources. In this work, photoluminescence spectra of pure InAs and core-shell InAs/CaF_2 and InAs/InP nanowires on silicon were studied in the near infrared spectral range at various levels of optical pumping and at different temperatures using a vacuum Fourier spectrometer operating in a step-scan mode. The observed peaks in the photoluminescence spectra correspond to interband transitions in InAs of sphalerite and wurtzite phases. The photoluminescence spectra of CaF_2-coated InAs nanowires demonstrated that surface passivation with CaF_2 does not change the spectral features. It was shown that the absolute value of photoluminescence intensity of InAs-core/InP-shell nanowires exceeds the intensity of pure InAs nanowires. It means that surface passivation can reduce an effect of surface states in nanowires on their optical properties.

Keywords: nanowires, passivation, photoluminescence, core/shell nanowires

Funding: This work was supported by the Russian Science Foundation (grant № 22-19-00494, https://rscf.ru/en/project/22-19-00494/).

Citation: Ustimenko R.V., Vinnichenko M. Ya., Karaulov D.A., Firsov D.A., Fedorov V.V., Mozharov A.M., Kirilenko D.A., Mukhin I.S., Interband photoluminescence of InAs(P)/Si nanowires, St. Petersburg State Polytechnical University Journal. Physics and Mathematics. 16 (1.3) (2023) 101–107. DOI: https://doi.org/10.18721/JPM.161.317

Материалы конференции
УДК 535.3
DOI: https://doi.org/10.18721/JPM/161.317

Межзонная фотолюминесценция нитевидных нанокристаллов InAs(P)/Si

Р.В. Устименко [1]✉, М.Я. Винниченко [1], Д.А. К р улов [1], Д.А. Фирсов [1], В.В. Фёдоров [1,2], А.М. Мож ров [2], Д.А. Кириленко [3,4], И.С. Мухин [1,2]

[1] Санкт-Петербургский политехнический университет Петра Великого, Санкт-Петербург, Россия;
[2] Алфёровский Университет, Санкт-Петербург, Россия;
[3] Университет ИТМО, Санкт-Петербург, Россия;
[4] Физико-технический институт им. А.Ф. Иоффе РАН, Санкт-Петербург, Россия
✉ ratmirustimenko@yandex.ru

Аннотация. Нитевидные полупроводниковые нанокристаллы имеют ряд преимуществ по сравнению с пленками и объемными полупроводниковыми материалами, которые позволяют использовать их для создания эффективных детекторов и источников

излучения. В настоящей работе были получены спектры фотолюминесценции радиально гетероструктурированных нитевидных нанокристаллов InAs, InAs/CaF_2 и InAs/InP (ядро/оболочка) в ближнем инфракрасном диапазоне при различных уровнях оптической накачки и различных температурах при помощи вакуумного фурье-спектрометра, работающего в пошаговом режиме. Обнаруженные в спектрах пики объяснены межзонными переходами носителей заряда в InAs разной кристаллической модификации: сфалерит и вюрцит. Из спектров нитевидных нанокристаллов, покрытых CaF_2, видно, что в этом случае пассивация поверхности не изменяет спектральные особенности люминесценции. В то же время интенсивность фотолюминесценции нитевидных нанокристаллов InAs/InP больше, чем у чистых нитевидных нанокристаллов InAs. Таким образом, поверхностная пассивация может уменьшить влияние поверхностных состояний на оптические свойства нитевидных нанокристаллов.

Ключевые слова: нитевидные нанокристаллы, пассивация поверхности, фотолюминесценция, нитевидные нанокристаллы ядро/оболочка

Финансирование: Исследование выполнено за счет гранта Российского научного фонда № 22-19-00494, https://rscf.ru/project/22-19-00494/.

Ссылка при цитировании: Устименко Р.В., Винниченко М.Я., Караулов Д.А., Фирсов Д.А., Фёдоров В.В., Можаров А.М., Кириленко Д.А., Мухин И.С. Межзонная фотолюминесценция нитевидных нанокристаллов InAs(P)/Si // Научно-технические ведомости СПбГПУ. Физико-математические науки. 2023. Т. 16. № 1.3. С. 101–107. DOI: https://doi.org/10.18721/ JPM.161.317

Introduction

Nanowires (NWs) based on A3B5 semiconductors have great prospects as a nanoscale platform for efficient electronic devices. The development of light-emitting and photo-converting devices based on NWs is a promising and urgent task [1]. NWs, due to their small lateral size and small area of contact with the substrate, have some significant advantages over films and bulk materials. They can be directly grown on various substrates, for example, silicon [2]. Thus, it is possible to produce cheap devices integrated with the silicon industrial platform. Among other A3B5 semiconductors, InAs NWs have a number of advantages owing to high mobility, low effective electron mass, low band gap *Eg* and high spin-orbit interaction energy. Also, the interest in the creation of InAs NWs is caused by the fact that selecting appropriate size of NWs can lead to the manifestation of waveguide properties and optical resonances (whispering gallery modes, Fabry-Perot and Mi resonances) in the visible and near-IR spectral ranges, which ensure the localization and concentration of light inside the NW. In this case, it is possible to achieve effective absorption of radiation in a small volume of the active region, which should reduce the dark current of optoelectronic devices. Surface passivation efficiently eliminates surface states in NWs [3]. Due to the high surface-to-volume ratio, it has a significant effect on the optical properties of NWs [4]. Light emission related to surface states of core/shell NWs can appear at photon energy greater or less than the energy of band gap of InAs NWs and can greatly reduce the luminescence efficiency. For InAs NWs, such states have a more essential effect on the emission intensity due to narrow *Eg* and significant contribution of Auger processes [5].

It is known that *Eg* of InAs-based NWs is larger than in the bulk material [6-8]. Therefore, the currently achieved sensitivity of existing detectors based on InAs NWs is limited by 3 μm wavelength, which is noticeably shorter than the experimentally observed cutoff wavelengths for InAs thin-film photodetectors (~3.8 μm). Moreover, there are several unresolved problems in creation of InAs NWs-based photodetectors. For example, the photodiodes described in the literature have a large dark current exceeding 130 mA/cm^2 [9, 10]. The effect of passivation of InAs NWs with a wider gap InP, as well as heterostructures of the *n*-InP/*i*-InAs/*p*-Si type, has not been studied in details yet. We report on optical characterization of such NWs, which can be used for developing new infrared photodetectors.

Materials and Experimental setup

Several arrays of InAs NWs were grown by means of solid-source molecular beam epitaxy (MBE) on SiO_x/Si(111) substrates within the self-induced approach. Boron-doped, vicinal *p*-type Si wafers were used (misorientation 4°, 0.3—0.5 Ohm×cm). Silicon surface oxide layer providing NW nucleation was prepared on HF-dipped Si by wet chemical oxidation in a boiling ammonia-peroxide solution (NH_4OH:H_2O_2:H_2O with a volume ratio of 1:1:3). Indium, As_4 and P_2 element fluxes were determined from beam equivalent pressures (BEP) measured by Bayard-Alpert ion gauge. For all the samples, the In flux was set to a BEP of 8×10^{-8} Torr, which corresponds to a growth rate of approximately 150 nm/h. The InAs NWs were formed at the growth temperature T_{gr} of 460 °C and a high incident As_4/In BEP flux ratio of 90, which exceeded the stoichiometric value by 5 times. To form a radial InAs-core/InP-shell heterostructure, InP was grown at the reduced T_{gr} of 400 °C and P_2/In BEP flux ratio of 32 promoting radial growth. Uniform deposition of amorphous CaF_2 was obtained at the T_{gr} of 100 °C.

Typical scanning electron microscope (SEM) image of cleaved Si substrate with pure InAs NWs is shown in Fig. 1, *a*. This morphology is typical for all studied NWs. The feature of this synthesis method is the possibility of achieving a high surface density of NWs ($\geq$10 μm^{-2}), which significantly reduces light scattering and manifests itself in the matte black surface of the sample. Depending on the growth time, the length of NWs can vary from 200 nm to 10 μm, and the diameter can vary from 40 to 300 nm. The average diameter of pure InAs NWs is approximatee ly equal to 160 nm, their length is about 2.5 μm. We also fabricated a number of samples with surface passivation having the structure of InAs-core/InP-shell and InAs-core/CaF_2-shell. SEM image of InAs-core/InP-shell NWs is presented in Fig. 1, *b*. The diameter of InAs-core/InP-shell NWs lies in the range from 130 to 250 nm for different samples, their length is about 2.5—4.5 μm.

a) *b*)

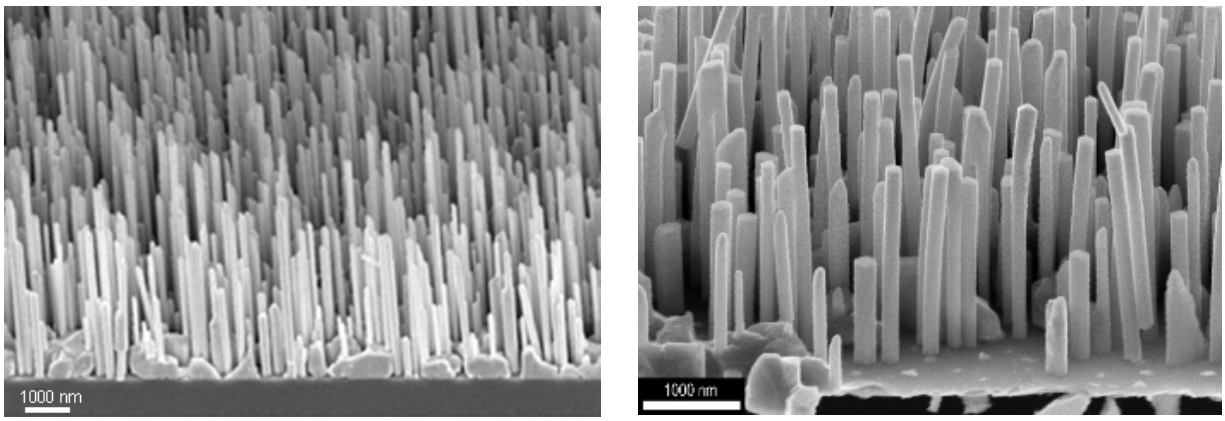

Fig. 1. SEM image of pure InAs NWs (*a*) and InAs-core/InP-shell NWs (*b*)

The crystal structure of NWs was studied by means of transmission electron microscopy (TEM) and electron microdiffraction (see Fig. 2). NWs have a hexagonal wurtzite structure; the NW growth axis coincides with the [0001] wurtzite axis. A large number of planar basal stacking fault are observed in NWs, and these defects can be of several types. Defects can be represented as inclusions of 1, 2 or 3 bi-layers of the sphalerite structure, inclusions of the cubic phase. All stacking faults are parallel to the (0001) growth plane. No other defects, for example, associated with the coalescence of neighboring NWs, were found. The electron microdiffraction pattern shows a characteristic broadening of reflections in the direction perpendicular to the plane of the defect.

Photoluminescence (PL) spectra were measured with a vacuum Fourier spectrometer operating in the step-scan mode with a spectral resolution of about 8 meV. We used the continuous wave (CW) laser radiation from a Nd:YAG solid-state laser for optical interband pumping of charge carriers in the samples. The pump radiation wavelength was 1064 nm. Nd:YAG solid-state laser was pumping by red diodes, therefore we cut this interfering light by IKS3 optical filter mounted

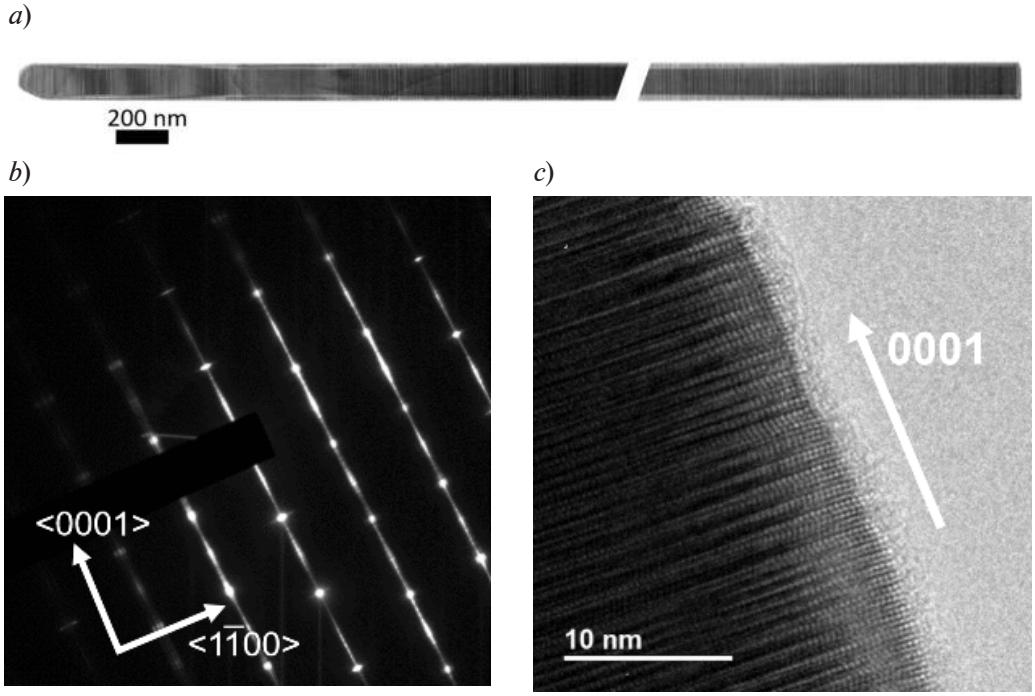

Fig. 2. TEM image of InAs-core / InP-shell NWs (*a*). Selected-area (electron) diffraction image along (*a*) <11$\bar{2}$0> WZ zone axes (*b*) and TEM image of InAs-core / InP-shell NWs (*c*)

in the optical bench. Laser radiation was modulated with a chopper at a frequency of 340 Hz and focused on the sample surface with a lens through a fused silica window of a bath cryostat. PL radiation from the sample was extracted from the cryostat through a ZnSe window aligned with the spectrometer ZnSe window. A KBr beam splitter and a liquid nitrogen-cooled InSb photodetector were used. The optical filter made from pure Ge was installed in front of the photodetector to prevent pumping radiation scattered from the sample surface to reach the detector. Samples were mounted by clamping holder on the cold copper finger of bath cryostat with liquid nitrogen. Platinum temperature controller was mounted near the sample. We varied a sample temperature from 77 to 300 K. In order to increase the measurement sensitivity, we used a phase-sensitive lock-in amplifier SR-830 synchronized with the chopper frequency.

Results and Discussion

Photoluminescence spectra were obtained in the near infrared (IR) range at different levels of optical pumping and different temperatures (77–300 K). All samples exhibited two or three PL peaks in the photon energy range from 300 to 550 meV.

PL spectra of pure InAs NWs are presented in Fig. 3, *a* for different pumping levels at the temperature of liquid nitrogen. Fig. 3, *b* shows similar results for the thinner pure InAs NWs with low surface concentration. The shape and spectral position of the peaks in these two samples are the same, but the PL intensity of peaks was significantly lower for thinner pure InAs. The increase of the sample temperature leads to a gradual quenching of the PL intensity. To analyze the PL spectra, they were fitted into three Gaussian contours (due to the inhomogeneous broadening of the PL peaks). Gaussian contours and their sum are presented as dash lines in Fig. 3, *a*. After fitting, three peaks were found at the photon energies of 350, 405, 440 meV. Two high energy peaks are associated with direct interband transitions in zincblende and wurtzite phases of InAs NWs [11]. Low-energy peak corresponds to indirect in real-space transitions in NWs between regions of the zincblende and wurtzite phases, which have different *Eg* [12]. It should be noted that the presence of alternating crystal modifications is confirmed by TEM images (see Fig. 2). Also, small inserts of zincblende phase could be considered as quantum wells in the wideband wurtzite phase. This can lead to additional localization of charge carriers at the heterointerfaces. The validity of our assumption is confirmed by the absence of peak energy shifts with increasing of pumping. Similar results were presented in Ref. [12], however, in

that case the peak associated with interband transitions experiences a significant blue shift with pumping increase which is opposed to our results. Also, the spectra presented in [12] contained the peak associated with donor-acceptor transitions.

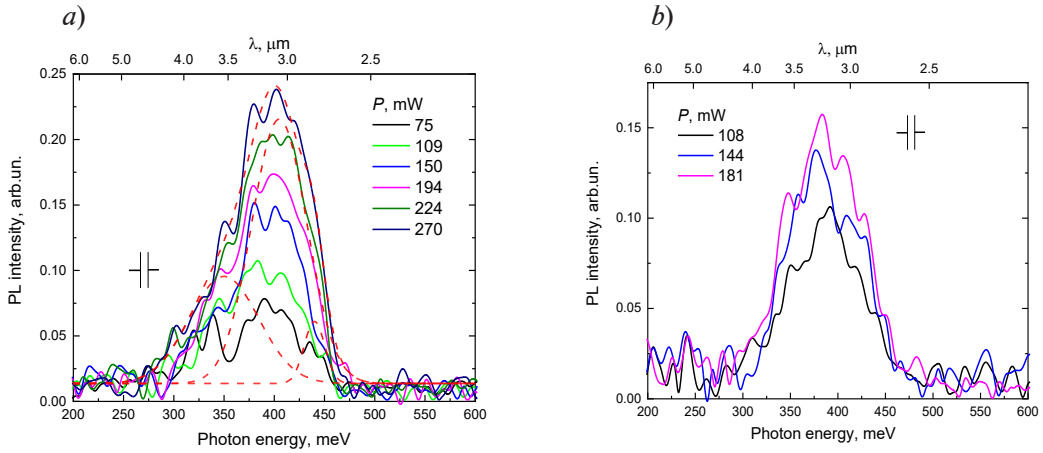

Fig. 3. PL spectra of pure InAs NWs at different pumping levels at 77 K (*a*); PL spectra of the thinner pure InAs NWs with low surface concentration (*b*)

Photoluminescence spectra of InAs-core/CaF_2-shell NWs (not shown here) demonstrated the same peak positions as it was observed in pure InAs NWs. The dependencies on temperature and pumping intensity also were the same. This indicates that the passivating CaF_2 layer is amorphous and does not affect the band structure of InAs NWs.

Photoluminescence spectra of InAs-core / InP-shell NWs are presented in Fig. 4, *a* for different pumping levels for NWs with thin shell. Interband PL peak position is about 445 meV, which corresponds to the direct carrier transitions in the wurtzite phase. The PL intensity of core/shell NWs is 2–3 times higher than intensity of pure NWs. The interband PL peak of InAs-core / InP-shell NWs with thick shell was observed at the photon energy about 480 meV (see Fig. 4, *b*). Thus, we can conclude that the InP shell over the InAs NWs provides a significant increase of *Eg*. It can be explained by deformation of the NW core lattice due to compression by the shell. Increasing the shell of NW causes the higher deformation and corresponding higher *Eg* (see blueshift of PL peak presented in Fig. 4, *b*). It is important to note that due to the passivation of the NW surface, not only the blue shift of the peak was occurred, but also, we observed an increase in its intensity. Additionally, it should be noted that longwavelength PL peak corresponded to indirect transitions has retained its position in coated NWs. It could be explained by the absence of the influence of passivation on the *Eg* of zincblende.

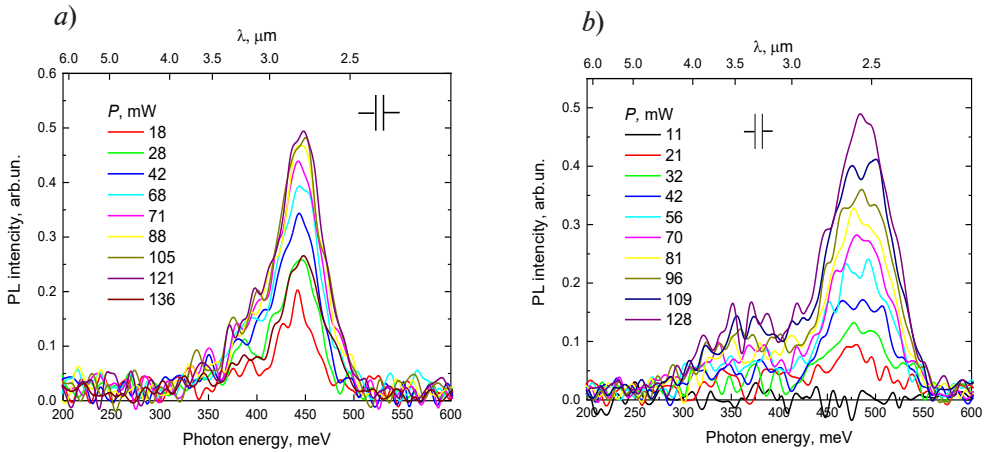

Fig. 4. PL spectra of InAs-core / InP-shell NWs with thick (*a*) and thin (*b*) shell at different pumping levels at the temperature of 77 K

Conclusion

Polytypism of InAs nanowires was found and proved by TEM and the measurements of interband PL spectra in the infrared spectral range. The positions of the PL peaks agree with the theoretical calculations of other authors. Also, it has been shown that InP passivation of InAs nanowires results in a blue shift of interband transitions due to the mechanical strain caused by the shell. The PL intensity of core/shell NWs exceeds the PL intensity of pure InAs NWs.

Acknowledgments

This work was supported by the Russian Science Foundation (grant № 22-19-00494, https://rscf.ru/en/project/22-19-00494/). TEM characterizations were performed using equipment of the Federal Joint Research Center "Material science and characterization in advanced technology" supported by the Ministry of Science and Higher Education of the Russian Federation (id RFMEFI62117X0018)

REFERENCES

1. **Xu T., Wang H., Chen X., Luo M., Zhang L., Wang Y., Chen F., Shan C., Yu C.,** Recent progress on infrared photodetectors based on InAs and InAsSb nanowires, Nanotechnology. 31 (2020) 294004.

2. **Zhang Y., Wu J., Aagesen M. Liu H.,** III−V nanowires and nanowire optoelectronic devices, Journal of Physics D: Applied Physics. 48 (2015) 463001.

3. **Jurczak P., Zhang Y., Wu J., Sanchez A.M., Aagesen M., Liu H.,** Ten-fold Enhancement of InAs Nanowire Photoluminescence Emission with an InP Passivation Layer, Nano letters. 17 (6) (2017) 3629–3633.

4. **Dayeh S.A.,** Electron transport in indium arsenide nanowires, Semiconductor Science and Technology. 25 (2010) 024004.

5. **Sun M.H., Joyce H.J., Gao Q., Tan H.H., Jagadish C., Ning C.Z.,** Removal of Surface States and Recovery of Band-Edge Emission in InAs Nanowires through Surface Passivation Nano letters. 12 (7) (2012) 3378–3384.

6. **Pournia S., Linser S., Jnawali G., Jackson H.E., Smith L.M., Ameruddin A., Caroff P., Wong-Leung J., Tan H.H., Jagadish C., Joyce H.J.,** Exploring the band structure of Wurtzite InAs nanowires using photocurrent spectroscopy, Nano Research. 13 (6) (2020) 1568–1591.

7. **De A., Pryor C.E.,** Predicted band structures of III-V semiconductors in the wurtzite phase, Physical Review B. 81 (15) (2010) 155210.

8. **Faria Junior P.E., Campos T., Bastos C.M.O., Gmitra M., Fabian J., Sipahi G.M.,** Realistic multiband k · p approach from *ab initio* and spin-orbit coupling effects of InAs and InP in wurtzite phase, Physical Review B. 93(23) (2016) 234204.

9. **Logeeswaran V.J., Oh J., Nayak A.P., Katzenmeyer A.M., Gilchrist K.H.,** A perspective on nanowire photodetectors: current status, future challenges, and opportunities, IEEE Journal of selected topics in quantum electronics. 17 (4) (2011) 1002–1032.

10. **Svensson J., Anttu N., Vainorius N., Borg B. M., Wernersson L.-E.,** Diameter-dependent photocurrent in InAsSb nanowire infrared photodetectors, Nano letters. 13 (4) (2013) 1380–1385.

11. **Rota M.B., Ameruddin A.S., Fonseka H.A., Gao Q., Mura F., Polimeni A., Miriametro A., Tan H.H., Jagadish C., Capizzi M.,** Bandgap Energy of Wurtzite InAs Nanowires, Nano Letters. 16 (8) (2016) 51917–5203.

12. **Möller M., de Lima Jr. M.M., Cantarero A., Chiaramonte T., Cotta M.A. Iikawa F.,** Optical emission of InAs nanowires, Nanotechnology. 23 (2012) 375704.

THE AUTHORS

USTIMENKO Ratmir V.
ratmirustimenko@yandex.ru
ORCID: 0000-0003-4123-4375

VINNICHENKO Maksim Ya.
mvin@spbstu.ru
ORCID: 0000-0002-6118-0098

KARAULOV Danila A.
karaulov.da@edu.spbstu.ru

FIRSOV Dmitry A.
dmfir@rphf.spbstu.ru
ORCID: 0000-0003-3947-4994

FEDOROV Vladimir V.
burunduk.uk@gmail.com
ORCID: 0000-0001-5547-9387

Mozharov Alexey M.
alex000090@gmail.com
ORCID: 0000-0002-8661-4083

Kirilenko Demid A.
zumsisai@gmail.com
ORCID: 0000-0002-1571-209X

Mukhin Ivan S.
imukhin@yandex.ru
ORCID: 0000-0001-9792-045X

Received 30.11.2022. Approved after reviewing 08.12.2022. Accepted 15.12.2022.

Conference materials
UDC 543.42
DOI: https://doi.org/10.18721/JPM.161.318

High-field terahertz time-domain spectroscopy of single-walled carbon nanotubes

M.G. Burdanova [1,2]✉, E.O. Chiglintsev [1,3], M.I. Paukov [1], P. Mishra [1,4], K.A. Brekhov [3,4], A.A. Arsenin [1], V. Volkov [1], A.I. Chernov [1,3]

[1] Center for Photonics and 2D Materials, Moscow Institute of Physics and Technology (MIPT), Dolgoprudny, Russia;

[2] Osipyan Institute of Solid State Physics RAS, Moscow, Russia;

[3] Russian Quantum Center, Skolkovo, Moscow region, Russia;

[4] Department of Nanoelectronics, MIREA - Russian Technological University, Moscow, Russia

✉ burdanova.mg@mipt.ru

Abstract. We experimentally demonstrated the high-field THz response of Single-Walled Carbon Nanotubes (SWCNT) in the broad frequency range from 0.2 to 2.0 THz. To investigate the impact of nanomaterial geometry on the absorption of THz radiation, two kinds of SWCNT films with different diameters and lengths were fabricated. The measured conductivity shows the change that can be attributed to the change of the Drude term of conductivity. This increase in conductivity at lower frequency was described either as the increase in the number or decrease in effective masses of free charge carriers different for two samples. Our study suggests that the conductivity of the SWNTs in strong THz fields is enhanced by inducing strong nonlinear electron dynamics as a result of several competing processes. Our findings can be used to predict the behavior of CNT devices (modulators, polarizes, lenses, etc.) in the THz high-field.

Keywords: carbon nanotubes, high-field THz spectroscopy, THz spectroscopy

Funding: This work is supported by the Ministry of Education and Science of the Russian Federation (state task No. FSFZ-0706-2020-0022) and Foundation (RSF) Project No. 21-79-10097 and Ministry of Science and Higher Education of the Russian Federation No. 0714-2020-0002.

Citation: Burdanova M.G., Chiglintsev E.O., Paukov M.I., Mishra P., Brekhov K.A., Arsenin A.V., Volkov V., Chernov A.I., High-field terahertz time-domain spectroscopy of single-walled carbon nanotubes, St. Petersburg State Polytechnical University Journal. Physics and Mathematics. 16 (1.3) (2023) 108–111. DOI: https://doi.org/10.18721/JPM.161.318

Материалы конференции
УДК 543.42
DOI: https://doi.org/10.18721/JPM.161.318

Спектроскопия временного разрешения одностенных углеродных нанотрубок в высоких терагерцевых полях

М.Г. Бурд нов [1,2]✉, Е.О. Чиглинцев [1,3], М.И. П уков [1], П. Мишр [1,4], К.А. Брехов [3,4], А.А. Арсенин [1], В. Волков [1], А.И. Чернов [1,3]

[1] Московский физико-технический институт, г. Долгопрудный, Московская область, Россия;

[2] Институт физики твердого тела им. Осипяна РАН, г. Черноголовка, Московская область, Россия;

[3] Российский Квантовый Центр, Сколково, Московская область, Россия;

[4] Кафедра наноэлектроники, РТУ МИРЭА, Москва, Россия

✉ burdanova.mg@mipt.ru

Аннотация. Мы экспериментально исследовали ТГц-пропускание одностенных углеродных нанотрубок (ОУНТ) в широком диапазоне частот от 0,2 до 2,5 ТГц при различных мощностях ТГц поля. Для исследования влияния геометрии наноматериала на поглощение терагерцового излучения были изготовлены два вида пленок, содержащих ОУНТ разного диаметра и длины. Измеренная проводимость для двух образцов можно объяснить изменением Друде-части проводимости. Это увеличение на более низкой частоте можно объяснить либо увеличением числа, либо уменьшением эффективных масс свободных носителей заряда, различных для двух образцов. Наше исследование предполагает, что в сильных терагерцовых полях проводимость ОСНТ увеличивается за счет создания сильной нелинейной динамики электронов в результате нескольких конкурирующих процессов. Результаты этой работы могут быть использованы для прогнозирования поведения устройств на основе УНТ (модуляторов, поляризаторов, линз и т. д.) в высоких терагерцовых полях.

Ключевые слова: углеродные нанотрубки, мощные терагерцовые поля, терагерцовая спектроскопия

Финансирование: Работа выполнена при поддержке Министерства образования и науки Российской Федерации (госзадание № FSFZ-0706-2020-0022), а также проект Российского научного фонда (РНФ) № 21-79-10097 и Министерства науки и высшего образования Российской Федерации № 0714-2020-0002.

Ссылка при цитировании: Бурданова М. Г., Чиглинцев Е.О., Пауков М.И., Мишра П., Брехов К.А., Арсенин А.А., Волков В., Чернов А.И. Спектроскопия временного разрешения одностенных углеродных нанотрубок в высоких терагерцевых полях // Научно-технические ведомости СПбГПУ. Физико-математические науки. 2023. Т. 16. № 1.3. С. 108–111. DOI: https://doi.org/10.18721/ JPM.161.318

Introduction

It is well-established that carbon nanotubes (CNT) exhibit unique properties associated with their quasi-one-dimensional structure, such as 1D ballistic conduction, large exciton binding energies, and strong many-body interactions. A thin-film CNT network shows exceptionally high effective macroscopic THz conductivity described by the Drude and plasmon models, where some fraction of free charges undergoes plasmon resonance, representing the confined collective motion of carriers along tubes, while other charges undergo a Drude-like free carrier response, indicative of delocalized intertube transport [1]. Numerous THz devices have been proposed based on these properties [1]. On the other hand, the influence of CNT response at internal electric fields up to 130 kV/m, important for THz communications, has been rarely studied.

A particular experimental study has found that strong THz fields generate excitons in semiconductor single-walled CNTs [2]. The free standing multi-walled CNT (MWCNTs) in intense THz field showed anisotropy both in linear and in nonlinear effects [3]. Oppositely to a previously reported article [2], theoretical analysis based on the Drude model suggests that strong THz fields enhance the permittivity of the MWNTs. In recent research [4], extraordinary nonlinear terahertz responses upon optical excitation were observed. It was attributed to field-effect mobility and field-induced carrier multiplications, which were considered to be competing processes governing the rise and fall of the conductivity.

In this study, we present an experimental investigation of the high-field THz time domain spectroscopy of two SWCNTs samples with different geometries. The strong THz radiation results in the non-linear absorption of SWCNTs, which is opposite to the field-induced transparency of SWCNTs typically observed for conducting medium. It was attributed to an increase in the number of free charge carriers accompanied by the decrease in the effective masses, which saturate at high field strengths.

Materials and Methods

SWCNT films with diameters ranging from 1.2–1.7 nm and length from 300 nm to 1 μm, and 1.6-2 nm with the corresponding lengths from 1 to 5 μm were studied, similarly to those published in [5]. The average thickness of all films was less than 100 nm. To investigate the impact of geometry (diameter and length) on the THz conductivity of free carriers at high field strengths, thin films of materials were produced by spray coating on z-cut quartz substrates.

Terahertz time-domain spectroscopy (THz-TDS) of SWCNTs was measured on the experimental setup based on the femtosecond Yb-doped diode-pumped solid-state amplifier system with a wavelength of 1030 nm and pulse duration of 30 fs and repetition rate of 1 kHz. For THz radiation emission, the BNA organic crystal was used. The generated THz radiation power was about 520 uW (measured by Ophir THz power meter RM9) and focused on CNT by the off-axis parabolic mirror to the spot of about 900 μm diameter. The duration of a THz pulse was about 1.25 ps, and its spectrum was up to 2.5 THz wide. The THz electric field strength was up to 130 kV/cm. The ZnTe crystal of 1mm thickness was used as a detector. The absence of nonlinear effects in the detection of a signal on a ZnTe crystal can be indirectly verified by checking the monotonicity of the dependence of the transmission and related parameters on the THz field. In addition, it is known from the literature that nonlinear effect appears at power significantly exceed 1 MV/cm [6].

Results and Discussion

Fig. 1, *a* shows the change the sheet conductivity for shorter SWCNT. The equilibrium conductivity of SWCNT films is well described by the Drude-plus-plasmon model [1]. With the increase in field strength, the conductivity increased in the low frequency range, indicating the change in the Drude component. We then used a model-independent approach, as described in [7], to evaluate the ratio of the effective density of electrons to effective mass, N_{eff}/m (Fig. 1, *b*). The magnitudes of the real part of the sheet conductivity at lower frequencies show the general tendency, increasing as the field strength goes up (Fig. 1, *c*). There are two main competing processes that are found to be influenced by the observed conductivity behavior [3, 4]. Firstly, intense THz fields reduce the conductivity of metallic materials, as an example of graphene, by increasing the electron temperature accompanied by the decrease of the scattering time [8]. On the other hand, conductivity goes up if intense THz fields increase carrier density by generating carriers by carrier multiplication by impact ionization and field induced interband tunneling [2]. These competing processes might be reflected in N_{eff}/m as follows the increase of the carrier density will result in the increase of N_{eff}/m, while the subband scatterings give rise to a higher effective mass for the carriers N_{eff}/m. Therefore, we calculated the ratio N_{eff}/m to evaluate this observation. In our experiments, both samples showed the increase of N_{eff}/m with a similar threshold field strength. This article guides a possible direction for feather investigation of SWCNT film's behavior in the high THz fields. The feather investigation of the samples with different diameters is required.

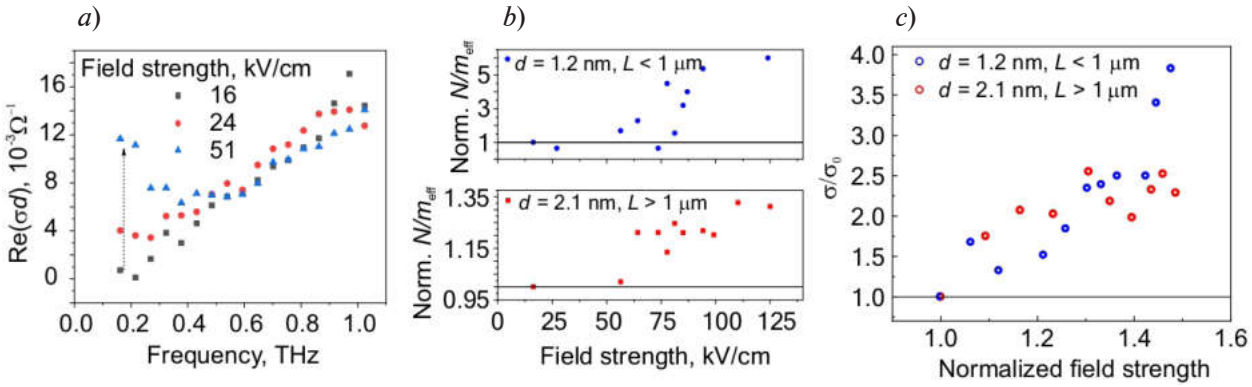

Fig. 1. Sheet conductivity of SWCNTs at different field strength (*a*); ratio of effective density of electrons to effective mass, N_{eff}/m, versus field strength (*b*); change in the conductivity ratio σ/σ_0 as a function of field strength (*c*)

Conclusion

In conclusion, strong THz pulses give rise to highly nonlinear conductivity in SWNTs. In particular, intense THz fields induce a large nonlinear dependence of N_{eff}/m obtained by using a model-independent approach. This theoretical analysis suggests that strong THz fields enhance the conductivity of the SWNTs, inducing strong nonlinear electron dynamics as the result of several competing processes influencing N_{eff}/m. However, we can't independently treat whether N_{eff} or m influenced such behavior. The results of this work can be used to predict the performance of CNT devices (modulators, polarizes, lenses, and so on) in the THz high-field.

REFERENCES

1. **Burdanova M.G., Tsapenko A.P., Kharlamova M.V., Kauppinen E.I., Gorshunov B.P., Kono J., Lloyd-Hughes J.,** A Review of the Terahertz Conductivity and Photoconductivity of Carbon Nanotubes and Heteronanotubes., Adv. Optical Mater. 9 (2021), 2101042.

2. **Watanabe S., Minami N., Shimano R.,** Intense terahertz pulse induced exciton generation in carbon nanotubes, Opt. Express, 19 (2011), 15388–15388.

3. **Lee B., Mousavian A., Paul M.J., Thompson Z.J., Stickel A.D., McCuen D.R., Yun E. Jang, Kim Y.H., Kyoung J., Kim D.-S., Lee Y.-S.,** Anisotropic high-field terahertz response of free-standing carbon nanotubes, Appl. Phys. Lett. 108, (2016), 241111.

4. **Lee B., Mousavian A., Bradley A.N., and Lee Y.-Sh.,** Anomalous nonlinear terahertz transmission of photoexcited carbon nanotubes, J. Opt. Soc. Am. B 38, (2021), 3130–3134.

5. **Karlsen P., Shuba M.V., Beckerleg C., Yuko D.I., Kuzhir P.P., Maksimenko S.A., Ksenevich V., Viet Ho, Nasibulin A.G., Tenne R., Hendry E.,** Influence of nanotube length and density on the plasmonic terahertz response of single-walled carbon nanotubes, J. Phys. D: Appl. Phys., (2018), 51 014003.

6. **Klarskov P., Jepsen P.U.,** THz induced nonlinear absorption in ZnTe, 2015 40th International Conference on Infrared, Millimeter, and Terahertz waves (IRMMW-THz), 2015, p. 1.

7. **Basov D.N., Averitt R.D., Marel D., Dressel M., Haule K.,** Electrodynamics of correlated electron materials Rev. Mod. Phys., 83 (2011) 471.

8. **Paul M.J., Chang Y.C., Thompson Z.J., Stickel A., Wardini J., Choi H., Minot E.D., Hou B., Nees J.A., Norris T.B., Lee Y.S.,** High-field terahertz response of graphene. New J. Phys., 15(8), (2013), p. 085019.

THE AUTHORS

BURDANOVA Maria G.
Burdanova.mg@mipt.ru
ORCID: 0000-0003-1039-3170

BREKHOV Kirill A.
brekhov_ka@mail.ru
ORCID: 0000-0001-9091-2609

CHIGLINTSEV Emil O.
chiglintsev.eo@phystech.edu
ORCID: 0000-0002-2576-4248

ARSENIN Aleksey V.
Arsenin.av@mipt.ru
ORCID: 0000-0002-7506-4389

PAUKOV Maksim I.
Paukov.mi@phystech.edu
ORCID: 0000-0003-1039-3170

VOLKOV Valentyn
vsv.mipt@gmail.com
ORCID: 0000-0003-2637-1371

MISHRA Prabhash
prabhash786@gmail.com
ORCID: 0000-0002-9098-3711

CHERNOV Alexander I.
a.chernov@rqc.ru
ORCID: 0000-0002-6126-7724

Received 13.12.2022. Approved after reviewing 28.02.2023. Accepted 19.03.2023.

Conference materials
UDC 538.915
DOI: https://doi.org/10.18721/JPM.161.319

Suppression of molecular anyon states in the magneto-photoluminescence spectra of InP/GaInP$_2$ quantum dots at a temperature of 30 K

K.M. Afanasev [1,2]✉, D.V. Lebedev [1], A.S. Vlasov [1],
P.A. Balunov [1,2], A.M. Mintairov [1,3]

[1] Ioffe Institute, St. Petersburg, Russia;
[2] Peter the Great St. Petersburg Polytechnic University, St. Petersburg, Russia;
[3] University of Notre Dame, Notre Dame, USA
✉ gruzaa01@gmail.com

Abstract. We used the photoluminescence spectra of a single InP/GaInP$_2$ quantum dot with a Wigner–Seitz radius of about 3.4, doped with 4 electrons, to measure the magnetic field dispersion of single quantum states in a range between 0 and 10 T at 30 K. The measurements show the formation of a molecular structure at high temperature and its transition to a puddle-like structure with a decrease of localization size from 110 nm to 70 nm. Fock–Darwin spectrum fitting shows a decrease in the cyclotron frequency and magnetic field shift, that are interpreted as the formation of an anyon structure in a QD with fractional charge 1/5, 2/3, 1/2 and a built-in magnetic field of −3T.

Keywords: single quantum dots, anyon, Wigner localization, Fock–Darwin spectrum, magneto-photoluminescence

Citation: Afanasev K.M., Lebedev D.V., Vlasov A.S., Balunov P.A., Mintairov A.M., Suppression of molecular anyon states in the magneto-photoluminescence spectra of InP/GaInP$_2$ quantum dots at a temperature of 30 K, St. Petersburg State Polytechnical University Journal. Physics and Mathematics. 16 (1.3) (2023) 112–116. DOI: https://doi.org/10.18721/JPM.161.319

Материалы конференции
УДК 538.915
DOI: https://doi.org/10.18721/JPM.161.319

Подавление молекулярных энионных состояний в спектрах магнито-фотолюминесценции квантовых точек InP/GaInP$_2$ при температуре 30 К

К.М. Аф н сьев [1, 2]✉, Д.В. Лебедев [1], А.С. Вл сов [1],
П.А. Б лунов [1, 2], А.М. Минт иров [1, 3]

[1] ФТИ им. А.Ф. Иоффе, Санкт-Петербург, Россия;
[2] Санкт-Петербургский политехнический университет Петра Великого, Санкт-Петербург, Россия;
[3] Университет Нотр-Дам, Нотр-Дам, США
✉ gruzaa01@gmail.com

Аннотация. Спектры фотолюминесценции легированной 4 электронами одиночной квантовой точки InP/GaInP$_2$ с радиусом Вигнера – Зейтца около 3,4 использовались в работе для измерения дисперсии одиночных квантовых состояний в диапазоне магнитного поля в 0–10 Т при температуре 30 К. Результаты измерений указывают на формирование молекулярной структуры при высокой температуре с переходом в «лужную» структуру при уменьшении размера локализации с 110 нм до 70 нм во внешнем магнитном поле.

В результате подгонки спектра Фока-Дарвина обнаружено уменьшение циклотронной частоты и сдвиг магнитного поля, что может быть связано с формированием в квантовой точке энионной структуры с дробным зарядом 1/5, 2/3, 1/2 и встроенным магнитным полем величиной в −3T.

Ключевые слова: одиночные квантовые точки, энионы, вигнеровская локализация, спектр Фока − Дарвина, магнето-фотолюминесценция

Ссылка при цитировании: Афанасьев К.М., Лебедев Д.В., Власов А.С., Балунов П.А., Минтаиров А.М. Подавление молекулярных энионных состояний в спектрах магнито-фотолюминесценции квантовых точек InP/GaInP$_2$ при температуре 30 K // Научно-технические ведомости СПбГПУ. Физико-математические науки. 2023. Т. 16. № 1.3. С. 112−116. DOI: https://doi.org/10.18721/ JPM.161.319

Introduction

The study considers atom-like single-particle quantum states of electrons (electron shells) in two-dimensional quantum dots (QDs) with a Wigner localization regime, i.e., Wigner−Seitz radius $r_s > 1$, where $r_s = 1/[a^*_B(\pi \cdot n)^{0.5}]$ (n is the electron density and a^*_B is the Bohr radius). These states generate magnetic flux quanta (i.e., vortices), producing anyon (magneto-electron) states that have a fractional charge of $\sim 1/k$ (k is the number of vortices). The resulting built-in (B_{in}) magnetic field corresponds to the filling factor $\nu = N/K$, where N is the number of electrons in the dot and K is the total number of vortexes. This is confirmed by measurements of magneto-photoluminescence spectra (magneto-PL) of self-organized InP/GaInP$_2$ QDs [1]. Molecular or composite ('puddle') anyon state structures were observed in these measurements at 10 K with the external magnetic field B_e ranging from 0 to 10 T for QDs with $N > 5$ and $r_s \sim 2.3$ and 1.3, respectively, and $\nu \sim 1/3$ and 5/2, respectively. In this paper, we present the measurement results for magneto-PL spectra of QDs for $r_s \sim 3.4$ and $N = 4$, allowing to observe the molecule-puddle transition, i.e., suppression of the molecular state corresponding to a change from $\nu \sim 1/5$ to 3/2. The transition was observed at a temperature $T = 30$ K, which indicates high temperature stability of the anyon state in InP/GaInP$_2$.

Materials and Methods

We studied InP/GaInP$_2$ QD samples grown on a GaAs [001] substrate by MOS-hydride epitaxy at 725 °C. The QDs were formed by the Stranski−Krastanov mechanism by depositing 3 monolayers of InP on a GaInP$_2$ $Ga_{0.48}In_{0.52}P$ (GaInP$_2$) layer, lattice-matched to the substrate and covered with a 40 nm GaInP$_2$ layer.

Magneto-PL spectra were measured using a near-field scanning optical microscope (NSOM) in illumination-collection mode at a temperature of 30 K and an external magnetic field B_e in the range from 0 to 10 T. The NSOM probes were tapered Al-coated fiber with an aperture of 50 − 100 nm. The spectra were excited by an Ar laser line with a wavelength of 514.5 nm.

Considering the anti-Stokes components (ASCs) of the PL spectra at minimum pumping, we determined that the QD has four electrons in the photo-excited state, i.e., three in the initial state, (see Fig. 1, *a*) forming an anyon Wigner molecule in both states [2, 3, 4].

Experimental results of magneto-PL

Fig. 1, *a* shows the PL spectra using the Stokes shift energy scale, where the zero peak denoted as the *s*-peak is e_0 (energy emission of the s-peak is 1.715 eV), with B_e increasing in the range from 0 to 10 T. Fig. 1, *b* shows the Stokes region of the spectra, and Fig. 1, *c* shows the shift of the Stokes component (SC) peak.

According to the experimental data, the magneto-PL spectra of the QD anyon state are divided into 3 regions, denoted as I, II, III, differing in the fractional charge and the configuration of the Wigner molecule.

Region I (B_e = 0–3 T). The system was in the molecular state, this state in the PL spectrum is characterized by the separation of ASCs peaks, which are anyons e_0, e_1, e_2, e_3, with the average $\Delta E \approx 2.5$ meV. The Wigner molecule configuration is determined by the SC emission of the vibrational mode (ω_0 = 3.75 meV) of the molecule (this issue is discussed in detail in [2]).

Region II (B_e = 3–6 T). The molecular state is destroyed and passes into the puddle state. We define the puddle state by the characteristic blurring of the emission peaks (e_0, e_1) and the jump-like change in the emission energy of the Wigner molecule SC with $\Delta\omega_0$ = 0.7 meV. The size of the Wigner molecule localization in this state is 110 nm, like in the I state.

Region III (B_e = 6–10 T). The puddle state is rearranged into a different configuration with mixing of ASCs emission peaks (e_0, e_1) and (e_2, e_3) and a second jump in the emission energy of the Wigner molecule SC ($\Delta\omega_0$ = 1.5 meV) with a decrease in the localization size from 110 nm (States I, II) to 70 nm.

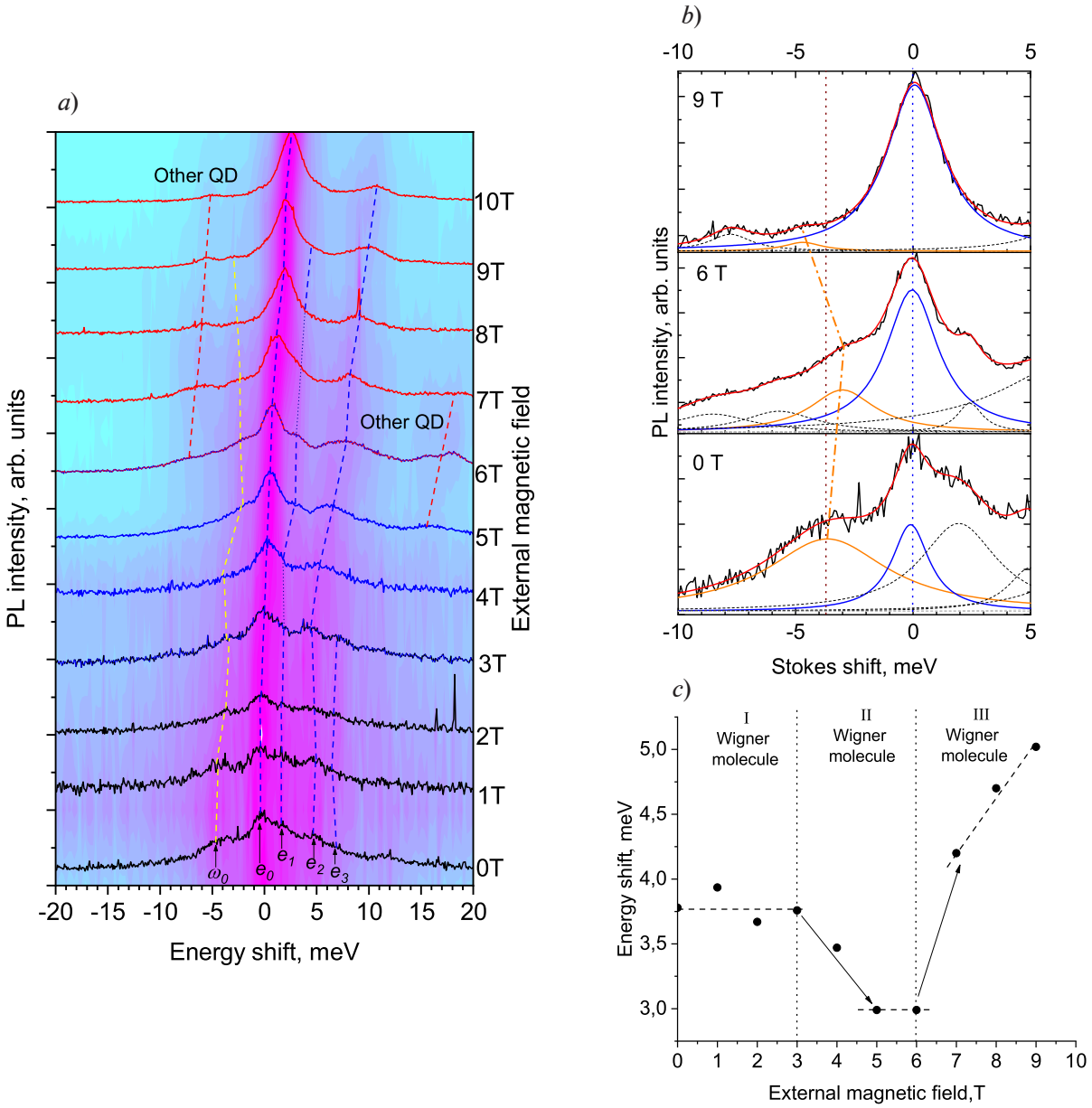

Fig. 1. PL spectrum of a single QD measured at B_e in the range from 0 to 10 T (*a*) (the black lines indicate the spectrum of State I, the blue lines that of State II, the red lines that of State III); PL spectrum in the Wigner molecule SC (orange line) for B_e = 0,6 and 9 T (*b*); position of the SC Wigner molecule peaks in the entire Be range (*c*)

Fock–Darwin spectrum

To analyze the shift of quantum levels of InP/GaInP$_2$ QDs in the magnetic field, we use the single-particle Fock–Darwin (FD) theoretical spectrum of electrons in a parabolic potential ($\hbar\omega_0$) [2, 5, 6] using adjustment of the cyclotron frequency to determine fractional charge, i.e., anyon state, for individual FD states, as described in [7,8].

In Fig.2, *a* on top of the experimental spectrum we plotted the FD spectrum calculated for $\hbar\omega_0 = 2.5$ meV and the *s*, *p*, *d*, and *f* levels. We can see that this fit poorly describes the experimental shift of the QD levels in the magnetic field, and clearly there is a strong deviation of the *s* and *d* peaks from the FD spectrum. The FD spectrum with a fit accounting for the electrons in the QD as anyon states with a fractional charge is plotted in Fig. 2, *b* on top of the experimental spectrum. Due to the built-in magnetic field (B_{in}), the total magnetic field of the system (B_{tot}) is characterized by the sum of the external field B_e and B_{in}, i.e., $B_{tot} = B_e + B_{in}$.

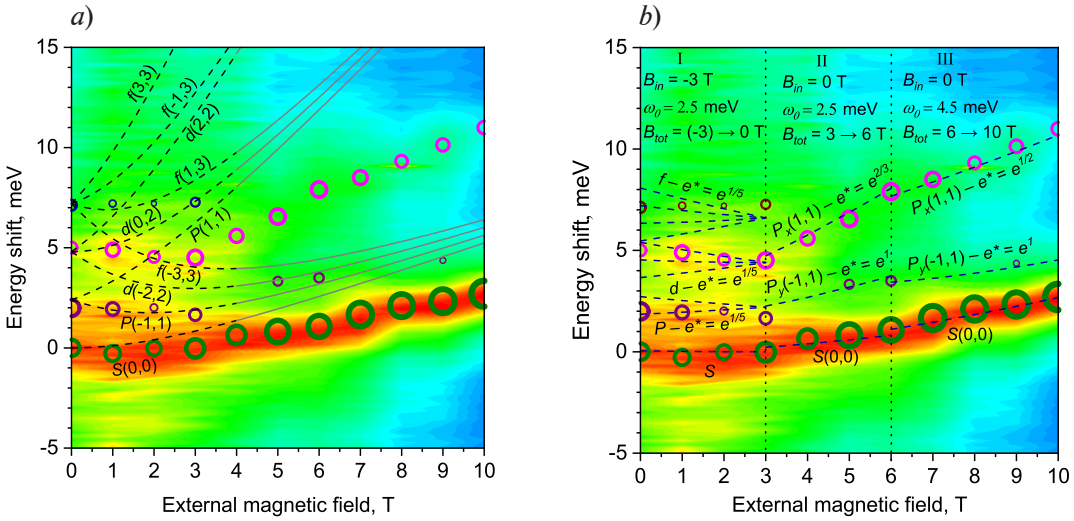

Fig.2. Contour maps of the ASC PL and FD spectrum (*a*) classical theory, with adjustment of the confinement. In the interpretation of the anyon state in the fractional quantum Hall effect mode with adjustment of the built-in magnetic field B_{in} and fractional charge, where $B_{tot} = B_e + B_{in}$ we are showing range of change $B_{tot} \in [-3,0]$ like B_{tot} (−3) → 0 T (*b*). We use an atom-like formalism to denote FD levels, in which quantization levels $n = 0,1,2$ is denoted as $s(m,0)$, $p(m,1)$, $d(m,2)$, respectively, where *m* is the magnetic number. To separate *p* levels with different magnetic number we use indices – $p_x = p(1,1)$ and $p_y = p(-1,1)$

For fitting, we divided the spectrum into 3 regions as in Fig. 1, *a*, *b*, *c*:

Region I (B_e = 0–3 T). This is the state of spontaneous anyon with $B_{in} = -3$ T, a quantum confinement of 2.5 meV, and the fractional charge $e^* = e^{1/5}$ for each level. In this case, B_{tot} varies between −3 T and 0 T, i.e., the FD spectrum is reversed. The filling of the *s*, *p*, *d* and *f* levels with single electrons is observed, which can be attributed to the total spin polarization of the system due to the high temperature of 30 K.

Region II (B_e = 3–6 T). There is a transition of spontaneous anyons to induced ones with a quantum confinement of 2.5 meV and $B_{in} = 0$ T, due to which a jump of B_e to 3 T is observed. In this state, the *f* peak disappears and only the *s*, p_x, and p_y levels remain filled. For induced anyons, each line is described by their own fractional charge, for p_x the fractional charge is $e^* = e^{2/3}$, and for py the charge is $e^* = e^1$. The B_{tot} jump and redistribution of the fractional charge leads to the destruction of the molecular state and rearrangement of the Wigner molecule.

Region III (B_e = 6–10 T). The system remains in the state with induced anyons with fractional charge $e^* = e^{1/2}$ for p_x and charge $e^* = e^1$ for p_y. We observe a jump in the Wigner molecule SC, which we interpret as a reverse rearrangement to the molecular state, which is accompanied by a redistribution of the fractional charge and a change of Wigner molecule isomer. For FD fitting, we describe this transition by changing the quantum confinement to 4.5 meV, which is interpreted as a reduction of the Wigner molecule size to 70 nm.

Conclusion

We used the magneto-PL method of a single InP/GaInP$_2$ QD with 4 doped electrons to demonstrate anyon state formation in a zero external magnetic field. We observed the molecular state disintegration and the transition of the puddle state of the anyon state in a QD by the shift of the Wigner molecule Stokes component. Analysis of the QD based on the theoretical spectrum of one-electron Fock-Darwin points to the formation of induced and spontaneous anyon states with different values of the fractional charge and the built-in magnetic field.

REFERENCES

1. **Mintairov A.M., Lebedev D.V., Vlasov A.S., et al.,** Sci Rep 11 (2021), 21440.4 (158) (2012) 9–15.
2. **Mintairov A.M., Kapaldo J., Merz J.L., Vlasov A.S., Blundell S.A.,** Physical Review B, 95 (11) (2017).
3. **Kim D.-W., Hwang S., Edgar T.F., Maksym P.A., Imamura H., Mallon G.P., Aoki, H.,** J. Phys.: Condens. Matter (Vol. 12) (2000).
4. **Prus T., Szafran B., Adamowski J., Bednarek S.,** Journal of Physics Condensed Matter, 16 (8) (2004), 1425–1437.
5. **Jacak L., Hawrylak P., Wojs A.,** Quantum Dots; Springer: Berlin/Heidelberg, Germany; p. (1998) 176.
6. **Kapaldo J., Rouvimov S., Merz J. L., Oktyabrsky S., Blundell S.A., Bert N., Brunkov P., Kalyuzhnyy N.A., Mintairov S.A., Nekrasov S., Saly R., Vlasov A.S., Mintairov A.M.,** Journal of Physics D: Applied Physics, 49 (47) (2016).
7. **Mintairov A.M., Lebedev D.V., Vlasov A.S., Bogdanov A., Ramezanpour S., Blundell S.A.,** Nanomaterials, 11 (2) (2021).
8. **Mintairov A.M., Lebedev D.V, Vlasov A.S., Blundell S.A.,** Nanomaterials 2022, 12 (6) (2022).

THE AUTHORS

AFANASEV Kirill M.
gruzaa01@gmail.com

LEBEDEV Dmitrii V.
lebedev_84@mail.ru
ORCID: 0000-0003-1475-6303

VLASOV Alexei S.
vlasov@scell.ioffe.ru

BALUNOV Petr A.
balunov239@yandex.ru

MINTAIROV Alexander M.
amintairov@mail.ioffe.ru

Received 13.12.2022. Approved after reviewing 01.02.2023. Accepted 16.02.2023.

Conference materials
UDC 538.9
DOI: https://doi.org/10.18721/JPM.161.320

Electrically controlled switching between spatially separated conducting channels in a quantum point contact

D.I. Sarypov [1, 2] ✉, D.A. Pokhabov [1], 2, A.G. Pogosov [1, 2],
E.Yu. Zhdanov [1, 2], A.K. Bakarov [1, 2]

[1] Rzhanov Institute of Semiconductor Physics, Novosibirsk, Russia;
[2] Novosibirsk State University, Novosibirsk, Russia
✉ d.sarypov@g.nsu.ru

Abstract. We demonstrate transverse magnetic focusing of electrons in semiconductor devices consisting of two trenched-type quantum point contacts (QPC) acting as an injector and a detector. The peak in the detector voltage, corresponding to the penetration of injected electrons into the detector, is observed. Applying the voltage difference between injector side gates is found to cause an abrupt shift of the peak position on the magnetic field scale. This shift can be explained by switching between spatially separated channels inside the multi-well potential formed inside a QPC-injector.

Keywords: ballistic electron transport, quantum point contact, multichannelity, multi-well potential, transverse magnetic focusing

Funding: The study was funded by the Russian Science Foundation (project 22-12-00343 — experimental measurements) and the Ministry of Science and Higher Education of the Russian Federation (project FWGW-2022-0011 — characterization of initial heterostructures).

Citation: Sarypov D.I., Pokhabov D.A., Pogosov A.G., Zhdanov E.Yu., Bakarov A.K., Electrically controlled switching between spatially separated conducting channels in a quantum point contact. St. Petersburg State Polytechnical University Journal. Physics and Mathematics. 16 (1.3) (2023) 117–123. DOI: https://doi.org/10.18721/JPM.161.320

Материалы конференции
УДК 538.9
DOI: https://doi.org/10.18721/JPM.161.320

Электрически контролируемое переключение между пространственно разделенными проводящими каналами в квантовом точечном контакте

Д.И. Сарыпов [1, 2] ✉, Д.А. Похабов [1, 2], А.Г. Погосов [1, 2],
Е.Ю. Жданов [1, 2], А.К. Бакаров [1, 2]

[1] Институт физики полупроводников им. А.В. Ржанова Сибирского отделения РАН, г. Новосибирск, Россия;
[2] Новосибирский государственный университет, г. Новосибирск, Россия
✉ d.sarypov@g.nsu.ru

Аннотация. Исследована магнитная фокусировка электронов в полупроводниковых устройствах, состоящих из двух одинаковых КТК траншейного типа (инжектор и детектор). Наблюдается пик в напряжении детектора, соответствующий попаданию инжектированных электронов в детектор. Приложение разности напряжений между затворами инжектора приводит к резкому смещению фокусировочного пика, что может быть объяснено переключением между пространственно разделенными проводящими каналами в КТК инжекторе.

Ключевые слова: баллистический электронный транспорт, квантовый точечный контакт, многоканальность, многоямный потенциал, магнитная фокусировка

Финансирование: РНФ (проект №22-12-00343 — экспериментальные измерения); Министерство науки и высшего образования РФ (проект №FWGW-2022-0011 — характеризация исходных гетероструктур).

Ссылка при цитировании: Сарыпов Д.И., Похабов Д.А., Погосов А.Г., Жданов Е.Ю., Бакаров А.К. Электрически контролируемое переключение между пространственно разделенными проводящими каналами в квантовом точечном контакте // Научно-технические ведомости СПбГПУ. Физико-математические науки. 2023. Т. 16. № 1.3. С. 117–123. DOI: https://doi.org/10.18721/ JPM.161.320

Introduction

The conductance quantization in units of $2e^2/h$ [1, 2] is a hallmark of quasi-one-dimensional electron transport inherent in quantum point contacts (QPC) — point microconstriction in a two-dimensional electron gas (2DEG) with a width comparable to the Fermi wavelength of electrons. Nowadays a number of conductance quantization features lying beyond a single particle model remain unclear. In recent contributions a trenched-type QPC created by means of lithographic trenches separating the conducting area from two side gates is shown to experience an unusual effect of multichannelity [3–7]. The effect consists in the formation of several channels inside the QPC, which conductances are separately quantized and add up. The effect observation is promoted by the feature of a trenched-type QPC allowing to apply both positive and negative potentials to the gates, as well as large voltage differences between the gates [8] and investigate the QPC conductance in a wide range of the sum and difference of gate voltages.

The physical mechanism of multichannelity is supposed to be linked with a correlated redistribution of charges in the heterostructure (electrons of 2DEG and positively charged donors) caused by their Coulomb interaction leading to the formation of multi-well confining potential. The self-consistent numerical calculation presented in [7] describes the formation conditions of a multi-well confining potential. The creation of multi-well potential due to Coulomb interaction is shown in simulations performed in other articles dealing with a split-gate QPC [9] and bilayer graphene [10].

The conductance measurements described above allow obtaining only the implicit evidence of multichannelity. Therefore, transverse magnetic focusing (TMF) [11, 12] was chosen to investigate the multichannelity since it can be used to directly discern the channels existing in the QPC through the separation of its contribution to the measured signal on a magnetic field scale [13, 14].

In the present work we report on the investigation of the multichannel electron transport in the trench-type QPC by means of the TMF experiments. The devices consisting of two trench-type QPCs are created for this purpose. Each of the QPCs is supplied with two symmetric side gates. In the experiment one QPC acts as a monochromatic injector of ballistic electrons, another one plays a role of a point detector. The focusing peaks corresponding to the registration of injected electrons emerge in the detector voltage as a function of magnetic field. The cyclotron diameter of 4 "μm" corresponding to the magnetic field of "70 mT" at the top of the peak is shown to coincide with the injector-detector separation of 4 "μm" . The application of gate voltage difference between side gates is found out to shift the focusing peak. The peak was shifted by 2 mT (by 3% of resonance magnetic field) which is the experimental evidence of conducting channel displacement in the QPC-injector at about 100 nm. This value is comparable with the characteristic distance between channels [4, 6]. Interestingly, the shift occurs abruptly, and that can be interpreted as switching between conducting channels inside the QPC-injector, which confining potential is multi-well.

Materials and Methods

Experimental samples are created from the GaAs/AlGaAs heterostructure grown by molecular beam epitaxy on a GaAs substrate (Fig. 1, *a*). It has a short-periodical AlAs/GaAs superlattice and a 13 nm GaAs layer located in the middle and acts as a symmetrical quantum well for electrons. Doping the heterostructure with Si δ -layers symmetrically relative to the quantum well allows electrons to fill it and form a 2DEG. A feature of the heterostructure used is that it contains low-mobility X-valley electrons localized on Si-donors, which characteristic concentration is $n_X \sim 10^{10}$ cm^{-2}. X-valley electrons do not give a contribution to the conductance but smooth the fluctuations of electrostatic potential of random impurities thereby increasing the 2DEG mobility [15]. The 2DEG density and mobility at $T = 4.2$ K are $n_{2D} = 7 \times 10^{11}$ cm^{-2} and $\mu = 2 \times 10^6$ cm^2/(V·s), respectively. The presence of the $Al_{0.8}Ga_{0.2}As$ layer does not affect the observation of multichannelity. This layer can be used to create suspended (separated from the substrate) nanostructures [16, 17], but we study the non-suspended structure.

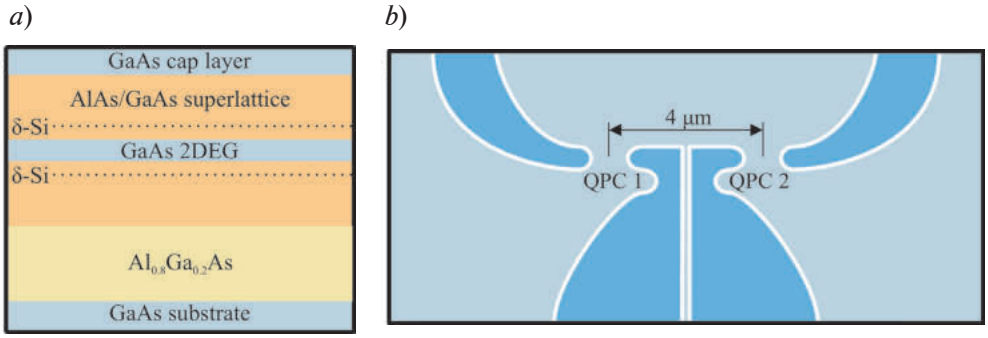

Fig. 1. Schematic images of the heterostructure with the 2DEG doped with Si δ -layers (*a*) and the experimental sample for transverse magnetic focusing (*b*). The lithographic trenches separating conducting area (lighter region) from the gates (darker regions) are marked in white

The devices for the TMF experiments consist of two parallel and similar trenched-type QPCs (injector and detector) separated at the distance of 4 μm (less than mean free path length $l \approx 20$ μm) from each other in the direction perpendicular to the channel direction (Fig. 1, *b*). Both the QPC-injector and QPC-detector have adiabatic form optimal for the magnetic focusing [18]. The injector and detector have individual sources and common drains. The lithographic width of the QPC is about 900 nm and the curvature radius of side gates near the QPC is 500 nm. The electron injection was carried out by the ac source-drain bias with the magnitude of 100 μV. The detector voltage was measured by means of the lock-in technique as a function of transverse magnetic field. All measurements were performed at $T = 1.6$ K.

Results and Discussion

The relative detector voltage $[V(B) - V(0)]/V(0)$ as a function of transverse magnetic field at fixed injector and detector conductance ($G_{inj} = G_{det} = 2e^2/h$) is shown in Fig. 2. The potentials on the side gates remained symmetrical. The measurement configuration is shown in the inset to Fig. 2. A distinct peak is seen at the field $B^* \approx -70$ mT. The cyclotron diameter corresponding to $B^* d_c = 2\hbar\sqrt{2\pi n_{2D}}/eB^* \approx 4$ μm turns out to be equal to the distance between the injector and detector. Therefore, geometrical resonance relating to the injected electron ingression into the detector is observed at this field. The corresponding ballistic trajectory is shown with the arrow in the inset to Fig. 2. A similar peak is not observed at $B > 0$ since electrons at the positive magnetic field move in the direction opposite to the detector. Further we will consider only the range of the field containing the focusing peak. The inversion of the detector and the injector leads to the similar picture due to their symmetry.

A series of the detector voltage dependences on the magnetic field shown in Fig. 3, *a* is obtained by applying voltage difference ΔV_G to the injector gates. Each curve corresponds to the different value of ΔV_G. The curves are vertically shifted from each other for clarity. The voltage difference ΔV_G was changed in a wide range of values from −20 to +20 V. The sum of gate voltages remained constant and equal $\Sigma V_G = -12$ V. Range of the field containing the focusing peak is shown in Fig. 3, *b* where the detector voltage maxima are marked by circles. The peak position as a function

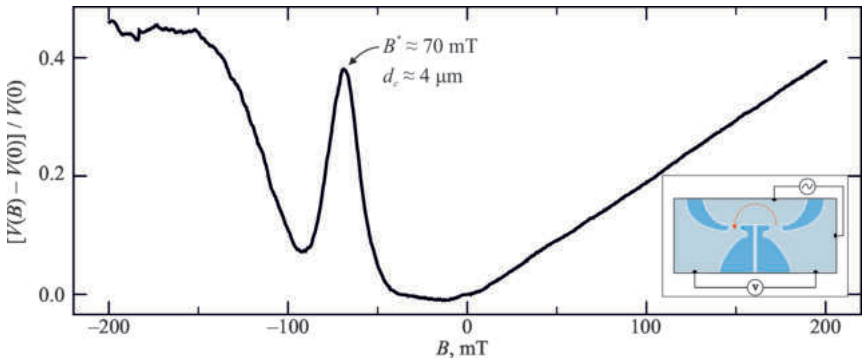

Fig. 2. Relative detector voltage as a function of the transverse magnetic field at symmetrical potentials on the side gates. The inset gives the measurement configuration. The trajectory at the resonance magnetic field is shown with the arrow

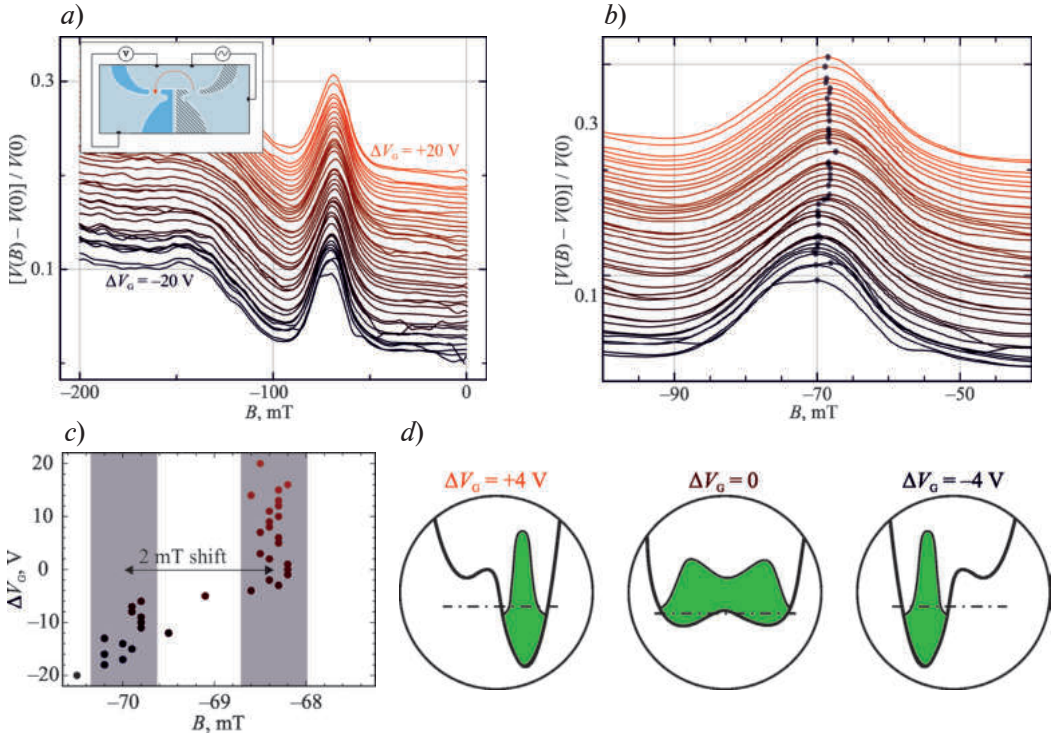

Fig. 3. Dependence of the detector voltage on the magnetic field at various ΔV_G of the injector (applied to dashed gates) changing from −20 to +20 V (*a*); the lower curve corresponds to −20 V, upper curve to +20 V. The sum of gate voltages was fixed ($\Sigma V_G = -12$ V). Measurement configuration is shown in the inset. The panel in (*b*) shows the dependence in (*a*) on an enlarged scale. The maxima of the detector voltage are marked by circles. Peak position as function of ΔV_G (*c*). Illustration of shift of the electron density in the injector when applying ΔV_G (*d*). Fermi energy is marked by a dash-dotted line

of ΔV_G is shown in Fig. 3, *c*. It is seen that, at $\Delta V_G < 0$ the focusing peaks are observed near $B_1 = -70$ mT, while at $\Delta V_G > 0$ they are concentrated near $B_2 = -68$ mT. Thus, we observe a abrupt shift of the focusing peak by $\Delta B \sim 2$ mT at $\Delta V_G \approx 0$. This rapid shift corresponds to the change of cyclotron diameter $\Delta d_c \sim 100$ nm (comparable with the characteristic distance between the channels determined from the analysis of the experimentally measured capacitance coefficients [4, 6]) that can be interpreted as an abrupt shift of the conducting channel inside the QPC-injector when the ΔV_G sign changes. The abrupt shift can be evidence of the formation of a double-well potential inside the QPC-injector. Applying the voltage difference to the gates gives an addition to the confining potential $\Delta U(x) = \alpha x$, linearly dependent on the coordinate x perpendicular to the channel in a 2DEG plane. If the potential was single-well, applying ΔV_G

would only shift the position of potential minimum and thus the conducting channel position in the lateral direction. Assuming the confinement has a conventional parabolic shape, we obtain that:

$$U(x) = \frac{m^*\omega^2 x^2}{2} + \alpha x = \frac{m^*\omega^2 (x - x_0)^2}{2},$$

where $x_0 = -\alpha/m^*\omega$ is the lateral shift. In this case in the experiment we would observe a smooth shift of the focusing peak as the ΔV_G changes. The case of double-well potential is qualitatively different because applying ΔV_G lowers one of the potential minima below the other one. At the same time the electron density relocates to the lower energy minimum (Fig. 3, *d*), i.e., the switching between two spatially separated conducting channels occurs. This shifting manifests itself in the experiment as the abrupt shift of the focusing peak. Besides the peak shift the doublet indicating the simultaneous filling of the both wells might have been expected. However, as seen from Fig. 3, *c*, this regime corresponds to the narrow range of ΔV_G values, which is impossible to analyze with the current accuracy.

Fig. 4, *a* describes a change of the focusing spectrum as the detector width changes by means of different sums of the gate voltages ΣV_G (the lower the ΔV_G is, the narrower the detector is) at $\Delta V_G = 0$. Each curve of the series corresponds to the different ΣV_G value that changed from −18 to −12 V. The measurement scheme is the same (see inset to Fig. 2). The peak height dependence on ΣV_G (Fig. 4, *b*) shows that widening the detector causes the focusing peak reduction. Indeed, the wider detector is, the more trajectories of ballistic electrons connect the injector and the detector, and a particular trajectory consequently becomes less resolvable.

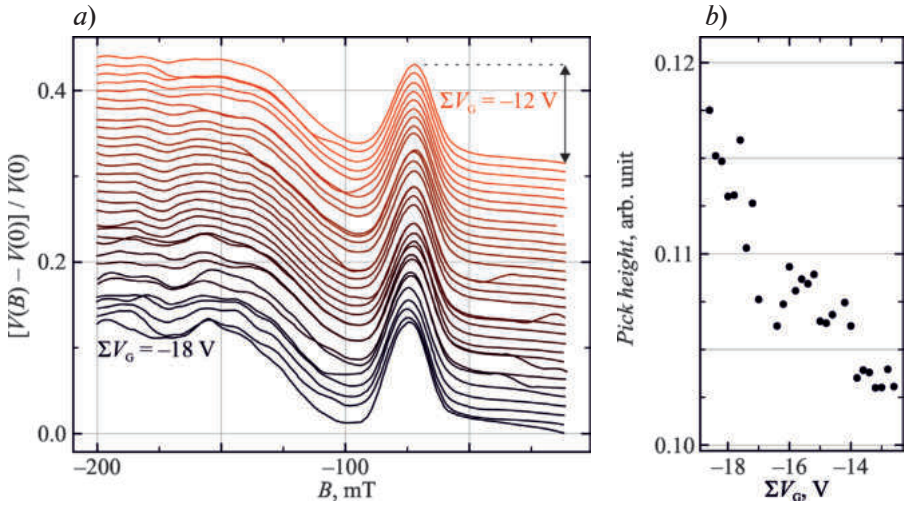

Fig. 4. Detector voltage dependence on the magnetic field at various detector ΣV_G values changing from −18 to −12 V (*a*). The lower curve corresponds to −18 V, and the upper curve to −12 V. The difference of gate voltages is zero. The measurement configuration is shown in the inset. The vertical arrow shows the focusing peak height. The focusing peak height as a function of the ΣV_G value (*b*)

Conclusion

We study the ballistic electron magnetotransport in the devices consisting of two similar trenched-type QPCs (injector and detector), located in the same plane and separated from each other at the distance of 4 μm. The detector voltage demonstrates the peak at the magnetic field corresponding to the cyclotron diameter equal to the distance between the injector and the detector, caused by the magnetic focusing. Increasing the detector width by means of gate voltage is shown to lead to the focusing peak suppression. The best focusing peak observation condition is found to be $G_{inj} = G_{det} \sim 2e^2/h$. Applying the in-plane electric field by the injector gates asymmetrization causes the abrupt shift of the focusing peak by 2 mT. The corresponding cyclotron diameter change is about 100 nm, which is comparable with the characteristic distance between the conducting channels. The observed abrupt peak shift can be interpreted as the switching between two spatially separated conducting channels inside the QPC-injector.

REFERENCES

1. **Wharam D.A., Thornton T.J., Newbury R., Pepper M., Ahmed H., Frost J.E.F., Hasko D.G., Peacock D.C., Ritchie D.A., Jones G.A.C.,** One dimensional transport and the quantisation of the ballistic resistance, J. Phys. C: Solid State Phys. 21 (1988) L209.

2. **van Wees B.J., van Houten H., Beenakker C.W.J., Williamson J.G., Kouwenhoven L.P., van der Marel D., Foxon C.T.,** Quantized conductance of point contacts in a two-dimensional electron gas, Phys. Rev. Lett. 60 (1988) 848.

3. **Masuda T., Sekine K., Nagase K., Wickramasinghe K.S., Mishima T.D., Santos M.B., Hirayama Y.,** Transport characteristics of InSb trench-type in-plane gate quantum point contact, Appl. Phys. Lett. 112 (2018) 192103.

4. **Pokhabov D.A., Pogosov A.G., Zhdanov E.Yu., Bakarov A.K., Shklyaev A.A.,** Suspended quantum point contact with triple channel selectively driven by side gates, Appl. Phys. Lett. 115 (2019) 152101.

5. **Pokhabov D.A., Pogosov A.G., Zhdanov E.Yu., Bakarov A.K., Shklyaev A.A.,** Double-Channel Electron Transport in Suspended Quantum Point Contacts with in-Plane Side Gates, Semiconductors 54 (2020) 1605.

6. **Pokhabov D.A., Pogosov A.G., Zhdanov E.Yu., Bakarov A.K., Shklyaev A.A.,** Crossing and anticrossing of 1D subbands in a quantum point contact with in-plane side gates, Appl. Phys. Lett. 118 (2021) 012104.

7. **Sarypov D.I., Pokhabov D.A., Pogosov A.G., Zhdanov E.Yu., Bakarov A.K.,** Multiwell Potential in a Trench-Type Quantum Point Contact, JETP Lett. 116 (2022) 360.

8. **Pokhabov D.A., Pogosov A.G., Zhdanov E.Yu., Schevyrin A.A., Bakarov A.K., Shklyaev A. A.,** Lateral-electric-field-induced spin polarization in a suspended GaAs quantum point contact, Appl. Phys. Lett. 112 (2018) 082102.

9. **Yakimenko I.I., Yakimenko I.P.,** Electronic properties of semiconductor quantum wires for shallow symmetric and asymmetric confinements, J. Phys.: Condens. Matter 34 (2022) 105302.

10. **Zarenia M., Neilson D., Peeters F.M.,** Inhomogeneous phases in coupled electron-hole bilayer graphene sheets: Charge Density Waves and Coupled Wigner Crystals, Sci. Rep. 7 (2017) 11510.

11. **Sharvin Yu.V.,** A Possible Method for Studying Fermi Surfaces, Zh. Eksp. Teor. Fiz. 48 (1965) 984.

12. **Tsoi V.S.,** Focusing of electrons in a metal by a transverse magnetic field, JETP Lett. 19 (1974) 114.

13. **Ho S.C., Chang H.J., Chang C.H., Lo S.T., Creeth G., Kumar S., Farrer I., Ritchie D.A., Griffiths J., Jones G., Pepper M., Chen T.M.,** Imaging the Zigzag Wigner Crystal in Confinement-Tunable Quantum Wires, Phys. Rev. Lett. 121 (2018) 106801.

14. **Yan C., Kumar S., Thomas K., See P., Farrer I., Ritchie D.A., Griffiths J., Jones G., Pepper M.,** Engineering the spin polarization of one-dimensional electrons, J. Phys.: Condens. Matter 30 (2018) 08LT01.

15. **Friedland K.-J., Hey R., Kostial H., Klann R., Ploog K.,** New Concept for the Reduction of Impurity Scattering in Remotely Doped GaAs Quantum Wells, Phys. Rev. Lett. 77 (1996) 4616.

16. **Pogosov A.G., Budantsev M.V., Zhdanov E.Yu., Pokhabov D.A., Bakarov A.K., Toropov A. I.,** Electron transport in suspended semiconductor structures with two-dimensional electron gas, Appl. Phys. Lett. 100 (2012) 181902.

17. **Pogosov A.G., Shevyrin A.A., Pokhabov D.A., Zhdanov E.Yu., Kumar S.,** Suspended semiconductor nanostructures: physics and technology, J. Phys.: Condens. Matter 34 (2022) 263001.

18. **Lee Y.K., Smith J.S., Cole J. H.,** Influence of Device Geometry and Imperfections on the Interpretation of Transverse Magnetic Focusing Experiments, Nanoscale Res Lett 17 (2022) 31.

THE AUTHORS

SARYPOV Daniil I.
d.sarypov@g.nsu.ru
ORCID: 0000-0003-1056-5235

POKHABOV Dmitriy A.
pokhabov@isp.nsc.ru
ORCID: 0000-0002-8747-0261

POGOSOV Arthur G.
pogosov@isp.nsc.ru

ZHDANOV Evgeniy Yu.
zhdanov@isp.nsc.ru

BAKAROV Askhat K.
bakarov@isp.nsc.ru
ORCID: 0000-0002-0572-9648

Received 14.12.2022. Approved after reviewing 03.02.2023. Accepted 10.02.2023.

Conference materials
UDC 537.86
DOI: https://doi.org/10.18721/JPM.161.321

Influence of DC current direction in graphene on the dispersion and amplification of plasmons in graphene

I.M. Moiseenko [1] ✉, D.V. Fateev [1]

[1] Kotelnikov Institute of Radio Engineering and Electronics (Saratov Branch), RAS, Saratov, Russia
✉ quikc@yandex.ru

Abstract. We investigate dispersion and amplification of plasmon eigen modes in graphene with a direct electric current (DC-current) directed arbitrarily relative to the direction of plasmon propagation. Graphene is described by tensor conductivity obtained in the hydrodynamic approximation. We detected the possibility of amplification of plasmons in graphene in a certain range of DC current directions at terahertz frequencies. The most effective amplification is achieved when the drift of charge carriers and plasmons propagate co-directionally. This is due to the most effective interaction of DC current with the electric field of plasmons.

Keywords: hydrodynamic graphene, terahertz radiation, surface plasmon amplification

Funding: The study was supported by the Russian Science Foundation Grant 22-79-00262.

Citation: Moiseenko I.M., Fateev D.V., Influence of DC current direction in graphene on dispersion and amplification of plasmons in graphene, St. Petersburg State Polytechnical University Journal. Physics and Mathematics. 16 (1.3) (2023) 124–127. DOI: https://doi.org/10.18721/JPM.161.321

Материалы конференции
УДК 537.86
DOI: https://doi.org/10.18721/JPM.161.321

Влияние направления постоянного тока в графене на дисперсию и усиление графеновых плазмонов

И.М. Моисеенко [1] ✉, Д.В. Ф теев [1]

[1] Саратовский филиал Института радиотехники и электроники им. В.А. Котельникова РАН, г. Саратов, Россия
✉ quikc@yandex.ru

Аннотация. В настоящей работе исследована дисперсия и усиление собственных плазмонных мод в графене с постоянным током, направленным произвольно относительно направления распространения плазмонов. Графен описывается тензорной проводимостью, полученной в рамках гидродинамического приближения. Показана возможность усиления плазмонов в графене в некотором диапазоне направлений постоянного тока на терагерцевых частотах. Наиболее эффективное усиление достигается, когда дрейф носителей заряда и плазмоны распространяются сонаправленно. Это связано с наиболее эффективным взаимодействием постоянного тока с электрическим полем плазмонов.

Ключевые слова: гидродинамический графен, терагерцевое излучение, усиление поверхностных плазмонов

Финансирование: Работа поддержана грантом РНФ № 22-79-00262.

Ссылка при цитировании: Моисеенко И.М., Фатеев Д.В. Влияние направления постоянного тока в графене на дисперсию и усиление графеновых плазмонов // Научно-

технические ведомости СПбГПУ. Физико-математические науки. 2023. Т. 16. № 1.3. С. 124–127. DOI: https://doi.org/10.18721/ JPM.161.321

Introduction

Graphene-based structures are currently being actively investigated to amplify and detect terahertz (THz) radiation, in particular due to graphene plasmonic properties [1, 2]. The amplification of THz plasmons in graphene with direct electric current (DC) has been studied theoretically [3, 4], and also demonstrated experimentally [5]. The dispersion of plasmon modes in graphene with a DC co-directed (oppositely directed) with the wave vector of plasmon was investigated in [6], which also shows plasmon amplification at THz frequencies associated with the Cherenkov effect.

Materials and Methods

In this paper, the dispersion and amplification of THz plasmons in graphene with a DC current arbitrary directed relative to the direction of plasmon propagation is investigated. The structure under study consists of a graphene layer located in the *xoz*-plane between two semi-infinite dielectrics with dielectric constants ε_1 and ε_2 (Fig. 1). Graphene is described by the conductivity obtained in tensor form in the hydrodynamic approximation. The use of the hydrodynamic approximation is justified in the case when the momentum scattering frequency in interparticle collisions prevails over the collision frequency of charge carriers with inhomogeneities of the graphene crystal lattice and the frequency of the acting field [7]. The hydrodynamic conductivity of graphene is obtained as a result of solving the hydrodynamic equations for the momentum and energy balance of charge carriers, as well as the continuity equation [7, 8]:

$$\frac{\partial N}{\partial t} + \frac{\partial (NV)}{\partial x} = 0, \tag{1}$$

$$\frac{\partial S}{\partial t} + \nabla \hat{\Pi} + eEN + \frac{e}{c} J \times B = -S\gamma, \tag{2}$$

$$\frac{\partial W}{\partial t} + V_{\mathrm{F}}^2 \nabla S + eEJ = 0 \tag{3}$$

where N is the number of particles, J is the current density, S is the macroscopic momentum, W is macroscopic energy, Π is the stress tensor, e is the electron charge, c is the speed of light, E and B electric and magnetic fields, respectively. Here $\gamma = 1/\tau$, τ is the momentum relaxation time of charge carriers in graphene. The relations between the quantities entering Eqs. (1)–(3) can be written as [7]:

$$S = MV,\ \hat{\Pi} = P + S \otimes V,\ P = M(V_{\mathrm{F}}^2 - V^2)/3,\ W = MV_{\mathrm{F}}^2 - P, \tag{4}$$

where M is the effective fluid mass density, P is the carrier pressure, V_F is the Fermi velocity in graphene. The energy relaxation time is much longer than the oscillation period and the energy conversion process is adiabatic, which causes zero on the right side of Eq. (3). Hydrodynamic Eqs. (1)–(3) are solved using the perturbation approach by decomposing every variable over degrees of the amplitude of the acting electric field and retaining only the linear terms of the perturbation series. Taking into account the DC current in graphene, leads to the tensor form of graphene conductivity:

$$\sigma = \begin{pmatrix} \sigma_{xx} & \sigma_{xz} \\ \sigma_{zx} & \sigma_{zz} \end{pmatrix}. \tag{5}$$

The expressions for the elements of the graphene conductivity tensor obtained using the analytical solution software package are too bulky, so they are not explicitly given in the article.

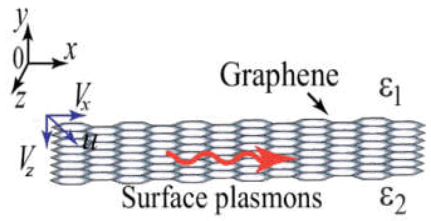

Fig. 1. Schematic view of structure

As a result of solving Maxwell's equations with electrodynamic boundary conditions, a dispersion equation was obtained for surface modes propagating along the ox-axis (the in-plane-of-graphene components of the wave vector is $k_z = 0$ and $k_x \neq 0$) in studied structure in the following form [8]:

$$\omega\varepsilon_0\left(\frac{\varepsilon_1}{k_{y1}}-\frac{\varepsilon_2}{k_{y2}}\right)+\sigma_{xx}+\frac{\sigma_{xz}\sigma_{zx}\mu_0\omega}{k_{y2}-k_{y1}-\sigma_{zz}\mu_0\omega}=0, \qquad (6)$$

where $k_{y1,2}=\pm\sqrt{\omega^2\varepsilon_{1,2}/c^2-k_x^2}$ are the out-of-plane-of-graphene components of the wavevectors in different media, ω is the angular frequency, ε_1 and ε_2 are the dielectric constants of the media above and below graphene, respectively, and c is the speed of light, ε_0 and μ_0 are the electric and magnetic constants, respectively. The signs of $k_{y1,2}$ are chosen from the condition of exponential decay of surface wave field away from the graphene layer.

Results and Discussion

In the case of a directed DC current and a plasmon wave vector, the real part of graphene conductivity can be negative at THz frequencies, which leads to an amplification of plasmons in this frequency range due to the Cherenkov effect [6]. Let us consider how the dispersion and amplification of surface plasmons in graphene with a DC current will change depending on its direction. Fig. 2 shows the real part of the plasmon wave number as a function of frequency for different directions of charge carriers drift, while the value of the drift velocity remains constant $u = 0.5V_F$, where $V_F = 10^6$ m/s is the Fermi velocity in graphene. The charge carriers drift velocity along the ox-axis is defined as $V_{x0}=\sqrt{u^2-V_{z0}^2}$. With increasing of the deviation of the charge carriers drift direction from the direction of plasmon propagation, their localization increases at a fixed frequency (Fig. 2), which is associated with a decrease in the projection of the drift velocity of charge carriers on the *ox*-axis and a decrease influence of the Doppler shift on the dispersion of plasmons. Despite the increasing localization of plasmons, the efficiency of their amplification decreases (Fig. 3). This is due to a decrease of the interaction efficiency of drifting electrons with the tangential electric field of plasmons.

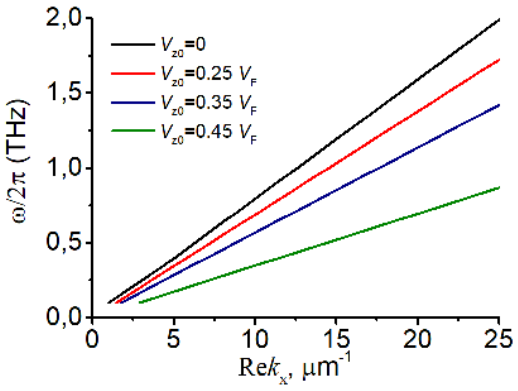

Fig. 2. Plasmon dispersion for different directions of charge carrier drift in graphene at the charge carrier drift velocity $u = 0.5V_F$. The direction of drift of charge carriers is determined from the expression $V_{x0}=\sqrt{u^2-V_{z0}^2}$. Graphene parameters: momentum relaxation time of the charge carrier is τ = 0.5 ps, the Fermi energy is ε_F = 200 meV.

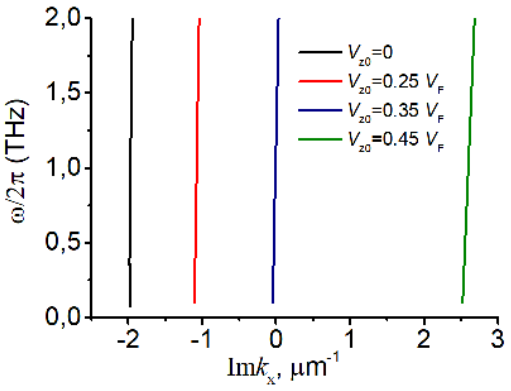

Fig. 3. Imaginary part of the plasmon wave number as a function of frequency for different directions of charge carrier drift in graphene at the charge carrier drift velocity $u = 0.5V_F$. Graphene parameters as in Fig. 2

Conclusion

Thus, the dispersion and amplification of plasmon eigen mode in graphene with a DC current directed arbitrarily relative to the direction of plasmon wave wector is investigated. The possibility of amplification of plasmons in graphene in a certain range of DC current directions at THz frequencies is shown. The most effective amplification is achieved when the charge carrier drift and plasmons propagate co-directionally due to the most effective interaction of the terahertz wave field with the drifting charge carriers.

REFERENCES

1. **Koppens F. H. L. et al.,** Photodetectors based on graphene, other two-dimensional materials and hybrid systems, Nature Nanotech 9 (2014) 780–793.

2. **Ryzhii V., Otsuji T., Shur M.,** Graphene based plasma-wave devices for terahertz applications, Appl. Phys. Lett., 116 (2020) 140501.

3. **Moiseenko I.M., Popov V.V., Fateev D.V.,** Terahertz plasmon amplification in a double-layer graphene structure with direct electric current in hydrodynamic regime, Phys. Rev. B, 103 (2021) 195430.

4. **Svintsov D.,** Emission of plasmons by drifting Dirac electrons: A hallmark of hydrodynamic transport, Phys. Rev. B, 100 (2019) 195428.

5. **Boubanga-Tombet S., et al.,** Room-Temperature Amplification of Terahertz Radiation by Grating-Gate Graphene Structures, Phys. Rev. X, 10 (2020) 031004.

6. **Polischuk O.V., Fateev D.V., Popov V.V.,** Features of the Damping and Amplification of Terahertz Plasmon Eigenmodes in Graphene Taking the Spatial Dispersion into Account, Semiconductors 55 (2021) 875–878.

7. **Narozhny B.N.,** Electronic hydrodynamics in graphene, Annals of Physics 411 (2019) 167979.

8. **Moiseenko I.M., Popov V.V., Fateev D.V.,** Terahertz transverse electric modes in graphene with DC current in hydrodynamic regime, J. Phys.: Condens. Matter 34 (2022) 295301 (6pp).

THE AUTHORS

MOISEENKO Ilia M.
quikc@yandex.ru

FATEEV Denis V.
fateevdv@yandex.ru

Received 14.12.2022. Approved after reviewing 23.01.2023. Accepted 24.01.2023.

Conference materials
UDC 538.975
DOI: https://doi.org/10.18721/JPM.161.322

Study of composite structure based on Ag and SiNWs

V.O. Bolshakov [1, 2], A.A. Ermina [1], K.V. Prigoda [1, 2], M.Yu. Maximov [2]
V.A. Tolmachev [1], Yu.A. Zharova [1] ✉

[1] Ioffe Institute, St. Petersburg, Russia;
[2] Peter the Great St. Petersburg Polytechnic University, St. Petersburg, Russia
✉ piliouguina@mail.ioffe.ru

Abstract. In this study, we propose a method for creating a composite structure consisting of an array of vertical silicon nanowires (SiNWs) and silver nanoparticles (AgNPs). To obtain SiNWs, the process of two-stage metal-assisted chemical etching of c-Si was used, and to obtain a uniform distribution of AgNPs in the SiNW array over their entire height, the atomic layer deposition method was used. The structural and optical characteristics of the AgNPs/SiNWs were studied by nondestructive spectroscopic ellipsometry and scanning electron microscopy before and after the preparation of the composite structure. The thickness (from 2.7 to 7.8 nm) of AgNPs layers deposited on a c-Si substrate and their complex dielectric functions were determined within the framework of the Drude-Lorentz model, on which resonance peaks of localized and bulk plasmons are observed. For an array of SiNWs, using a multilayer model and the effective Bruggeman medium approximation, the height of sublayers and the Si fraction in them, as well as the Ag fraction in the Ag/SiNWs composite structure, are determined. The c-Si:Ag composite structure has been characterized by comparing the calculation and experiment. The optical properties of Ag/SiNWs structures with complex spatial geometry are modeled using the COMSOL Multiphysics software package. The expected localization of the electric field is observed on the surface and near the AgNP as a result of the excitation of localized plasmon resonance. The calculated enhanced factor reached 10^{10}, which suggests that composite AgNPs/SiNWs structure is promising to use as a substrate for surface-enhanced Raman scattering.

Keywords: Ag nanoparticles, Si nanowires, atomic layer deposition, metal-assisted chemical Etching (MACE), spectroscopic ellipsometry, localized plasmon resonance

Funding: The study was supported by the Ministry of Science and Higher Education of the Russian Federation as part of State Assignment (Project 0040-2019-0012).

Citation: Bolshakov V.O., Ermina A.A., Prigoda K.V., Maximov M.Yu., Tolmachev V.A., Zharova Yu.A., Study of composite structure based on Ag and SiNWs, St. Petersburg State Polytechnical University Journal. Physics and Mathematics. 16 (1.3) (2023) 128–134. DOI: https://doi.org/10.18721/JPM.161.322

Материалы конференции
УДК 538.975
DOI: https://doi.org/10.18721/JPM.161.322

Исследование композитной структуры на основе серебра и кремниевых нанонитей

В.О. Больш ков [1, 2], А.А. Ермин [1], К.В. Пригод [1, 2], М.Ю. М ксимов [2]
В.А. Толм чев [1], Ю.А. Ж ров [1] ✉

[1] Физико-технический институт им. А.Ф. Иоффе РАН, Санкт-Петербург, Россия;
[2] Санкт-Петербургский политехнический университет Петра Великого, Санкт-Петербург, Россия
✉ piliouguina@mail.ioffe.ru

Аннотация. В данной работе мы предлагаем метод создания композитной структуры Ag/Si, состоящей из массива вертикальных кремниевых нанонитей (КНН), декорированного наночастицами серебра (Ag НЧ). Для получения кремниевых нанонитей применен процесс двухстадийного металл-стимулированного химического травления Si, а для декорирования КНН Ag НЧ – метод атомно-слоевого осаждения, с помощью которого было получено равномерное распределение Ag НЧ в массиве КНН по всей их высоте.

Ключевые слова: наночастицы серебра, кремниевые нанонити, атомно-слоевое осаждение, металл-стимулированное химическое травление (МСХТ), спектральная эллипсометрия, локализованный плазмонный резонанс

Финансирование: Исследование проводилось при поддержке Министерства науки и высшего образования Российской Федерации в рамках государственного задания (проект № 0040-2019-0012).

Ссылка при цитировании: Большаков В.О., Ермина А.А., Пригода К.В., Максимов М.Ю., Толмачев В.А., Жарова Ю.А. Исследование композитной структуры на основе серебра и кремниевых нанонитей // Научно-технические ведомости СПбГПУ. Физико-математические науки. 2023. Т. 16. № 1.3. С. 128–134. DOI: https://doi.org/10.18721/ JPM.161.322

Introduction

Localized plasmon resonance (LPR) in metal nanoparticles (NPs) is excited by the interaction of incident light with their electrons [1]. The LPR parameters depend on the shape of the NPs, the distance between them, and their size, as well as on the optical properties of the substrate and the environment, which can be chosen to control the plasmon characteristics. As a rule, metal NPs are deposited on flat substrates made of dielectrics or semiconductors, and air serves as the environment. Of particular interest among semiconductors are Si substrates, which are widely used in nanoelectronics [2] and optoelectronics [3]. Nowadays, high-aspect Si structures can be obtained with a highly developed surface in the form of porous Si [4] or arrays of vertical Si nanowires (SiNWs) [5] by anisotropic [6], electrochemical [4] or metal-assisted chemical etching (MACE) [7] of a single-crystal (c-Si) substrate. The creation and study of the properties of composite structures based on high-aspect Si structures decorated with noble metal NPs is a promising direction in the creation of new functional structures.

A suitable method for the uniform deposition of NPs on such high-aspect Si structures is atomic layer deposition (ALD) [8], which can be used to control the deposition thickness with great accuracy, and without any special requirements on the surface topology compared to the CVD method. In the ALD process, sequential chemisorption of reactant vapors on the substrate surface occurs [9]. The cyclical nature of the ALD processes ensures precise thickness control down to sub-nanometers. In addition, self-limiting surface reactions at the substrate-gas phase interface provide layer-by-layer growth of films and allow conformal deposition of thin films on complex three-dimensional and porous substrates.

The goal of this work was to create Ag/SiNWs composite structures in the form of an array of SiNW decorated with AgNPs using ALD method, to study their structural and optical properties, and to calculate an enhanced factor of a composite structure using the COMSOL Multiphysics software.

Materials and Methods

To create an array of SiNW, we used p-type c-Si (100) with a resistivity of 10 Ohm·cm. The two-stage MACE method was used to obtain SiNWs [7, 10]. Firstly, Ag island film was deposited onto the surface of the c-Si substrate from a solution of 0.02M $AgNO_3$ + 5M HF (1:1)

for 30 seconds (Fig. 1, 1st step). Then the *c*-Si substrate was placed in the electrolyte solution 5M HF + H_2O_2 (10:1) (Fig. 1, 2nd step), where etching and formation of SiNWs took place for 10 (sample O1) and 20 (sample O2) seconds to obtain structures of different heights. After the removal of Ag in HNO_3 solution, the ALD process was carried out to decorate SiNWs with AgNPs (Fig. 1, 3rd step).

The AgNPs were deposited by ALD with a Picosun R-150 setup as described in [9]. To determine the optimal growth condition the reactor temperatures (142–184 °C), precursor 2,2-dimethyl-6,6,7,7,8,8,8-heptafluorooctane-3,5-dionato) silver(I) triethyl-phosphine (Ag(fod)(PEt_3), $C_{16}H_{25}AgF_7O_2P$) (98 %, Strem Chemicals, Newburyport, MA, USA), reagents pulse times (2-4 sec) and number of pulses (1-11) in one ALD cycle were varied. The optimal conditions for the growth of Ag on the surface of *c*-Si substrates were determined.

The JSM-7001F Scanning Electron Microscope (SEM) (JEOL, Japan) was used to study the morphology of nanostructures. A statistical analysis of nanostructures was carried out (average size, coverage factor) according to SEM-images and using open-source ImageJ software.

The ellipsometric characteristics were studied using a Semilab SE2000 spectral ellipsometer (Budapest, Hungary) in the wavelength range λ from 400 to 1700 nm at an angle of incidence φ = 70°.

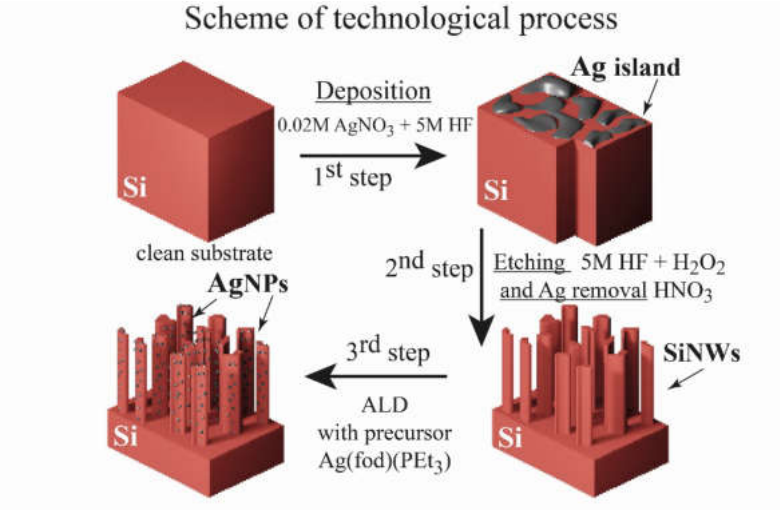

Fig. 1. Schematic representation of the stages for obtaining a composite structure of Ag/SiNWs

The simulation of the electromagnetic field propagation was carried out using the COMSOL Multiphysics software, which applied the 3D Finite Element Method (FEM).

Results and Discussion

At the first stage, to optimize the ALD regimes, AgNPs were deposited on flat c-Si substrates (Fig. 2, *a*). As a result of the analysis of this SEM-image in ImageJ software, the average diameter of nanoparticles $d_{Ag} = 22 \pm 3$ nm was obtained with a filling factor of 18 % (Fig. 2, *b*).

The selection of optimal conditions is the most important criterion in the preparation of coatings by the ALD method. Therefore, at the first stage of the search for optimal conditions for the ALD method, the influence of the Ag(fod)(PEt_3) evaporator temperature was studied. Next, the dependence of the coating growth rate on the reactor temperature was studied and the optimal reactor temperature range of 155–165 °C was established, at which the growth rate was increased and a layer of AgNPs with a thickness of $d \sim 8$ nm was deposited at a number of 2300 cycles. As a result, 3 samples of layers with different thickness were obtained, (d_{Ag} = 2.3, 3.5, and 7.8 nm measured using ellipsometry). By measuring the ellipsometric angles ψ_{exp} and Δ_{exp} for 3 samples and using the Drude-Lorentz model with the calculated angles ψ_{calc} and Δ_{calc}, they were in good agreement with the experiment. As a result, the parameters of this model were extracted: real (ε_1) (Fig. 2, *c*) and imaginary (ε_2) (Fig. 2, *d*) permittivities and Ag layer thicknesses.

Analyzing the behavior of the function ε_1 for all 3 samples, it can be seen that they are located mainly in the negative region of energy E, which is typical for the structure of metals. The imaginary part of the function ε_2 demonstrates a narrow volume plasmon resonance peak at E = 3.9 eV for all obtained AgNPs structures on a Si substrate, and for a sample with d_{Ag} = 7.8 nm.

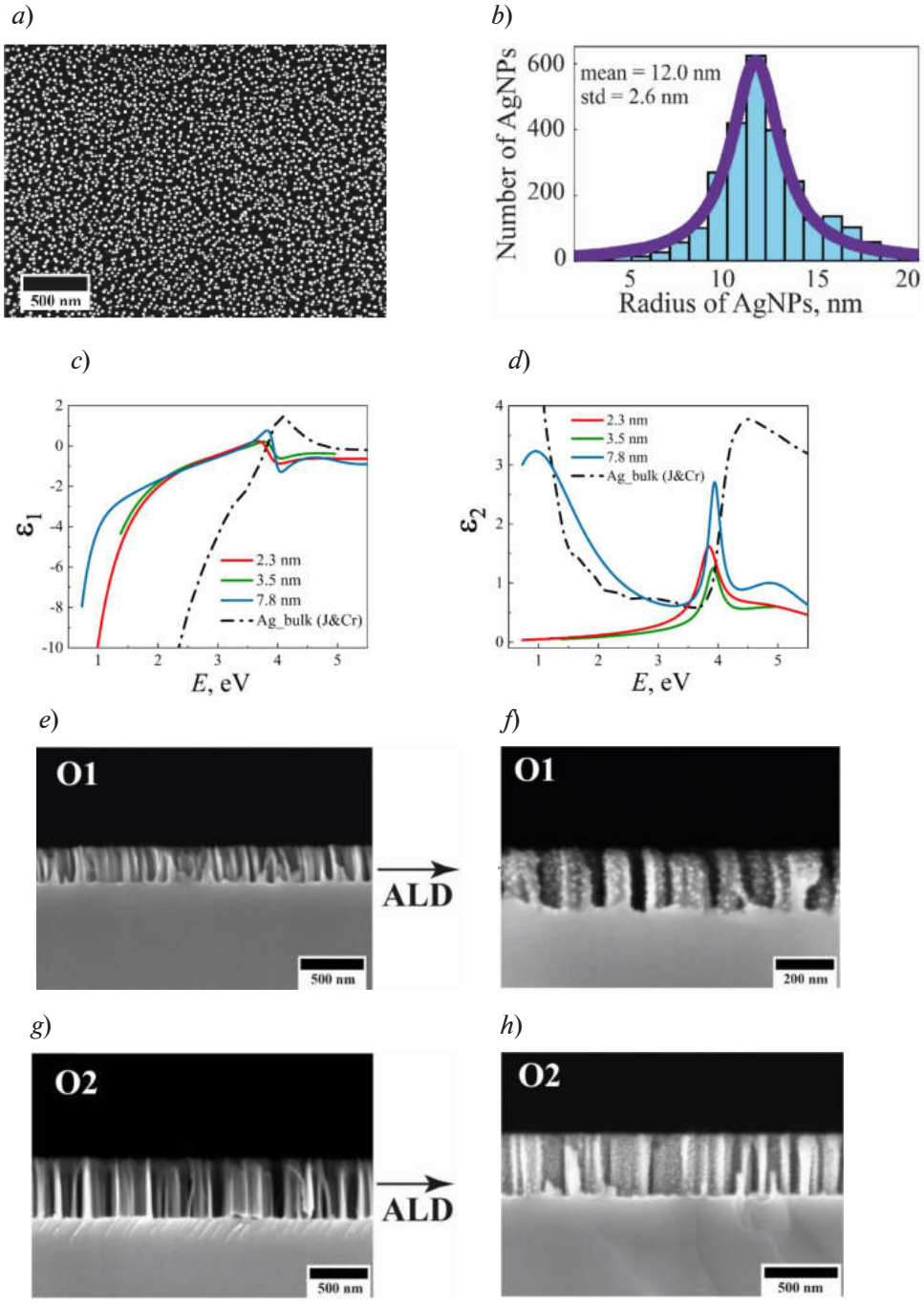

Fig. 2. Top view SEM image of AgNPs deposited by ALD on Si wafer (*a*) and their size distribution (*b*). Spectral dependences of the real part ε_1 (*c*) and imaginary part ε_2 (*d*) of the complex permittivity defined within the framework of the Drude–Lorentz model for three obtained layers of AgNPs with d_{Ag} from 2.3 to 7.8 nm. Cross-section SEM images of the original arrays of SiNW: O1 (*e*) and O2 (*g*). After the deposition of AgNPs by ALD method: Ag/SiNWs (O1) (f) and Ag/SiNWs (O2) (*h*)

The cross-sections SEM-images show the sample O1 (Fig. 2, *e*) with NWs height $h_{SiNWs} = 234$ nm and the sample O2 (Fig. 2, *g*) with $h_{SiNWs} = 469$ nm before ALD process.

Both initial samples of SiNWs (O1 and O2) were placed in the same chamber during AgNPs deposition with flat samples to control the thickness of the Ag layers. The cross-section SEM images for these two samples of Ag/SiNWs are shown in Fig. 2, *f*, *h*. The average diameter of AgNPs deposited on SiNWs using the ALD method was 12 ± 2 nm, which turned out to be almost two times smaller than the AgNP diameter deposited on a flat Si substrate.

To interpret the ellipsometric data of SiNW samples before AgNPs deposition, a model with three-dimensional array of vertical rods of cylinders (Fig. 3, *a*) was chosen, structures located on the substrate is divided into several conditional layers with boundaries parallel to the substrate [10]. Thus, it is possible to model each of the layers with the appropriate height parameters. In addition, since each of the layers is located in a certain array, it is separated by a certain medium (in our case, air), such an array can be considered as a composite consisting of Si and air. For such structures, the effective medium approximation (EMA) is usually used. In our case, a three-layers model was used, in which the parameters of the thickness and Si fraction (h_{Si} and f_{Si}) of each of the three sublayers were fitted. The value of the f_{Si} and the fraction of voids $f_{voids} = (1 - f_{Si})$ dependent on it were determined in the framework of the Bruggeman EMA (B-EMA) [11]. The optical constants of *c*-Si were taken from the handbook [12].

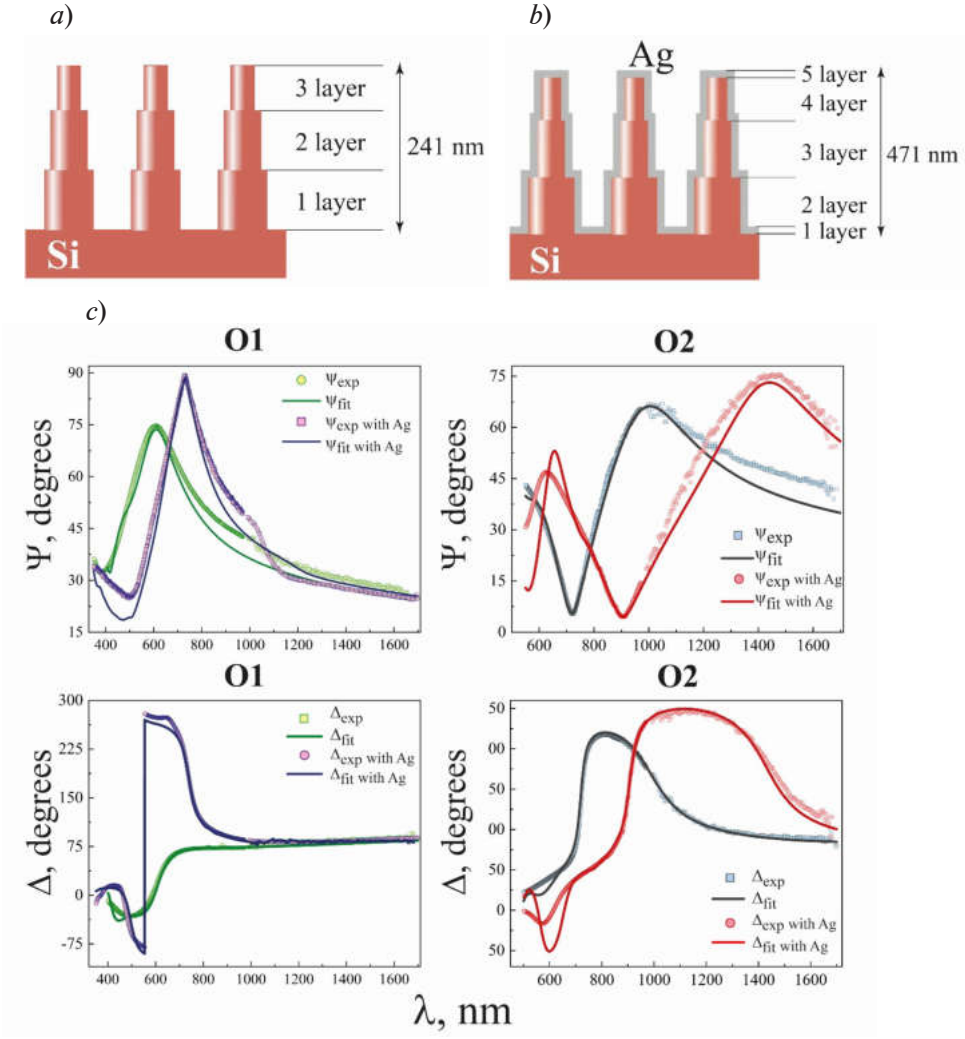

Fig. 3. Schematic model for the structure of SiNWs (sample O1 and O2) (*a*), model for the Ag/SiNW structure with AgNPs layers on the entire surface of SiNWs (*b*). Experimental (exp) and calculated (calc) ellipsometric spectra of SiNWs before (green) and after (violet) AgNPs deposition for sample O1 (*c*). Ellipsometric spectra of SiNWs before (gray) and after (red) AgNPs deposition for sample O2

Calculated ellipsometric angles (ψ and Δ) after fitting for this model are shown in Fig. 3, *c* (green). As a result, f_{Si} and h_{Si} were determined for each of the three sublayers. When summing h_{Si} of all three sublayers, the total height $h_{Si} = 241$ nm is obtained, which is close to the height of 234 nm obtained from the SEM image in Fig. 2, *e*.

To interpret the ellipsometric data for an array of SiNW with AgNPs, the same model was used as for SiNWs, but with the addition of an AgNPs layer that was deposited on the surface of the NWs (Fig. 3, *b*). According to this model, the AgNPs layer fills a certain volume f_{Ag}, which somewhat reduces the f_{voids}, while the f_{Si} should remain unchanged. As a result of fitting these parameters in Fig. 3, *c*, the convergence of the experimental and calculated spectra for the O1 sample with AgNPs ψ(λ) and Δ(λ) (red), respectively, was obtained. It was found that $f_{Ag} = 0.03$ for the 1st sublayer, $f_{Ag} = 0.04 – 0.02$ for layers 2–4, and $f_{Ag} = 0.12$ for the 5th sublayer. A similar approach in interpreting the ellipsometry data was used for another sample (O2) with a SiNWs height approximately 2 times higher than that of the previous sample. Fig. 3, *c* show the measured spectra of the ellipsometric angles ψ_{exp} and Δ_{exp}, as well as the calculated spectra ψ_{calc} and Δ_{calc} before (gray) and after (red) the deposition of AgNPs. The total height of each layer in the original SiNWs structure was estimated as $h_{SiNWs} = 471$ nm. This value is close to the value obtained from the cross-section SEM image of this sample from Fig. 2, *g* with the $h_{SiNWs} = 469$ nm. As in the previous example, a f_{Ag} is added to each wall of the SiNWs in the B-EMA model, assuming some Ag in the sublayers, including the upper and lower sublayers. Fitting the calculated ellipsometric angles (ψ_{calc} and Δ_{calc}) for this model, the convergence to the experiment was obtained. It was found that $f_{Ag} = 0.3$ for the 1st sublayer, $f_{Ag} = 0.08–0.02$ for sublayers 2–4 and $f_{Ag} = 0.22$ for the 5th sublayer.

On the example of two SiNWs samples, after the deposition of AgNPs on them, a shift of the experimental spectra ψ(λ) to the long wavelength region is observed (Fig. 3, *c*), which can be considered a qualitative confirmation of the appearance of an additional component in the structure. And the interpretation of this effect using a multilayer model and of the B-EMA makes it possible to obtain optical data indicating the presence of AgNPs in the Ag/SiNWs composite structure. SEM and non-destructive ellipsometry are complementary techniques for studying arrays of complex high-aspect composite structures.

To numerically calculate the enhanced factor (EF) from the structures under study, we used the model representing a Si substrate on which a cylindrical SiNWs with spheroid AgNPs on its surface were located. A periodic boundary conditions were set on the side faces of the model. The light source is located on the top face of the model. Under the substrate there is a perfectly matched layer that absorbs the radiation falling into it, which makes it possible to reduce the thickness of the simulated substrate. Geometrical parameters (the length of the NW: 250 nm; its diameter: 50 nm; the diameter of the AgNPs: 12 nm and distance between them of 20 nm) were estimated from the SEM image of the experimental sample. As a result, the maximum values of $EF = 2 \cdot 10^6$ at $\lambda = 366$ nm and $4.9 \cdot 10^{10}$ at $\lambda = 780$ nm were obtained for the structure.

Conclusion

SiNWs samples with heights of 234 and 469 nm were obtained by two-stage MACE method. AgNPs were deposited in the high-aspect SiNWs structure by ALD method with the Ag(fod)(PEt_3) precursor.

The fabricated SiNW array and AgNPs layers were studied before and after the preparation of the Ag/SiNWs composite structure using spectroscopic ellipsometry and SEM. From the measured ellipsometric characteristics, the structure of SiNWs was determined using a multilayer model and the B-EMA. The height of the SiNW arrays was determined using spectroscopic ellipsometry, which is in good agreement with the cross-sectional SEM images.

The use of a non-destructive ellipsometric technique made it possible to study the optical characteristics of the Ag/SiNWs structure, as well as their morphological features, which ensured the obtaining of setted thickness and properties of AgNPs when implementing precision ALD technology. The parameters of the experimentally obtained samples were used for further modeling. The expected localization of the electric field on the surface and near the AgNP as a result of the excitation of LPR is observed, and the calculated EF reaches 10^{10}.

REFERENCES

1. **Maier S.A.,** Plasmonics: Fundamentals and Applications, Springer New York, New York 2007.
2. **Schmidt V., Riel H., Senz S., Karg S., Riess W., Gцsele U.,** Realization of a silicon nanowire vertical surround-gate field-effect transistor, Small. 2 (2006) 85–88.
3. **Priolo F., Gregorkiewicz T., Galli M., Krauss T.F.,** Silicon nanostructures for photonics and photovoltaics, Nat. Nanotechnol. 9 (2014) 19–32.
4. **Canham L.,** Handbook of Porous Silicon, first ed., Springer Cham, Cham, 2014.
5. **Hsu S.H., Liu E.S., Chang Y.C., Hilfiker J.N., Kim Y.D., Kim T.J., Lin C.J., Lin G.R.,** Characterization of Si nanorods by spectroscopic ellipsometry with efficient theoretical modeling, Phys. Status Solidi A. 205 (2008) 876–879.
6. **Tolmachev V.A., Astrova E.V., Pilyugina J.A., Perova T.S., Moore R.A., Vij J.K.,** 1D photonic crystal fabricated by wet etching of silicon, Opt. Mater. 27(5) (2005) 831–835.
7. **Huang Z., Geyer N., Werner P., de Boor J., Gösele U.,** Metal-assisted chemical etching of silicon: A review, Adv. Mater. 23 (2011) 285–308.
8. **Miikkulainen V., Leskelä M., Ritala M., Puurunen R.L.,** Crystallinity of inorganic films grown by atomic layer deposition: Overview and general trends, J. Appl. Phys. 113 (2013) 021301.
9. **Nazarov D., Ezhov I., Yudintceva N., Shevtsov M., Rudakova A., Kalganov V., Tolmachev V., Zharova Y., Lutakov O., Kraeva L., Rogacheva E., Maximov M.,** Antibacterial and Osteogenic Properties of Ag Nanoparticles and Ag/TiO2 Nanostructures Prepared by Atomic Layer Deposition. J. Funct. Biomater. 13(2) (2022) 62.
10. **Zharova Y., Ermina A., Pavlov S., Koshtyal Y., Tolmachev V.,** Spectroscopic Characterization of Silicon Wire-Like and Porous Nanolayers in the Process of Metal-Assisted Chemical Etching of Single-Crystal Silicon. Phys. Status Solidi A. 216 (2019) 1900318.
11. **Bruggeman D.A.G.,** Berechnung verschiedener physikalischer Konstanten von heterogenen Substanzen. I. Dielektrizitдtskonstanten und Leitfдhigkeiten der Mischkцrper aus isotropen Substanzen, Ann Phys. 416 (1935) 636–664.
12. **Palik E. D.,** Handbook of optical constants of solids, first ed., Academic Press, Orlando, 1985.

THE AUTHORS

BOLSHAKOV Vladimir O.
lion080895@gmail.com

ERMINA Anna A.
annaermina97@gmail.com
ORCID: 0000-0001-9010-7482

PRIGODA Kristina V.
kristina_prigoda@mail.ru
ORCID: 0000-0002-9728-1982

MAXIMOV Maxim Yu.
maximspbstu@mail.ru
ORCID: 0000-0001-7870-4751

TOLMACHEV Vladimir A.
tva@mail.ioffe.ru
ORCID: 0000-0002-4387-9655

ZHAROVA Yuliya A.
piliouguina@mail.ioffe.ru
ORCID: 0000-0001-7002-5084

Received 14.12.2022. Approved after reviewing 23.01.2023. Accepted 31.01.2023.

Conference materials
UDC 535-4
DOI: https://doi.org/10.18721/JPM.161.323

Enhancing single-photon emission of silicon-vacancy centers in nanodiamonds by a gold film

A.M. Romshin [1] ✉, A.V. Gritsienko [2], A.S. Ilin [3], R.K. Bagramov [4]
V.P. Filonenko [4], A.G. Vitukhnovsky [2], I.I. Vlasov [1]

[1] Prokhorov General Physics Institute, RAS, Moscow, Russia;
[2] Moscow Institute of Physics and Technology (National Research University), Dolgoprudny, Moscow region, Russia;
[3] Kotel'nikov Institute of Radioengineering and Electronics, Fryazino, Moscow region, Russia;
[4] Vereshchagin Institute of High Pressure Physics RAS, Moscow, Russia
✉ alex_31r@mail.ru

Abstract. In this work, the single-photon emission of SiV-centers in HPHT-nanodiamonds positioned on the surface of silicon plate and gold film was investigated. Fluorescence spectra, saturation curves and fluorescence decay curves were measured for a number of SiV-emitters. A reduction in the fluorescence lifetime by ~20%, as well as a spectral shift and a decrease in the width of the zero-phonon line of SiV fluorescence were observed for most emitters. Analysis of the saturation curves revealed an increase in the emission rates by an average of 3 times, and up to 13 times for some particles. The wide variation is primarily associated with the orientation of the dipole moment of the SiV centers and the size of diamond particles, which are the key parameters regulating the coupling of the emitter with surface plasmons in the gold film.

Keywords: nanodiamonds, color centers, single photon, fluorescence, plasmonics

Funding: The study was supported by the Russian Science Foundation grant 22-19-00324.

Citation: Romshin A.M., Gritsienko A.V., Ilin A.S., Bagramov R.K., Filonenko V.P., Vitukhnovsky A.G., Vlasov I.I., Enhancing single-photon emission of silicon-vacancy centers in nanodiamonds by a gold film, St. Petersburg State Polytechnical University Journal. Physics and Mathematics. 16 (1.3) (2023) 135–139. DOI: https://doi.org/10.18721/JPM.161.323

Материалы конференции
УДК 535-4
DOI: https://doi.org/10.18721/JPM.161.323

Усиление однофотонной эмиссии кремний-вакансионных центров в наноалмазах с помощью золотой пленки

А.М. Ромшин [1] ✉, А.В. Грициенко [2], А.С. Ильин [3], Р.Х. Баграмов [4],
В.П. Филоненко [4], А.Г. Витухновский [2], И.И. Власов [1]

[1] Институт общей физики им. А.М. Прохорова, РАН, Москва, Россия;
[2] Московский физико-технический институт (национальный исследовательский университет), г. Долгопрудный, Московская область, Россия;
[3] Институт радиотехники и электроники им. В.А. Котельникова РАН, г. Фрязино, Московская область, Россия;
[4] Институт физики высоких давлений им. Л.Ф. Верещагина РАН, Москва, Россия
✉ alex_31r@mail.ru

Аннотация. В настоящей работе исследовалась однофотонная эмиссия кремний-вакансионных центров в HPHT-наноалмазах, расположенных на поверхности кремния и золотой пленки. Для каждой из частиц записывались спектры люминесценции,

измерялись кривые насыщения и кривые затухания флуоресценции. Для большинства эмиттеров было обнаружено сокращение времени жизни флуоресценции на ~20%, а также зафиксирован спектральный сдвиг и уменьшение ширины бесфононной линии флуоресценции кремний-вакансионных центров. Анализ кривых насыщения позволил обнаружить увеличение скорости однофотонной эмиссии в среднем в 3 раза, а для некоторых частиц – до 13 раз. Широкий разброс связан с ориентацией дипольного момента кремний-вакансионных центров и размером алмазных частиц, являющимися ключевыми параметрами, регулирующими взаимодействие эмиттера с поверхностными плазмонами в золотой пленке.

Ключевые слова: наноалмазы, центры окраски, однофотонная эмиссия, плазмоника

Финансирование: Работа выполнена при поддержке гранта РНФ № 22-19-00324.

Ссылка при цитировании: Ромшин А.М., Грициенко А.В., Ильин А.С., Баграмов Р.Х., Филоненко В.П., Витухновский А.Г., Власов И.И. Усиление однофотонной эмиссии кремний-вакансионных центров в наноалмазах с помощью золотой пленки // Научно-технические ведомости СПбГПУ. Физико-математические науки. 2023. Т. 16. № 1.3. С. 135–139. DOI: https://doi.org/10.18721/ JPM.161.323

Introduction

In recent decades, optical quantum networks rapidly progress in the direction of information processing and transmission [1, 2]. An indispensable building brick for realization of such devices is single photon emitter (SPE) that should meet the requirements of high spectral purity, unprecedented brightness and directivity of radiation. One of the most promising solid-state SPE is the silicon-vacancy (SiV) diamond color center, which has an intense and narrow zero-phonon line (ZPL) at ~738 nm, as well as high spectral and temporal stability [3, 4]. This center possesses near nanosecond fluorescent lifetime resulting in high emission rates with low phonon-mediated acts of emission – more than 70% of total emission is concentrated in ZPL. To improve optical properties and primarily detected count rates the emitters are typically coupled to different microcavities which are aimed to increase local density of optical states and modify the directivity of emission. Many approaches are used for these purposes, including dielectric Fabry-Perot microcavity [5, 6], photonic crystals [7], metasurfaces [8], plasmonic nanoantennas and microstructures [9, 10]. However, despite numerous studies of complex structures, the behavior of single photon emitters even in simple diamond-on-metal systems is still not entirely unclear.

In this paper, we comprehensively study the single photon emission of SiV-centers in HPHT-produced nanodiamonds positioned on the silicon and gold surfaces. By means of confocal spectroscopy and Hanbury-Brown-Twiss interferometry, the fluorescence spectra, saturation curves and decay times of SPE were measured for ten different NDs and the results were quantitively compared for those two surfaces. Such a plain “diamond-on-metal”-structure revealed more than order enhancement of fluorescent signal.

Materials and Methods

The NDs under study were synthesized by high-pressure high-temperature (HPHT) method from a mixture of adamantane ($C_{10}H_{16}$) and detonation nanodiamonds at a pressure ~7.5 GPa, temperatures 1600–1700 °C and time exposition 20 s. To form SiV-centers in diamond matrix a small amount of tetrakis(trimethylsilyl)silane ($C_{12}H_{36}Si_5$) was added to final mixture with the ratio ~Si/(Si+C) = 0.0001%. The 0.1 mg of output ND-powder was diluted in 2 ml of ethanol and then sonicated in ultrasonic bath during 30 min to form homogeneous suspension of NDs. Eventually, 2 μl of the resulting suspension was applied to both silicon and gold surfaces. Pre-characterization in scanning electron microscope (SEM) revealed the size distribution of NDs between 150 nm and 500 nm.

Optical properties of NDs were studied in a home-built confocal microscope equipped with two laser sources, continuous at 660 nm and pulsed at 630 nm ($\tau_{pulse} \sim 80$ ps). To prove the single photon nature of color centers, an emission Hanbury-Brown-Twiss (HBT) interferometer with two avalanche photodiodes (APDs, Excelitas SPCM-AQRH-14-FC) was used. The fluorescence spectra were recorded with an Ocean Insight QEPro spectrometer, and for saturation measurements the APDs with a band pass filter (728–749) were employed. Notice that a long-distance objective Mitutoyo ×100, NA = 0.7 was used in all these measurements. The fluorescence decay rates were analyzed with a Picoquant MicroTime 200 time-correlated single photon counting (TC SPC) module and Olympus lens (×100, NA = 0.95).

Results and Discussion

First, we chose ten random NDs emitters on each of the two substrates – silicon and gold – whose emission is satisfied to criteria of the single photon statistics. An identification of such sources was carried out by measuring the second order autocorrelation function $g^{(2)}(\tau)$ for SiV emission. Fig. 1, *a* demonstrates an example of $g^{(2)}(\tau)$-functions for NDs on silicon (ND-S) and gold (ND-G). The dip at zero time-delay ($\tau = 0$) is less than 0.5 indicating a subpoissonian statistics of light and consequently its single photon nature.

Next, the fluorescence spectra were recorded for selected NDs (Fig. 1, *b*). The narrow line near 738 nm corresponds to the ZPL of the SiV-fluorescence. For each emitter the spectral position (λ_{center}) and full width at half maximum (FWHM) of the ZPL were determined (Fig. 1, *c*). The set of red dots (ND-Ss) is concentrated primarily in short-wavelength range with $\langle \lambda^{Si}_{center} \rangle = 738.7$ nm and $\langle \Delta\lambda^{Si} \rangle = 3.9$ nm. However, some points are far away from mean values (e.g., ~741 nm) which may be explained by the local intrinsic stress in diamond lattice [4]. In contrast, the ZPLs for ND-Gs (blue dots) are narrower on average by factor of 1.7 and red-shifted with $\langle \lambda^{Si}_{center} \rangle = 739.1$ nm. Although the distribution spread is wider for ND-Gs, we believe some of them could be effectively coupled with surface plasmon in gold film resulting in ZPL shift and narrowing.

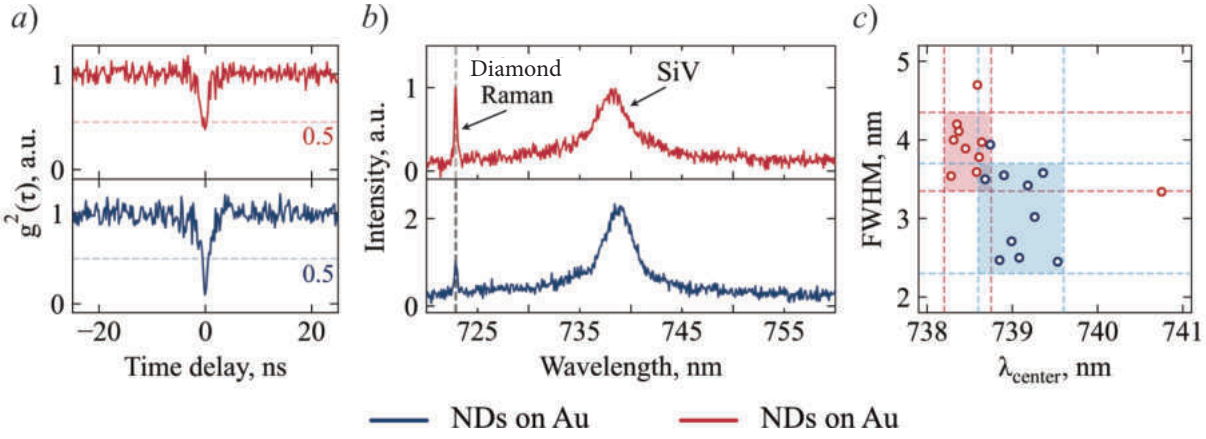

Fig. 1. Optical properties of the emitters in NDs placed on silicon substrate (red) and surface of gold film (blue): a second order autocorrelation function $g^{(2)}(\tau)$ for two NDs (*a*); an instance of fluorescence spectra for two distinct NDs (*b*); post-processing of ZPL λ_{center} and FWHM for ten points for NDs on silicon and gold (*c*).

All data were obtained at 3 mW (before objective) power of continuous 660 nm laser source

To quantify the comparison between ND-Gs and ND-Ss the saturation measurements were performed. For clarity, saturation curves for three NDs on each substrate are demonstrated in (Fig. 2, *b*). The dependences can be described as $I(P) = I^{\infty} \cdot P/(P + P^{sat})$, where I^{∞} is the peak count rate in the limit of large P, P^{sat} is the saturation power. The values I^{∞} and P^{sat} obtained for different NDs on the silicon and gold are presented in (Fig. 2, *c*). One can see the superiority of the emission rate for ND-Gs in high power limit by an enhancement factor (EF) of 3.1 while the EF for distinct emitters reaches the value of $EF_{max} = 13$. The saturation power on average decreases from $\langle P^{sat}_{Si} \rangle = 46.1$ mW to $\langle P^{sat}_{Au} \rangle = 23.9$ mW reflecting an increased extinction of excitation power for ND-Gs.

We also performed time-resolved fluorescence intensity measurements for the NDs (Fig. 2, *a*). The fluorescence decays for ND-Ss demonstrate mono-exponential behavior. In contrast, for ND-Gs deeply sub-ns component was revealed which we believe is not related to SiV-fluorescence, but rather to a diamond-enhanced background from the gold surface [11]. The SiV-fluorescence decay times extracted from the decay curves were averaged over ten NDs and compared between each other. The relaxation time reduces by ~20% on average for emitters on gold surface.

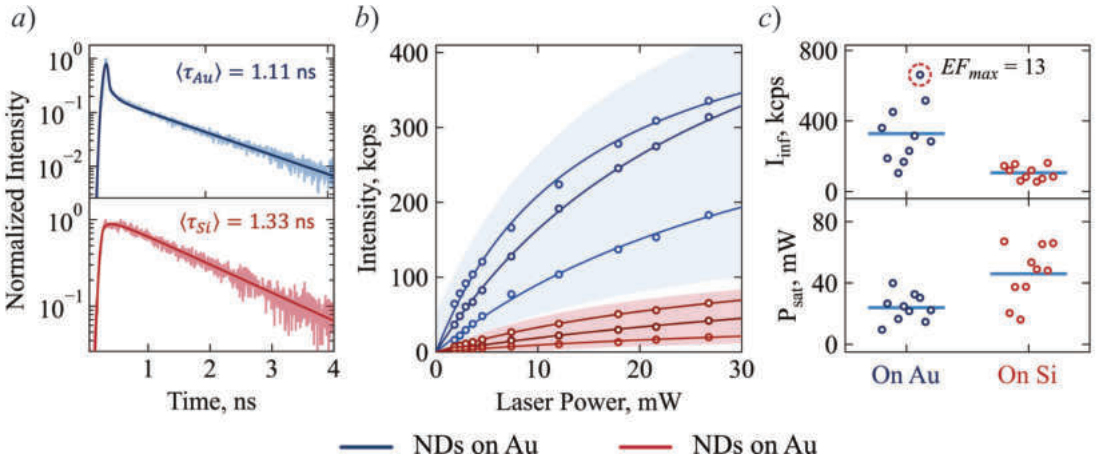

Fig. 2. Decay curves measurements for NDs on silicon (red) and gold surfaces (blue) (*a*). The insets show the decay times averaged over ten NDs on both silicon and gold. Excitation power dependences of the ZPL intensity for three random NDs on different substrates (*b*). The shadow regions illustrate typical scopes for the rest NDs not presented on the graph. Extracted I^{∞} and P^{sat} for ten NDs on both silicon and gold surfaces (*c*). Light blue bars indicate the averaged over ten emitters values

The wide spread of the EF obtained for ND-Gs could be explained by analyzing the major mechanisms affecting the EF. First, observed changes in fluorescence lifetime do not cover the gap for bright emitters (e.g., $EF_{max} > 5$), therefore the Purcell enhancement of spontaneous emission is only minor contributing factor. Second, the P^{sat} reduction hints on increased extinction of excitation power resulting in more effective (by a factor of ~2) photoexcitation of the SiV-centers. The possible reason for this behavior is the size distribution of the NDs which covers a part of the range where Mie-resonances take place. Finally, we believe the dipole orientation relative to the surface normal plays a crucial role in the pronounced enhancement leading to more efficient extraction of the fluorescence signal and resonant interaction with surface plasmon mode in gold film which is partially confirmed by alterations of ZPL spectral characteristics.

Conclusion

In summary, the fluorescent properties of the single SiV-centers in HPHT nanodiamonds on silicon and gold surfaces were studied. Such simple system diamond-on-metal demonstrates an enhancement of SiV-fluorescence by more than an order of magnitude. Relying on the spectral and fluorescent decay measurements we relate the major contribution to the enhancement to the orientation of dipole moment and its coupling to the surface plasmon in gold film. The results obtained serve as a good starting point for the development gold nanocavities and antennas with consequent nanodiamonds integration for the state-of-the-art nanophotonic applications.

Acknowledgments

R.K.B. and V.P.F. synthesized nanodiamonds, A.S.I. prepared silicon substrates and gold film, A.M.R. performed confocal saturation and spectral measurements, A.V.G. measured the fluorescent decay rates, A.M.R. processed the data, prepared illustrations and develop the draft of the manuscript, A.G.V. and I.I.V. supervised the direction of the study. All authors contributed to conceptualization of the study and reviewing of the manuscript.

REFERENCES

1. **Lo H.K., Curty M., Tamaki K.,** Secure quantum key distribution. Nature Photonics, 8(8) (2014), 595–604.

2. **Weber J., Koehl W., Varley J., Janotti A., Buckley B., Walle C., Awschalom D.,** Quantum computing with defects. Proceedings of the National Academy of Sciences, 107(19) (2010), 8513–8518.

3. **Vlasov I., Barnard A., Ralchenko V., Lebedev O., Kanzyuba M., Saveliev A., Konov V., Goovaerts E.,** Nanodiamond photoemitters based on strong narrow-band luminescence from silicon-vacancy defects. Advanced Materials, 21(7) (2009), 808–812.

4. **Pasternak D., Dai J., Kalashnikov D., Sedov V., Martyanov A., Ralchenko V., Krivitsky L., Vlasov I.,** Low-Temperature Silicon-Vacancy Luminescence of Individual Chemical Vapor Deposition Nanodiamonds Grown by Seeding and Spontaneous Nucleation. physica status solidi (a), 218(5) (2021), 2000274.

5. **Romshin A., Kudryavtsev O., Pasternak D., Ekimov E., Vlasov I.,** Coupling of SiV-containing nanodiamonds to a Fabry-Perot microcavity. In Journal of Physics: Conference Series (pp. 012142) (2020).

6. **Benedikter J., Kaupp H., Hummer T., Liang Y., Bommer A., Becher C., Krueger A., Smith J., Hänsch T., Hunger D.,** Cavity-enhanced single-photon source based on the silicon-vacancy center in diamond. Physical Review Applied, 7(2) (2017), 024031.

7. **Schroder T., Schell A., Kewes G., Aichele T., Benson O.,** Fiber-integrated diamond-based single photon source. Nano letters, 11(1) (2011), 198–202.

8. **Kan Y., Ding F., Zhao C., Bozhevolnyi S.,** Directional off-normal photon streaming from hybrid plasmon-emitter coupled metasurfaces. ACS Photonics, 7(5) (2020), 1111–1116.

9. **Bogdanov S., Shalaginov M., Lagutchev A., Chiang C.C., Shah D., Baburin A., Ryzhikov I., Rodionov I., Kildishev A., Boltasseva A., Shalaev V.,** Ultrabright room-temperature sub-nanosecond emission from single nitrogen-vacancy centers coupled to nanopatch antennas. Nano letters, 18(8) (2018), 4837–4844.

10. **Kumar S., Wu C., Komisar D., Kan Y., Kulikova L.F., Davydov V.A., Agafonov V.N., Bozhevolnyi S.I.,** Fluorescence enhancement of a single germanium vacancy center in a nanodiamond by a plasmonic bragg cavity. The J. Chem. Phys. 154 (2021), 044303.

11. **Hugall J.T., Baumberg J.J.,** Demonstrating photoluminescence from au is electronic inelastic light scattering of a plasmonic metal: The origin of SERS backgrounds. Nano Lett. 15 (2015), 2600–2604.

THE AUTHORS

ROMSHIN Alexey M.
alex_31r@mail.ru
ORCID: 0000-0001-9278-6765

GRITSIENKO Alexander V.
grits_alex@rambler.ru

ILIN Alexey S.
alexey.ilin@phystech.edu
BAGRAMOV Rustem K.
bagramov@mail.ru

FILONENKO Vladimir P.
vpfil@mail.ru

VITUKHNOVSKY Alexey G.
alexei@sci.lebedev.ru

VLASOV Igor I.
vlasov@nsc.gpi.ru

Received 14.12.2022. Approved after reviewing 23.01.2023. Accepted 06.02.2023.

Conference materials
UDC 538.958
DOI: https://doi.org/10.18721/JPM.161.324

Polarimetry of waveguiding heterostructures with quantum well-dots

A.A. Kharchenko [1] ✉, A.M. Nadtochiy [1,2,3], S.A. Mintairov [3],
N.A. Kalyuzhnyy [3], M.V. Maximov [1]

[1] Alferov University, St Petersburg, Russia;
[2] National Research University Higher School of Economics, St Petersburg, Russia;
[3] Ioffe Institute, St Petersburg, Russia
✉ antoshkerrr@gmail.com

Abstract. The effect of the waveguide and the quantum well-dot active region on polarization of transmitted light in laser-like heterostructures was studied with the polarimetry technique. The waveguide structures with quantum well-dots were demonstrated to have almost no effect on the transmitted radiation polarization when it is parallel or perpendicular to active region layers. However, in the case of intermediate angle of linear polarization, the transmitted radiation represents a mixture of elliptically polarized and unpolarized light. The largest degree of depolarization found was at 45° of linear polarization angle of the input radiation. Depolarization was found to increase with decreasing of number of QWD layers and reaches 23% for a single layer.

Keywords: optical polarization, Stokes parameters, quantum well-dots, waveguiding heterostructures

Funding: The study was supported by the Ministry of Science and Higher Education of the Russian Federation as part of project FSRM-2023-0010.

Citation: Kharchenko A.A., Nadtochiy A.M., Mintairov S.A., Kalyuzhnyy N.A., Maximov M.V., Polarimetry of waveguiding heterostructures with quantum well-dots, St. Petersburg State Polytechnical University Journal. Physics and Mathematics. 16 (1.3) (2023) 140–145. DOI: https://doi.org/10.18721/JPM.161.324

Материалы конференции
УДК 538.958
DOI: https://doi.org/10.18721/JPM.161.324

Поляриметрия волноводных гетероструктур с квантовыми яма-точками

А.А. Х рченко [1] ✉, А.М. Н дточий [1,2,3], С.А. Минт иров [3],
Н.А. К люжный [3], М.В. М ксимов [1]

[1] Академический университет имени Ж.И. Алфёрова РАН, Санкт-Петербург, Россия;
[2] Национальный исследовательский университет "Высшая школа экономики",
Санкт-Петербургский филиал, Санкт-Петербург, Россия;
[3] Физико-технический институт им. А.Ф. Иоффе РАН, Санкт-Петербург, Россия
✉ antoshkerrr@gmail.com

Аннотация. Методом поляриметрии исследовано влияние волновода и активной области лазерных гетероструктур на основе квантовых яма-точек на поляризацию проходящего излучения. Установлено, что волноводные структуры с квантовыми яма-точками практически не оказывают влияния на проходящее излучение с поляризацией, параллельной или перпендикулярной слоям активной области. Однако, при вводе излучения

с промежуточным углом линейной поляризации, выходящее излучение представляет собой смесь эллиптически поляризованного и неполяризованного света. Обнаружено, что деполяризация излучения максимальна при угле поляризации входящего излучения 45°, при этом она обратно пропорционально зависит от количества слоев квантовых яма-точек в активной области, достигая 23% для однослойной структуры.

Ключевые слова: оптическая поляризация, параметры Стокса, квантовые яма-точки, волноводные гетероструктуры

Финансирование: Работа выполнена при поддержке Министерства науки и высшего образования Российской Федерации в рамках проекта FSRM-2023-0010.

Ссылка при цитировании: Харченко А.А., Надточий А.М., Минтаиров С.А., Калюжный Н.А., Максимов М.В. Поляриметрия волноводных гетероструктур с квантовыми яма-точками // Научно-технические ведомости СПбГПУ. Физико-математические науки. 2023. Т. 16. № 1.3. С. 140–145. DOI: https://doi.org/10.18721/ JPM.161.324

Introduction

At present time, there is a great interest in studies of quantum heterostructures with an intermediate properties between quantum wells and quantum dots [1], for example such as a quantum wires [2], well-island [3], wire-on-well [4], etc. Quantum well-dots (QWDs) are one of such type of structures, which can be described as InGaAs/GaAs quantum well (QW) modulated in thickness and composition or a superdense array of small InGaAs quantum dots (QDs). QWDs are free of some of the drawbacks of both QWs and QDs but keeps their key features. For example, QWDs have a significantly higher gain (absorption) compared to InAs/GaAs QDs, and moreover allow growing more than 15 stacked dislocation-free layers, which is hard to realize in case of InGaAs/GaAs QWs [5, 6]. QWDs have been intensively studied over the past decade. Recently, it was found that planar waveguides with QWDs demonstrate TE-selective ground state absorption [7]. The selectivity of absorption was found to strongly decrease with an increase in either the waveguide length or the number of QWDs layers. This behavior is highly likely due to a depolarization of radiation in the waveguide. In this work, the influence of a waveguide and the QWD active region on transmitted radiation polarization is studied by polarimetry technique. At the present time a lot of experimental studies of emission polarization of nanostructures have been published, but they dealt mainly with spontaneous or stimulated emission of the structures themselves [8, 9]. Transmitted light polarimetry has been investigated for passive optical waveguides [10]. To the best of our knowledge this is the first study of the of transmitted light polarimetry of waveguides with a nanostructure active region.

Materials and Methods

The samples based on AlGaAs *p-i-n*-structures, similar in design to typical edge-emitting lasers, were grown by metalorganic vapor-phase epitaxy (MOVPE) on a vicinal GaAs(100). The active region located in the center of the 800 nm thick GaAs waveguide layer contains 1, 2, 5, or 10 QWD layers separated with 40 nm thick GaAs spacers. Each QWD layer, in turn, is formed by deposition of 8 monolayers of $In_{0.4}Ga_{0.6}As$. Broad-area (50 μm and 100 μm wide) stripe waveguide samples of 2-mm length were studied in the experiment. Facet coatings were not used. The details of growth and processing can be found in other sources [1]. The scheme of the experimental setup is shown in Fig. 1.

A tunable laser (Sacher Lasertechnik) was set at wavelength 1050 nm corresponding to the QWD ground state absorption maximum [7]. A half-wave plate in combination with a Glan-Taylor prism was used as a rotator of linear polarization (LP). Then the radiation was focused on the front waveguide facet by the microlens. The sample was operated in the short circuit mode. The light focusing was monitored by a photocurrent level. The output radiation after passing through the combination of a quarter-wave plate and a linear analyzer was detected by a Si

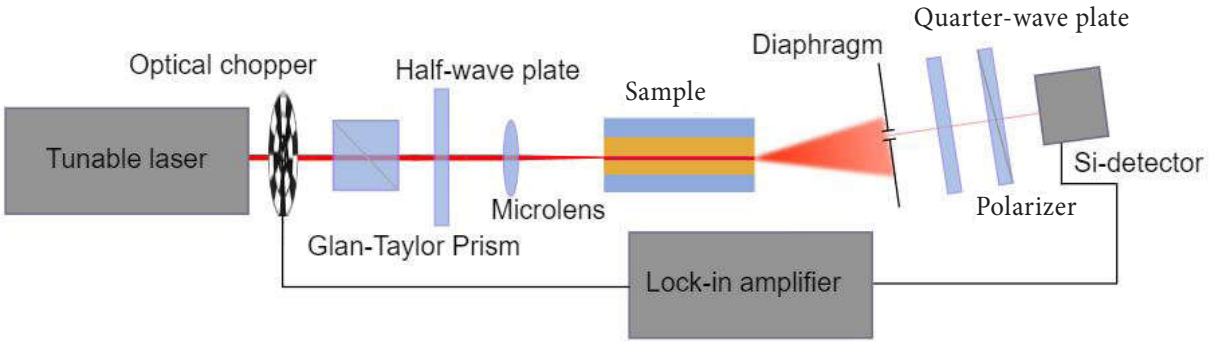

Fig. 1. Schematic representation of experimental setup

photodiode using a lock-in amplifier. To minimize a detection of radiation crosstalk, we used a diaphragm. Thus, we were able to define the Stokes parameters of radiation passed through the sample by caring out the six measurements of the flux P (table. 1) [11].

Table 1

Measuring of Stokes parameters

Measured flux	Experimental setup configuration
P_{H}	Linear polarizer is set to 0° (i.e., polarizer is set to TE-transmission). Quarter-wave plate is not used.
P_{v}	Linear polarizer is set to 90° (i.e., polarizer is set to TM-transmission). Quarter-wave plate is not used.
P_{45}	Linear polarizer is set to 45°. Quarter-wave plate is not used.
P_{135}	Linear polarizer is set to 135°. Quarter-wave plate is not used.
P_{r}	Linear polarizer is set to 45° and quarter-wave plate is set to 0° (by fast axe).
P_{L}	Linear polarizer is set to 135° and quarter-wave plate is set to 0°.

Results and Discussion

The obtained data were used to calculate the Stokes vector:

$$\boldsymbol{S} = \begin{bmatrix} s_0 \\ s_1 \\ s_2 \\ s_3 \end{bmatrix} = \begin{bmatrix} P_H + P_V \\ P_H - P_V \\ P_{45} - P_{135} \\ P_R - P_L \end{bmatrix}. \quad (1)$$

These parameters allow us to separate the depolarized part of radiation and to plot polarization ellipses, which represent the trajectory of the electric field vector **E**. For instance, these ellipses are shown in Fig. 2 for single QWD layer sample and different initial LP. The unpolarized part of the radiation is schematically shown as a dash circle and input LP radiation is also marked as red dotted line.

Polarization parameters such as the degree of polarization (DOP), ellipticity, azimuth of ellipse orientation (major axis) have been calculated as described in insets of Fig. 3 and plotted as functions of the angle of the LP of input radiation, α (Fig. 3) for the given structures 2 mm in length with a different number of QWD layers (1, 2, 5, 10).

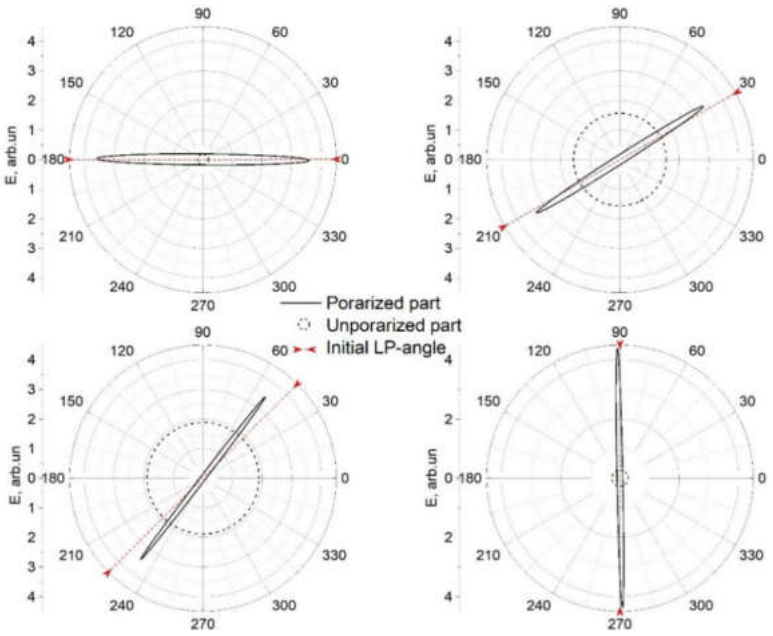

Fig. 2. Polarization ellipses of output radiation from single QWD layer sample. Unpolarized part of the radiation is schematically shown as a dash line circle. The angle of LP of input radiation is marked with red dotted line

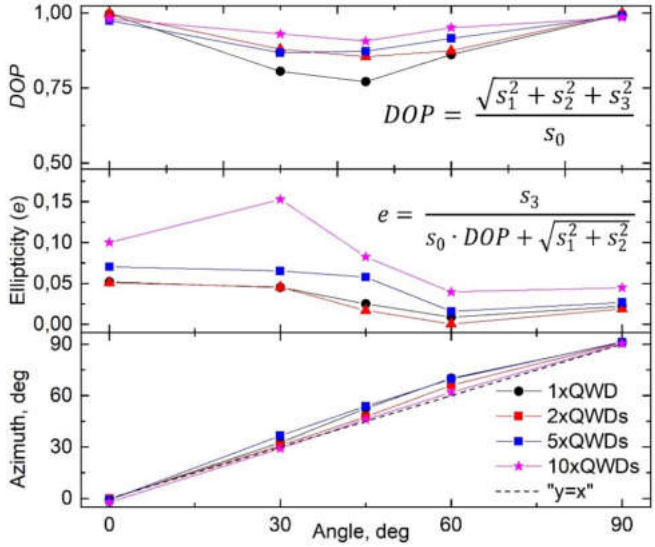

Fig. 3 Degree of polarization (DOP), ellipticity *e* and angle of ellipse orientation (azimuth) as functions of angle of LP of input radiation α for samples 2 mm in length with different number of QWD layers

In terms of polarization one can separate two different cases. In the first one, TE- or TM-polarization of the input radiation remains practically unchanged except of slightly increased ellipticity. Also, there are some differences in the amplitude of transmitted TE- and TM-polarized radiation arising from TE-selectivity of absorption of QWDs [7] which is out of the scope of the paper. In the second case, namely intermediate polarization angle α of the input radiation (not pure TE or TM) the transmitted radiation represents a mixture of depolarized and elliptically polarized light. The azimuth of the ellipse of the transmitted radiation follows, in general, the angle of LP of the input radiation α being slightly shifting towards the TM component. This shift occurrs due to anisotropy of QWDs absorption, which is to say that absorption of the TE component during transmission of the radiation in the waveguide results in TM dominance at the end and, therefore, in a small rotation of the ellipse.

Dependences of ellipticity of the transmitted radiation on α are complicated. However, the tendency of increase of ellipticity with the number of QWD layers is clearly seen. We attribute this behavior to the presence of birefringence of the investigated samples due to both difference of effective index between TE and TM optical modes in the waveguide of the structures and birefringence of the QWDs themselves because of their dichroism. Therefore, for LP light with intermediate polarization angles, such waveguides represent a waveplate meaning that ellipticity of transmitted light may increase or decrease depending on the waveguide length and α. The experimental point for the 10xQWDs sample at $\alpha = 30°$ seems like an outlier which however does not affect the above tendency.

It is of the greatest interest to analyze the dependences of DOP. As discussed in [7], depolarization results in conversion of the TM-polarized light to TE-polarized one inside waveguides with QWDs. This effect causes strong absorption of TM-polarized radiation in long waveguide structures with QWDs, which is unexpected because QWDs active region predominantly absorb TE-polarized emission. It is the polarization conversion that is responsible for this phenomenon. As evident from Fig. 3, DOP is minimal at $\alpha \approx 45$ degrees and is as small as 0.77 (i.e., depolarization, (1-DOP) reaches 23%) in case of single QWD layer. Moreover, depolarization is tending to decrease with an increase in the number of QWD layers. This observation is contradicting to that reported earlier data [7], in which the larger QWD layer quantity resulted in the higher degree of the depolarization. We suggest that the increase in the number QWD layers leads to an increase in TE-absorption countervailing the effect of TM to TE conversion due to the depolarization. We are carrying out additional investigations to prove this suggestion.

Conclusion

Laser-like waveguide structures with different number of QWD layers were studied with polarimetry technique. Transmission of TE- or TM- polarized radiation through the waveguides was found to occur without significant change of polarization state, whereas transmission of linearly polarized light with intermediate polarization angle results in an output of elliptically polarized light with an addition of depolarized one. The depolarization reached 23% at 45° LP angle for single QWD layer structure, and is found to decrease with the number of QWD layers in the waveguide. The results obtained may be useful for engineering waveguide-based devices with a QWD-based active medium.

REFERENCES

1. **Maximov M.V., Nadtochiy A.M., Mintairov S.A., Kalyuzhnyy N.A., Kryzhanovskaya N.V., Moiseev E.I., Gordeev N.Y., Shernyakov Y.M., Payusov A.S., Zubov F.I., Nevedomskiy V.N., Rouvimov S.S., Zhukov A.E.,** Light emitting devices based on quantum well-dots, Appl. Sci. 10(3) (2020) 1038.

2. **Al Saqri N.A., Felix J.F., Aziz M, Kunets V.P., Jameel D., Taylor D., Henini M., Abd El-Sadek M.S., Furrow C., Ware M.E., Benamara M., Mortazavi M., Salamo G.,** Investigation of electrically active defects in InGaAs quantum wire intermediate-band solar cells using deep-level transient spectroscopy technique, Nanotechnology. 28(4) (2017) 045707.

3. **Yu Q., Li X., Jia Y., Lu W., Zheng M., Zhang X., Ning Y., Wu J.,** InGaAs-Based Well-Island Composite Quantum-Confined Structure with Superwide and Uniform Gain Distribution for Great Enhancement of Semiconductor Laser Performance, ACS Photonics 5 (2018) 4896−4902.

4. **Cho H., Toprasertpong K., Sodabanlu H., Watanabe K., Sugiyama M., Nakano Y.,** Stability and controllability of InGaAs/GaAsP wire-on-well (WoW) structure for multi-junction solar cells, J. Cryst. Growth 464 (2017) 86−93.

5. **Mintairov S.A., Kalyuzhnyy N.A., Maximov M.V., Nadtochiy A.M., Rouvimov S., Zhukov A.E.,** GaAs quantum well-dots solar cells with spectral response extended to 1100 nm, Electron. Lett. 51 (2015) 1602−1604.

6. **Nadtochiy A.M., Gordeev N.Y., Kharchenko A.A., Mintairov S.A., Kalyuzhnyy N.A., Shernyakov Y.M., Maximov M.V., Zhukov A.E., Berdnikov Y.,** Saturated layer gain in waveguides with InGaAs quantum well-dot heterostructures, J. Light. Technol. 39(23) (2021) 7479–7485.

7. **Kharchenko A.A., Nadtochiy A.M., Mintairov S.A., Shernyakov Y.M., Serin A.A., Gordeev N.Y., Maximov M.V., Zhukov A.E.,** Study of waveguide absorption in InGaAs "quantum well-dots" heterostructures, Nano-Structures and Nano-Objects. 25 (2021) 100628.

8. **Yu Q.N., Jia Y., Lu W., Wang M.Q., Li F., Zhang J., Ning Y.Q., Wu J.,** Experimental characterization of true spontaneous emission rate of optically-pumped InGaAs/GaAs quantum-well laser structure, AIP Advances 7(8) (2017) 085319.

9. **Konishi K., Nomura M., Kumagai N., Iwamoto S., Arakawa Y., Kuwata-Gonokami M.,** Circularly polarized light emission from semiconductor planar chiral nanostructures, Physical review letters 106(5) (2011) 057402.

10. **Erofeeva M.S., Dmitriev A.L.,** High-accuracy IR polarimetry of waveguide optical elements, Journal of Optical Technology. 74(6) (2007) 419–423.

11. **Bass M., Van Stryland E.W., Williams D.R., Wolfe W.L., Bowers J.E., Wey Y.G.,** Handbook of Optics: Fundamentals, Techniques and Design. McGraw-Hill, (1995) 22.8–22.10.

THE AUTHORS

KHARCHENKO Anton A.
antoshkerrr@gmail.com
ORCID: 0000-0001-9686-2649

NADTOCHIY Alexey M.
al.nadtochy@mail.ioffe.ru
ORCID: 0000-0003-0982-907X

MINTAIROV Sergey A.
sergey.mintairov@solardots.ru
ORCID: 0000-0002-6176-6291

KALYUZHNYY Nikolay A.
nickk@mail.ioffe.ru
ORCID: 0000-0001-8443-4663

MAXIMOV Mikhail V.
maximov.mikh@gmail.com
ORCID: 0000-0002-9251-226X

Received 14.12.2022. Approved after reviewing 25.01.2023. Accepted 03.02.2023.

Optoelectronic and nanoelectronic devices

Conference materials
UDC 538.9
DOI: https://doi.org/10.18721/JPM.161.325

Stretchable carbon-nanotube films as opto-mechanically controllable modulators of terahertz radiation

M.I. Paukov [1] ✉, V.V. Starchenko [1], D.V. Krasnikov [2], S.S. Zhukov [1],
B.P. Gorshunov [1], A.G. Nasibulin [2], A.V. Arsenin [1], V. Volkov [1]

[1] Moscow Institute of Physics and Technology (State University), Dolgoprudny, Moscow Region, Russia;
[2] Skolko Institute of Science and Technology, Moscow, Russia
✉ paukov.mi@phystech.edu

Abstract. This study considers the optical modulation parameters of THz radiation generated via optical-pump terahertz probe spectroscopy, passing through thin films of single-walled carbon nanotubes (SWCNT), attached onto the stretchable substrate. We investigated the dependence of photoconductivity of the stretched film on the elongation and orientation of its direction towards THz beam polarization. We interpreted the changes observed, establishing the key factors affecting the photoconductive pathways. The obtained modulators were characterized practically: the wide range of modulation depths (MD) (up to 100%) and fast lifetimes of photoinduced charge carriers (5 ps) were marked. This research guides the way to construct the devices of switchable optoelectronics, which are of a perspective in the THz data transfer systems.

Keywords: Terahertz modulator, carbon nanotubes, THz-TDS, optical-pump terahertz probe spectroscopy, ultrafast devices

Funding: This study was funded by a Russian Science Foundation grant 21-79-10097.

Citation: Paukov M.I., Starchenko V.V., Krasnikov D.V., Zhukov S.S., Gorshunov B.P., Nasibulin A.G., Arsenin A.V., Volkov V., Stretchable carbon-nanotube films as opto-mechanically controllable modulators of terahertz radiation, St. Petersburg State Polytechnical University Journal. Physics and Mathematics. 16 (1.3) (2023) 146–150. DOI: https://doi.org/10.18721/JPM.161.325

Материалы конференции
УДК 538.9
DOI: https://doi.org/10.18721/JPM.161.325

Растягиваемые плёнки углеродных нанотрубок как опто-механически контролируемые модуляторы терагерцового излучения

М.И. П уков [1] ✉, В.В. Ст рченко [1], Д.В. Кр сников [2], С.С. Жуков [1],
Б.П. Горшунов [1], А.Г. Н сибулин [2], А.В. Арсенин [1], В. Волков [1]

[1] Московский физико-технический институт (государственный университет),
г. Долгопрудный, Московская область, Россия;
[2] Сколковский институт науки и технологий, Москва, Россия
✉ paukov.mi@phystech.edu

Аннотация. В данной работе изучались параметры оптической модуляции терагерцового сигнала при прохождении через тонкие плёнки одностенных углеродных нанотрубок УНТ, нанесённых на растягиваемую подложку, методом спектроскопии оптической

накачки терагерцового зондирования. Было проведено исследование поведения фотопроводимости в зависимости от ряда параметров: относительного удлинения и сжатия плёнки, расположения по отношению к поляризации терагерцового излучения. Мы представили интерпретацию изменения параметров фотопроводимости в зависимости от растяжения, отметив факторы, влияющие на изменение фотопроводящих путей. Полученные модуляторы также были охарактеризованы с практической точки зрения: были отмечены широкий диапазон глубины модуляции (от 5 до 100%) и малое время релаксации фотовозбуждённых носителей зарядов (порядка 5 пс), Данное исследование позволяет создавать устройства перестраиваемой оптоэлектроники перспективные в терагерцовых системах передачи информации.

Ключевые слова: Терагерцовый модулятор, углеродные нанотрубки, терагерцовая спектроскопия во временной области, спектроскопия оптической накачки терагерцовой пробы, ультрабыстрые устройства

Финансирование: РНФ №21-79-10097.

Ссылка при цитировании: Пауков М.И., Старченко В.В., Красников Д.В., Жуков С.С., Горшунов Б.П., Насибулин А.Г., Арсенин А.В., Волков В. Растягиваемые плёнки углеродных нанотрубок как опто-механически контролируемые модуляторы терагерцового излучения // Научно-технические ведомости СПбГПУ. Физико-математические науки. 2023. Т. 16. № 1.3. С. 146–150. DOI: https://doi.org/10.18721/ JPM.161.325

Introduction

Terahertz radiation has found application in many spheres of life, from detection of exploding weapons to tumor diagnostics. Thanks to wide bandwidth and relatively small attenuation, THz waves may come into practice for secure connections, which makes them promising candidates for high-speed wireless data transfer. Modulation of a signal is an important feature which should be taken into account in design of these communications. It is determined by the conductivity of the medium through which THz radiation is passing. This makes it possible to control the modulation parameters optically, thermally and electrically.

Traditional bulk semiconductors like GaAs, Ge and Si, being modulated electrically or optically, have only one high parameter, either modulation depth or modulation speed (order of hundreds of GHz) [1–3]. At the same time, low dimensional structures like graphene, carbon nanotubes and 2D transition metal dichalcogenides demonstrate both high MD and modulation speed (MS).

However, no stretchable modulators with such parameters are found. In this paper, the parameters of opto-mechanical THz modulation for the samples of carbon nanotube films, applied onto stretchable substrate, are studied by means of OPTP spectroscopy. The given modulators are characterized from practical view. High modulation depth (approximately 100%) and small relaxation time of photoinduced charge carriers (5 ps) have been reported. This study allows to construct switchable devices for optoelectronics, promising for THz-range systems for data transfer.

Materials and Methods

SWCNTs were synthesized by the aerosol chemical vapor deposition (CVD) method and then transferred on a 0.2 mm thick elastomer [4, 5]. The SWCNT film with thicknesses of 106 nm, corresponding to optical transmittance of 60% at 550 nm wavelength, consisted of one-third metallic and two-thirds semiconducting SWCNTs, which were initially randomly aligned. SWCNT film on the elastomer was placed into the home-made mechanical stretcher. The film holder was placed into the spectrometer so that the probe THz beam polarization was perpendicular and parallel according to the stretching direction.

The pump beam was generated by an optical parametric amplifier, seeded by a 1 kHz, 40 fs, 800 nm pulse. The average pump power was estimated as 3.92 mW, the and the width of the pump beam on the sample was 0.9 mm. Here, a wavelength of 600 nm for pump was used (above the E11 and E_{22} excitonic transitions of the CNTs). The probe beam was generated using home-made conventional THz-TDS setup as described in [6], allowing us to measure both equilibrium conductivity and photoconductivity. The extraction of the photoconductivity was implemented according to our previous study [7].

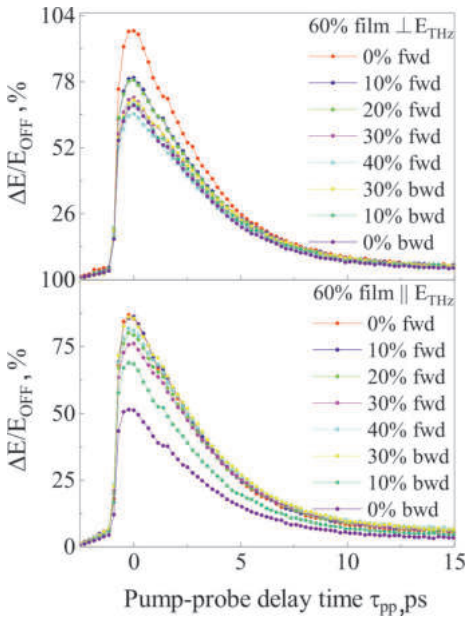

Fig. 1. Modulation depth in transmission as a function of pump-probe delay time when the elongation is perpendicular (top) and parallel (bottom) to the polarization of the THz probe beam.

Results and Discussion

Studying the dynamics of photoinduced charged carriers for different stretching parameters, we discovered that the modulation depth, defined at the peak (see Fig. 1), decreases with growing elongation and becomes irreversible when compressed. It is observed that CNTs possess high modulation depth of approximately 100% at the start, which was seldom reported for any other materials. In addition, CNTs demonstrate high modulation speed (MS), which is a frequency of relaxation and defined as the inverted lifetime of the photoexcited charge carriers. The latter was estimated from the exponential decay as the time, when the amplitude of the detected THz radiation is reduced by e times with respect to its maximum. Since the relaxation time is approximately estimated as 5 ps, MS is 210–250 GHz (it is different due to the stretching). Particular factors that may affect the behavior of photoconductivity and the defined parameters MD and MS include alignment of the SWNTs in the direction of stretching and their tendency to form bundles because of the electrostatic interaction between nanotubes. These contributions influence the photoconductivity pathways and, hence, the aforementioned quantities. However, these changes should be analyzed separately for clearer understanding.

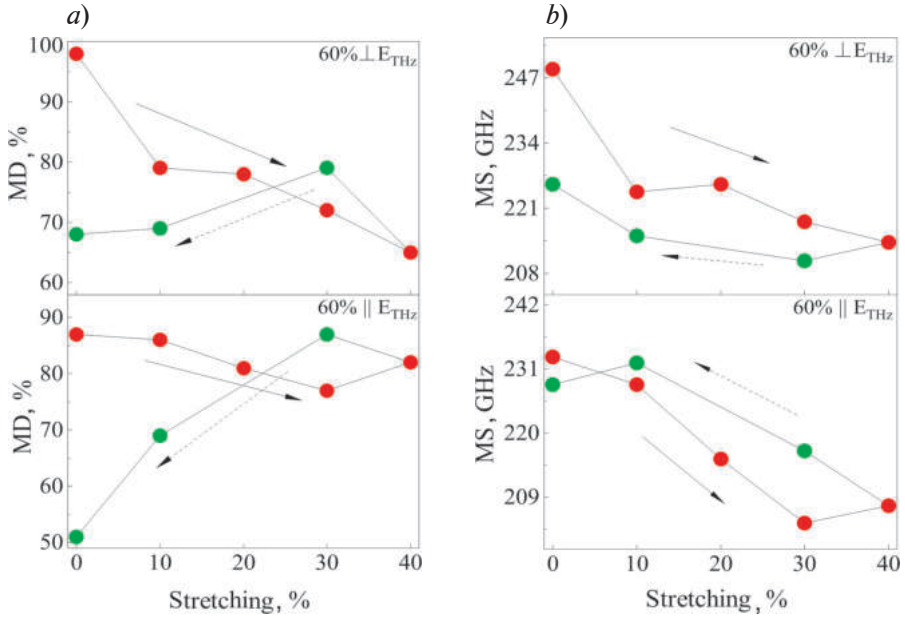

Fig. 2. Transmission-mode MD (*a*) and MS (*b*) for sample with transmission 60% at 600 nm (60% film in Fig. 1) at stretching varying from 0 to 40 % ('fwd' in the graph) and compression from 40 to 0 % ('bwd' in the graph). The arrows indicate the direction of stretching and the following compression.

Conclusion

In this work, we showed the influence of stretching on optically controlled SWCNT modulators for the first time. They show almost 100% modulation depth and relatively high modulation speed of almost 250 GHz. At the same time, it was shown that the simultaneous optical modulation and stretching make modulators more tunable. This information can be used to predict the performance of stretchable modulators based on SWCNT. The backward contraction reveals that modulation depth before and after stretching is different, which reflects irreversible properties of SWCNTs photoconductivity. However, once the mechanical modulation is performed, then it can be corrected via the change of the optical pump.

Acknowledgments

The authors would like to thank the Warwick Centre for Ultrafast Spectroscopy (University of Warwick, UK) for access to the OPTP spectrometer used.

REFERENCES

1. **Rahm M., Li J.-S., and Padilla W.J.,** THz wave modulators: A brief review on different modulation techniques, Journal of Infrared, Millimeter, and Terahertz Waves, vol. 34, no. 1, 330 Nov. 2012. pp. 1–27.

2. **Beard M.C., Turner G.M., Schmuttenmaer C.A.,** Subpicosecond carrier dynamics in low-temperature grown GaAs as measured by time-resolved terahertz spectroscopy, Journal of Applied Physics, vol. 90, no. 12, pp., Dec. 2001, 5915–5923.

3. **Che Z. et al.,** Graphene controlled brewster angle device for ultra broadband terahertz 335 modulation, Nature Communications, vol. 9, no. 1, Nov. 2018.

4. **Khabushev E.M. et al.,** Machine learning for tailoring optoelectronic properties of single-walled carbon 369 nanotube films, The Journal of Physical Chemistry Letters, vol. 10, no. 21, 370 Oct. 2019, pp. 6962–6966.

5. **Khabushev E.M. et al.,** Structure-dependent performance of single-walled carbon nanotube films in transparent and 374 conductive applications, Carbon, vol. 161, May 2020, pp. 712–717.

6. **Monti M. et al.,** Efficient Intraband Hot Carrier Relaxation in the Perovskite Semiconductor $Cs_{1-x}Rb_xSnI_3$ Mediated by Strong Electron-Phonon Coupling, Journal of Physical Chemistry 384 C, vol. 122, no. 36, 2018, pp. 20669–20675.

7. **Burdanova M.G. et al.,** Giant negative terahertz photoconductivity in controllably doped 386 carbon nanotube networks, ACS Photonics, vol. 6, no. 4, 2019, pp. 1058–1066.

8. **Gokus T. et al.,** Exciton decay dynamics in individual carbon nanotubes at room temperature, APL 92, 2008, 153116.

9. **Gilshteyn E.,** Components for stretchable electronics based on single-walled carbon nanotubes, PhD thesis, Moscow, 2018.

THE AUTHORS

PAUKOV Maksim I.
Paukov.mi@phystech.edu
ORCID: 0000-0003-1039-3170

STARCHENKO Vladimir V.
Starchenko.vv@ phystech.edu

KRASNIKOV Dmitriy V.
d.krasnikov@skoltech.ru
ORCID: 0000-0002-6721-6530

GLADUSH Yuriy G.
y.gladush@skoltech.ru
ORCID: 0000-0002-1289-2654

ZHUKOV Sergey S.
zhukov.ss@mipt.ru

GORSHUNOV Boris P.
bpgorshunov@gmail.com
ORCID: 0000-0002-6534-1880

NASIBULIN Albert G.
a.nasibulin@skoltech.ru
ORCID: 0000-0002-1684-3948

ARSENIN Alexey V.
Arsenin.av@mipt.ru
ORCID: 0000-0002-7506-4389

VOLKOV Valentyn S.
vsv@mipt.ru
ORCID: 0000-0003-2637-1371

BURDANOVA Maria G.
Burdanova.mg@mipt.ru
ORCID: 0000-0001-5439-2933

Received 10.12.2022. Approved after reviewing 13.02.2023. Accepted 22.03.2023.

Conference materials
UDC 535.3
DOI: https://doi.org/10.18721/JPM.161.326

Optically controlled memristor based on $ZrO_2(Y)$ film with Au nanoparticles

M.A. Ryabova [1] ✉, D.O. Filatov [1], A.S. Novikov [1], M.E. Shenina [1],
I.N. Antonov [1], V.E. Kotomina [1], D.A. Liskin [1], A.V. Ershov [1], O.N. Gorshkov [1]

[1] Lobachevskii University of Nizhnii Novgorod, Nizhnii Novgorod, Russia
✉ rmargo01@mail.ru

Abstract. We report on the fabrication and investigation of prototype optically controlled memristors based on $ZrO_2(Y)$ (12% mol. Y_2O_3) with Au nanoparticles (NPs) of 2–3 nm in diameter formed by layer-by-layer magnetron deposition of $ZrO_2(Y)/Au/ZrO_2(Y)$ stacks followed by annealing. The upper contacts of the memristor stacks were made from indium-tin oxide (ITO) to provide the access of photoexcitation to the active Au NP array. The cross-point memristor devices with the active region sizes of 2020 μm^2 were defined by standard photolithography with wet etching. A shift of the switching voltages from the high resistance state into the low resistance one and back has been observed under the photoexcitation at the wavelength of 650 nm corresponding to the collective plasmon resonance in the dense Au NP array. The effect was related to the charging of the Au NPs due to the internal photoemission of the electrons from the Au NPs into the $ZrO_2(Y)$ matrix enhanced by the plasmon resonance. It leads to the redistribution of the electric field near the Au NPs that, in turn, stimulates the switching process. The optically-controlled memristors investigated are promising for application in various fields of memristive photonics.

Keywords: memristor, Au nanoparticles, plasmon resonance

Funding: This study was funded by the Ministry of Science and Higher Education of the Russian Federation within the Project Part of the State Assignment No. 0729-2020-0058).

Citation: Ryabova M.A., Filatov D.O., Novikov A.S., Shenina M.E., Antonov I.N., Kotomina V.E., Liskin D.A., Ershov A.V., Gorshkov O.N., Optically controlled memristor based on $ZrO_2(Y)$ film with Au nanoparticles, St. Petersburg State Polytechnical University Journal. Physics and Mathematics. 16 (1.3) (2023) 151–156. DOI: https://doi.org/10.18721/JPM.161.326

Материалы конференции
УДК 535.3
DOI: https://doi.org/10.18721/JPM.161.326

Оптически управляемый мемристор на основе пленки $ZrO_2(Y)$ с наночастицами Au

М.А. Рябов [1] ✉, Д.О. Фил тов [1], А.С. Новиков [1], М.Е. Шенин [1],
И.Н. Антонов [1], В.Е. Котомин [1], Д.А. Лискин [1], А.В. Ершов [1], О.Н. Горшков [1]

[1] Нижегородский государственный университет им. Н.И. Лобачевского, г. Нижний Новгород, Россия
✉ rmargo01@mail.ru

Аннотация. Получены и исследованы лабораторные макеты оптически переключаемых мемристоров на основе плёнок $ZrO_2(Y)$ (12% мол. Y_2O_3) толщиной 20 нм с массивами наночастиц (НЧ) Au диаметром 2–3 нм, сформированными методом послойного магнетронного осаждения с последующим отжигом. Обнаружено смещение напряжений переключения мемристора между высокоомным и низкоомным состояниями при фото-

возбуждении на длине волны 650 нм, соответствующей плазмонному резонансу в НЧ Au. Обнаруженный эффект связан с заряжением НЧ Au вследствие внутренней фотоэмиссии электронов из НЧ в матрицу $ZrO_2(Y)$, усиленной плазмонным резонансом, что приводит к перераспределению электрического поля вблизи НЧ и, как следствие, стимулирует переключение мемристора.

Ключевые слова: мемристор, наночастицы Au, плазмонный резонанс

Финансирование: Работа выполнена при поддержке Министерства высшего образования и науки РФ (проектная часть государственного задания № 0729-2020-0058).

Ссылка при цитировании: Рябова М.А. и др. Оптически управляемый мемристор на основе пленки ZrO2(Y) с наночастицами Au // Научно-технические ведомости СПбГПУ. Физико-математические науки. 2023. Т. 16. № 1.3. С. 151–156. DOI: https://doi.org/10.18721/ JPM.161.326

Introduction

A memristor is a solid state electronic device based on a capacitor-like stack with the insulator capable of changing its resistance reversibly between two (or more) metastable states under a voltage applied to the plates (so called resistance switching (RS) effect) [1]. Memristors are promising for applications in non-volatile computer memory [2], novel (non-von Neumann) computer architectures allowing in-memory computing [3], neuromorphic electronics [4], etc.

Most works published to date were dedicated to studying so-called filamentary RS mechanism based on formation of conductive filaments (CFs) inside the memristor stack insulator during so-called forming process, which is a controlled incomplete reversible local breakdown of the insulator. The CFs in memristors based on oxides consist of oxygen vacancies (VOs) [5]. The CFs can be destroyed by a voltage pulse of appropriate polarity. As a result, the memristor switches from low-resistance state (ON) into high resistance state (OFF). In turn, the CF can be restored by a voltage pulse of the opposite polarity, and so forth.

Recently, photosensitive memristors attracted the attention of researchers in the scope of potential applications in active image sensors for internet of things, security systems, environment monitoring, etc. [6]. Such devices enable built-in image preprocessing using the neural network algorithms (for example, image recognition, etc.). In particular, the effect of light on the RS in Au/$ZrO_2(Y)$/*n*-Si MOS stacks was reported [7]. The effect was attributed to the surface photovoltage at the $ZrO_2(Y)$/Si interface due to intrinsic optical absorption in the Si substrate that leads to the enhancement of the electric field in the $ZrO_2(Y)$ layer stimulating the RS. Furthermore, the light-activated RS in ITO/SiO_x/*p*-Si MOS stacks was reported [8]. The effect was related to injection of photoexcited electrons from the Si substrate into the SiO_x layer that stimulates the formation of VOs constituting the CFs. The effect of infrared radiation (with the wavelength $\lambda \approx 1550$ nm) on the Ag/*a*-SiO_2/Pt point contact memristor junctions was observed [9]. The optical excitation of plasmons in the Ag nanotips led to the thermally activated redistribution of the Ag atoms inside the *a*-SiO_2 layer that, in turn, resulted in a digital change of the contact resistance. An enhancement of RS in a $ZrO_2(Y)$ film with embedded Au nanoparticles (NPs) of ~2 nm in diameter by illumination at $\lambda \approx 650$ nm corresponding to the plasmon resonance (PR) in the Au NPs was reported [10]. The effect was related to the charging of the Au NPs due to the PR-enhanced internal photoemission of electrons from the NPs into the $ZrO_2(Y)$ matrix [11]. It leads to the local enhancement of the electric field strength F near the NPs promoting the growth of CFs. The light-induced charging of the Au NPs in the $ZrO_2(Y)$ films was confirmed experimentally by Kelvin Probe Force Microscopy.

In the present paper, we report on the fabrication and investigation of prototype photosensitive memristors based on $ZrO_2(Y)$ films with Au NP arrays.

Materials and Methods

The $ZrO_2(Y)$ films with embedded Au NPs were prepared using layer-by-layer magnetron

deposition of $ZrO_2(Y)/Au/ZrO_2(Y)$ stacks followed by annealing. Torr International® MSS-3GS vacuum setup for deposition of thin films was employed.

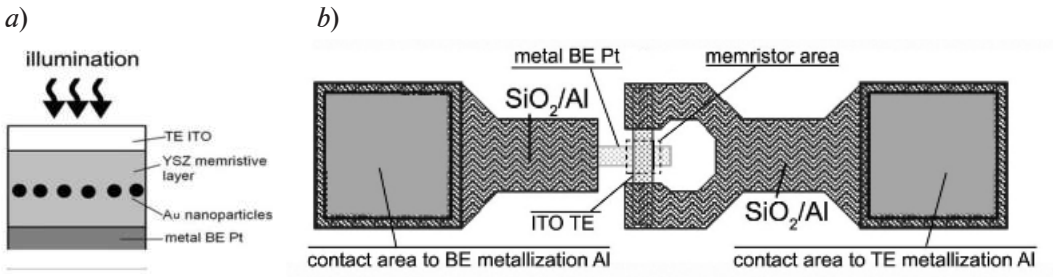

Fig. 1. Schematic representations of the structure of the active region (cross-section, *a*) and of the topology of the prototype memristor (top view, *b*)

The $ZrO_2(Y)$ films were deposited by radio-frequency (rf) magnetron sputtering from pressed powder ZrO_2–Y_2O_3 (≈12% mol.) targets in Ar–O_2 (50:50% mol.) ambient at a pressure of ≈ $1.7 \cdot 10^{-2}$ Torr and at the substrate temperature T_g = 250 °C. The metal films were deposited by direct current (dc) magnetron sputtering in Ar ambient at T_g = 200 °C. The cross-section of the memristor stack is shown in Fig. 1, *a*. First, the bottom electrodes (BEs) from Pt of 10 nm in thickness with the 10-nm Ti adhesion sublayers were deposited onto the n^+-Si(100) substrates (the specific resistivity ρ ≈ 0.005 Ω·cm). Then, the underlying $ZrO_2(Y)$ layers of ~10 nm in thickness were deposited onto the Pt BEs. Next, the Au films with an average thickness ~1 nm were deposited and capped with 10 nm thick cladding $ZrO_2(Y)$ layers. Finally, the stacks were annealed at ~450 °C in Ar ambient for ≈ 2 min. The structure and optical properties of the $ZrO_2(Y)$:NP-Au films prepared using the procedure described above were studied earlier [12]. Cross-sectional transmission electron microscopy has shown the Au films in the $ZrO_2(Y)/Au/ZrO_2(Y)$ stacks prepared in the same regime to transform into dense arrays of nearly spherical Au NPs of 2–3 nm in diameter arranged almost in a single sheet inside the $ZrO_2(Y)$ films. The surface density of the Au NPs was ~10^{12} cm^{-2}. The optical transmission spectra (300 K) manifested the absorption peaks at λ = 630–650 nm attributed to the collective PR in the dense Au NP arrays.

The cross-point prototype memrisor devices were fabricated from the $ZrO_2(Y)$:NP-Au films using standard photolithography with wet etching using Planar® lithographic line (Belarus). The topology of the devices is shown in Fig. 1, *b*. The top electrodes (TEs) were made from conductive transparent ITO films of 200 nm in thickness deposited by Electron Beam Evaporation followed by annealing in air to complete the oxidation. The motivation for the choice of ITO as the TE material was to provide the access of the photoexcitation to the active $ZrO_2(Y)$:NP-Au layers. The metal contacts to TEs and BEs with the contact pads were made from Al. The whole device structures were protected by SiO_2 coating.

The electrical parameters of the prototype memristors were examined with Agilent® B1500A semiconductor device analyzer. The electrical contacts to the contact pads were provided using EverBeing® EB-6 probe station. The current compliance during the electroforming and measuring the cyclic I–V curves was set to +0.5 mA. The devices were illuminated with a continuous wave laser diode (LD) with the emission wavelength λ = 650 nm, ouput power ~1 W and the beam diameter ~1 mm. The photoexcitation intensity was attenuated by a set of glass light filters.

Results and Discussion

Fig. 2, *a* shows the cyclic I–V curves of the memristor measured in the dark and under illumination by the LD at λ = 650 nm. The illumination resulted in a decrease in the voltage of switching from the high resistance (OFF) state into the low resistance (ON) one U_{SET}. Also, the absolute value of the voltage of switching back from the ON state into the OFF one $|U_{RESET}|$ increased. The effect can be explained as follows [11]. The plasmonic absorption of the light in the Au NPs results into the internal photoemission of the electors from the Fermi level in the Au NPs into the conduction band of $ZrO_2(Y)$ (Fig. 2, *b*). The Plasmon resonance enhances the interaction of the incident light with the electrons confined in the Au NPs [13] that, in turn,

increases the photoemission current [14]. As a result, the Au NPs become charged positively. Fig.2, *b* presents the calculated band pictures of the ITO/ZrO_2(Y):NP-Au/Pt stack when the positive voltage $U = 1$ V is applied to the ITO TE relative to the Pt BE for the cases when the Au NP is charged with different numbers of the elementary charges *e*: from 0*e* to +5*e*. The calculation procedure was described in details elsewhere [11]. The charging of the Au NP results in a local enhancement of the electric field strength *F* at the NP surface (at the side closest to the Pt BE). Correspondingly, *F* decreases (or even changes its sign) at the opposite side of the NP (directed towards the ITO TE biased positively).

As it has been already mentioned above (see Introduction), in the memristors based on oxides, the CFs consist of the positively-charged VOs [5].

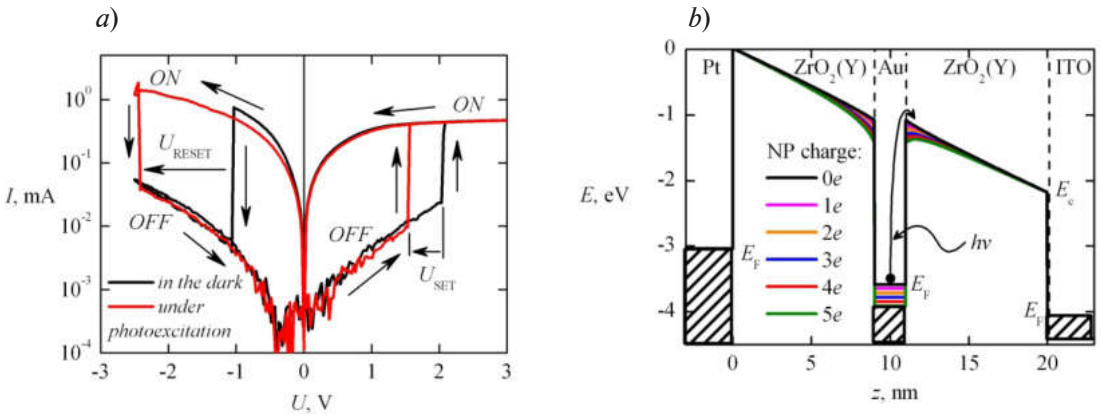

Fig. 2. Effect of illumination with the LD emission (λ ≈ 650 nm) on the cyclic *I*–*V* curves of the memristor (*a*); calculated band diagram of the memristor stack for 6 different values of the Au NP charge (from 0*e* to +5*e*), U = 1 V (*b*)

When a positive bias is applied to the TE, the VOs are attracted to the negaievely-biased BE where the vacancy clusters nucleate. Once a cluster has nucleated, the local electric field strength at its top increases accelerating further growth until the cluster reaches the TE thus forming a CF. On the other hand, a metal sphere (or ball) placed inside an insulator of a flat capacitor is known to concentrate the electric field strength near the sphere even if this one remains neutral as a whole. Consequently, if an array of the metal NPs is embedded into the insulator of a memristor, the CFs grow preferably through the NPs acting as the local electric field concentrators [15]. The charging of Au NPs due to the internal photoemission of electrons enhances this effect even more. As a result, the restoration of the CFs (taking place near the NP surface) during switching from the OFF state into the ON one (so-called SET process) takes place at smaller values of U_{SET} as compared to the switching in the dark.

The rupture of the CFs during switching from the ON state into the OFF one (so-called RESET process) goes preferentially via the diffusion of the VOs out of the CFs enhanced by Joule heating of the CFs by the reverse electric current flowing through the CFs when a reverse bias is applied [2]. In this case, the charging reduces F at the NP surface directed towards the BE thus preventing the rupture of the CF. As a result, greater absolute values of U_{RESET} are necessary to switch the memristor from the ON state into the OFF one.

It is worth noting that due to small NP size, its potential changes considerably (as compared to the thermal energy $kT \approx 26$ meV at the room temperature $T = 300$ K, k being the Boltzmann constant) in a digital manner with the emission of every next electron from the NP (see Fig. 2, *b*) that is a clear manifestation of the single electron charging effect [11].

Moreover, it can be observed that the electric current still flows through the device in the OFF state at $U = 0$ (see Fig. 2, *b*). This can be attributed to the ion migration polarization effect in ZrO_2(Y) [16].

Fig. 3, *a* shows a waveform of the current flowing through the memristor *I*(*t*) recorded when illuminating with a 0.5 s light pulse. Initially, the memristor was set to the OFF state in the dark, and a constant voltage $U = +2.0$ V (slightly below U_{SET}) was applied to the memristor. Next, the illumination of the memristor with the LD was switched on at $t = 0$ for ~ 0.5 s. Under

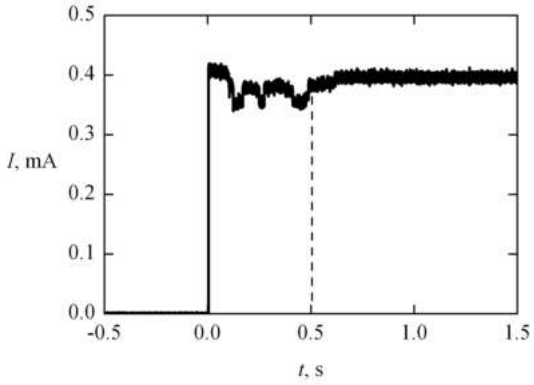

Fig. 3. Waveform of the current flowing through the memristor $I(t)$ when illuminating with a 0.5 s light pulse ($0 < t < 0.5$ s, $\lambda \approx 650$ nm), $U = +2.0$ V

the illumination, the memristor switched to the ON state and remained in this state after switching the illumination off. The instability and partial quenching of I during illumination was attributed to the photoinjection of the electrons into the VO-related electron traps in $ZrO_2(Y)$ [11] leading to the screening of the electric field inside the $ZrO_2(Y)$:NP-Au active layer.

Conclusions

The prototype optically controlled memristors based on the $ZrO_2(Y)$:NP-Au films were obtained. The functioning of the devices is based on the PR enhanced internal photoemission of the electrons from the Au NPs. The shift of the cyclic $I-V$ curves of the memristor under illumination as well as the optically-induced switching of the memristor were demonstrated. The results show the investigated devices to be promising for application in memristor photonics.

REFERENCES

1. **Strukov D.B., Snider G.S., Stewart D.R., Williams R.S.,** The missing memristor found, Nature 453 (7191) (2008) 80–83.

2. **Lee S.H., Zhu X., Lu W.D.,** Nanoscale resistive switching devices for memory and computing applications, Nano Research. 13(5) (2020) 1228–1243.

3. **Ielmini D., Wong H.S.P.,** In-memory computing with resistive switching devices, Nature Electronics. 1 (6) (2018) 333–343.

4. **Zhang Y., Wang Z., Zhu J., Yang Y., Rao Y., Song W., Zhuo Y., Zhang X., Cui M., Shen L., Huang R., Yang J. J.,** Brain-inspired computing with memristors: Challenges in devices, circuits, and systems, Applied Physics Review. 7 (1) (2020) 011308.

5. **Waser R., Aono M.,** Nanoionics-based resistive switching memories, Nature Materials. 6 (11) (2007) 833–840.

6. **Vasileiadis N., Ntinas V., Fyrigos I.-A., Karamani R.-E., Ioannou-Sougleridis V., Normand P., Karafyllidis I., Sirakoulis G. Ch., Dimitrakis P.,** A new 1P1R Image Sensor with In-Memory Computing Properties Based on Silicon Nitride Devices, In: Proceedings of IEEE International Symposium on Circuits and Systems (ISCAS), Daegu, Korea, 22 – 28 May 2021, INSPEC Accession No. 20947147. Institute of Electrical and Electronic Engineers (IEEE). 2021.

7. **Tikhov S.V., Gorshkov O.N., Koryazhkina M.N., Antonov I.N., Kasatkin A.P.,** Light-induced resistive switching in silicon-based metal–insulator–semiconductor structures, Technical Physics Letters. 42 (5) (2016) 536–538.

8. **Mehonic A., Gerard T., Kenyon A. J.,** Light-activated resistance switching in SiOx RRAM devices, Applied Physics Letters. 111 (23) (2017) 233502.

9. **Emboras A., Alabastri A., Ducry F., Cheng B., Salamin Y., Ma P., Andermatt S., Baeuerle B., Josten A., Hafner C., Luisier M., Nordlander P., Leuthold J.,** Atomic Scale Photodetection Enabled by a Memristive Junction, ACS Nano. 12 (7) (2018) 6706–6713.

10. **Novikov A.S., Filatov D.O., Antonov D.A., Antonov I.N., Shenina M.E., Gorshkov O.N.,** Conductive atomic force microscopy study of the photoexcitation effect on resistive switching in $ZrO_2(Y)$ films with Au nanoparticles, Journal of Physics: Conference Series. 993 (2018) 012026.

11. **Novikov A.S., Filatov D.O., Shenina M.E., Antonov I.N., Antonov D A., Nezhdanov A.V., Vorontsov V.A., Pavlov D.A., Gorshkov O.N.,** A mechanism of effect of optical excitation on resistive switching in ZrO2(Y) films with Au nanoparticles, Journal of Physics D: Applied Physics 54 (48) (2021) 485303.

12. **Gorshkov O., Antonov I., Filatov D., Shenina M., Kasatkin A., Bobrov A., Koryazhkina M., Korotaeva I., Kudryashov M.,** Fabrication of Metal Nanoparticle Arrays in the $ZrO_2(Y)$, $HfO_2(Y)$,

and GeO_x Films by Magnetron Sputtering, Advances in Materials Science and Engineering. (2017) 1759469.

13. **Pelton M., Bryant G.W.,** Resistive Switching: From. Introduction to Metal-Nanoparticle Plasmonics, Wiley, Hoboken, 2013.

14. **Filatov D.O., Antonov I.N., Sinutkin D.Yu., Liskin D.A., Gorshkov A.P., Gorshkov O.N., Kotomina V.E., Shenina M.E., Tikhov S.V., Korotaeva I.S.,** Plasmon Resonance Induced Photoconductivity in the Yttria Stabilized Zirconia Films with Embedded Au Nanoclusters, Semiconductors. 52 (4) (2018) 465–467.

15. **Guan W., Long S., Jia R., Liu M.,** Nonvolatile resistive switching memory utilizing gold nanocrystals embedded in zirconium oxide, Applied Physics Lett.ers. 91 (6) (2007) 062111.

16. **Tikhov S., Gorshkov O., Antonov I., Koryazhkina M., Morozov A., Filatov D.,** Ion migration polarization in the yttria stabilized zirconia based metal-oxide-metal and metal-oxide-semiconductor stacks for resistive memory, Advances in Condensed Mater Physics. (2018) 2028491.

THE AUTHORS

RYABOVA Margarita A.
rmargo01@mail.ru
ORCID: 0000-0002-2678-4152

KOTOMINA Valentina E.
kotominav@list.ru
ORCID: 0000-0001-7601-997X

FILATOV Dmitrii O.
dmitry_filatov@inbox.ru
ORCID: 0000-0001-5231-5037

LISKIN Dmitrii A.
dmitry_liskin@mail.ru
ORCID: 0000-0002-2034-4965

NOVIKOV Alexey S.
gomerbc1995@gmail.com
ORCID: 0000-0002-8474-0529

ERSHOV Alexey V.
ershov@phys.unn.ru
ORCID: 0000-0001-7337-2743

SHENINA Maria E.
cyrix@bk.ru
ORCID: 0000-0001-7661-9211

GORSHKOV Oleg N.
gorshkov@nifti.unn.ru
ORCID: 0000-0001-8947-5827

ANTONOV Ivan N.
ivant@nifti.unn.ru
ORCID: 0000-0002-3117-8640

Received 07.12.2022. Approved after reviewing 06.02.2023. Accepted 19.02.2023.

Conference materials
UDC 538.958, 535.37
DOI: https://doi.org/10.18721/JPM.161.327

Multi-state lasing in microdisk lasers with InAs/GaAs quantum dots

A.A. Karaborchev [1] ✉, I.S. Makhov [1], M.V. Maximov [2],
N.V. Kryzhanovskaya [1], A.E. Zhukov [1]

[1] HSE University, St. Petersburg, Russia;
[2] Alferov University, St. Petersburg, Russia
✉ alex_karaborchev@mail.ru

Abstract. The paper reports on the implementation of two-level lasing in injection microlasers with self-organized InAs/GaAs quantum dots. Emission bands related to the radiative electron-hole recombination involving ground and several excited states of quantum dots are observed in the spontaneous electroluminescence spectra. We investigated two-level lasing via the ground and first excited states of quantum dots in microdisks with different cavity diameters. A decrease in the threshold currents is observed for both ground and first excited transitions in quantum dots with a decrease in the microdisk diameter. The temperature dependences of the threshold current density for microdisks of various diameters suggest that two-level lasing is observed up to 90–100 °C.

Keywords: Two-state lasing, quantum dots, microdisks, electroluminescence

Funding: This study was supported by Russian Science Foundation grant 22-72-00028 (https://rscf.ru/project/22-72-00028/). Support of optical measurements was implemented in the framework of the Basic Research Program at the National Research University Higher School of Economics (HSE University).

Citation: Karaborchev A.A., Makhov I.S., Maximov M.V., Kryzhanovskaya N.V., Zhukov A.E., Multi-state lasing in microdisk lasers with InAs/ GaAs quantum dots, St. Petersburg State Polytechnical University Journal. Physics and Mathematics. 16 (1.3) (2023) 157–162. DOI: https://doi.org/10.18721/JPM.161.327

Материалы конференции
УДК 538.958, 535.37
DOI: https://doi.org/10.18721/JPM.161.327

Многоуровневая лазерная генерация в микродисковых лазерах с InAs/GaAs квантовыми точками

А.А. Карборчев [1] ✉, И.С. Махов [1], М.В. Максимов [2],
Н.В. Крыжановская [1], А.Е. Жуков [1]

[1] Национальный исследовательский университет "Высшая школа экономики", Санкт-Петербургский филиал, Санкт-Петербург, Россия;
[2] Академический университет им. Ж.И. Алфёрова РАН, Санкт-Петербург, Россия
✉ alex_karaborchev@mail.ru

Аннотация. В данной работе исследованы особенности реализации двухуровневой лазерной генерации в инжекционных микролазерах с активной областью на основе самоорганизованных InAs/GaAs квантовых точек. В спектрах спонтанной электролюминесценции обнаружены полосы излучения, связанные с оптическими электрон-дырочными переходами через основное и возбужденные состояния квантовых точек. Обнаружен спад пороговых токов для лазерной генерации через основное и первое возбужденное состояния квантовых точек при уменьшении диаметра микродискового лазера. Ис-

следованные температурные зависимости пороговых токов двухуровневой генерации в микролазерах демонстрируют возможность реализации двухуровневой генерации в InAs/GaAs квантовых точках вплоть до 90–100 °C.

Ключевые слова: Двухуровневая лазерная генерация, квантовые точки, микродиски, электролюминесценция

Финансирование: Исследование выполнено за счет гранта Российского научного фонда № 22-72-00028 (https://rscf.ru/project/22-72-00028). Поддержка оптических измерений осуществлялась в рамках программы фундаментальных исследований Национального исследовательского университета "Высшая школа экономики" (НИУ ВШЭ).

Ссылка при цитировании: Караборчев А.А., Махов И.С., Максимов М.В., Крыжановская Н.В., Жуков А.Е. Многоуровневая лазерная генерация в микродисковых лазерах с InAs/GaAs квантовыми точками // Научно-технические ведомости СПбГПУ. Физико-математические науки. 2023. Т. 16. № 1.3. С. 157–162. DOI: https://doi.org/10.18721/ JPM.161.327

Introduction

In the past decades, substantial progress has been achieved in the field of injection lasers with a quantum-dot (QD) active region. Self-organized InAs/GaAs quantum dots emitting in the spectral range of 1–1.3 μm allow to achieve low threshold current densities and sufficiently high temperature stability of laser characteristics [1], showing promise for applications in various fields including data transmission. Depending on the type of cavity, structures with the same active region may have different purposes and advantages. In particular, microdisk cavities supporting the propagation of whispering gallery modes also allow to reduce threshold currents, achieve small lateral sizes and reach high Q compared to Fabry–Perot cavities [2,3]. Vertical-cavity surface-emitting lasers have the same advantages as microdisks, however, the ease of manufacture and the possibility of radiation output in the lateral direction make microdisk lasers promising radiation sources for use in photonic integrated circuits [4].

The effect of two-level lasing has been previously observed in lasers with an active region with quantum dots [5]. Lasing at relatively low pumping currents occurs upon the ground state (GS) transition of quantum dots, while lasing at high pumping levels occurs at a different wavelength, corresponding to the first excited-state (ES) transition of quantum dots. This effect can be used to increase the data transmission rate by introducing spectral coding. However, the implementation of two-level generation in injection microdisk lasers has not been studied to date. For this reason, this work considers the effect of two-level lasing in microdisk lasers with quantum dots.

Materials and Methods

The heterostructure for microlasers was grown by molecular beam epitaxy on an n-GaAs substrate with a 500 nm thick GaAs buffer layer doped with donors with a concentration of $3 \cdot 10^{18}$ cm^{-3}. Then an n-emitter of n-$Al_xGa_{1-x}As$ was grown with a thickness of about 2500 nm. An active region of the heterostructure was represented with 10 layers of self-assembled InAs quantum dots separated from each other with 35 nm thick GaAs layers. Finally, a p-emitter of a 2200 nm thick p-$Al_xGa_{1-x}As$ layer and a p-GaAs of 200 nm thick contact layer were grown over the active region.

Microdisk cavities with diameters of 12, 16, 20, 24, 28 and 32 μm were formed from the grown heterostructure using a photolithography and plasma chemical etching processes. Multilayered metallic contacts were also deposited on both sides of the heterostructure.

Electroluminescence spectra of the microlasers were obtained in pulsed-current mode (300 ns, 4 kHz). Individual electric contact to each microlaser was achieved with a conductive microprobe. The radiation of microlasers was collected by a 50x objective supplemented with an optical fiber, the output of which was located in front of the entrance slit of the Andor Shamrock 500i grating monochromator. Detection of radiation was carried out by a TE-cooled InGaAs array.

Temperature measurements were carried out with a PID-controlled heater built-in into the measuring table.

Results and Discussion

For the initial analysis of the structures, the spectra of spontaneous electroluminescence in the structure without a cavity were measured. The emission spectrum measured at a high current density of about 23 kA/cm^2 is shown in Fig. 1. It is seen that the spectrum can be well approximated by 4 Gaussian functions, which correspond to the ground (GS in Fig. 1) and first, second and third excited (ES1, ES2, ES3 in Fig. 1, respectively) state optical transitions in quantum dots. In addition, radiation from the wetting layer (WL in Fig. 1) of the structure is observed in the short-wavelength region of the luminescence spectrum. The obtained spectral positions of emission bands are in good agreement with studies of similar QD structures made by other scientific groups, however the designation of these excited optical transitions in different articles varies slightly (1st, 2nd ..., or GS, ES1 ...., or *s*-, *p*-, *d*- etc.) [6–8]. This characterization of the active region makes it possible to determine the spectral range where two-level lasing can be observed in the studied QDs.

Typical electroluminescence spectra measured at different injection currents for a microdisk laser with a diameter of 28 μm are shown in Fig. 2, *a*. Spontaneous electroluminescence is only observed at the lowest injection current. An increase in the current above 3 mA leads to the appearance of lasing lines (at 1160 and 1183 nm), that corresponds to the GS transition. These lasing lines correspond to different whispering gallery modes propagating in the microcavity. It is worth mentioning that the intensity of the spontaneous emission remains practically unchanged beyond the lasing threshold, which reflects the Fermi level pinning. With the further increase of the injection current up to 13 mA, lasing also occurs via the first ES transition of quantum dots at the wavelength of about 1099 nm. This corresponds to the beginning of two-state lasing. For microdisk lasers of other diameters, a similar behavior is observed, but with different threshold currents for the onset of GS and ES1 lasing. The lasing wavelength corresponded to the ES1 transitions in microdisks of other diameters lies in the range of 1090–1110 nm.

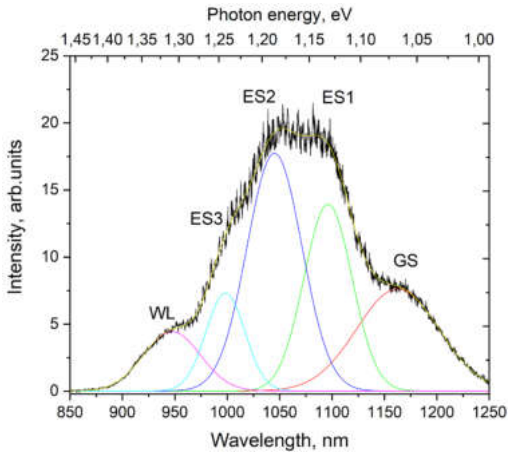

Fig. 1. Spontaneous electroluminescence spectrum from the active region of the structure, measured at the injection current density of about 23 kA/cm^2 and the room temperature

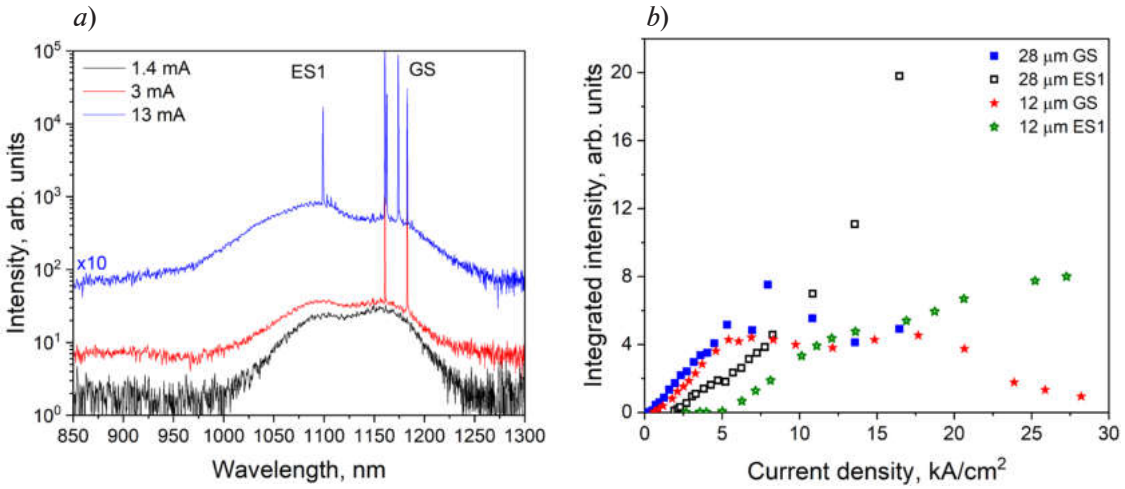

Fig. 2. Electroluminescence spectra of the microlaser with cavity diameter of 28 μm, measured at different pumping currents at the room temperature (*a*) and dependences of the integrated intensity of lasing modes for the GS and ES1 transitions on the current density for microlasers with cavity diameters of about 28 and 12 μm (*b*)

Fig. 2, *b* shows the dependences of the integrated emission intensity for the laser modes involving the ground and first excited states of quantum dots on the current density in microlasers with cavity diameter of 28 and 12 μm, obtained from the analysis of electroluminescence spectra, measured at the different injection currents. According to the Fig. 2, *b* and the abovementioned discussion, laser generation occurs at first for the ground-state optical transitions leading to the increase in its integrated intensity with the current density. At relatively high injection currents, lasing occurs for the optical transitions via the first excited state of quantum dots corresponding to the two-state lasing regime. At the same time, as certain current densities above the ES1 lasing threshold are reached, this results in saturation and subsequent decrease in the integrated stimulated emission intensity for the GS-induced optical transition for both 12 and 28 μm microdisk lasers. The observed decline of the GS lasing intensity is related to the effective depopulation of hole states in quantum dots due to the ES1 induced optical transitions. The energy distance between the lower hole states in the studied QDs is much lower than thermal energy at room temperature. In this case, the competition between electrons from the ground and first excited states of QDs for common holes is observed. However, due to the greater degeneration factor for the first excited state than for the ground state ones, ES1 induced optical transitions starts to dominate resulting in the decrease of the GS lasing intensity [9].

The dependences of threshold currents for the GS and ES1 lasing on the diameter of the microdisk cavities were investigated at room temperature. For each diameter, several microdisks were investigated. The obtained dependences of threshold currents for the ES1 and GS lasing on the diameter of microdisk lasers are shown in Fig. 3, *a*. As can be seen from the experimental data, a decrease in the diameter of the microdisk laser leads to a decrease in the threshold current for lasing at both ground and first excited optical transitions of quantum dots. Such a decrease in the threshold current for the GS lasing was already observed in Ref. [10]. In our case, the dependences of the threshold currents for GS and ES1 lasing on the microcavity diameter are almost quadratic leading to slight dependence of the threshold current densities on the microdisk diameter.

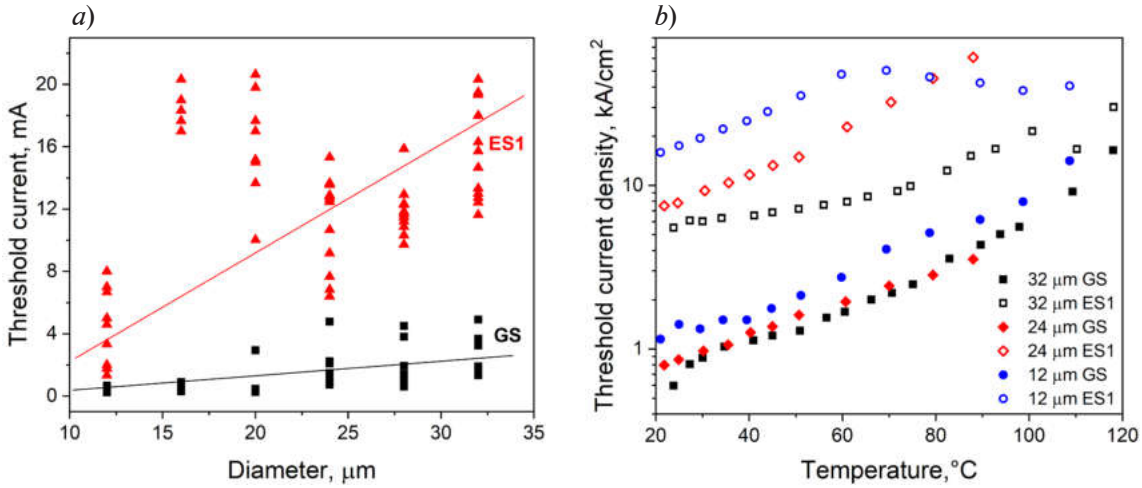

Fig. 3. Dependences of threshold currents for the ground and first excited induced optical transitions on the diameter of the microdisk lasers (*a*) and on the temperature for microdisks of different diameters (*b*). Solid lines in the left panel are guides for the eye

It is worth noting that a deviation of the threshold currents from the approximation curve based on the data for microdisks of other diameters is observed for microdisks with diameters of 16 and 20 μm. This spike is probably related to the deviation of the parameters of microlasers with cavity diameters of 16 and 20 μm from the technological parameters of microlasers of other sizes, arising at the stages of cavity formation by photolithography and plasma chemical etching.

It was also important to obtain the temperature dependences of the threshold current, which makes it possible to determine the optimal operating temperatures for different diameters of microdisks. The resulting dependences are shown in Fig. 3, *b* for the microdisks of different cavity diameters. The temperature increase leads to the increase in the threshold current density for both ground and first excited state transitions in all investigated microdisks. Such increase in the

threshold current is associated with several factors. First, the increase in temperature results in the thermal broadening of the charge carrier distribution function and the corresponding redistribution of charge carriers between the states of quantum dots. Second, an increase in temperature leads to the increase in the equilibrium concentration of charge carriers in the waveguide layers of the structure, which leads to an increase in free carrier absorption and a corresponding increase in internal loss in microlasers.

It is worth noting that two-level lasing up to 90–100 °C is observed for all studied microlasers of different diameters. With a decrease in the size of microdisks the characteristic temperature remains constant for the GS lasing and is about 44 K. The decline of the characteristic temperature was observed for the excited state lasing with the cavity diameter decrease. We associate it with a greater influence microlaser self-heating in microdisks of smaller diameters at high injection currents corresponded to the ES1 lasing conditions. In addition to the above-mentioned effects, as the temperature increases, the probability of charge carriers escape from quantum dots is essential for the excited states of quantum dots, which also affects the growth of the threshold current with temperature.

Conclusion

We considered two-level lasing in injection microdisks with InAs quantum dots grown in the GaAs matrix. The two-level lasing emission involving ground and first excited states of quantum dots was detected in microlasers with cavity diameters of 12–32 μm. The dependences of integrated intensity of laser lines on the injection current for ground and first excited induced optical transition in quantum dots were studied. The emergence of the first excited state lasing leads to the decrease of the ground state lasing with the injection current increase. We have observed a decrease in the GS and ES1 threshold currents with a decrease in the microlaser cavity diameter. The temperature dependences of the current thresholds suggest that two-state lasing does not disappear with an increase in temperature up to 100 °C, however, there is an increase in the current density values.

Acknowledgments

The work was carried out on the equipment of the unique scientific setup “Complex optoelectronic stand”.

REFERENCES

1. **Zhukov A.E.,** Quantum dot diode lasers Laser Physics and Applications. Subvolume B: Laser Systems Part 1 (Landolt-Bornstein: Numerical Data and Functional Relationships in Science and Technology—New Series: Group VIII ‘Advanced Materials and Technologies vol 1) ed H Weber, P Loosen and R Poprawe (Berlin: Springer). VIII/1B3 (2011) 95–131.

2. **Moiseev E.I., Kryzhanovskaya N.V., Zubov F.I., Mikhailovskii M.S., Abramov A.N., Maximov M.V., Kulagina M.M., Guseva Yu.A., Livshits D.A., Zhukov A.E.,** Record low threshold current density in quantum dot microdisk laser, Semiconductors 53 (14) (2019) 1888.

3. **Guha B., Marsault F., Cadiz F., Morgenroth L., Ulin V., Berkovitz V., A Lemaotre A., Gomez C., Amo A., Combrié S., Gérard B., Leo G., Favero I.,** Surface-enhanced gallium arsenide photonic resonator with quality factor of 6×10^6, Optica 4 (2017) 218.

4. **Kryzhanovskaya N., Zhukov A., Moiseev E., Maximov M.,** III–V microdisk/microring resonators and injection microlasers, Journal of Physics D: Applied Physics 54 (2021) 453001.

5. **Markus A., Chen J.X., Paranthoën C., Fioreet A.,** Simultaneous two-state lasing in quantum-dot lasers, Applied Physics Letters 82(12) (2003) 1818.

6. **Shoji H., Nakata Y., Mukai K., Sugiyama Y., Sugawara M., Yokoyama N., Ishikawa H.,** Room temperature CW operation at the ground state of self-formed quantum dot lasers with multi-stacked dot layer, Electronic Letters 32(21) (1996) 2023.

7. **Talalaev V., Kryzhanovskaya N.V., Tomm J.W., Rutckaia V., Schilling J., Zhukov A.,** Dynamics of broadband lasing cascade from a single dot-in-well InGaAs microdisk, Scientific Reports 9 (2019) 5635.

8. **Jayavel P., Tanaka H., Kita T., Wada O., Ebe H., Sugawara M., Tatebayashi J., Arakawa Y., Nakata Y., Akiyama T.,** Control of optical polarization anisotropy in edge emitting luminescence of InAs/GaAs self-assembled quantum dots, Applied Physics Letters 84 (2004) 1820.

9. **Korenev V.V., Savelyev A.V., Zhukov A.E., Omelchenko A.V., Maximov M.V.,** Analytical approach to the multi-state lasing phenomenon in quantum dot lasers, Applied Physics Letters 102(11) (2013) 112101.

10. **Kryzhanovskaya N.V., Moiseev E.I., Zubov F.I., Mozharov A.M., Maximov M.V., Kalyuzhnyy N.A., Mintairov S.A., Guseva Yu.A., Kulagina M.M., Blokhin S.A., Berdnikov Yu., Zhukov A.E.,** Evaluation of energy-to-data ratio of quantum-dot microdisk lasers under direct modulation, Journal of Applied Physics 126 (2019) 063107.

THE AUTHORS

KARABORCHEV Aleksei A.
alex_karaborchev@mail.ru
ORCID: 0000-0001-8743-1943

KRYZHANOVSKAYA Natalia V.
nkryzhanovskaya@hse.ru
ORCID: 0000-0002-4945-9803

MAKHOV Ivan S.
imahov@hse.ru
ORCID: 0000-0003-4527-1958

ZHUKOV Alexey E.
zhukale@gmail.com
ORCID: 0000-0002-4579-0718

MAXIMOV Mikhail V.
maximov@beam.ioffe.ru
ORCID: 0000-0002-9251-226X

Received 13.12.2022. Approved after reviewing 31.01.2023. Accepted 01.02.2023.

Conference materials
UDC 621.373.826
DOI: https://doi.org/10.18721/JPM/161.328

1.55 μm optical-fiber transmitter based on vertical cavity surface emitting laser obtained by wafer fusion technology

Ya.N. Kovach [1] ✉, S.A. Blokhin [1], A.V. Babichev [2], M.A. Bobrov [1],
A.A. Blokhin [1], A.G. Gladyshev [3], I.I. Novikov [2],
L.Ya. Karachinsky [2], K.O. Voropaev [4], A.Yu. Egorov [3]

[1] Ioffe Institute, St. Petersburg, Russia;
[2] ITMO University, St. Petersburg, Russia;
[3] Connector Optics LLC, St. Petersburg, Russia;
[4] JSC OKB-Planeta, Veliky Novgorod, Russia
✉ yakovachyakov@gmail.com

Abstract. In this work, the static and dynamic characteristics of a 1.55 μm optical-fiber transmitter based on wafer-fused VCSEL were studied. The device demonstrated single-mode lasing with SMSR >30 dB over a wide range of currents, and the maximum optical output power at the fiber end more than 2.5 mW. The measured −3 dB modulation bandwidth exceeded 11 GHz, and the maximum bit rate achieved was 25 Gbps. Analysis of the lasing spectra under different amplitude modulations was carried out. Positive chirping (spectra broadening) and fiber chromatic dispersion were limiting factors for the data transmission over SMF-28 fiber.

Keywords: VCSEL, optical-fiber transmitter, chirping, wafer-fusion, data transmission

Funding: The authors from ITMO University were funded by Advanced Engineering Schools Federal Project for studies on the dynamic characteristics, and by the Ministry of Science and Higher Education of the Russian Federation for studies on the static characteristics (Project 2019-1442).

Citation: Kovach Ya.N., Blokhin S.A., Babichev A.V., Bobrov M.A., Blokhin A.A., Gladyshev A.G., Novikov I.I., Karachinsky L.Ya., Voropaev K.O., Egorov A.Yu., 1.55 μm optical-fiber transmitter based on vertical cavity surface emitting laser obtained by wafer fusion technology. St. Petersburg State Polytechnical University Journal. Physics and Mathematics. 16 (1.3) (2023) 163–169. DOI: https://doi.org/10.18721/JPM.161.328

Материалы конференции
УДК 621.373.826
DOI: https://doi.org/10.18721/JPM.161.328

Волоконно-оптический передатчик спектрального диапазона 1.55 мкм на основе вертикально-излучающего лазера, изготовленного с применением технологии спекания пластин

Я.Н. Ков ч [1] ✉, С.А. Блохин [1], А.В. Б бичев [2], М.А. Бобров [1],
А.А. Блохин [1], А.Г. Гл дышев [3], И.И. Новиков [2],
Л.Я. К р чинский [2], К.О. Вороп ев [4], А.Ю. Егоров [3]

[1] Физико-технический институт им. А.Ф. Иоффе РАН, Санкт-Петербург, Россия;
[2] Университет ИТМО, Санкт-Петербург, Россия;
[3] ООО "Коннектор Оптикс", Санкт-Петербург, Россия;
[4] ОАО "ОКБ-Планета", г. Великий Новгород, Россия
✉ yakovachyakov@gmail.com

Аннотация. В работе были исследованы статические и динамические характеристики оптоволоконного передатчика на основе ВИЛ спектрального диапазона 1.55 мкм, полученного технологией спекания пластин. Прибор демонстрирует одномодовую генерацию с SMSR >30 дБ в широком диапазоне рабочих токов, а максимальная оптическая мощность на выходе волокна превышает 2.5 мВт. Измеренная эффективная частота модуляции превышает 11 ГГц, а максимальная достигнутая скорость передачи данных составила 25 Гбит/с. Был проведен анализ спектров излучения при различной амплитудной модуляции. Положительный чирпинг-эффект (уширение спектра) и хроматическая дисперсия волокна лимитируют дальность передачи данных.

Ключевые слова: ВИЛ, волоконно-оптический передатчик, чирпинг-эффект, спекание пластин, передача данных

Финансирование: Работа авторов из Университета ИТМО выполнена при финансовой поддержке федерального проекта «Передовые инженерные школы» в части исследований ряда динамических характеристик, а также при поддержке Министерства науки и высшего образования Российской Федерации, проект тематики научных исследований № 2019-1442 в части ряда исследований статических характеристик.

Ссылка при цитировании: Ковач Я.Н., Блохин С.А., Бабичев А.В., Бобров М.А., Блохин А.А., Гладышев А.Г., Новиков И.И., Карачинский Л.Я., Воропаев К.О., Егоров А.Ю. Волоконно-оптический передатчик спектрального диапазона 1.55 мкм на основе вертикально-излучающего лазера, изготовленного с применением технологии спекания пластин // Научно-технические ведомости СПбГПУ. Физико-математические науки. 2023. Т. 16. № 1.3. С. 163–169. DOI: https://doi.org/10.18721/ JPM.161.328

Introduction

The demands for the traffic-carrying capacity are constantly growing, which increases the requirements for the data rate of near-IR vertical cavity surface emitting lasers (VCSELs) used in optical interconnects based on multimode fiber [1], but stimulates interest in the search for new optical interconnects based on long-wavelength VCSELs for use in large data centers [2]. The manufacturing of VCSELs based on monolithic InAlGaAsP/InP heterostructures (created in a single epitaxial process) is associated with poor thermal conductivity and low contrast in the refractive indices of ternary and quaternary solutions, which negatively affects both the optical output power of the laser and its high-speed performance [3]. The most promising way for VCSEL manufacturing in the 1.3/1.55 μm spectral range is the hybrid integration of an active region based on InAlGaAs/InP materials either with high-contrast dielectric mirrors based on $CaF_2(AlF_3)$/ZnS materials [4–6], or with distributed Bragg reflectors (DBR) based on AlGaAs/GaAs materials using wafer-fusion technology (WF-VSCEL) [7–10]. In terms of the active region used, two main approaches can be distinguished: thick InAlGaAs quantum wells [4–6, 10] or thin strained InGaAs quantum wells [8, 9].

In this paper, we present the results of studies of an optical-fiber transmitter based on 1.55 μm WF-VCSEL with strained InGaAs quantum wells used as active region. An evaluation of the maximum bit rate and range of data transmission over single-mode fiber with different lengths has also been carried out.

Device Structure and Fabrication

The main element of studied optical-fiber transmitter (VCSEL-based transmitter) was VCSEL with current injection implemented by *n*-InP intracavity contacts and n^{++}-InAlGaAs/p^{++}-InAlGaAs tunnel junction (TJ). Active area of VCSEL contained seven strained quantum wells InGaAs with InAlGaAs barrier layers. The optical cavity with the total length 3λ confined by top and bottom DBR based on 35 and 22 quarter-wave pairs of AlGaAs/GaAs layers. Current and optical confinements were implemented within the concept of a buried tunnel junction (BTJ). Due to partial planarization of surface relief in TJ layers, single-mode lasing was feasible at large BTJ mesa diameters.

A detailed description of the VCSEL hybrid heterostructure and VCSEL chip manufacturing is presented in [11] and [12]. A single VCSEL chip with 7 μm BTJ mesa diameter was mounted in an HF-case with a SMA-connector and an optical FC/APC connector. The VCSEL was optically coupled into a SMF-28 fiber by conical microlens formed on the fiber end.

Device Characterizations and Discussions

Fig. 1 shows the basic static and spectral characteristics of the VCSEL-based transmitter. The efficiency of optical coupling into a single-mode fiber was about 45 %, which ultimately limited the maximum output optical power to 2.5 mW (Fig. 1, *a*). At the same time the value of threshold current did not exceed 1.4 mA. The studied optical-fiber transmitter showed single-mode lasing with side mode suppression ratio (SMSR) more than 30 dB in the wide range of operating current (Fig. 1, *b*).

The frequency splitting of the fundamental mode is associated with the degeneracy removal of the two orthogonal polarized modes (birefringence) [13], which was caused by transverse anisotropy of the cavity resulted from the asymmetric form of the re-grown BTJ mesa [7] and/or the elasto-optic effect induced by the mechanical strain after the double wafer-fusion [14]. An analysis of frequency splitting mechanisms is beyond the scope of this paper.

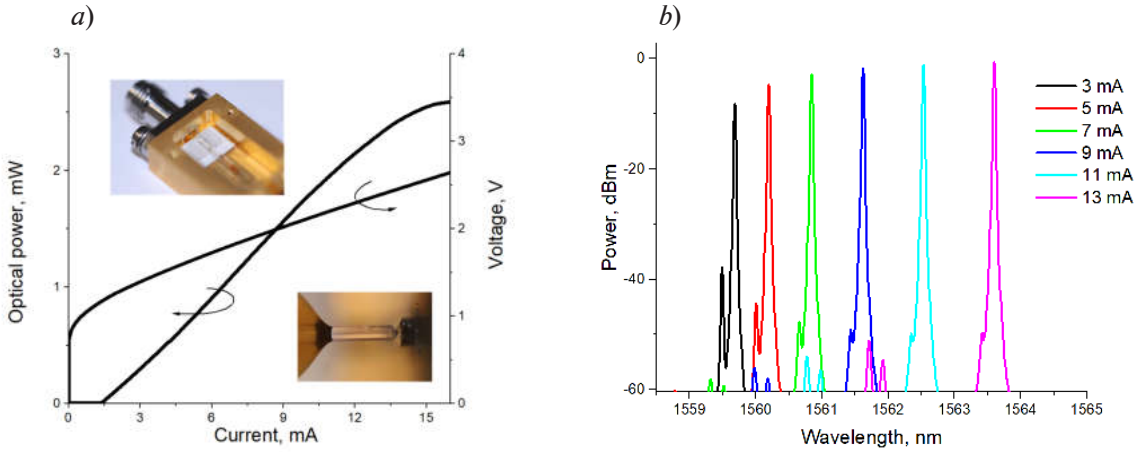

Fig. 1. Light output power and voltage as function of the current (*a*) and the typical optical spectra obtained at 20 °C (*b*)

Fig. 2 shows the results of small-signal modulation analysis of the VCSEL-based transmitter using a Rodhe & Schwarz ZVA 40 network analyzer and a New Focus 1434 photodetector at 25 GHz. Above the threshold current the −3 dB modulation bandwidth gradually increased with modulation current efficiency factor ~3.8 GHz/mA$^{0.5}$ and reached saturation at the values of 11.5-12 GHz under the current over 10 mA. The rate of resonance frequency increment with current above threshold (D-factor) reached 2.7 GHz/mA$^{0.5}$ and showed tendency to saturate at higher injection current. In addition, resonant frequency is below the -3 dB modulation bandwidth in the entire range of operating currents. The K-factor estimated from the dependence of the intrinsic damping factor on the square of the resonant frequency was 0.35 ns at moderate photon densities. The achieved modulation bandwidth of the optical-fiber transmitter was higher in comparison with unmounted VCSEL chip [9], which can be explained by the improvement of the electrical matching between the mounted VCSEL chip and a microwave signal source in the frequency range of 6-10 GHz. The high-speed performance of direct modulated laser is determined by the damping of the relaxation oscillation, the thermal effect and the cut-off frequency of the electrical parasitic [15]. The maximum theoretical bandwidth limited by damping was estimated to be 25 GHz, however the effects of self-heating and gain saturation at large currents enhanced the damping. The maximum theoretical bandwidth limited by the electrical parasitics was more than 20 GHz, while the maximum theoretical bandwidth limited by the thermal effects was about 16 GHz. Thus, the high-speed performance of the VCSEL-based transmitter was limited by a combination of thermal effects with damping of relaxation oscillations.

To evaluate the data transmission capacity under on-off keying modulation the optical-fiber transmitter was modulated by a large non-return-to-zero (NRZ) signal. A Keysight M8195A arbitrary waveform generator was used to form a pseudorandom binary sequence (PRBS) with the length of (2^7-1) bit. Eye diagrams were registered by a Keysight UXR0204A real-time oscilloscope with a Keysight N7004A optical-electrical converter. Fig. 3, *a* shows the measured eye

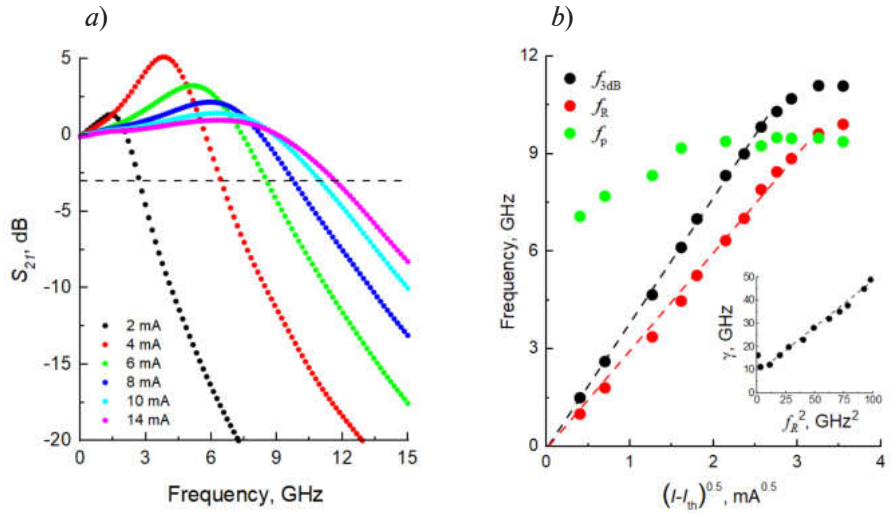

Fig. 2. Measured small signal modulation response S_{21} at the different currents (*a*); parasitic cut-off frequency f_p, resonance frequency f_R and −3dB modulation bandwidth f_{-3dB} as function of the squared root of the current above threshold (*b*). The inset shows the dependence of the intrinsic damping factor γ on the square of the resonant frequency f_R^2. The temperature of measurements was 20 ºC

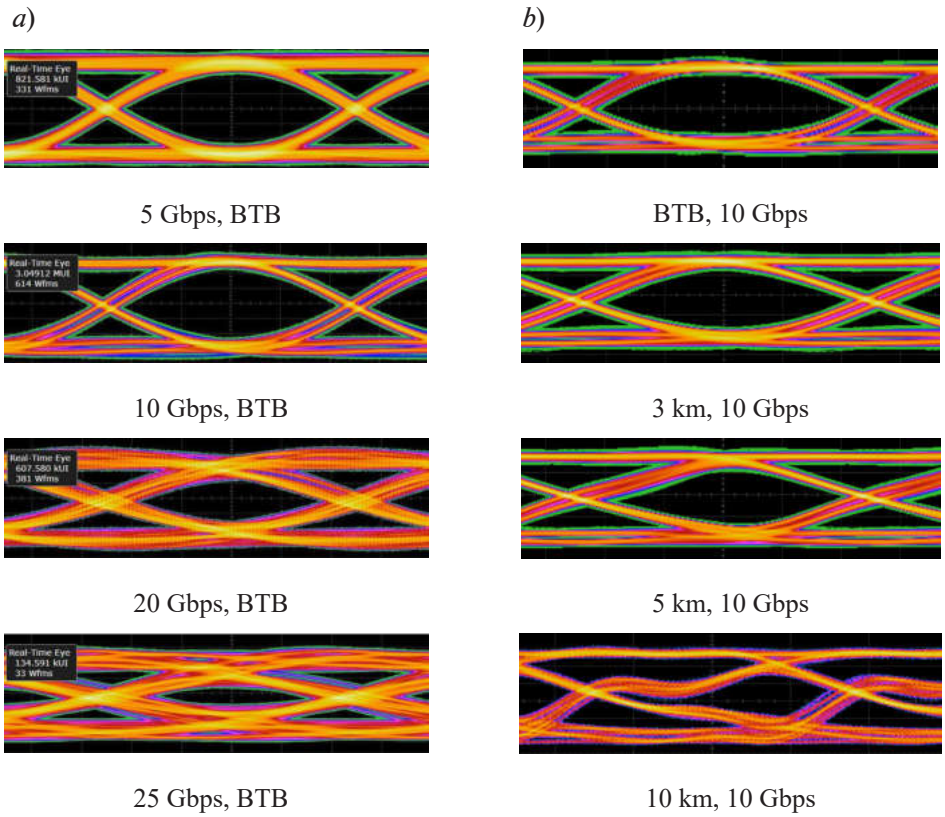

Fig. 3. Optical eye diagrams at different bit rates across a 1 m SMF-28 fiber (*a*); optical eye diagrams at 10 Gbps for different lengths of SMF-28 fiber (*b*). The operating current was 10 mA, the modulating voltage was 0.5 V. The measurement temperature was 20 ºC

diagrams of optical-fiber transmitted at different data rates for short transmission line (back-to-back, BTB). At the bit rates higher than 10 Gbps, enhancement of inter-symbol interference can be seen, which leads to increase in jitter and decrease in eye height, despite the relatively high optical modulation amplitude. It should be mentioned that high rise and fall times (~25 ps) of input electrical signal, which is formed by PRBS-generator, also negatively affect the shape of the decision area (eye width and height). Influence of SMF transmission on the shape of the eye diagrams was also studied at bit rate of 10 Gbps (Fig. 3, *b*). As the fiber length increases, the rise/fall time firstly increases from ~40 to ~100 ps, and the pulse splits within the clock interval into separate groups of lines with different signal rise/fall times (after 7 km SMF transmission).

Fig. 4, *a* shows the optical spectra of the VCSEL-based transmitter at different bit rates of PRBS (2^7-1) NRZ modulation. Compared to CW operation, a decrease in the bit rate leads to the greater red shift of the lasing spectrum, while an increase in the bit rate leads to a significant spectrum broadening (positive chirp). A wider spectrum of the optical signal leads to an increase in the rise and fall edges of the signal due to the chromatic dispersion of the optical fiber, which correlates with the experimental eye diagrams (Fig. 3, *b*).

In order to clarify the influence of individual bit sequences on the lasing spectrum of a fiber-optic transmitter, the spectra were studied under amplitude modulation by rectangular pulses of various durations with a repetition rate of 500 MHz, simulating a sequence of *n* bits "1" at bit rate of 10 Gbit/s. As shown in Fig. 4, *b*, as the pulse duration increases (the sequence of bits "1"), a red shift of the emission spectrum is observed, which is due to fluctuations in the material parameters of the laser cavity and the active region caused by the modulation of the charge carrier density. Therefore, it can be assumed that the faster components of the eye diagram, corresponding to the bit sequence 01010, are blue shifted compared to the slower components of the eye diagram, corresponding to sequences of identical bits. Thus, the combination of positive chirp of optical pulses and positive chromatic dispersion of the SMF-28 fiber leads to an increase in the rise/fall time of the slower components of the eye diagram compared to the faster components, which ultimately leads to distortion of the shape of the eye diagram for a fiber length more than 7 km.

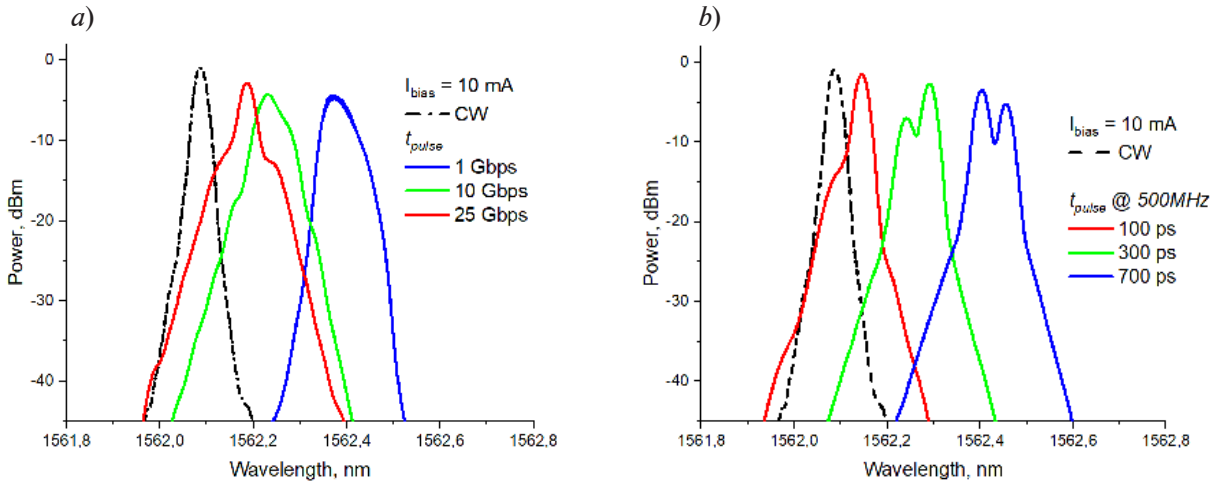

Fig. 4. Optical spectra of the VCSEL-based transmitter modulated at different bit rates (*a*); optical spectra of the VCSEL-based transmitter modulated at 500 MHz frequency with different pulse time (*b*)

Conclusion

The static and dynamic characteristics of a 1.55 μm VCSEL-based transmitter were studied. The device demonstrates single-mode generation with SMSR >30 dB over a wide range of currents, and the maximum optical power at the fiber end exceeds 2.5 mW. According to small-signal modulation experiments the -3 dB modulation bandwidth exceeded 11 GHz. The high-speed performance of the device is limited by thermal effects and damping of relaxation oscillations.

The analysis of the maximum bit rate and fiber length was carried out. The maximum bit rate exceeded 25 Gbps and was limited by the characteristics of the PRBS generator. With an increase of the fiber length, an increase of the rise and fall times was observed, which was caused by the dynamic broadening of the spectrum (chirping). According to the analysis of the emission spectra for various modulations, the slower components were red shifted compared to the fast components. As a result, the chromatic dispersion of the fiber led to increased inter-symbol interference and limited the length of the fiber for data transmission.

REFERENCES

1. **Padullaparthi B.D., Tatum J., Kenichi I.,** VCSEL Industry: Communication and Sensing. John Wiley & Sons, 2021.

2. **Zhang L., Van Kerrebrouck J., Lin R., Pang X., Udalcovs A., Ozolins O., Spiga S., Amann M.-C., Van Steenberge G., Gan L., Tang M., Fu S., Schatz R., Popov S., Liu D., Tong W., Xiao S., Torfs G., Chen J., Yin X.,** Nonlinearity Tolerant High-Speed DMT Transmission With 1.5-μm Single-Mode VCSEL and Multi-Core Fibers for Optical Interconnects. Journal of Lightwave Technology, 37(2), (2019), 380–388.

3. **Park M.-R., Kwon O.-K., Han W.-S., Lee K.-H., Park S.-J., Yoo B.-S.,** All-epitaxial InAlGaAs-InP VCSELs in the 1.3-1.6-/spl mu/m wavelength range for CWDM band applications. IEEE Photonics Technology Letters, 18(16), (2006), 1717–1719.

4. **Muller M., Hofmann W., Grundl T., Horn M., Wolf P., Nagel R. D., Amann M. C.,** 1550-nm high-speed short-cavity VCSELs. IEEE Journal of selected topics in Quantum Electronics, 17(5), (2011), 1158–1166.

5. **Spiga S., Schoke D., Andrejew A., Boehm G., Amann M.-C.,** Effect of Cavity Length, Strain, and Mesa Capacitance on 1.5-μm VCSELs Performance. Journal of Lightwave Technology, 35(15), (2017), 3130–3141.

6. **Spiga S., Soenen W., Andrejew A., Schoke D. M., Yin X., Bauwelinck J., Boehm G., Amann M.-C.,** Single-Mode High-Speed 1.5-μm VCSELs. Journal of Lightwave Technology, 35(4), (2017), 727–733.

7. **Sirbu A., Iakovelv V., Mereuta A., Caliman A., Suruceanu G., Kapon E.,** Wafer-fused heterostructures: application to vertical cavity surface-emitting lasers emitting in the 1310 nm band. Semiconductor Science and Technology, 26(1), (2011), 014016.

8. **Blokhin S.A., Babichev A.V., Gladyshev A.G., Novikov I.I., Blokhin A.A., Bobrov M.A., Maleev N.A., Andryushkin V.V., Denisov D.V., Voropaev K.O., Ustinov V.M., Bougrov V.E., Egorov A.Y., Karachinsky L.Y.,** 20-Gbps 1300-nm range wafer-fused vertical-cavity surface-emitting lasers with InGaAs/InAlGaAs superlattice-based active region. Optical Engineering, 61(09), (2022).

9. **Babichev A.V., Karachinsky L.Y., Novikov I.I., Gladyshev A.G., Blokhin S.A., Mikhailov S., Iakovlev V., Sirbu A., Stepniak G., Chorchos L., Turkiewicz J.P., Voropaev K.O., Ionov A.S., Agustin M., Ledentsov N.N., Egorov A.Y.,** 6-mW Single-Mode High-Speed 1550-nm Wafer-Fused VCSELs for DWDM Application, IEEE Journal of Quantum Electronics, 53 (6) (2017) 1–8.

10. **Ellafi D., Iakovlev V., Sirbu A., Grigore S., Mickovic Z., Caliman A., Mereuta A., Kapon E.,** Effect of Cavity Lifetime Variation on the Static and Dynamic Properties of 1.3-μm Wafer-Fused VCSELs. IEEE Journal of Selected Topics in Quantum Electronics, 21(6), (2015), 414–422.

11. **Blokhin S.A., Bobrov M.A., Blokhin A.A., Kuzmenkov A.G., Maleev N.A., Ustinov V.M., Kolodeznyi E.S., Rochas S.S., Babichev A.V., Novikov I.I., Gladyshev A.G., Karachinsky L.Y., Denisov D.V., Voropaev K.O., Ionov A.S., Egorov A.Y.,** Analysis of the Internal Optical Losses of the Vertical-Cavity Surface-Emitting Laser of the Spectral Range of 1.55 μm Formed by a Plate Sintering Technique, Optics and Spectroscopy, 127(1), (2019), 140–144.

12. **Voropaev K.O., Seleznev B.I., Prokhorov A.Y., Ionov A.S., Blokhin S.A.,** The fabrication technology of VCSELs emitting in the 1.55 μm waveband, Journal of Physics: Conference Series, 1658(1), (2020), 012069.

13. **Volet N., Iakovlev V., Sirbu A., Caliman A., Suruceanu G., Mereuta A., Kapon E.,** Polarization mode structure in long-wavelength wafer-fused vertical-cavity surface-emitting lasers. In Semiconductor Lasers and Laser Dynamics V, 8432, (2012), 76–86.

14. **Yu J.L., Chen Y.H., Jiang C.Y., Ye X.L., Zhang H.Y.,** Detecting and tuning anisotropic mode splitting induced by birefringence in an InGaAs/GaAs/AlGaAs vertical-cavity surface-emitting laser. Journal of Applied Physics, 111(4), (2012), 043109.

15. **Blokhin S.A., Maleev N.A., Bobrov M.A., Kuzmenkov A.G., Sakharov A.V., Ustinov V.M.,** High-speed semiconductor vertical-cavity surface-emitting lasers for optical data-transmission systems. Technical Physics Letters, 44(1), (2018), 1–16.

THE AUTHORS

KOVACH Yakov N.
yakovachyakov@gmail.com
ORCID: 0000-0003-4858-4968

BLOKHIN Sergey A.
blokh@mail.ioffe.ru
ORCID: 0000-0002-5962-5529

BABICHEV Andrey V.
andrey.babichev@connector-optics.com
ORCID: 0000-0002-3463-4744

BOBROV Mikhail A.
bobrov.mikh@gmail.com
ORCID: 0000-0001-7271-5644

BLOKHIN Alexey A.
bloalex91@yandex.ru
ORCID: 0000-0002-3449-8711

GLADYSHEV Andrey G.
andrey.gladyshev@connector-optics.com
ORCID: 0000-0002-9448-2471

NOVIKOV Innokenty I.
innokenty.novikov@itmo.ru
ORCID: 0000-0003-1983-0242

KARACHINSKY Leonid Ya.
leonid.karachinsky@connector-optics.com
ORCID: 0000-0002-5634-8183

VOROPAEV Kirill O.
kirill.voropaev@novsu.ru
ORCID: 0000-0002-6159-8902

EGOROV Anton Yu.
anton.egorov@connector-optics.com
ORCID: 0000-0002-0789-4241

Received 14.12.2022. Approved after reviewing 25.01.2023. Accepted 25.01.2023.

Conference materials
UDC 628.9.038
DOI: https://doi.org/10.18721/JPM.161.329

Current and temperature dependences of optical characteristics of powerful deep UV AlGaN LED (λ = 270 nm)

A.E. Ivanov [1] ✉, N.A. Talnishnikh [1], A.E. Chernyakov [1,2], A.L. Zakgeim [1]

[1] Submicron Heterostructures for Microelectronics Research and Engineering Center of the RAS, St. Petersburg, Russia;

[2] St. Petersburg State Electrotechnical University "LETI", St. Petersburg, Russia

✉ a-e-ivano-v@yandex.ru

Abstract. The main goal of this work was to study the energy characteristics of deep ultraviolet light-emitting diodes and to establish the physical reasons for the limiting of output optical power and conversion efficiency of such devices. The voltage-current, light-current and spectral characteristics of the AlGaN multiquantum wells flip-chip light-emitting diodes emitting at a wavelength of 270 nm were experimentally studied in a wide range of operating current densities of 0.01–2.5 kA/cm^2 and ambient temperatures of 200–350 K. Using the ABC-model, it was found that at a relatively high internal quantum efficiency of radiation of ~70–90% and a quite acceptable value of series resistance of ~1 Ω. The main factor (key obstacle) limiting the energy possibilities of devices is low light extraction efficiency. The latter is due to the strong absorption of the generated light in the chip volume and on the contacts, as well as total internal reflection on the AlGaN/sapphire and sapphire/air interfaces.

Keywords: AlGaN, deep UV, light-emitting diodes, internal quantum efficiency, light-extraction efficiency, ABC-model, light-current characteristic

Citation: Ivanov A.E., Talnishnikh N.A., Chernyakov A.E., Zakgeim A.L., Current and temperature dependences of optical characteristics of powerful deep UV AlGaN LED (λ = 270 nm). St. Petersburg State Polytechnical University Journal. Physics and Mathematics. 16 (1.3) (2023) 170–175. DOI: https://doi.org/10.18721/JPM.161.329

Материалы конференции
УДК 628.9.038
DOI: https://doi.org/10.18721/JPM.161.329

Токовые и температурные зависимости оптических характеристик мощного AlGaN светодиода глубокого УФ диапазона (λ = 270 nm)

А.Е. Ив нов [1] ✉, Н.А. Т льнишних [1], А.Е. Черняков [1,2], А.Л. З кгейм [1]

[1] Научно-технологический центр микроэлектроники и субмикронных гетероструктур РАН, Санкт-Петербург, Россия;

[2] Санкт-Петербургский государственный электротехнический университет «ЛЭТИ» им. В.И. Ульянова (Ленина), Санкт-Петербург, Россия

✉ a-e-ivano-v@yandex.ru

Аннотация. Целью данной работы было изучение энергетических характеристик светодиодов глубокого ультрафиолетового излучения и установление физических причин ограничения выходной оптической мощности и эффективности преобразования энергии в таких устройствах. В ходе работы были экспериментально исследованы электрооптические характеристики мощных AlGaN flip-chip светодиодов глубокого ультрафиолетового диапазона (λ = 270 нм) в широком диапазоне токов и температур. На основе анализа полученных зависимостей в рамках ABC-модели сделаны выводы, что при относительно высокой внутренней квантовой эффективности излучения ~70–90% и значении последовательного сопротивления ~1 Ω, основным фактором, ограничивающим энергетические возможности устройств, является низкая эффективность

экстракции света. Последнее обусловлено сильным поглощением генерируемого света в объеме чипа и на контактах, а также полным внутренним отражением на границах AlGaN/сапфир и сапфир/воздух.

Ключевые слова: AlGaN, глубокий ультрафиолет, светодиод, внутренний квантовый выход, коэффициент вывода излучения, ABC-модель, ватт-амперная характеристика, ультрафиолетовый светодиод

Ссылка при цитировании: Иванов А.Е., Тальнишних Н.А., Черняков А.Е., Закгейм А.Л. Токовые и температурные зависимости оптических характеристик мощного AlGaN светодиода глубокого УФ диапазона (λ = 270 nm) // Научно-технические ведомости СПбГПУ. Физико-математические науки. 2023. Т. 16. № 1.3. С. 170–175. DOI: https://doi.org/10.18721/ JPM.161.329

Introduction

Over the past decade, significant efforts have been directed to improving epitaxial technologies and designs of deep ultraviolet (DUV) light-emitting diodes (LEDs) based on AlGaN quantum-well heterostructures emitting in UV-C spectral region that spans from 100 nm to 280 nm [1, 2]. UV-C radiation covers wide range of applications including polymer curing, biochemistry and analytical systems using fluorescence, spectrometry, military fields, etc. But the main interest is attracted by the bactericidal effect of UV-C radiation, which can be used to deactivate pathogens (e.g., bacteria, spores and viruses), air and water purifiers, disinfection and sterilization of various items. Currently, one of the most effective methods for disinfecting is the use of discharge mercury lamps, for example, type DB 75. However, they have a number of well-known disadvantages, including size, power systems, insufficient service life and mercury disposal. With the replacement of lamps with LEDs, great prospects are associated, but today they are hampered by low energy parameters of DUV LEDS: output optical power (P_{out}), external quantum efficiency (η_{EQE}) and, respectively, wall-plug efficiency (WPE). So, for similar in design flip-chip blue (λ = 470 nm) LEDs based on AlInGaN multiquantum wells (MQWs) heterostructures a peak η_{EQE} of more than 80% has been attained [3]. This allows, at sufficiently high operating currents, to get P_{out} up to tens of watts at the $WPE > 40\%$ [4, 5]. At the same time, for DUV LED $\eta_{EQE} \sim 20\%$ has been achieved for record laboratory LEDs [6], while for commercial devices it is only a few percent and $P_{out} < 100$ mW [7].

Experimental details

We studied a high-power AlGaN multiquantum well DUV LEDs with a wavelength $\lambda_{peak} \sim 270$ nm. Emitting chips have “flip-chip” design with a multilevel distributed system of p- and n-contacts on the back side [9]. As is known, such LED design is the most efficient in terms of radiation output, current distribution and heat removal [10, 11]. The dimensions of the emitting chip are 1280 × 1160 μm^2, so the total area is $S = 1.4$ mm^2 and the active area under the p-contact is $S_{act} = 0.75$ mm^2 (used to calculate the current density J). The chip for contacts with additional metallization is mounted by soldering on the AlN electrode and heat-removing carrier-board.

The power and spectral characteristics of DUV LEDs at room temperature and moderate currents (up to 350 mA) were measured in continuous mode using a 6-inch integrating sphere of the OL770-LEDUV/VIS (200–780 nm) High-speed LED Test and Measurement System [12].

At high currents (units - tens of amperes), a pulsed operation mode was used, excluding self-heating (τ = 100–300 ns, $F = 100$ Hz). The power supply current pulses were provided by an Agillent 8114A generator with a PicoLAS LDP-V 80–100 V3.3 amplifier, the optical signal was recorded by a remote high-speed photodetector THORLABS DET02AFC and a Tektronix TDS3044B oscilloscope in relative units. The conversion to the absolute values was carried out according to the calibration obtained in the OL770-LED. The emission spectrum was recorded with an Avantes AvaSpec-2048 spectrometer. The investigated temperature range 200–350 K was set by a cryostat with an optical window CCS-450 (Janis Research Company Inc.).

Results and discussion

Fig. 1, *a* shows typical room temperature electroluminescent (EL) spectra of the DUV LED in a wide range of currents (I = 0.001–20 A), respectively, current densities (J = 0.0001–2.6 kA/cm^2). Calculated on the basis of Fig. 1, *a*, the current dependences of the peak wavelength λ_{peak} and full width at half maximum (FWHM) are presented in Fig. 1, *b*. For comparison, similar typical dependences for blue (λ ~460 nm) flip-chip AlInGaN LED are shown by dashed curves. As can be seen from Fig. 1, *a*, the emission spectra of DUV LEDs are distinguished by a very high current stability, in comparison with similar blue LEDs. The short-wavelength shift $\Delta\lambda_{peak}$ with a change in current density by 3 orders for DUV LED is only ~ 1−1.5 nm, while the FWHM remains within ~10−11 nm. For blue LEDs, the short-wavelength shift with current change within the same limits is ~25 nm, and FWHM increases from 21 nm to 32 nm. Such a difference in the spectral behavior of DUV LEDs and blue LEDs is explained by the fact that for highly polar "blue" structures containing In in the quantum well ($In_{0.16}Ga_{0.84}N$), the short-wavelength current shift λ_{peak} and the expansion FWHM are mainly affected by screening injected carriers of the internal field, which causes the quantum confined Stark effect (QCSE). In DUV LEDs, the $Al_{0.4}Ga_{0.6}N$ active quantum well does not contain In and is not strongly spontaneously polarized. A small change in the spectrum with current is associated with an increase in the carrier concentration and their energy distribution.

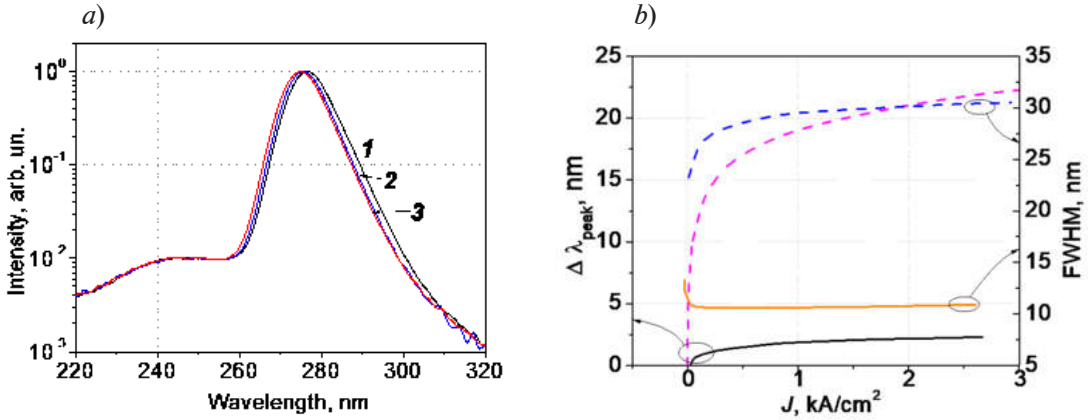

Fig. 1. Spectra of DUV LED emission at different current, T = 293 K, curve *1* corresponds to J = 0.05 kA/cm^2, curve *2* to J = 0.5 kA/cm^2, curve *3* to J = 2.5 kA/cm^2 (*a*); current dependence of $\Delta\lambda_{peak}$ and FWHM. For comparison, the same dependences for blue LED are shown by the dashed line (*b*)

Fig. 2, *a* shows the emission spectra of the DUV LED at an average current value I = 0.5 A (J ~ 70 A/cm^2) in the temperature range T = 200−350 K. It is clearly observed from Fig. 2, *a* that the changes in λ_{peak} and FWHM for DUV LEDs with temperature are within 2.0−3.0 nm, i.e., the temperature coefficient $TC\lambda_{peak}$ < 0.02 nm/K (for blue LEDs $TC\lambda_{peak}$ ~ 0.1 nm/K). Thus, both in terms of current and temperature stability of the spectrum, DUV LEDs are noticeably better than blue LEDs. Fig. 2, *a* also shows on a semi-logarithmic scale the view of the short wavelength shoulder of the emission spectrum as a function of energy ($h\nu$ [eV] = 1239.6/λ [nm]), which makes it possible to estimate the carrier temperature T_c from the slop of shoulder (based on their Boltzmann distribution) [13].

$$T_c = [-k_B \frac{\partial(\ln P)}{\partial(h\nu)}]^{-1}. \quad (1)$$

As follows from Fig. 2, *a*, there is a good correlation of the carrier temperature with the temperature of the LED package, which indicates the absence of noticeable self-heating in the pulsed operating mode. Therefore, the energy current dependences considered below have a purely electronic character.

Fig. 2, *b* shows the main energy characteristics of the DUV LED: the dependences of the external quantum efficiency η_{EQE} on the current density. As can be seen from Fig. 2, *b*, the maximum value of η_{EQE}^{max} was 3.4%, at current density J = 5 A/cm^2. For comparison, the val-

ue of η_{EQE}^{max} of the blue LED of similar design approaches to ~ 70%, and at high current η_{EQE} remains at the level of ~30%. [4] at low current densities. With such a cardinal difference in energy efficiency, it is of undoubted interest for research and applications to find out which of the factors, i.e., transport and injection of carriers, internal quantum efficiency or efficiency of radiation extraction, plays a major role in limiting possibilities of DUV LEDs.

To answer this question, in addition to the temperature dependences of emission spectra already described above, we consider the temperature dependences of η_{EQE}. Fig. 2, *b* shows the dependences of the η_{EQE} on the current on an enlarged scale in the moderate current range for temperatures set from 200 K to 350 K with a step of 10 K. Two important consequences follow from Fig. 2, *b*. First, the values of η_{EQE} gradually increase with decreasing temperature, since reducing the rate of nonradiative Shockley-Reed-Hall recombination. And, secondly, for the same reason, the current density decreases, where the value η_{EQE}^{max} is reached. It is important that at low temperatures 223–233 K, the possibility of a clear identification of the position of the η_{EQE}^{max} on the current dependences $\eta_{EQE} = f(J)$ opens up. The form of the dependence, for example, at T = 223 K, with a pronounced maximum η_{EQE}^{max} on the curve, allows us to apply *ABC*-model for estimating the internal quantum efficiency η_{IQE} [14].

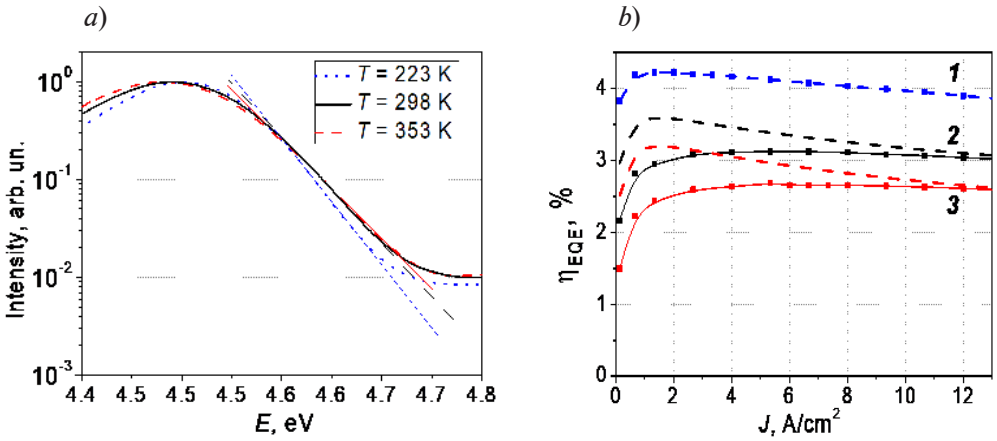

Fig. 2. Normalized DUV LED emission spectra as a function of temperature at a current density of 13 A/cm^2 and the short-wavelength shoulder of the same spectra recalculated in energy coordinates (*a*). Dependence of η_{EQE} on the current at three temperatures 223 K (*1*), 298 K (*2*); 353 K (*3*). Experimental and calculated data according to the *ABC*-model (dotted line) (*b*)

In the ABC-model, η_{IQE} is determined by the competition of three recombination mechanisms in the active region:

$$\eta_{EQE} = \eta_{ext},\ \eta_{IQE} = \eta_{ext}\frac{Bn^2}{An + Bn^2 + Cn^3}, \qquad (2)$$

where A, B, C are the coefficients corresponding to the mechanisms of nonradiative Shockley-Read–Hall recombination, radiative bimolecular recombination and nonradiative Auger recombination, n is the concentration of injected carriers in the active region. Determining the parameters A, B, C separately is an experimentally difficult task, which, as a rule, gives only approximate estimates. However, using the well-known transformations [15] when plotting the experimental dependences of the $\eta_{EQE}^{max}/\eta_{EQE}$ on the sum of the roots of the powers $(p^{1/2} + p^{-1/2})$, where $p = P_{out}/P_{out}^{max}$, and P_{out}^{max} is the power at a current corresponding to η_{EQE}^{max}, we obtain an expression to determine the main parameters of radiative recombination:

$$\frac{\eta_{EQE}^{max}}{\eta_{EQE}} = \eta_{IQE}^{max} + \frac{p^{1/2} + p^{-1/2}}{Q+2}, \qquad (3)$$

where the invariant $Q = B/(A \cdot C)^{1/2}$ – "quality factor" is a fundamental characteristic of the LED: $\eta_{EQE}^{max} = Q/(Q+2)$. Considering the graph based on expression (3) with the extrapolated $(p^{1/2} + p^{-1/2}) \to 0$, we can determine η_{EQE}^{max}, and Q from the slope of the curve. Taking into account

$\eta_{EQE} = \eta_{ext}\eta_{IQE}$ knowing η_{IQE}, and experimentally measured η_{EQE}, it is possible to determine η_{ext}, that is, all the main parameters of the LED. The results of corresponding calculations based on the 5th experimental dependence $\eta_{EQE} = f(J)$ in the region of moderate currents (0.01-0.1 A) at $T = 223$ K gave the following values: $\eta_{IQE}^{max} = 0.87$, $\eta_{EQE}^{max} = 0.042$, $\eta_{ext} = 0.048$. As the temperature rises to room $T = 293$ K, assuming reasonably that ηext does not depend on temperature, it follows from Fig. 2, *b* that η_{IQE}^{max}, drops to 0.68 due to an increase in nonradiative recombination.

Conclusion

The experimental dependences $\eta_{EQE} = f(J)$ for DUV LED ($\lambda = 270$ nm) are well described by the *ABC*-model, which made it possible to estimate $\eta_{IQ}E$ which has a rather acceptable value of 70–90% in the temperature range $T = 200$–350 K. The low value of η_{EQE} ~3–4 % is due to the smallness of η_{ext}. The latter is due to the absence of the effect of 'multi-passage' of light in UV-C emitting chips because of absorption at the contacts, which occupy a large area. This is the main difference from blue LEDs, where the contacts have sufficient reflectivity. Further efforts to improve the energy parameters of DUV LEDs are primarily related to improving the design of the emitting chip: Bragg reflectors, micro mesa-reflectors etc., increasing the chance of light output.

REFERENCES

1. **Kneissl M., Seong T., Han J. Amano H.,** The emergence and prospects of deep-ultraviolet light-emitting diode technologies, Nature Photonics. 13 (2019) 233–244.

2. **Hsu T.-C., Teng Y.-T., Yeh Y.-W., Fan X., Chu K.-H., Lin S.-H., Yeh K.-K., Lee P.-T., Lin Y., Chen Zh., Wu T., Kuo H.-Ch.,** Perspectives on UVC LED: Its Progress and Application, Photonics 8(6) (2021) 196–215.

3. **Karpov S.Yu.,** Light-emitting diodes for solid-state lighting: searching room for improvements, Proc. SPIE 9768 Light-Emitting Diodes: Materials, Devices and Applications for Solid State Lightning XX. 9768 (2016) 976–980.

4. OSRAM Datasheet LE B Q8WP. URL: https://www.osram.com/ecat/OSRAM%20OSTAR%C2%AE%20Projection%20Compact%20LE%20B%20Q8WP/com/en/class_pim_web_catalog_103489/prd_pim_device_2191200/ Accessed Dec. 12, 2022.

5. **Zakgeim A.L., Aladov A.V., Ivanov A.E., Talnishnikh N.A., Chernyakov A.E.,** Limiting Energy Capabilities of Powerful AlInGaN LEDs. Pis'ma v Zhurnal Tekhnicheskoi Fiziki. 48 (13) (2022) 33–36.

6. **Takano T., Mino T., Sakai J., Noguchi N, Tsubaki K., Hirayama H.,** Deep-ultraviolet light-emitting diodes with external quantum efficiency higher than 20% at 275nm achieved by improving light-extraction efficiency, Applied Physics Express. 10 (3) (2017) 1–4.

7. High Power UV-C LED Product Specifications 6060 SMD TL Packaged LEDs. URL: https://bolb.co/wp-content/uploads/2021/08/Bolb_SMD_6060_packaged_UVCLED-SpecSheetV1.85TL2.pdf Accessed Dec. 12, 2022.

8. **Schubert E.F.,** Light-Emitting Diodes, 2nd edition. Cambridge University Press, Cambridge, 2006.

9. Laser components, UV-C LED. URL: https://www.lasercomponents.com/de/?embedded=1&file=fileadmin/user_upload/home/Datasheets/bolb/smd6060-uvc-led-high-power.pdf&no_cache=1 Accessed Dec. 12, 2022.

10. **Shchekin O., Epler J., Trottier T., Margalith T., Steigerwald D., Holcomb M., Martin P., Krames M.,** High performance thin-film flip-chip InGaN–GaN light-emitting diodes, Applied Physics Letters. 89 (7) (2006) 110–119.

11. **Zakgeim D., Smirnova I., Roznanskiy L., Gurevich S., Kulagina M., Arakcheeva E., Onushkin G., Zakgeim A.L., Vasil'eva E., Itkinson G.,** High-Power Flip–Chip Blue Light-Emitting Diodes Based on AlGaInN, Semiconductors. 39 (7) (2005) 851–855.

12. OL 770-LED TEST AND MEASUREMENT SYSTEM. URL: https://optroniclabs.com/products/spectroradiometers/ol-770-led-test-and-measurement-system/ Accessed Dec. 12, 2022.

13. **Vaitonis Z., Vitta P., Žukauskas A.,** Measurement of the junction temperature in high-power light-emitting diodes from the high-energy wing of the electroluminescence band, Journal of Applied Physics. 103 (9) (2008) 93–100.

14. **Karpov S.Yu.,** ABC-model for interpretation of internal quantum efficiency and its droop in III-nitride LEDs: a review, Optical and Quantum Electronics 47 (2015) 1293–1303.

15. **Titkov I.E., Karpov S.Yu., Yadav A., Zerova V.L., Zulonas M., Galler B., Strassburg M., Pietzonka I., Lugauer H., Rafailov E. U.,** Temperature-dependent internal quantum efficiency of blue high-brightness light-emitting diodes, IEEE Journal of Quantum Electronics. 50 (11) (2014) 911–920.

THE AUTHORS

IVANOV Anton E.
a-e-ivano-v@yandex.ru
ORCID: 0000-0003-2819-1534

TALNISHNIKH Nadezhda A.
nadya.fel@mail.ru

CHERNYAKOV Anton E.
chernyakov.anton@yandex.ru
ORCID: 0000-0002-8153-9512

ZAKGEIM Alexander L.
zakgeim@mail.ioffe.ru

Received 14.12.2022. Approved after reviewing 09.02.2023. Accepted 09.02.2023.

Conference materials
UDC 621.383.51
DOI: https://doi.org/10.18721/JPM.161.330

Formation of radial amorphous hydrogenated silicon *p-i-n* solar cells on silicon nanowire arrays toward flexible photovoltaics

E.A. Vyacheslavova [1, 2] ✉, A.V. Uvarov [1], A.A. Maksimova [2],
A.I. Baranov [1], A.S. Gudovskikh [1, 2]

[1] Alferov University, St. Petersburg, Russia;
[2] Saint Petersburg Electrotechnical University "LETI", St. Petersburg, Russia
✉ cate.viacheslavova@yandex.ru

Abstract. The influence of silicon nanowire (SiNWs) geometry on the efficiency of radial *p-i-n* junction solar cell is studied using experimental measurements. Solar cells based on vertically aligned structures with the SiNWs less than 10 μm in height are practically on par with the planar element in terms of the open-circuit voltage, exceeding it in terms of short-circuit current density by up to 1.5 times (3.9–4.9 mA/cm^2). The increase in the short-circuit current density is associated with the broadening of the quantum efficiency (EQE) spectrum. There is a significant broadening of the EQE boundary to the short-wavelength region with a decrease in the diameter of the SiNWs (from 1.8 to 0.7 μm). A decrease in the open-circuit voltage and a decrease in the absolute value of EQE are observed for structures with SiNWs more than 10 μm in height.

Keywords: radial *p-i-n* junction, amorphous silicon, silicon nanowires, solar cell

Funding: The study was performed with the financial support of Project FSEE-2020-0008, carried out within the framework of State Assignment 075-01024-21-00 of Ministry of Science and Higher Education of the Russian Federation.

Citation: Vyacheslavova E.A., Uvarov A.V., Maksimova A.A., Baranov A.I., Gudovskikh A.S., Formation of radial amorphous hydrogenated silicon *p-i-n* solar cells on silicon nanowire arrays toward flexible photovoltaics, St. Petersburg State Polytechnical University Journal. Physics and Mathematics. 16 (1.3) (2023) 176–181. DOI: https://doi.org/10.18721/JPM.161.330

Материалы конференции
УДК 621.383.51
DOI: https://doi.org/10.18721/JPM.161.330

Формирование солнечных элементов на основе вертикально-ориентированных структур с радиальным *p-i-n* переходом для гибкой фотовольтаики

Е.А. Вячеслав [1, 2] ✉, А.В. Уваров [1], А.А. Максимов [2],
А.И. Баранов [1], А.С. Гудовских [1, 2]

[1] Академический университет им. Ж.И. Алфёрова РАН, Санкт-Петербург, Россия;
[2] Санкт-Петербургский государственный электротехнический университет «ЛЭТИ» имени В.И. Ульянова (Ленина), Санкт-Петербург, Россия
✉ cate.viacheslavova@yandex.ru

Аннотация. В работе исследуется влияние геометрии кремниевых нановолокон (КН) на производительность солнечных элементов на основе радиальных *p-i-n* *a*-Si:H структур, осажденных на КНН. Солнечные элементы на основе

вертикально-ориентированных структур с высотой КН менее 10 мкм по значениям напряжения холостого хода практически не уступают планарному элементу, а по значениям плотности тока короткого замыкания превосходят его до 1.5 раз (3.9–4.9 мА/см^2). Увеличение значения тока короткого замыкания связано с расширением спектра квантовой эффективности, причем с уменьшением диаметра кремниевых нановолокон (с 1.8 до 0.7 мкм) наблюдается существенное расширение границы спектра квантовой эффективности в коротковолновую область. Для структур с высотой кремниевых нановолокон более 10 мкм отмечается снижение значения напряжения холостого хода и уменьшение абсолютного значения EQE.

Ключевые слова: радиальный *p-i-n* переход, аморфный кремний, кремниевые нановолокна, солнечный элемент

Финансирование: Исследование выполнено при финансовой поддержке проекта № FSEE-2020-0008, который был осуществлен в рамках государственного задания Министерства науки и высшего образования Российской Федерации № 075-01024-21-00.

Ссылка при цитировании: Вячеславова Е.А., Уваров А.В., Максимова А.А., Баранов А.И., Гудовских А.С. Формирование солнечных элементов на основе вертикально-ориентированных структур с радиальным *p-i-n* переходом для гибкой фотовольтаики // Научно-технические ведомости СПбГПУ. Физико-математические науки. 2023. Т. 16. № 1.3. С. 176–181. DOI: https://doi.org/10.18721/ JPM.161.330

Introduction

The terrestrial photovoltaic industry is still dominated by crystalline silicon (*c*-Si) solar cells due to their stability, relatively low cost and abundance of silicon [1, 2]. The record efficiency of silicon solar cells based on *a*-Si:H/*c*-Si heterojunction is currently 26.7% [3] and is approaching the 29.4% [4] Auger-recombination-constrained Shockley–Queisser limit. The use of multijunction solar cell was one of the ways to overcome theoretical limit and increase the total energy generated by the modules. A new design of a multijunction Si solar cell was proposed [5], where the bottom junction is based on *a*-Si:H/*c*-Si heterojunction, and the top junction is based on SiNWs coated with *p-i-n* structures of *a*-Si:H. The radial design of top *p-i-n* junction is a way to enhance absorption in undoped (*i*)*a*-Si:H layer without increasing its thickness and therefore can provide an increase in the short-circuit current density J_{SC}. Thus, it is possible to solve major problem of a classic planar *a*-Si:H/*c*-Si solar cell, which consists in current matching with the bottom junction. In addition, the use of SiNWs is a promising way to fabrication flexible solar cells. The SiNWs solar cell embedded in a polymer matrix have enhanced mechanical stability compared to conventional planar element.

The influence of SiNWs radius on the efficiency of *a*-Si:H/*c*-Si solar cells was experimentally studied [6]. It is reported that in order to reduce recombination losses, it is necessary to use SiNWs with a radius exceeding the space charge region in Si.

The computer simulation of multijunction solar cells based on *p-i-n* structures and SiNWs was carried out [7]. The dependence of the solar cell characteristics on the SiNWs geometry was calculated. It is shown that an increase in wire length leads to a decrease in the open-circuit voltage V_{OC} and saturation of J_{SC}. At the same time, the value of 10 μm is the critical length of the wire.

In this article, we study the influence of the SiNWs geometry on the efficiency of the top radial *p-i-n* junction using experimental measurements.

Experimental section

Double-sided polished *n*-type antimony doped Si (100) wafers (0.008 Ω·cm) were used for solar cell fabrication. A planar *p-i-n* structure was fabricated as a reference solar cell.

Vertically aligned structures were obtained using latex sphere lithography and dry etching in a SF_6/O_2 gas mixture at cryogenic temperatures (–120 °C). Plasma etching processes were carried out using Oxford Plasmalab System 100 ICP380 setup. In general, the formation of SiNWs includes three subsequent dry etching steps. First, the reducing of the latex spheres diameter in O_2 plasma. Secondly, etching of SiO_2 layer in CHF_3 plasma via latex spheres. Thirdly, deep cryogenic etching of Si via the formed hard SiO_2 mask. We varied the etching time in O_2 plasma and the etching time in the cryogenic process to obtain SiNWs of different geometries. More details about the formation of SiNWs can be found in our previously published articles [8, 9]. The structure parameters of the obtained vertically aligned structures are shown in Table 1.

Table 1

Parameters of vertically aligned silicon structures

Etching time, sec		Structure parameter	
O_2 plasma	Cryoprocess	height, μm	diameter, μm
260	170	5.3	1.6
220		5.3	1.8
260	300	7	0.7
220		8.5	1.3
260	450	12	1.4

A *p-i-n a*-Si:H structure on SiNWs was deposited via plasma-enhanced chemical vapor deposition (PECVD) at a temperature of 250 °C using the Oxford instruments Plasmalab 100 PECVD setup. Undoped (*i*)*a*-Si:H layer was deposited from a gas mixture of silane (SiH_4) and hydrogen (H_2); *n*-type phosphorus doped *a*-Si:H layer was deposited by adding phosphine (PH_3) to the gas mixture. P-type boron doped *a*-Si:H layer was formed due to the addition of trimethylboron (TMB) to SiH_4 gas, respectively.

A 10 nm thick (*n*)*a*-Si:H layer was deposited on the back side of the substrates to obtain ohmic contact. Vacuum evaporated silver (Ag) layer was used for the bottom contact. Further, a layer of a transparent conductive electrode based on indium tin oxide (ITO) was sputtered on the front side. On the front side, point contacts were formed using Ag paste, followed by drying at 170 °C for 10 min. In the future, it is planned to optimize the front contact and form an Ag grid. Figure 1 shows a schematic of the radial *p-i-n* solar cell design.

The *I*–*V* curves under AM1.5G simulator (Abet Technology SunLite) were measured using a Keithley 2400 electrometer with software control in a LabVIEW environment. The EQE spectra were carried out using an SLS M266 monochromator, a halogen lamp and a reference solar cell based on *c*-Si. The total reflection spectra were measured using an integrating sphere and an AvaSpec SensLine spectrometer.

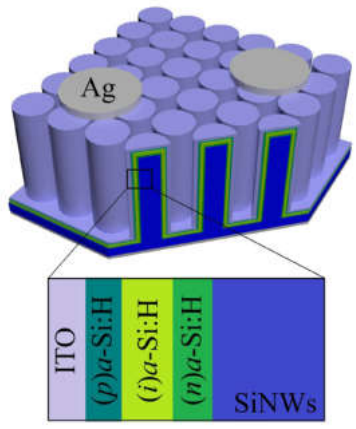

Fig. 1. Solar cell based on radial *p-i-n* junction

Results and Discussion

Scanning electron microscopy (SEM) and transmission electron microscopy (TEM) were used to study the morphology and structural properties of the obtained *p-i-n* structures. The elemental composition was carried out directly in the TEM setup by the EDX studies.

Fig. 2, *a* shows a TEM image of a section on the SiNW covered with ITO. According to the TEM image, the ITO layer thickness is about 80 nm.

The elemental composition a section of the side SiNW surface is presented in Fig. 2, *b*. The spectral distribution of the EDX signal shows the components of the ITO layer on

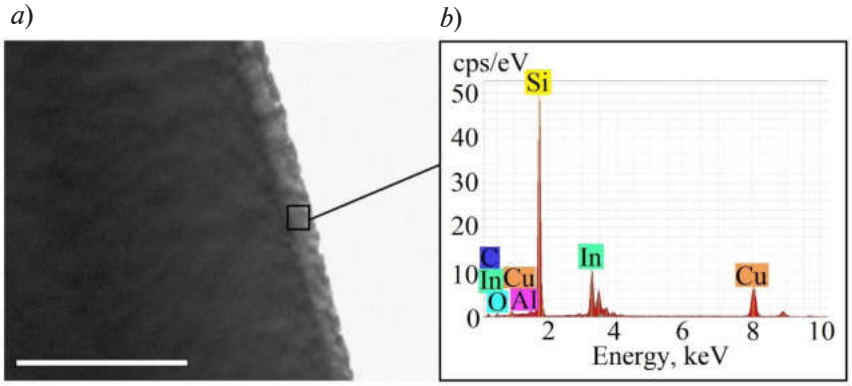

Fig. 2. TEM image of wire covered with ITO (*a*) and EDX spectrum from a section of the side SiNW surface (*b*); the scale bar is 500 nm

wire. The presence of copper and carbon in the EDX spectrum could be due to the experimental procedure of the analyses. Furthermore, the elemental mapping analysis was performed on the SiNW covered with ITO (Fig. 3).

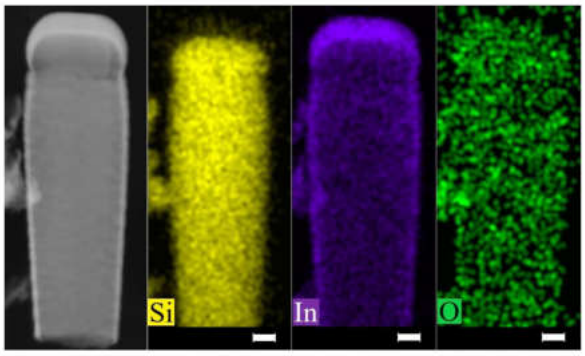

Fig. 3. HAADF STEM image and EDX-elemental mapping analysis on the wire surface

The elemental mapping analysis indicated the uniform distribution of Si, In and O on the wire. Thus, the ITO layer completely covers vertically aligned structures.

The $J-V$ curves and the photovoltaic parameters of the radial *p-i-n* solar cell are shown in Fig. 4, *a* and in Table 2, respectively. Photovoltaic parameters such as V_{OC}, J_{SC} and fill factor (FF) were calculated from illuminated $I-V$ curves. To study the efficiency of the solar cells based on the *p-i-n* structure, EQE curves were measured and are demonstrated in Fig. 4, *b*.

The characteristics of the solar cells based on radial *p-i-n* structures with a SiNWs height of less than 10 μm demonstrate a definite advantage compared to the planar *p-i-n* structure. In terms of V_{OC} radial *p-i-n* structures are practically not inferior to the planar element, and in terms of J_{SC} they are exceeding it. The increase in J_{SC} is associated with the broadening of the EQE spectra, which are shown in Fig. 4, *b*. For solar cell based on the radial *p-i-n* junction, a broadening of the boundary of the EQE spectrum is observed both in the long-wavelength region, but mainly in the short-wavelength region. Moreover, there is a definite dependence of the broadening of the EQE

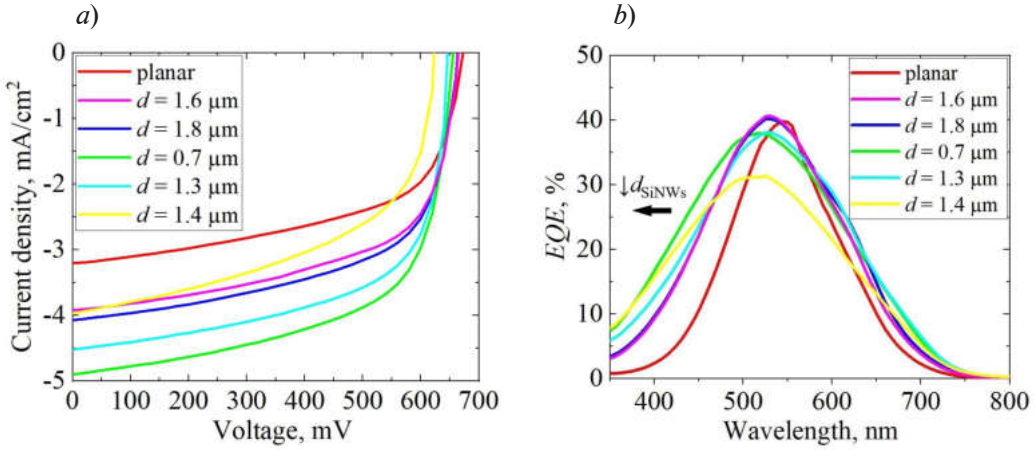

Fig. 4. $J-V$ characteristics (*a*) and EQE spectra (*b*) of solar cells based on *p-i-n* structure; the scale bar is 0.2 μm

Table 2

Photovoltaic characteristics of the radial *p-i-n* solar cells

p-i-n structure		V_{OC}, mV	J_{SC}, mA/cm^2	FF, %
SiNWs				
height, μm	diameter, μm			
~5.3–7	1.6	660	3.9	60
	1.8	660	4.07	60
	0.7	660	4.9	61
~8.5–12	1.3	640	4.52	63
	1.4	620	3.97	52
planar		680	3.22	57

boundary to the short-wavelength region with a decrease in the SiNWs diameter. It is worth noting that for SiNWs with a height of more than 10 μm, there is a decrease in V_{OC} and a decrease in the absolute value of EQE. This is due to the fact that with such a long wire length at its base, light absorption will decrease. This leads to an uneven distribution of charge carriers. This effect was predicted during the computer simulation of the dependence of the solar cell characteristics on the geometry of SiNWs [7]. It has been shown that an increase in wire length leads to a decrease in V_{OC} and saturation of J_{SC}. At the same time, similarly, the critical wires length was about 10 μm, above which the efficiency of solar cells did not increase.

To analysis the causes for the detected dependence of the broadening of the short-wavelength boundary with a decrease in the SiNWs diameter, measurements of the optical properties of the studied structures were mainly carried out. Fig. 5 shows the total reflection spectra of the solar cells based on radial *p-i-n* structures. The dependence of EQE and total reflection on the wires diameter at a wavelength of 400 nm also is presented in right-upper corner. It can be seen that the total reflection in the short-wavelength region of the spectrum almost does not depend on the SiNWs diameter. Therefore, does not affect the position of the short-wavelength boundary. SEM images analysis for *p-i-n* structures deposited on SiNWs with different diameters showed that for them the thicknesses of the *a*-Si:H and ITO layers practically do not differ. It is possible that the expansion is related to optical phenomena, in particular the waveguide phenomenon on vertically aligned structures [10].

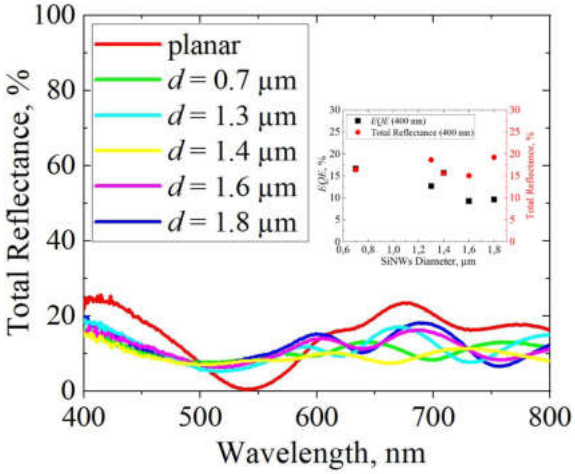

Fig. 5. Total reflection spectra of solar cells based on *p-i-n* structure

Conclusion

In this article, we investigated the influence of the SiNWs geometry on the efficiency of radial *p-i-n* junction solar cell. Solar cell based on vertically aligned structures with a wire height of less than 10 μm are practically not inferior to the planar element in terms of the V_{OC}

and in terms of J_{SC} exceed it up to 1.5 times (3.9-4.9 mA/cm^2). The increase in J_{SC} is associated with the broadening of the EQE spectrum. There is a significant broadening of the EQE boundary to the short-wavelength region with a decrease in the wires diameter. This may be due to the waveguide phenomenon on SiNWs. For solar cells based on vertically aligned structures with a SiNWs height of more than 10 μm, a decrease in the V_{OC} and a decrease in the absolute value of EQE are observed, which is associated with low absorption at the base of the wires.

Acknowledgments

The study was performed with the financial support of Project FSEE-2020-0008, carried out within the framework of State Assignment 075-01024-21-00 of Ministry of Science and Higher Education of the Russian Federation.

REFERENCES

1. Global Market Outlook for Solar Power 2021-2025 – Solar Power Europe. URL: https://www.solarpowereurope.org. Accessed Des. 04, 2022.

2. **Green M.A., Dunlop E.D., et al.,** Solar cell efficiency tables (version 58), Progress in Photovoltaics. 29(7) (2021) 657–667.

3. **Yoshikawa K., Kawasaki H., et al.,** Silicon heterojunction solar cell with interdigitated back contacts for a photoconversion efficiency over 26%, Nature Energy. 2(5) (2017) 17032.

4. **Richter A., Hermle M., Glunz S.W.,** Reassessment of the limiting efficiency for crystalline silicon solar cells, IEEE J. of Photovoltaics. 3(4) (2013) 1184–1191.

5. **Gudovskikh A.S., Morozov I.A., et al.,** Multijunction *a*-Si:H/*c*-Si solar cells with vertically-aligned architecture based on silicon nanowires, Materials Today: Proceedings. 4(7) (2017) 6797–6803.

6. **Gudovskikh A.S., Kudryashov D.A., et al.,** Impact of Interface Recombination on Quantum Efficiency of *a*-Si:H/*c*-Si Solar Cells Based on Si Wires, Physica Status Solidi (a). 2100339.

7. **Kudryashov D.A., Morozov I.A., Gudovskikh, A.S.,** Full Silicon Tandem Solar Cells Based on Vertically Aligned Nanostructures, International J. of Photoenergy. 2022 (2022) 8799060.

8. **Morozov I.A., Gudovskikh A.S., et al.,** The Study of Latex Sphere Lithography for High Aspect Ratio Dry Silicon Etching, Physica Status Solidi. 217 (4) (2019) 1900535.

9. **Vyacheslavova E.A., Morozov I.A., et al.**, Formation of SiO_2 hard mask using dry etching and nanosphere lithography, J. of Physics: Conference Series. 1697 (1) (2020) 012188.

10. **Dan Y., Seo K., et al.,** Dramatic reduction of surface recombination by in situ surface passivation of silicon nanowires, Nano Letters.11(6) (2011) 2527–2532.

THE AUTHORS

VYACHESLAVOVA Ekaterina A.
cate.viacheslavova@yandex.ru
ORCID: 0000-0001-6869-1213

BARANOV Artem I.
itiomchik@yandex.ru
ORCID: 0000-0002-4894-6503

UVAROV Alexander V.
lumenlight@mail.ru
ORCID: 0000-0002-0061-6687

GUDOVSKIKH Alexander S.
gudovskikh@spbau.ru
ORCID: 0000-0002-7632-3194

MAKSIMOVA Alina A.
deer.blackgreen@yandex.ru
ORCID: 0000-0002-3503-7458

Received 14.12.2022. Approved after reviewing 19.01.2023. Accepted 27.01.2023.

Conference materials
UDC 621.383
DOI: https://doi.org/10.18721/JPM.161.331

Formation of ohmic contacts to *n*-$Al_xGa_{1-x}N$:Si layers with a high aluminum content

A.N. Semenov [1] ✉, D.V. Nechaev [1], D.S. Berezina [1], Yu.A. Guseva [1], M.M. Kulagina [1], I.P. Smirnova [1], Yu.M. Zadiranov [1], S.I. Troshkov [1], N.M. Shmidt [1]

[1] Ioffe Institute, St. Petersburg, Russia
✉ semenov@beam.ioffe.ru

Abstract. The paper describes the results of optimizing rapid thermal annealing (RTA) of ohmic contacts to AlGaN:Si layers with a high aluminum content (70 mol%) and various electron concentration. The contact characteristics were measured using the transmission line method (TLM). It has been found that for highly doped $Al_{0.7}Ga_{0.3}N$:Si layers (>10^{18}cm^{-3}), the RTA annealing of Ti(25nm)/Al(80nm)/Ti/Au contact at a temperature 900 °C for 60 s makes it possible to obtain the minimum contact resistance of 8 Ω×mm and specific contact resistivity of 9×10^{-4} Ω·cm^2 with high uniformity over the surface of a 2-inch substrate. For lightly doped $Al_{0.7}Ga_{0.3}N$:Si layers (<10^{17} cm^{-3}), almost the same contact characteristics can be achieved at a higher RTA temperature of about 1000C and an increase in the thickness of the Al contact layer to 250 nm.

Keywords: AlGaN solid alloys, contact resistance, transmission line method, rapid thermal annealing, ohmic contacts

Funding: The work was carried out under the grant of the Ministry of Science and Education of the Russian Federation, agreement No. 075-15-2022-1224.

Citation: Semenov A.N., Nechaev D.V., Berezina D.S., Guseva Yu.A., Kulagina M.M., Smirnova I.P., Zadiranov Yu.M., Troshkov S.I., Shmidt N.M., Formation of ohmic contacts to *n*-$Al_xGa_{1-x}N$:Si layers with a high aluminum content. St. Petersburg State Polytechnical University Journal. Physics and Mathematics. 16 (1.3) (2023) 182–187. DOI: https://doi.org/10.18721/JPM.161.331

Материалы конференции
УДК 621.383
DOI: https://doi.org/10.18721/JPM.161.331

Формирование омических контактов к слоям *n*-$Al_xGa_{1-x}N$:Si с высоким содержанием алюминия

А.Н. Семенов [1] ✉, Д.В. Неч ев [1], Д.С. Березин [1], Ю.А. Гусев [1], М.М. Кул гин [1], И.П. Смирнов [1], Ю.М. З дир нов [1], С.И. Трошков [1], Н.М. Шмидт [1]

[1] Физико-технический институт им. А.Ф. Иоффе РАН, Санкт-Петербург, Россия
✉ semenov@beam.ioffe.ru

Аннотация. Статья описывает результаты оптимизации быстрого термического отжига (RTA) омических контактов к слоям AlGaN:Si с высоким содержанием алюминия (70 мол.%) и различной концентрацией электронов. Контактные характеристики были измерены с использованием метода TLM. Установлено, что для сильнолегированных слоев $Al_{0.7}Ga_{0.3}N$:Si (>10^{18}см$^{-3}$) отжиг контакта Ti(25нм)/Al(80нм)/Ti/Au при температуре 900 °C в течение 60 с позволяет получить минимальное контактное сопротивление 8 Ом×мм и удельное контактное сопротивление 9×10^{-4} Ом·см^2 при высокой однородности по поверхности 2-дюймовой подложки. Для слаболегированных слоев $Al_{0.7}Ga_{0.3}N$:Si (<10^{17} см$^{-3}$) практически такие же контактные характеристики могут быть достигнуты при

более высокой температуре RTA-отжига (~1000 °C) и увеличении толщины контактного слоя Al до 250 нм.

Ключевые слова: твердые растворы AlGaN, контактное сопротивление, TLM-метод, быстрое термическое вжигание контактов, омический контакт

Финансирование: Работа выполнена в рамках гранта министерства науки и образования РФ соглашение № 075-15-2022-1224.

Ссылка при цитировании: Семенов А.Н., Нечаев Д.В., Березина Д.С., Гусева Ю.А., Кулагина М.М., Смирнова И.П., Задиранов Ю.М., Трошков С.И., Шмидт Н.М. Формирование омических контактов к слоям *n*-$Al_xGa_{1-x}N$:Si с высоким содержанием алюминия // Научно-технические ведомости СПбГПУ. Физико-математические науки. 2023. Т. 16. № 1.3. С. 182–187. DOI: https://doi.org/10.18721/ JPM.161.331

Introduction

Photodetectors operating in the solar-blind ultraviolet (UV) wavelength range of less than 290 nm, are typically based on diode structures containing $Al_xGa_{1-x}N$ layers with a high content of Al ($x \geq 0.5$) [1, 2]. Due to the difficulty of *p*-type doping such layers in *p-i-n* photodiodes, Schottky photodiodes with only *n*-type AlGaN:Si layers are an attractive alternative [3]. However, the performance of these devices deteriorates greatly with an increase in both the resistivity of bulk layers and the resistivity of ohmic contacts to them. In AlGaN alloys with $x \geq 0.6$, the former effect is due to an increase in the donor activation energy and enhanced generation of compensating defects in the layer [4–5]. Titanium and aluminum with low work functions (~4.3 eV) are commonly used to make ohmic contacts to III-N compounds. The difficulties in obtaining low contact resistance with increasing Al content in the AlGaN:Si layers are associated with a decrease in their electron affinity to values much lower than the work function of titanium contact layer. This leads to the formation of a potential barrier for electrons, which determines the non-ohmic behavior of the standard multi-layer contact Ti/Al/Au/Ti. Only rapid thermal annealing (RTA) of this metal stack at temperatures above 700 °C allows to achieve low-resistive ohmic contacts even for $Al_xGa_{1-x}N$ layers with $x > 0.6$. This occurs due to reaction of Ti with nitrogen in the AlGaN layers, resulting in a formation of Ti-N and Ti-Al-N layers, which increases the electron concentration at the interface [5–7]. However, both titanium and aluminum are highly reactive and tend to oxidize even at room temperature. To solve this problem, a thin layer of Au is usually used to prevent oxidation [5]. To prevent the Au diffusion and the formation of the Al_2Au, a barrier layer is added, which is most often one of these metals: Ti, Ni, Mo, or Pt. [5, 8].

Studies of the above processes have shown that the contact resistance most significantly depends on the Ti/Al thickness ratio and its optimal value for GaN layers and AlGaN layers with a low Al-content is ~1/2.5 [8]. Since there is no general theory of contact to ternary AlGaN, especially for layers with a high Al-content ($x > 0.6$), there is an urgent need for experimental studies of contact resistance in this material.

This paper describes the formation of ohmic contacts to $Al_{0.7}Ga_{0.3}N$:Si layers with different electron concentration using the standard metallization Ti/Al/Ti/Au with different Al thickness and parameters of rapid thermal annealing (RTA) varied to minimize the contact resistance.

Materials and Methods

Si-doped $Al_{0.7}Ga_{0.3}N$ layers with a thickness of about 600 nm were grown by plasma-assisted molecular beam epitaxy on AlN/*c*-Al_2O_3 templates with a threading dislocation density of less than $5 \cdot 10^9$ cm^{-2}, as described in [9]. The layers were grown at metal-rich conditions with periodic growth interruptions to achieve an atomically smooth droplet-free surface of AlGaN layers [10]. The temperatures 1240 and 1290 °C of a solid-state Si effusion cell were used to change the electron concentration in the layers.

Mesa-structures for measuring contact resistance by Transmission Line Method (TLM) were fabricated using contact photolithography and reactive ion-plasma etching in an inductively coupled plasma reactor with a high concentration of reactive ions and BCl_3 radicals. The structures were metallized using explosive (reverse) photolithography. Metal stacks Ti(25 nm)/Al(80–250 nm)/Ti(60 nm)/Au(100 nm) were deposited by a vacuum thermoresistive sputtering setup. The deposited metal stacks were annealed using STE RTA 100 setup with the annealing temperature varied within 700–1000 °C and the duration 30–180 s. The electron concentrations (n) in the AlGaN:Si layers were determined from CV measurements. For measurements of the resistances by TLM, a Keysight B2901A was used. Fig. 1, *a*) shows identical rectangular pads with the same length d = 100 μm, width W = 300 μm, and different distances between the contact pads L_i = 100, 80, 40 and 20 μm.

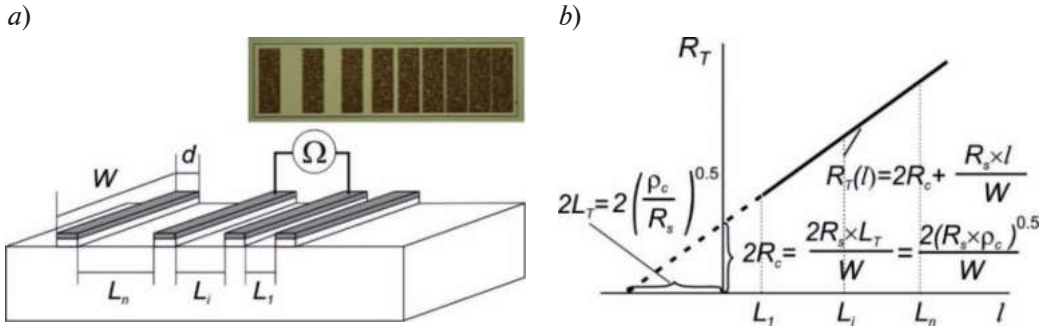

Fig. 1. Schematic illustration of TLM and optical microscope image of the contact pads used in this method (*a*); the dependence of the measured resistances on the distance between the pads (*b*)

Fig. 1, *b* shows the measured total resistance as a function of inter-contact distance $R_T(\ell) = 2R_C + \frac{R_S\ell}{W}$, where $R_C = \frac{R_S L_T}{W}$ is the measured contact resistance, R_S is the sheet resistance of the AlGaN layer, and L_T is the so-called "transfer length" measured from the intersections of interpolation line of $R_T(\ell)$ with abscissa axis [11]. The assumptions of a uniform distribution of R_S over the measurement area and the validity of the inequalities $2L_T < d$, $W >> d$ enabled the relationship for the specific contact resistance $\rho_c = R_S \cdot L_T^2$ Ohm·cm^2 to be invoked. The value $r_c = R_C W$ Ohm·mm was also used to characterize the contact resistance.

Result and discussion

The $Al_{0.7}Ga_{0.3}N$:Si layers grown at the highest temperature of Si-cell of 1290 °C demonstrated electron concentrations above 10^{18} cm^{-3}. Initially, we studied the layers with the contacts having a standard Ti/Al thickness ratio of 1/2.5. The unannealed layers did not demonstrate ohmic contact characteristics. Fig. 2, *a*, *b* show the dependences of r_c and ρ_c of these layers on the RTA temperatures and duration, respectively, which indicate an appearance of ohmic contact at T_{an} above 700 °C and a minimum specific contact resistivity below 10^{-3} Ohm·cm^2 in the layers annealed at a temperature of 900 °C for 60 seconds. A further increase in the temperature did not lead to a significant decrease in the contact resistance, but the surface morphology of the contact pads deteriorated (see Fig. 2, *c*). The optimal RTA duration of 60 s was chosen due to enormous inhomogeneity of the contact resistance over the sample surface at shorter durations of RTA and its increase at longer durations, as shown in Fig. 2, *d*).

In addition, we compared the obtained results with the contact characteristics for the GaN:Si layer with $n > 10^{18}$ cm^3 and the same contacts annealed at the optimal RTA regimes (t_{an} = 60 sec and T_{RTA} = 900 °C). The binary layers showed significantly lower values of r_c = 0.1 Ohm×mm and $\rho_c = 5\cdot10^{-6}$ Ohm·cm^2.

These results are consistent with the general view on the formation of ohmic contacts in AlGaN layers with a high aluminum content, where this process is hindered by lower electron affinity of ternary alloys compared to work function of titanium, while this problem is completely absent in binary GaN. Moreover, the appearance of an ohmic contact, according to the literature data [4,5], is associated with the diffusion of nitrogen atoms from AlGaN into Ti layer. The contact

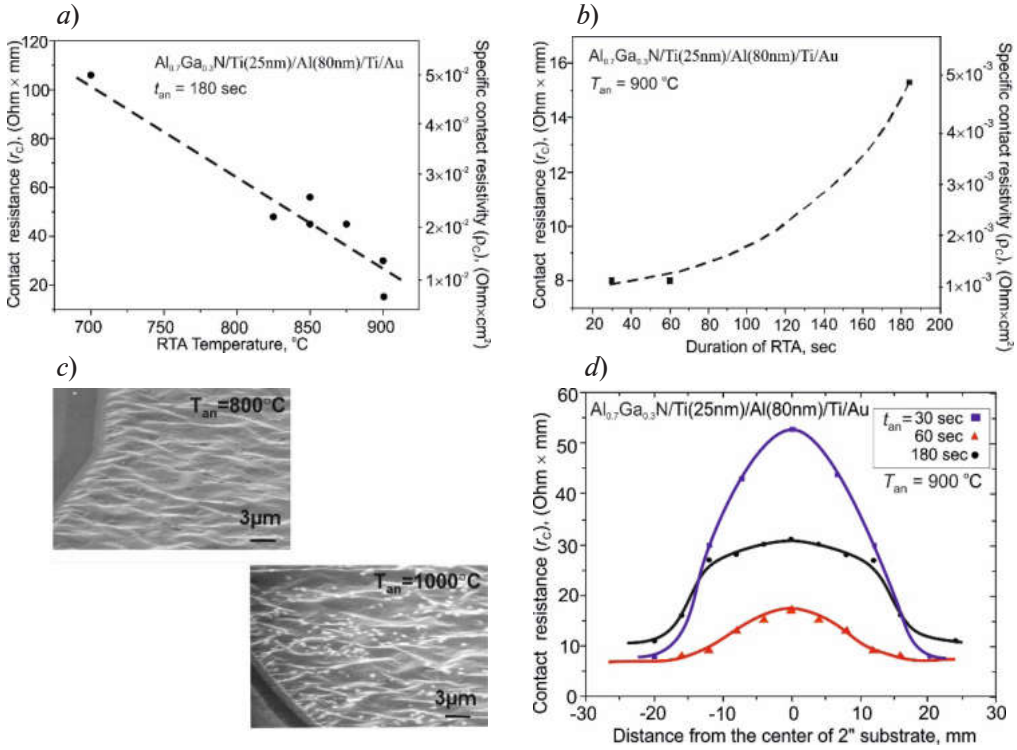

Fig. 2. Dependences of the contact resistance (r_c, Ohm·mm) and specific contact resistivity (ρ_c, Ohm·cm^2) on RTA temperature (*a*) and duration of RTA at 900 °C (*b*). SEM images of the contact surface (*c*). Distributions of contact resistances over the areas of the two-inch substrates (*d*). The dots are the experimental results, the lines are the approximations

improvement is associated with the appearance of nitrogen vacancies near the metal interface. These vacancies create donor states, pinning the Fermi level and thus creating a tunnel junction, which reduces the contact resistance. The described diffusion is able due to the higher enthalpy of formation of TiN compared to GaN (–265.5 and –110.9 kJ/mol, respectively), but it must be considered that the higher enthalpy of formation of AlN (–318.8 kJ/mol) restricts the extraction of N from AlGaN layers compared to GaN ones. These values explain the fact that even under optimal conditions for RTA of the Ti/Al/Ti/Au contact stacks, the difference between contact resistances of the $Al_{0.7}Ga_{0.3}N$:Si and GaN:Si layers exceeds three orders, and further process optimization is required.

Next, we investigated $Al_{0.7}Ga_{0.3}N$:Si layers doped using a low Si-cell temperature of 1240 °C, which resulted in an electron concentration lower than 10^{17} cm^{-3}. Figure 3, *a* shows the strong dependences of r_c and ρ_c on the Al thickness in the Ti(25 nm)/Al/Ti/Au contact stacks deposited on these layers. They demonstrate a decrease in contact resistance by more than 5 times with an increase in Al thickness from the standard value of 80 nm to 240 nm with Ti/Al thickness ratios of 2.5 and 10, respectively.

On the other hand, too strong interaction of Ti with AlGaN at high T_{an} can result in local transformation of the AlGaN ternary alloy into the highly defected Al + Ti + N phase, increasing the contact resistance. Therefore, a way must be found to decrease the high reactivity of Ti, and its reaction with the upper Al in the metallization stack can play this role. Indeed, Al in metallization schemes can alloy with Ti layer below, leading to reducing its reactivity. This mechanism explains the influence Al thickness on contact resistance in $Al_{0.7}Ga_{0.3}N$:Si/Ti/Al/Ti/Au contacts with a relatively low electron concentration below 10^{17} cm^{-3}.

The proposed model is confirmed by comparative measurements of the temperature dependences of the contact resistances of heavily (> 10^{18} cm^{-3}) and lightly (< 10^{17} cm^{-3}) Si-doped $Al_{0.7}Ga_{0.3}N$ layers with the same Ti(20 nm)/Al(250 nm)/Ti/Au contacts. Fig. 3, *b*) shows that only the latter layer shows a clear temperature dependence in the T_{an} = 900–1000 °C range, while its counterpart doesn't reveal such dependence.

It should be noted that $Al_xGa_{1-x}N$:Si layers with $x > 0.7$ used in sub-250 nm UVC- LED and

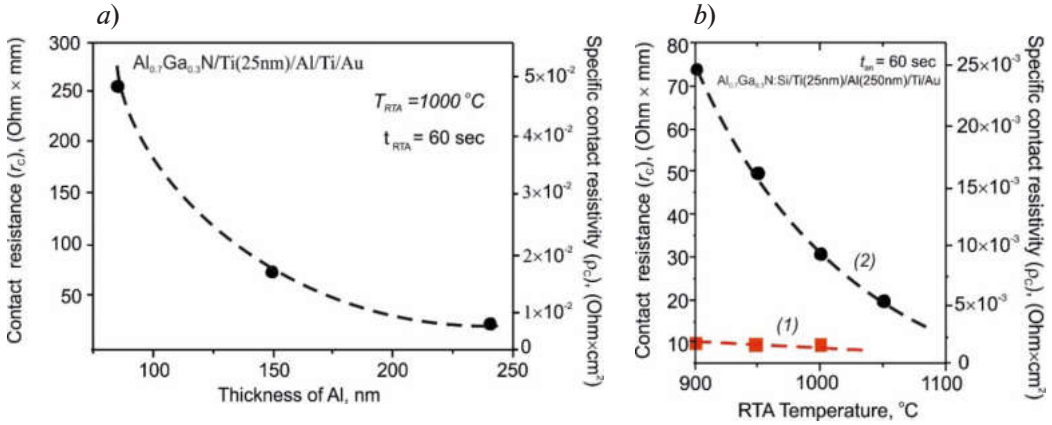

Fig. 3. Dependence of contact and specific resistance on the thickness of the aluminum (*a*). Dependence of $Al_{0.7}Ga_{0.3}N$ contact and specific resistance on the RTA temperature for: *1* – $n > 10^{18}$ cm^{-3}; *2* – $n < 10^{17}$ cm^{-3} (*b*)

photodetectors usually have an electron concentration below 10^{17} cm^{-3} due to high activation energy of Si-dopant in such layers. Therefore, the results obtained in this work for lightly doped AlGaN layers will be useful for designing of these devices.

Conclusion

The technologies of the forming Ti/Al/Ti/Au ohmic contacts to $Al_{0.7}Ga_{0.3}N$:Si layers with electron concentration from below 10^{17} cm^{-3} to higher than 10^{18} cm^{-3} have been optimized. The best results were obtained for Ti(25 nm)/Al(80 nm)/Ti/Au contacts annealed by RTA at a temperature of 900 °C for 60 sec. These conditions provided minimum values of a contact resistance of 8 Ohm·mm and a specific contact resistivity of 9×10^{-4} Ohm·cm^2 with a reasonable uniformity over a 2-inch substrate. It has been established that increasing the RTA temperature up to 1000 °C and Al thickness in metallization stack up to 250 nm improve contact characteristics in lightly doped $Al_{0.7}Ga_{0.3}N$:Si layers.

Acknowledgments

The authors are thankful to the Ministry of Science and Education of the Russian Federation, agreement No. 075-15-2022-1224.

REFERENCES

1. **Razeghi M.,** Short-wavelength solar-blind detectors-status, prospects, and markets Proceedings of the IEEE, 90 (2002), 1006–1014.

2. **Rehm R., Driad R., Kirste L., Leone S., Passow T., Rutz F., Watschke L., Zibold A.,** Toward AlGaN Focal Plane Arrays for Solar Blind Ultraviolet Detection Phys. Status Solidi A, 1900769 (2019) 1–6.

3. **Tut T., Biyikli N., Kimukin I., Kartaloglu T., Aytur O., Unlu M.S., Ozbay E.,** High bandwidth-efficiency solar-blind AlGaN Schottky photodiodes with low dark current Solid-State Electronics, 49 (2005) 117−122.

4. **Liang Y.-H., Towe E.,** Progress in efficient doping of high aluminum-containing group III-nitrides. Appl. Phys. Rev. 5 (2018) 011107.

5. **Van Daelea, Van Tendeloo G., Ruythooren W., Derluyn J., Leys M.R., Germain M.,** The role of Al on Ohmic contact formation on n-type GaN and AlGaN/GaN Appl. Phys. Lett 87 (2005) 061905.

6. **Iucolano F., Greco G., Roccaforte F.,** Correlation between microstructure and temperature dependent electrical behavior of annealed Ti/Al/Ni/Au Ohmic contacts to AlGaN/GaN heterostructures. Appl. Phys. Lett. 103 (2013) 201604.

7. **Nebauer E., Osterle W., Hilsenbeck J., Wurfl J., Klein A.,** XTEM and TFXRD investigations of ohmic Ti/Al/Ti/Au/WSiN contacts on AlGaN/GaN HFET layer systems. Semicond. Sci. and Technol. 17 (2002) 249−254.

8. **Motayed A., Bathe R., Wood M.C., Diouf O.S., Vispute R.D., Mohammad S.N.,** Electrical, thermal, and microstructural characteristics of Ti/Al/Ti/Au multilayer Ohmic contacts to *n*-type GaN. J. Appl. Phys. 93 (2003) 1087−1094.

9. **Nechaev D.V., Koshelev O.A., Ratnikov V.V., Brunkov P.N., Myasoedov A.V., Sitnikova A.A., Ivanov S.V., Jmerik V.N.,** Effect of stoichiometric conditions and growth mode on threading dislocations filtering in AlN/*c*-Al_2O_3 templates grown by PA MBE. Superlattices and Microstructures 138 (2020) 106368.

10. **Nechaev D.V., Brunkov P.N., Troshkov S.I., Jmerik V.N., Ivanov S.V.,** Pulsed growth techniques in plasma-assisted molecular beam epitaxy of $Al_xGa_{1-x}N$ layers with medium Al content (x = 0.4–0.6) J. Crystal. Growth 425 (2015) 9.

11. **Reeves G.K., Harrison H.B.,** Obtaining the specific contact resistance from transmission line model measurements. IEEE Electr. Dev. Leter. 3 (1982) 111–113.

THE AUTHORS

SEMENOV Aleksey N.
semenov@beam.ioffe.ru

NECHAEV Dmitrii V.
nechayev@mail.ioffe.ru

BEREZINA Daria S.
dariya.burenina@mail.ioffe.ru

GUSEVA Yulia A.
Guseva.Julia@mail.ioffe.ru

KULAGINA Marina M.
Marina.Kulagina@mail.ioffe.ru

SMIRNOVA Irina P.
Irina@quantum.ioffe.ru
ORCID: 0000-0003-3746-5170

ZADIRANOV Yurii M.
Zadiranov@mail.ioffe.ru

TROSHKOV Sergei S.I.
S.Troshkov@mail.ioffe.ru

SHMIDT Natalia M.
Natalia.Shmidt@mail.ioffe.ru

Received 14.12.2022. Approved after reviewing 23.01.2023. Accepted 31.01.2023.

Novel materials

Conference materials
UDC 3937
DOI: https://doi.org/10.18721/JPM.161.332

Switchable supercavity modes in metasurfaces based on phase change materials

A.A. Kutuzova [1] ✉, M.V. Rybin [1,2]

[1] ITMO University, St. Petersburg, Russia;

[2] Ioffe Institute, St. Petersburg, Russia

✉ a.kutuzova@metalab.ifmo.ru

Abstract. The paper considers a switchable high-index metasurface made of $Ge_2Sb_2Te_5$ compound. Varying the lattice spacing between the scatterers, we examined the fundamental dipole-type mode defining the metamaterial properties. At a certain lattice spacing, the structure has the reliable resonance in spectrum for the case of crystalline phase of $Ge_2Sb_2Te_5$, while the resonance in the case of amorphous phase degrades completely.

Keywords: bound states in the continuum (BIC), supercavity modes, metasurface, GST

Funding: RNF 21-19-00677.

Citation: Kutuzova A.A., Rybin M.V. Switchable supercavity modes in metasurfaces based on phase change materials, St. Petersburg State Polytechnical University Journal. Physics and Mathematics. 16 (1.3) (2023) 188–191. DOI: https://doi.org/10.18721/JPM.161.332

Материалы конференции
УДК 3937
DOI: https://doi.org/10.18721/JPM.161.332

Переключаемые суперрезонансные состояния в метаповерхностях на основе материалов с фазовой памятью

А. А. Кутузов [1] ✉, М.В. Рыбин [1,2]

[1] Университет ИТМО, Санкт-Петербург, Россия;

[2] Физико-технический институт им. А.Ф. Иоффе РАН, Санкт-Петербург, Россия

✉ a.kutuzova@metalab.ifmo.ru

Аннотация. Мы исследуем переключаемуя высокоиндекснуя метаповерхность на основе соединения $Ge_2Sb_2Te_5$. Мы изменяем параметр решетки между рассеивателями и исследуем основную моду дипольного типа, определяющую метаматериальные свойства структуры. При определенном периоде решетки система поддерживает резонансное состояние для случая кристаллической фазы $Ge_2Sb_2Te_5$, тогда как в случае аморфной фазы резонанс полностью деградирует.

Ключевые слова: связанные состояния в континууме (ССК), суперрезонансные моды, метаповерхность, GST

Финансирование: РНФ 21-19-00677.

Ссылка при цитировании: Кутузова А.А., Рыбин М.В. Переключаемые суперрезонансные состояния в метаповерхностях на основе материалов с фазовой памятью // Научно-технические ведомости СПбГПУ. Физико-математические науки. 2023. Т. 16. № 1.3. С. 188–191. DOI: https://doi.org/10.18721/ JPM.161.332

Introduction

The problem of electromagnetic waves confinement in small volume has a great applied potential for creating sensors, lasers, modulators, and other nonlinear devices. The study of high-quality (Q) resonance modes provides an opportunity to find a solution.

Recently, considerable attention has been paid to research of bound states in the continuum (BIC), which appeared to be perfect resonances with no radiation losses into free space [1]. It was established theoretically that no perfect resonances can exist in finite structures given that permittivity does not take extremal values. However, practical systems still allow for BIC-related supercavity modes with a high-Q factor limited by saturation due to size.

Metasurfaces made of high-index materials were reported to support BIC caused by Mie resonances arising in individual structural elements [2]. Many promising photonic devises require elements with switchable optical properties [3]. Composite phase transition materials based on the Ge-Sb-Te (GST) compound attract significant interest because of high modulation of dielectric index with non-volatile transition between crystalline and metastable amorphous phases. The most studied compound, $Ge_2Sb_2Te_5$, exhibits a change in dielectric permittivity from 15 (amorphous phase) to 35 (crystalline) in the infrared range [3]. Metamaterial properties are known to emerge in periodic systems when the dielectric index of structural elements reaches a certain critical value [4]. Thus, a GST-based structure might become a metasurface supporting BIC under the transition in the phase change material.

Results

We have previously studied metasurface-supported supercavity modes. The metasurface consists of silicon cylinders with a circular profile [5]. In this work, we consider a metasurface containing parallel composed of GST microblocks which have the width $w = 300$ μm, the height $h = 300$ μm and the lattice constant $a = 750$ μm (Fig. 1). The metasurface is shown in Fig. 1. We study TE polarized waves, that is, the electric field oscillates along the axis z. In contrast to cylindrical structural elements, allowing to describe the system analytically, metasurfaces made of $Ge_2Sb_2Te_5$ composite microblocks with a square profile represent a system with a more technologically accessible configuration for lithographic methods.

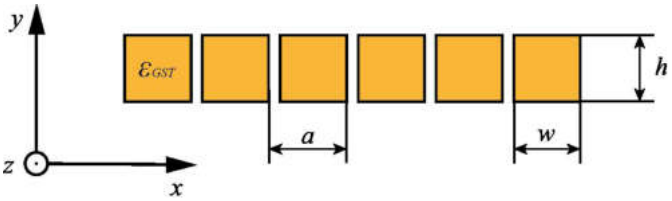

Fig. 1. Schematic view of GST metasurface composed of microblocks with rectangular profile

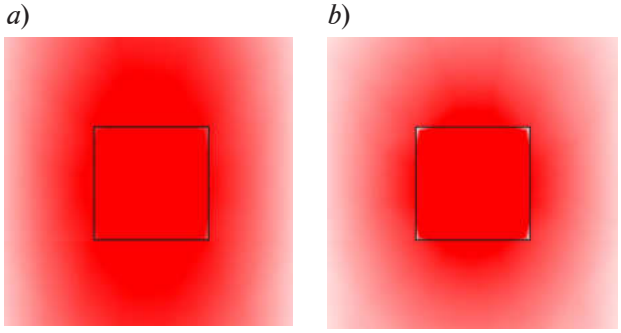

Fig. 2. Magnetic field distribution of the dipole type mode for amorphous GST phase (*a*) and crystalline GST phase (*b*). TE polarization, $a = 1.75$ mm, $h = 500$ μm, $w = 500$ μm

Here we consider a dipole-type mode supported by the structure. Fig. 2 compares magnetic field distribution for crystalline and amorphous GST microblocks which were simulated with COMSOL Multiphysics software. We assume that GST permittivity in the terahertz spectral range has no losses, $\varepsilon = 35$ in the crystalline phase and $\varepsilon = 15$ in the amorphous phase with no frequency dispersion. The block with a higher index exhibits stronger field localization, since the mode frequency is lower and near-field penetration into the outer space is linear to the wavelength in vacuum.

We analyze the reflection spectra of the metasurface whose properties are related to the dipole resonance sustained by each structural element, which is a GST microblock. Since the modes lie under the light cone, we shift half of the blocks by $a/20$ along the x direction. The spectra were simulated by means of rigorous coupled wave analysis (RCWA) involving over 100 plane waves in the x direction, which is sufficient for reliable convergence.

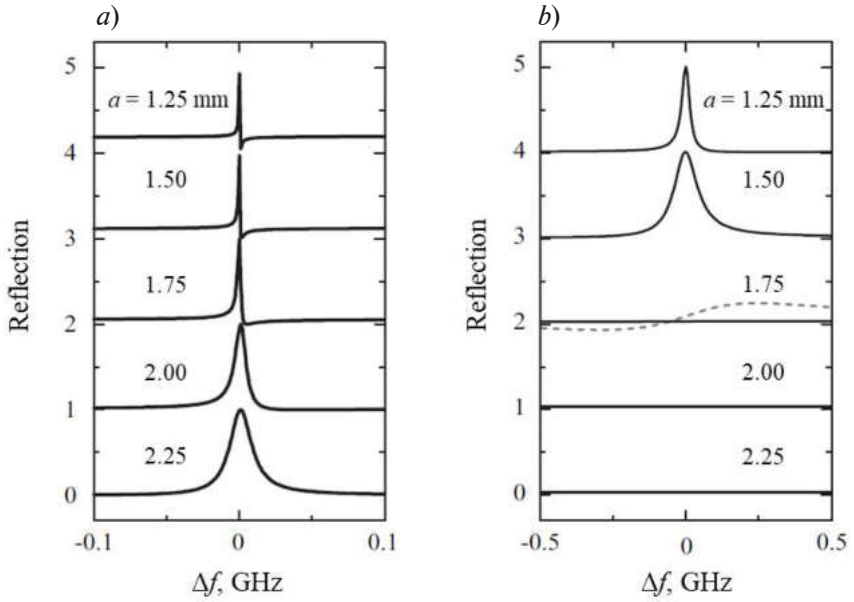

Fig. 3. Reflection spectra of GST-based metasurfaces as a function of lattice spacing: amorphous phase of GST (a) and crystalline phase of GST (*b*). The spectra are shifted along the vertical axis for convenience. The horizontal axis is the frequency detuning. The additional reflection spectra of the structure with a = 1.75 mm are shown in panel (*b*) at 50x magnification (dashed curve)

Fig. 3 shows the reflection spectra around the resonance depending on the lattice spacing a, while the sizes of microblocks are kept unchanged. The resonance position shifts to lower frequencies with an increase in lattice spacing (Fig. 4). For the case of crystalline GST, the dipole peak in reflection is clearly seen in the entire range of the lattice spacing from 1.25 to 2.25 mm. The quality factor of the mode decreases with a. The amorphous GST structure exhibits a different dependence. The dipole peak is observed in the structures with $a < 1.75$ mm and disappears for greater lattice spacings. At a = 1.75 mm, the resonance can be recognized with a 50x magnification. Thus, the structure ceases to be a metasurface operating due to dipole resonance.

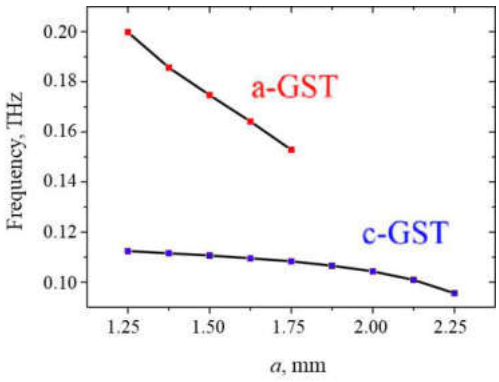

Fig. 4. Shift of the dipole resonance with a change in the lattice period for both amorphous and crystalline phases. The data was calculated with RCWA solver

When the distance between neighboring microblocks is small, a collective mode is formed and the structure acts as a metasurface. For large distances, the microblocks scatter the electromagnetic waves almost independently, so they cannot be regarded as a single system. Studies of a dimer [7] and especially photonic phase transitions to a metamaterial regime [4, 6] reveal that there exists a critical distance between the structural elements for a collective mode to form. Fig. 3, *b* shows that the collective dipole mode responsible for the metasurface regime exhibits rapid degradation when the distance approaches the critical distance about $a_{cr} \sim 1.75$ mm. In our structure, the critical distance increases with the dielectric permittivity of the scatterer similar to other systems [4, 6, 7] in spite of stronger localization of the electromagnetic fields in the structural elements. It is therefore possible to switch the system between metasurface and independent scatterer regimes by means of nonreversible transition of GST.

Conclusion

To summarize, we have demonstrated on/off switching for the metasurface regime. The switching is conditioned by amorphous-to-crystalline phase transition of $Ge_2Sb_2Te_5$. It is important

for applications that this transition occurs fast and is nonreversible: that is, the structure does not return to its previous state for arbitrary time after switching. We have found that the chain of amorphous GST microblocks ceases to be a metasurface when the lattice spacing exceeds $a = 1.75$ mm, while crystalline GST microblocks allow for the metasurface regime at least for the lattice spacing $a = 2.5$ mm and larger.

Acknowledgments

This work was supported by the Russian Science Foundation (21-19-00677).

REFERENCES

1. **Han S., et al.,** All-Dielectric Active Terahertz Photonics Driven by Bound States in the Continuum //Advanced Materials. 2019. T. 31. №. 37. C. 1901921.

2. **Kodigala A., et al.,** Lasing action from photonic bound states in continuum //Nature. 2017. T. 541. №. 7636. C. 196-199.

3. **Makarov S.V., et al.,** Light-induced tuning and reconfiguration of nanophotonic structures // Laser & Photonics Reviews. 2017. T. 11. №. 5. C. 1700108.

4. **Li S.V., Kivshar Y S., Rybin M.V.,** Toward silicon-based metamaterials //ACS Photonics. 2018. T. 5. №. 12. C. 4751–4757.

5. **Kutuzova A.A., Rybin M.V.,** Supercavity modes in silicon-based metasurfaces //AIP Conference Proceedings. – AIP Publishing LLC, 2020. T. 2300. №. 1. C. 020074.

6. **Rybin M.V., et al.,** Phase diagram for the transition from photonic crystals to dielectric metamaterials //Nature communications. 2015. T. 6. №. 1. C. 1–6.

7. **Dmitriev A.A., Rybin M.V.,** Combining isolated scatterers into a dimer by strong optical coupling // Physical Review A. 2019. T. 99. №. 6. C. 063837.

THE AUTHORS

KUTUZOVA Aleksandra A.
a.kutuzova@metalab.ifmo.ru
ORCID: 0000-0002-9164-9643

Rybin Mikhail V.
m.rybin@metalab.ifmo.ru
ORCID: 0000-0001-5097-4290

Received 20.12.2022. Approved after reviewing 07.02.2023. Accepted 20.02.2023.

CONFERENCE ORGANIZERS AND SPONSORS

Organizers

Peter the Great St. Petersburg Polytechnic University (SPbPU)
Alferov University, Saint Petersburg
Ioffe Institute, Saint Petersburg
St. Petersburg State University
Russian-Armenian University, Yerevan

Sponsors

Ministry of Science and Higher Education of the Russian Federation (state assignment)
St. Petersburg Electrotechnical University
Tydex LLC, Saint Petersburg

Program Committee

R.A. Suris, Ioffe Institute, St. Petersburg (*Chair*)
D.A. Firsov, Peter the Great St. Petersburg Polytechnic University (*Vice-Chair*)

V.Ya. Aleshkin, Istitute for Physics of Microstructures, Nizhny Novgorod

V.F. Agekyan, St. Petersburg State University

S.Yu. Verbin, St. Petersburg State University

M.M. Glazov, Ioffe Institute, St. Petersburg

A.E. Zhukov, Alferov University, Saint Petersburg

V.I. Zubkov, Saint-Petersburg Electrotechnical University

M.S. Kagan, Institute of Radioengineering and Electronics, Moscow

V.P. Kochereshko, Ioffe Institute, St. Petersburg

I.V. Rozhansky, Ioffe Institute, St. Petersburg

H.A. Sarkisyan, Russian-Armenian University, Yerevan

D.R. Khokhov, Moscow State University

T.V. Shubina, Ioffe Institute, St. Petersburg

Organizing Committee

D.A. Firsov, Peter the Great St. Petersburg Polytechnic University, (Chair)
M.Ya. Vinnichenko, SPbPU, Peter the Great St. Petersburg Polytechnic University (Vice-Chair)
N.Yu. Kharin, SPbPU, Peter the Great St. Petersburg Polytechnic University (*Secretary*)

E.V. Vladimirskaya, SPbPU
T.A. Gavrikova, SPbPU
V.E. Gasumyants, SPbPU
A.Yu. Egorov, Alferov University
V.A. Zykov, SPbPU
V.P. Kochereshko, Ioffe Institute
G.A. Melentev, SPbPU
V.Yu. Panevin, SPbPU
A.D. Petruk, SPbPU
H.A. Sarkisyan, Russian-Armenian University
A.V. Filimonov, Alferov University
V.A. Shalygin, SPbPU
I.I. Schipacheva, SPbPU

Journal

ST. PETERSBURG STATE POLYTECHNICAL UNIVERSITY JOURNAL: PHYSICS AND MATHEMATICS

Vol. 16, No. 1.3, 2023

Founder and publisher: Peter the Great St. Petersburg Polytechnic University

The journal is registered with the Federal Service for Supervision of Communications, Information Technology and Mass Media (Roskomnadzor).
Certificate ПИ ФС77-51457 issued 19.10.2012.

Phone +7 (812) 552-62-16

Website https://physmath.spbstu.ru/

E-mail: physics@spbstu.ru

Typesetting by *N.A. Bushmanova*

Published 30.04.2023. Format 60x84/8. Digital print.

Printer's sheets Print circulation 1000. Order ID .